VOLCANIC FACIES ARCHITECTURE AND EVOLUTION OF MILOS, GREECE

by

Andrew L. Stewart
B.Sc. (Hons) Macquarie University.

UNIVERSITY OF TASMANIA

Submitted in fulfilment of the requirements
for the degree of Doctor of Philosophy

University of Tasmania
Australia
July, 2003

STATEMENT AND AUTHORITY OF ACCESS

This thesis contains no material which has been accepted for a degree or diploma by the University or any other institution and, to the best of my knowledge and belief, no material previously published or written by another person except where due acknowledgement is made in the text of this thesis.

This thesis may be made available for loan and limited copying in accordance with the *Copyright Act* 1968.

Date:

Andrew L. Stewart

ABSTRACT

The volcanic island of Milos Island, Greece, is a relatively small (~151 km^2) but significant portion of the active Southern Aegean Volcanic Arc. Milos comprises an Upper Pliocene-Pleistocene, thick (up to 700 m), and compositionally and texturally diverse succession of calc-alkaline, volcanic and sedimentary rocks that record a transition from a relatively shallow but dominantly below-wave-base submarine setting to a subaerial one. The shallow marine part of the succession hosts several significant epithermal gold deposits.

Twenty-two main submarine and twelve subaerial volcanic, sedimentary and intrusive facies have been identified, and arranged into eleven compositionally and texturally distinct facies associations. The principal volcanic facies are (1) coherent rhyolite, dacite, andesite, basaltic andesite (lavas, domes, cryptodomes, dykes and sills), and associated autoclastic facies (autobreccia, hyaloclastite and intrusive hyaloclastite); (2) submarine and subaerial pyroclastic deposits; and (3) volcanogenic sedimentary facies. The volcanic and intrusive facies are interbedded with a sedimentary facies association comprising sandstone and/or fossiliferous mudstone mainly derived from erosion of pre-existing volcanic deposits. The main facies associations are interpreted to have conformable, disconformable, and interfingering contacts, and there are no mappable angular unconformities or disconformities within the volcanic succession.

The facies architecture indicates depositional environments evolved from below to above the wave base to subaerial in most areas, except at the southeastern sector of the island where more uniform subaerial environments dominated. The architecture of the dominantly felsic-intermediate volcanic succession reflects contrasts in eruption style, proximity to source, depositional environment and emplacement processes. The volcanic facies architecture comprises interfingering proximal (near vent), medial (volcano flanks), and distal (volcano margin) facies associations related mainly to submarine and subaerial felsic cryptodome-pumice cone volcanoes, dacitic to basaltic andesite lava domes and pyroclastic cones. Submarine felsic cryptodome-pumice cone volcanoes are the most voluminous and common type of volcano identified. Submarine explosive eruptions from these centres generated pumiceous gravity-current deposits and thick beds of very coarse, water-settled pumice. In proximal sections, thick felsic pumice breccia intervals were intruded by compositionally similar, porphyritic, rhyolitic and

dacitic cryptodomes and sills.

New SHRIMP U-Pb data from four major volcanic facies, in combination with detailed mapping and facies analysis, have enabled construction of an enhanced, internally consistent time-stratigraphic framework for the evolution of Milos. The volcanic activity began at 2.66 ± 0.07 Ma and has been more or less continuous since then. Subaerial emergence probably occurred at 1.44 ± 0.08 Ma, in response to a combination of volcanic constructional processes and fault-controlled volcano-tectonic uplift. Recent phreatic craters are the youngest (200 BC-200 AD) expressions of volcanism, and are spatially associated with an active, high-enthalpy geothermal field.

The succession contains several significant epithermal, precious and base metal deposits that display a range of textural, mineralogical, and compositional characteristics. The majority of these epithermal ores occur within and at the top a single, submarine felsic cryptodome-pumice cone volcano near the stratigraphic base of the succession. The palaeogeography during mineralisation probably comprised scattered islands (volcanic domes) flanked by shallow-marine areas. A modern analogue for the setting of the epithermal-style mineralisation is the shallow submarine to subaerial volcanic complex of the island of Panarea, in the active Aeolian volcanic arc (Tyrrhenian Sea, Italy).

ACKNOWLEDGEMENTS

This research was supported by an Australian Post Graduate Research Award and the Centre for Ore Deposit Research, University of Tasmania.

I would like to thank my supervisor Associate Professor Jocelyn McPhie for her support, encouragement, advice, and guidance throughout the project. In particular I would like to thank Jocelyn for the invaluable time she spent with me in the field and the effort and patience she took in reviewing my work.

I would like to thank Don Baker (Royal Gold Inc.), George Xydous (Silver & Baryte Ore Mining CO. SA.) and the geological staff of Midas SA. for logistic support in the field.

Special thanks go to Rod and Petrinela Feldtmann for their hospitality at the Kafenio and their availability for discussions on Miloan matters and assistance they provided me while in the field. I would especially like to thank Rod for shareing his invaluable geological knowledge. I would also like to thank Georges Vougioykalakis for providing work-permits and use of unpublished bathymetric maps and Mirko Rinaldi and Claudia Principe for valuable discussions in the field. Marc Norman is thanked for obtaining SHRIMP data at the Australian National University.

Numerous colleagues have cast their critical eye over various chapters in this thesis. These colleagues include Sharon Allen, Kate Bull, Julie Donnelly-Nolan, Greg Ebsworth, Yoshi Goto, Richard Fiske, Vern Manville, Karin Orth, Don Swanson and Setsuya Nakada. They are all thanked for their constructive comments and discussions on early versions of the thesis and helpful critical reviews.

Many people have helped me in various ways throughout this project and I would like to thank them collectively. In particular, Peter Cornish, Fernando Della-Pasqua, Wally Herrmanm, Christine Higgins, June Pongratz, Phil Robinson, Dianne Steffens and Simon Stephens without which this project would not have been possible.

Finally, special thanks are due to my family and my friends for their continued support over the three years of this study.

TABLE OF CONTENTS

This thesis contains a total 252 pages.

Chapter 1
Introduction

1.1 Introduction

The volcanic island of Milos is a relatively small but significant portion of the active Southern Aegean Volcanic Arc (SAVA), Greece. Milos comprises a thick (up to 700 m) compositionally and texturally diverse Upper Pliocene-Pleistocene succession of calc-alkaline volcanic rocks that record a transition from a relatively shallow but dominantly below-wave-base submarine setting to a subaerial one. The felsic-intermediate volcanic succession comprises syn-volcanic intrusions, lavas, domes and volcaniclastic rocks which host several significant epithermal gold deposits. This thesis describes and interprets the volcanic geology of Milos, presenting the first research on the character and geometry of volcanic facies, types of volcanoes and location of volcanic centres, enabling construction of well constrained, internally consistent time-stratigraphic framework for the evolution of Milos.

1.2 Aims and significance

The principal aims of this thesis are:

1. to clarify the volcanic and sedimentary facies architecture of a felsic arc volcanic island that hosts potentially important ore deposits;
2. to interpret the styles and setting of volcanism, including identification of proximal, medial and distal facies associations;
3. to provide age constraints on the longevity of the volcanic field as a whole;
4. to evaluate the genetic links and relationships between volcanism and mineralisation, providing facies models for mineralised felsic volcanic centres and volcanological guides for mineral exploration within submarine-subaerial settings.

The amount of research carried out on felsic volcanic islands or seamounts is much less than that on their mafic counterparts, despite their apparent abundance in mod-

ern oceans and in ancient volcanic terrains. The growth and development of submarine felsic volcanoes are difficult to observe, and records of eruptions are extremely restricted (e.g. 1953–1957 Tuluman eruption, Reynolds et al. 1980; 1952-1953 Myojinsho eruption, Fiske et al. 1998). Volcanological studies rely instead on modern oceanographic submersible surveys (e.g. Yusa 1995; Fiske et al. 2001), bathymetric surveys (e.g. Yusa et al. 1991; Yamamoto et al. 1991) and dredge sampling (e.g. Kato 1987; Wright and Gamble 1999; Wright et al. 2003), or on ancient successions that have been uplifted to subaerial settings (e.g. Fiske and Matsuda 1964; Pichler 1965; de Rosen-Spence et al. 1980; Allen 1992; McPhie and Allen 1992; Kerr and Gibson 1993; Sohn 1995; Allen et al. 1996; Brown et al. 2002). Although there are published descriptions of the wholly submarine or subaerial parts of these felsic volcanoes, there are no comprehensive published descriptions of complete submarine to subaerial successions of volcano construction. This emission is partly due to the fact that these successions can be complex and may be easily eroded therefore are rarely preserved in the geological record.

This thesis addresses a number of specific problems which are relevant to understanding other modern and ancient, transitional shallow submarine-to-subaerial, felsic volcanic successions. At present, knowledge of the internal facies associations and the volcano types that generate them, structures and evolution of felsic volcanic islands is limited. The present study has contributed to a better understanding of the complex facies architecture of felsic volcanic islands by identifying the proximal (near vent), medial (volcano flanks), and distal (volcano margin) volcanic and post-eruptive volcanogenic facies associations related to five main volcano types. In addition, this research documents the setting of syn-volcanic mineralisation of a shallow submarine succession and provides volcanological guides for mineral exploration within these complex felsic volcanic islands.

The most obvious characteristic of these successions is their complexity in terms of the geometry, distribution and character of volcanic facies and overall evolution. To a large extent the facies characteristics vary due to the differences in eruption volume, water depth of the depositional environment (tens to hundreds of metres), vent setting (subaerial or submarine) and inferred eruption mode (effusive, explosive or intrusive). The presence of seawater can have significant effects on eruptive styles and volcanic products of shallow submarine vents, especially in cases involving felsic magmas: (1) the seawater column may exert sufficient confining pressure to suppress explosive ex-

pansion of magmatic volatiles and/or steam (e.g. McBirney 1963); (2) below wave base, particle transport mechanisms are dominated by either water-settled fallout or by gravity flows; (3) lavas and juvenile pyroclasts are rapidly quenched. In addition, submarine settings are at least in part, depocentres so thick accumulations of low-density, water-saturated sediment may be present and sedimentation from intrabasinal and extrabasinal (possibly subaerial) non-volcanic or volcanic sources may occur concurrently. Finally, volcanic centres that are partly subaerial or above-wave-base are easily eroded. These effects are reflected by the facies architecture of shallow submarine successions.

Understanding these complex hybrid successions is particularly important because they may host very sizeable precious and base metal deposits (e.g. Eskay Creek, Roth et al. 1999; Boliden, Allen et al. 1996; Horne, Kerr and Gibson 1993; Lerokis and Kali Kuning, Sewell and Wheatley 1994). Moreover, contemporary seafloor exploration has identified the presence of active hydrothermal systems in these shallow island arc settings (e.g. Panarea, Gamberi et al. 1999; Kavachi and Kana Keoki, McConachy and McInnes, 2001; Conical Seamount, Herzig et al. 1999, Petersen et al. 2002). These shallow submarine ore deposits and active hydrothermal systems are broadly characterised by ore and alteration mineral assemblages that commonly occur in both conventional subaerial epithermal and submarine volcanic-hosted massive sulfide (VHMS) deposits (Hannington and Herzig 2001).

Based on the detailed volcanological and sedimentological studies presented in this thesis, a general model for the development of epithermal mineralisation on Milos will be presented and implications of this model for global exploration strategies will be discussed. In addition to its relevance to mineral exploration, this research explores the complex character of a well-exposed, shallow submarine-to-subaerial volcano-sedimentary succession.

1.3 Location and access

Milos (*'the island of colours'*) is the most south-westerly of the Cyclades group of islands in the Aegean Sea of Greece, lying approximately 150 km southeast of the port city of Piraeus in Athens and 60 km northwest of the island of Santorini (Figure 1.1). Milos is the largest island (Figure 1.2) of the Milos archipelago, covering approximately 151

km², and its rugged coastline is approximately 125 km long. Other islands of the archipelago include Kimolos (35 km²), Polyegos (17 km²) and Antimilos (8 km²). Polyegos and Antimilos are uninhabited.

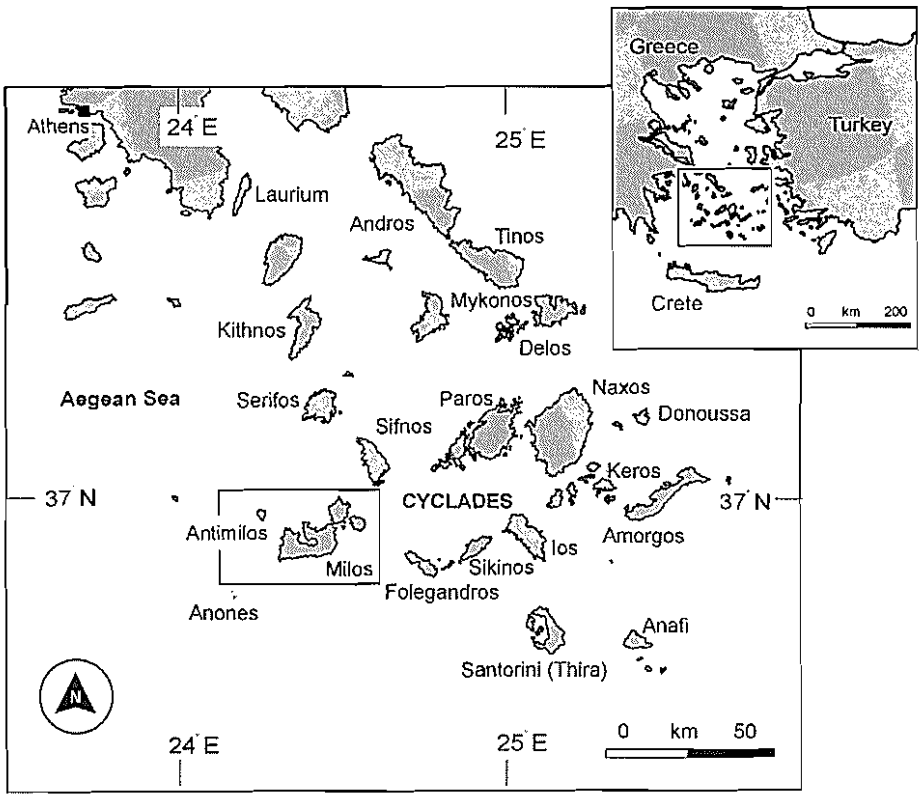

Figure 1.1 Location of Milos archipelago (black box), within the Cyclades group of islands in the Aegean Sea of Greece.

Olympic Airlines operate one flight daily in winter and two in summer months from Athens International Airport. The flight takes approximately 40 minutes. Milos Island can also be reached via high-speed catamaran from Piraeus (4-6 hours depending on ocean conditions), and by conventional ferry (8-10 hours).

1.4 Physiography and exposure

The physiography of Milos Island is characterised by a steep and rugged outer coastline (Figure 1.3A and B) and an inner broad central gulf (Gulf of Milos), which provides a natural harbour, giving the island a horseshoe shape (Figure 1.4). The topography is generally subdued with a maximum elevation of 752 m at Mt Profitis Illias. The geology is generally poorly exposed in the interior of the island, being partly covered by Quater-

nary alluvial deposits particularly in the east. Exposure is also restricted due to locally cultivation and shallowly incised drainage, as a consequence of the Mediterranean climate. However, exposure along the coast is particularly good, providing almost three-dimensional information on facies geometry-a rarely met circumstance. As a consequence, geological mapping was largely restricted to the coastline. Vegetation is sparse and consists of grasses and rare low-lying shrubs.

Figure 1.2 Landsat SPOT (false colour composite) image of the Milos archipelago.

The climate is temperate, typical of the Mediterranean, with a mean annual temperature slightly under 18°C. The average annual rainfall is 400 mm, most of which is restricted to the winter months. Cooling winds, the Cycladic Meltemi, blow from the north almost daily between the summer months of June to late August.

There is a good network of roads on the island. In the north, east and south, most roads are sealed or unsealed and graded. The rugged and remote western sector of the island is uninhabited and restricted to four-wheel-drive access. Small boats may be hired from local fishing villages to gain access to inaccessible ocean cliffs, rock platforms, beaches or uninhabited surrounding islands.

Figure 1.3 Typical landforms and physiography of the Milos coastline. Views looking east along the rugged northern coast west of Firopotamos beach (**A**) and west along the southern coast at Tsigardo beach (**B**).

1.5 Previous work on Milos

Since the discovery of gold mineralisation on Milos in the late eighteen hundreds, several workers have made significant contributions to understanding of the volcanic succession. The earliest published geological investigation of Milos and surrounding islands was carried out by Richard Sonder (Sonder 1924) in 1923. Sonder produced the first detailed geological map using 1:75200 scale British Admiralty bathymetric and topographic maps. Since then, numerous reports and papers have been written on the geology, alteration, mineralisation and geothermal activity. One of the most significant contributions to the interpretation of the volcanic stratigraphy was the production of a 1:25000 geological map by Fytikas (1977), as part of his doctoral thesis, and a series of accompanying reports (Fytikas and Marinelli 1976). This work was later revised by Fytikas et al. (1986), resulting in the subdivision of the volcanic succession into major stratigraphic units.

Figure 1.4 This view from Profitis Illias summit looks northwest across the topographically subdued natural harbour of Milos Gulf.

Several important mineralogical and isotope geochemistry studies were carried out on volcanic rocks on Milos during the late seventies and early eighties, including Fytikas et al. (1976), Innocenti et al. (1981), Barton et al. (1983), Fytikas et al. (1984) and Briqueu et al. (1986). These studies gave rise to a better understanding of the overall compositional variation of stratigraphic units within the volcanic successions on Milos and of the tectonic setting of Milos within the broader framework of the Aegean area.

Numerous mining companies have explored the island over the last decade. The main exploration period started in 1991 and continues to the present. Exploration has resulted in the discovery of several economically significant gold deposits and many prospects. Exploration is ongoing and continues to be successful in defining new mineralised areas. Much detailed prospect-scale mapping was carried by company geologists during exploration and a broad understanding of the stratigraphy, mineralisation and alteration was established and documented in unpublished company reports.

Research on the epithermal gold mineralisation on Milos is limited and comprises a number of published geological, mineralogical and fluid inclusion studies (e.g. Voureadis and Mourabas 1935; Christanis and Seymour 1995; Constadinidou et al. 1998; Kilias et al. 2001). These studies deciphered the mechanisms of gold deposition and addressed the fluid sources by comparing the ancient hydrothermal system with a nearby modern equivalent. Similar important studies have been carried out on the abundant base metal deposits at Cape Vani (e.g. Liatsikas 1955; Liakopoulos 1987; Liakopoulos 2001). Hauck (1988) described the Triades base metal deposit and compared it to the Japanese Kuroko VHMS deposits, prompting Sillitoe (1995) and Vickery (1995) to suggest that this deposit formed by sub-seafloor replacement. Vaveldis and Melfos (1998) and Spartali (1994) considered Triades to be an example of epithermal style-mineralisation.

Studies of the industrial minerals (e.g. alunite, bentonite, montmorillonite and kaolinite) have been prolific and many different authors, including Liatsikas (1955), Bentz and Martini (1968), Wetzenstein (1972), Kelepertsis (1989), Kelepertsis et al. (1990), Christidis and Dunham (1993), Christidis et al. (1995), Christidis (1995), Christidis and Macropoulos (1995), Decher et al. (1996) and Christidis and Dunham (1997), have advocated different models for clay genesis. Much of this detailed research involved understanding the systematic variations in major elements related to hydrothermal alteration in and around active mining operations.

Detailed investigations have been carried out on the active geothermal reservoir beneath Milos (e.g. Fytikas and Marinelli 1976; Mendrinos 1988; Delliou 1989; Fytikas et al. 1989) and on the thermal springs (Minissale et al. 1997). This research contributed to the understanding of geothermal circulation under Milos. Comprehensive descriptions of the offshore hydrothermal activity around Milos occur in Dando et al. (1995), Botz et al. (1996), Fitzsimons et al. (1997), Cronan and Varnavas (1999) and Stuben and Glasby (1999). Much of this recent research on the offshore areas of Milos was concerned with delineating the hydrothermal processes that occur in the shallow-water sectors of arc volcanoes.

A variety of geophysical investigations ranging from gravity (e.g. Thanassoulas 1983, Tsokas 1985, Tsokas 1996), seismological (Ochmann et al. 1989) and self-potential (Thanassoulas 1989) studies have been carried out on Milos. Much of this geophysical research focused on identifying the major tectonic features which have shaped the relief of the metamorphic basement, and the main fault systems associated with the development of the active geothermal system.

1.6 Methods of investigation

This project was mainly field-based and involved systematic field mapping and core logging carried out over the northern hemisphere summers of 2000 and 2001 (approximately nine months in total). Detailed field mapping and logging of key sections were concentrated in domains where exposure is optimum and alteration is minimal. Map data were plotted on to 1:5000 scale Greek topographic maps.

The methods used to achieve the aims are as follows:

1. Regional reconnaissance traverses to establish a general outline of the volcanic facies associations and their distribution and to allow reconciliation with earlier geological maps;
2. Detailed volcanic and sedimentary facies mapping (1:5000) in areas of least alteration, together with diamond drill core and reverse-circulation chip logging (1:200), in order to define the vertical and lateral variations in facies associations; Data recorded included: grainsize, components and mineralogy, primary depositional structures, contact relationships and geometry;

3. Compilation of field data on to 1:5000 scale Greek topographic maps to make regional geological correlations and interpretations;
4. A combination of facies analysis, petrography and whole-rock geochemistry to determine provenance, eruption and emplacement processes, environments and composition;
5. Construction of stratigraphic logs and interpretive facies architecture diagrams;
6. SHRIMP U-Pb zircon dating of four major felsic volcanic units on Milos Island.

1.7 Thesis organisation

In total, this thesis comprises ten chapters. Each chapter addresses one or more of the principal aims of this project. Chapter 1 introduces the main aims of the research topic, location and physiography of the field area and previous work, providing the necessary background for the subsequent chapters. Chapter 2 is an introductory chapter that outlines the tectonic setting and regional geology of Milos. These chapters do not contain new data resulting from this research.

Chapter 3 provides a brief synopsis of the regional geological setting of Milos and outlines the current interpretations of the volcanic stratigraphy.

Chapter 4 presents detailed descriptions and interpretations of the submarine volcanic and sedimentary facies of Milos. Chapters 5 and 6 give detailed descriptions and interpretations of two important facies associations from Milos. Chapter 5 describes the internal structure and geometry of a very well exposed dacitic cryptodome. Chapter 6 discusses the character and origin of a very coarse grained rhyolitic pumice breccia. Chapters 5 and 6 have been published in the Journal of Volcanology and Geothermal Research (Stewart and McPhie 2003) and in the Bulletin of Volcanology (Stewart and McPhie in press) respectively. Chapter 7 presents detailed descriptions and interpretations of the subaerial volcanic facies of Milos.

Chapter 8 explores the facies architecture of Milos. The eruption style, transport and depositional processes, environments of deposition and proximity to source are constrained using textural evidence, depositional structures, contact relationships and facies geometry. A reconstruction of the volcanic facies architecture and evolution of Milos is

presented, incorporating results from U-Pb in zircon age dating.

Chapter 9 focuses on temporal and spatial relationships between the host volcanic facies and ore deposits. Textural and lithological characteristics of the host succession are used to constrain the style and setting of volcanism during mineralisation.

Chapter 10 provides a brief synthesis of the main outcomes of this research.

Chapter 2
Geotectonic setting of Milos in the Southern Aegean Volcanic Arc

2.1 Introduction

The Aegean region lies in an area of extension- and subduction-related tectonics (Jackson 1994). The region has a long geological history with large changes occurring during the Alpine orogeny (Eocene-late Oligocene) and in the Late Tertiary as a consequence of post-collisional extension and major re-adjustments of the plate boundaries. The Aegean region is thought to be moving towards the southwest where the Aegean microplate overrides the African continental plate. The collision has created the Hellenic Trench to the south of Crete where the African continental plate is subducted beneath the Aegean microplate at about 1.5 cm a^{-1}. The active South Aegean Volcanic Arc (SAVA), which lies inboard from the Hellenic Trench, extends from the Greek mainland in the west, through to the islands of Kos and Nisyros in the east (Figure 2.1). The arc is the magmatic expression of active, northward subduction of the African continental plate beneath the Aegean microplate. The volcanic products are calc-alkaline, and range continuously in composition from basalt to rhyolite, with dacite being most common (Fytikas et al. 1984).

This chapter focuses on the tectonic evolution of the Aegean region and provides a brief synopsis of the geotectonic setting of Milos within the complex and poorly constrained framework of the SAVA. It outlines the current interpretations of the Tertiary-Quaternary geological history of the SAVA in time and space.

2.2 Tectonic setting of the Aegean region

The Aegean region is located between the African and European lithospheric plates that converge at a rate of about 1.5 cm a^{-1} (Figure 2.1). It is centred on the small, continental Aegean microplate (McKenzie 1970; Le Pichon and Angelier 1979; Jackson 1994), which incorporates part of mainland Greece, the Greek islands, Crete and west-

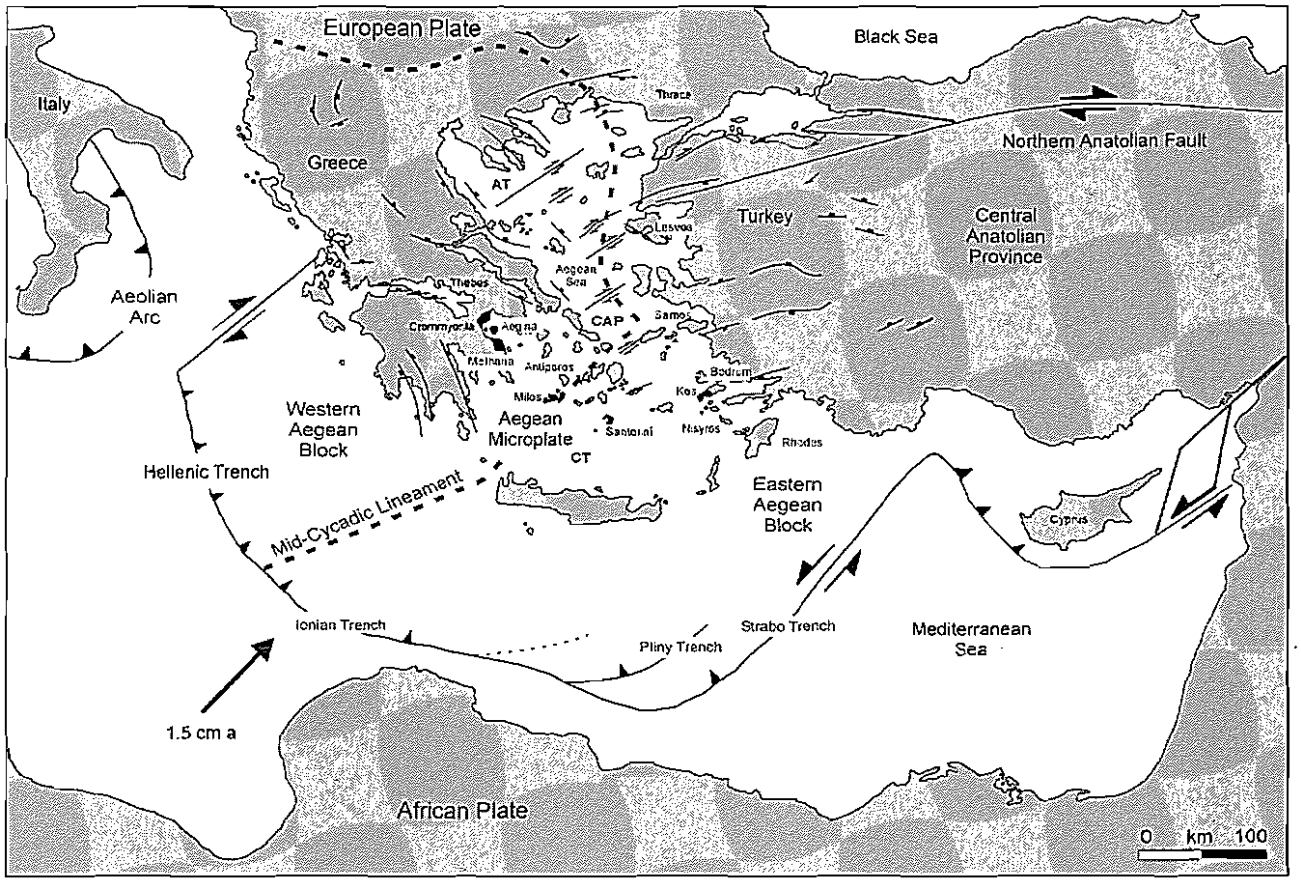

Figure 2.1 Geotectonic map of the Eastern Mediterranean, based on Jackson (1994). The volcanic centres of SAVA (in black) extend from Crommyonia in the west to the islands of Kos and Nisyros in the east. Dashed lines show principal active faults, boxes mark the downthrown-sides of normal faults (Jackson 1994). The position of the Mid Cycladic Lineament is taken from Walcott and White (1998). CT, Cretan Trough; AT, Anatolian Trough; CAP, Central Aseismic Plateau. The arrow in the bottom left is the convergence vector.

ern Turkey. It is perhaps one of the most rapidly deforming parts of the Tethyan (Alpine-Himalayan) collisional system, lying at the confluence of two mountain chains: the Hellenic chain of Greece and the Pontide-Tauride chain of western Turkey (Jackson 1994). Relative to Asia, the Aegean microplate is moving southwest at about 3.5 cm a^{-1} and this is believed to be partly a response to the westward motion of Turkey along the North Anatolian Fault system (Jackson 1994).

The basic framework of the modern Aegean region formed during the final collision of the African and European continental plates in the Oligocene and Early Miocene (McKenzie 1970). In essence, the region was shortened, imparting a strong structural fabric in the form of folds, thrusts and deep sutures which trend NW-SE in mainland Greece, and E-W across the central Aegean (Robertson and Dixon 1984).

Tertiary arc volcanism in the northern Aegean and over much of Turkey (Figure 2.2A) was related to initial subduction of the African plate beneath the European plate (Fytikas et al. 1976). Following this preliminary period of volcanism, lithospheric fragmentation occurred and numerous fault-bounded blocks were subsequently formed (Dewey et al. 1973; Angelier 1979), with markedly contrasting structural trends (Morris and Anderson 1996; Walcott and White 1998; Duermeijer et al. 2000).

The Aegean microplate stabilised in the Middle Miocene, probably in response to the commencement of northward subduction of the African plate beneath the Aegean microplate. The actual age of subduction along the SAVA is a contentious issue. Le Pichon and Angelier (1979) suggested subduction began during the Early Miocene, based on the onset of extensional faulting in the southern Aegean. In comparison, McKenzie (1978), Mercier (1989), and Pe-Piper et al. (1983) proposed a start to subduction as recent as 5 Ma, based on the 5-7 Ma date of both a regional compressional event, and the oldest exposed volcanic rocks related to the current phase of subduction (located on the island of Aegina).

During the Middle-Late Miocene (17-8 Ma), plutons were intruded along the line of the present-day SAVA, synchronous with the late stages of extensional exhumation behind the Hellenic Trench (Figure 2.1; Lee and Lister 1992; Blake et al. 1981). Pluton emplacement accompanied a regional transformation from dominantly compressional tectonics involving over-thickened crust to extension and substantial crustal thinning and

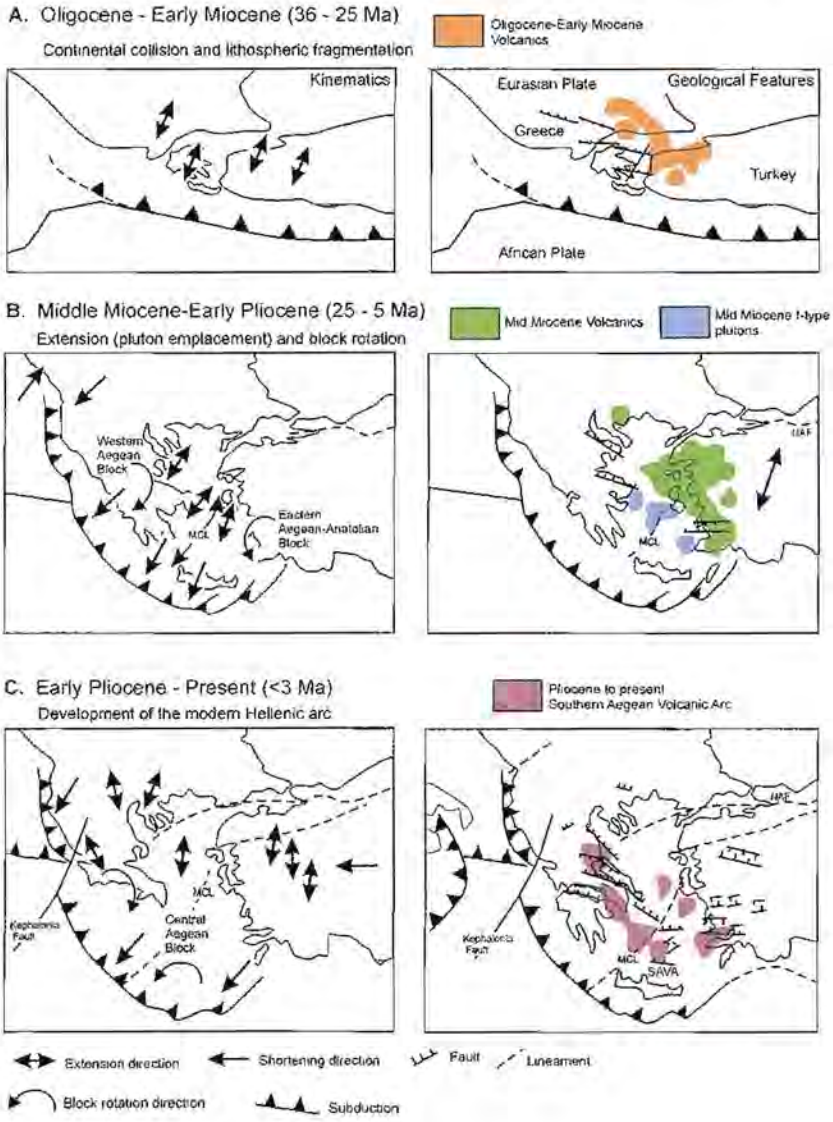

Figure 2.2 Generalised tectonic model for the Cainozoic evolution of the SAVA in the Aegean, after McKenzie (1970), Le Pichon and Angelier (1979), Jackson (1994) and Walcott and White (1998). **A** Following continental collision, regional extension and arc volcanism began during the Late Oligocene and Middle Miocene in northern Greece. **B** In the Middle Miocene, extension took place in the central Aegean. The Mid Cycladic Lineament (MCL) acted as a continental fracture zone, accommodating the rotation of the Western Aegean Block and the Eastern Aegean-Anatolian Block. Volcanism occurred during the late stages of extensional exhumation behind the Hellenic Trench. NAF-Northern Anatolian Fault. **C** The present day Benioff Zone passes south of Crete and dips at an angle of about 30° northeast.

subsidence (Figure 2.2C). Extensional tectonics are thought to reflect a combination of collapse of the over-thickened continental crust and roll-back of the subducting slab (Jolivet et al. 1994), and produced structural and metamorphic characteristics typical of Cordilleran-type metamorphic core complexes (Lister et al. 1984).

The extension direction changed from NE-SW (Late Miocene), to NNE-SSW (Pliocene-Early Pleistocene) and is currently N-S to NW-SE (Mercier et al. 1989). Extension occurred contemporaneously with outward-diverging, clockwise (~30^0) rotation of the Western Aegean Block and anticlockwise (~19^0) rotation of the Eastern Aegean-Anatolian Block (separated by the Mid-Cycladic Lineament, Walcott and White 1998). Subsequently, the Mid-Cycladic Lineament ceased activity and the Northern Anatolian Fault propagated into the northern Aegean area (Walcott and White 1998), forming the Central Aegean Block (Figure 2.2C; Walcott and White 1998).

The present-day Benioff zone passes south of Crete and dips at an angle of about 30^0 northeast. The convergence rate is 1.5 cm a^{-1} (Kalogeropoulos and Paritsis 1990; Jackson 1994) and the subduction direction is northeast. The Hellenic Trench has two main branches (McKenzie 1978; Le Pichon et al. 1979; Angelier et al. 1982). The Ionian Trench strikes almost at right-angles to the subduction direction, whereas the Pliny and Strabo Trenches strike almost parallel to the subduction direction (Figure 2.1).

Continental crust underlies the entire Aegean region (Makris 1978); crustal thicknesses vary from 20 to 32 km. As the crust beneath the rest of Greece and Turkey is 40-60 km thick, McKenzie (1978) estimated that the crustal thickness of the Aegean has been halved by extension in the last 5 Ma. Stretching has been concentrated in two deep grabens, the Cretan and Anatolian troughs. Between these troughs lies the Central Aseismic Plateau, a relatively stable crustal block characterised by low seismicity (Figure 2.1).

The present-day arc volcanoes lie on the faulted southern boundary of the Central Aseismic Plateau. Regionally, the Aegean area has many active faults which are accommodating extension. Faults in the central and northern Aegean are dominated by sets of E-W or ENE-WNW right-lateral strike-slip faults, whereas in the western Aegean and on mainland Greece, NW-SE normal faults are most abundant (Jackson 1994; Figure 2.1).

2.3 Geology of the crystalline basement

The crystalline rocks of the Cycladic Crystalline Complex form the basement of the SAVA. The basement had a complex evolution that may extend back to Proterozoic (Andriessen 1978; Andriessen et al. 1987) and is linked to similar metamorphic rocks of

Central Greece and the Menderes Massif in Turkey (Schliestedt et al. 1987). In the Middle Miocene, numerous plutons were emplaced into the metamorphic complex (Blake et al. 1981).

The Alpine orogeny

The sedimentary and igneous protoliths to the metamorphic rocks are believed to be Late Palaeozoic or Early Mesozoic in age and were laid down on older, Palaeozoic Hercynian basement (Schliestedt et al. 1987). The rocks comprise greenschist and blueschist facies, typically consisting of psammitic schist, chlorite-actinolite and glaucophane schist, marble, dolomite and amphibolite (Blake et al. 1981).

Radiometric dates of metamorphism are available from basement schists on Milos. Muscovite in the blueschist facies gave a K/Ar date of 64.2 Ma, whereas the muscovite in the greenschist facies gave 33.2 Ma (Fytikas et al. 1976). Radiometric dates indicate the basement metamorphic rocks have been subject to at least two main regional metamorphic and deformation events that occurred during the Alpine Orogeny (Altherr et al. 1982): (1) Eocene high-pressure, low-temperature phase (blueschist-facies units); and (2) Oligocene medium-pressure, higher temperature phase (greenschist-facies units; Lister et al. 1984).

Granitoid emplacement during the Miocene

In the Middle Miocene, numerous plutons were intruded over a large area into the Cycladic Crystalline Complex (Figure 2.3; Blake et al. 1981). Pluton emplacement was synchronous with regional extension and mid-crustal detachment faulting (Lee and Lister 1992). Three main groups of plutonic rocks have been recognised: (1) the oldest (17-12 Ma) are granodiorites found in the islands of the central Cyclades (e.g. Tinos, Mykonos, Delos, Naxos, Santorini, Ikaria); (2) of intermediate age (ca. 11 Ma) is a large zoned granodiorite on Serifos; and (3) the youngest (10-8.5 Ma) are small intrusions in the eastern Aegean (e.g. Kos, Samos; Figure 2.3; Blake et al. 1981; Pe-Piper et al. 2002). Most of the plutons have I-type characteristics (Altherr et al. 1982, 1988), although minor small intrusions or dykes of peraluminous granite with S-type characteristics are found on Tinos, Paros, Naxos and Ios (Pe-Piper et al. 2002).

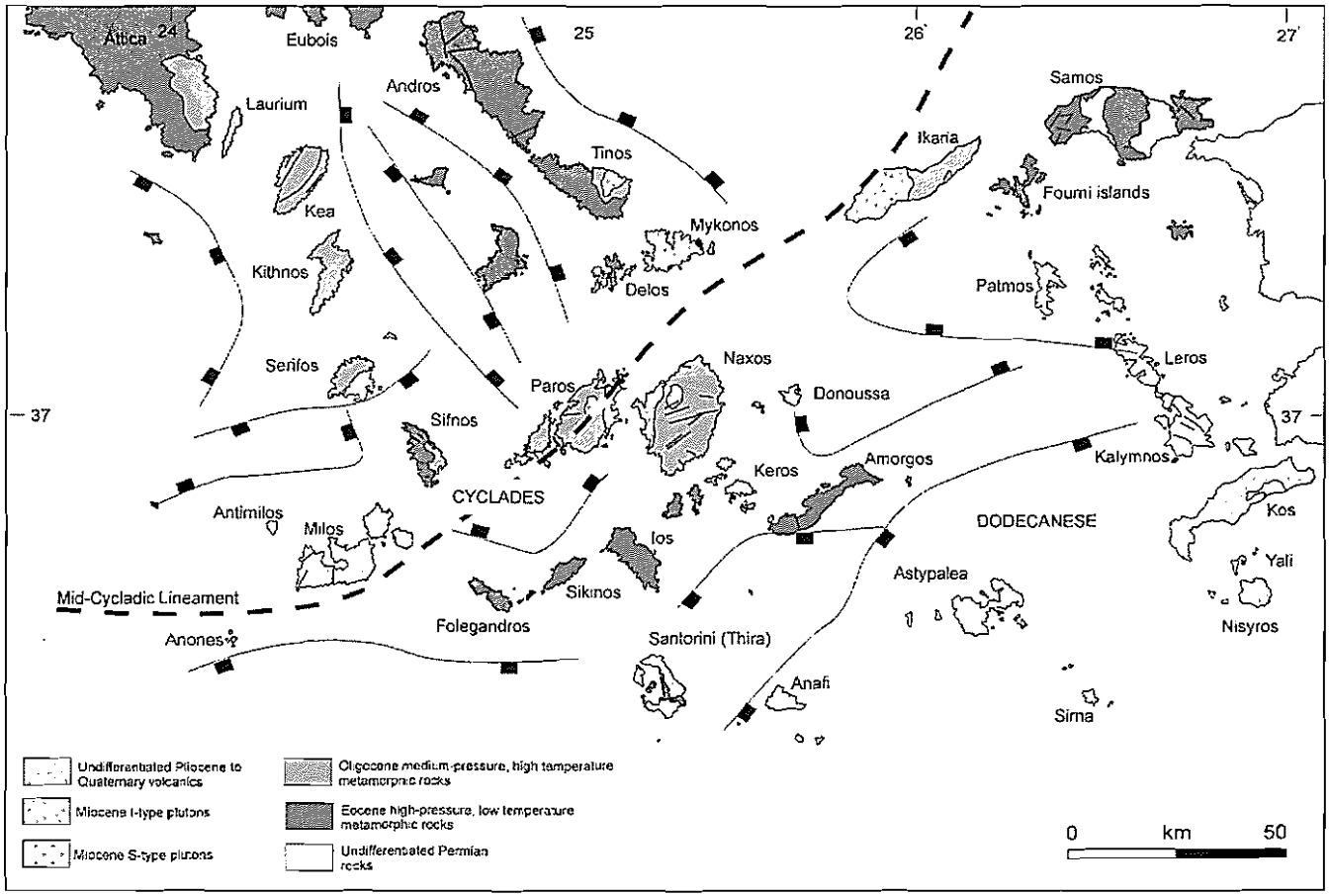

Figure 2.3 Simplified geological map of the southern Aegean, modified after Schliestedt et al. (1987) and Fytikas et al. (1984). The map shows the distribution of the main units of the Cycladic Crystalline Complex, Miocene granitoids and Pliocene to Quaternary volcanic products in the Aegean and Western Anatolia areas. Also shown are the principal active faults (boxes mark the downthrown sides of normal faults) and the location of the Mid-Cycladic Lineament from Walcott and White (1998).

2.4 Volcanism in the Aegean

Widespread volcanic activity has occurred in the Aegean region and western Anatolia since the Oligocene (Fytikas et al. 1984). Two main phases of volcanic activity have been recognised. The first phase of voluminous volcanic activity occurred in the Oligocene and Middle Miocene times (Northern Aegean Tertiary Activity-NATA) and the second started in the Pliocene and continues to the present day (Southern Aegean Volcanic Arc-SAVA; Fytikas et al. 1984). Between the two main episodes of activity, scattered, volumetrically minor Late Miocene volcanism of variable petrogenetic affinity occurred along the main zones of extension at the margins of the Aegean microplate (e.g. Samos and Patmos) in the central Aegean (Fytikas et al. 1984).

Northern Aegean Tertiary Activity (NATA)

The NATA volcanism occurred in a belt extending from continental Greece (Thrace) through the central Aegean (e.g. Limnos and Lesvos) to Central Anatolia in Turkey (Figure 2.4). The NATA developed along the margin of the Rhodope Massif (Fytikas et al. 1984). Geophysical data show that the thickness of the crust is around 40 km (Makris 1977), despite the Neogene extension. The products are mainly intermediate and calc-alkaline or shoshonitic; silicic and mafic compositions are minor (Fytikas et al. 1984).

The Southern Aegean Volcanic Arc (SAVA)

The island of Milos is situated in the central part of the SAVA (Figure 2.1), which is the surface expression of active, northward subduction of the African plate beneath the Aegean microplate. The arc is no more than 20 km wide, and is interpreted to have a double structure: an inner arc stretches from Thebes, through Antiparos, to eastern Kos (Figure 2.4), and an outer arc extends from Crommyonia through Methana, Aegina, Paros, Milos, Santorini, to Nisyros and western Kos. Volcanism occurred concurrently along both segments (Fytikas et al. 1976; Innocenti et al. 1979; Fytikas et al. 1984). Arc volcanism began at the end of the Early Pliocene (McKenzie 1978; Mercier 1989; Pe-Piper et al. 1983; Fytikas et al. 1984). Methana, Milos, Santorini and Nisyros have each had historic eruptions and are best considered dormant. (Keller et al. 1990).

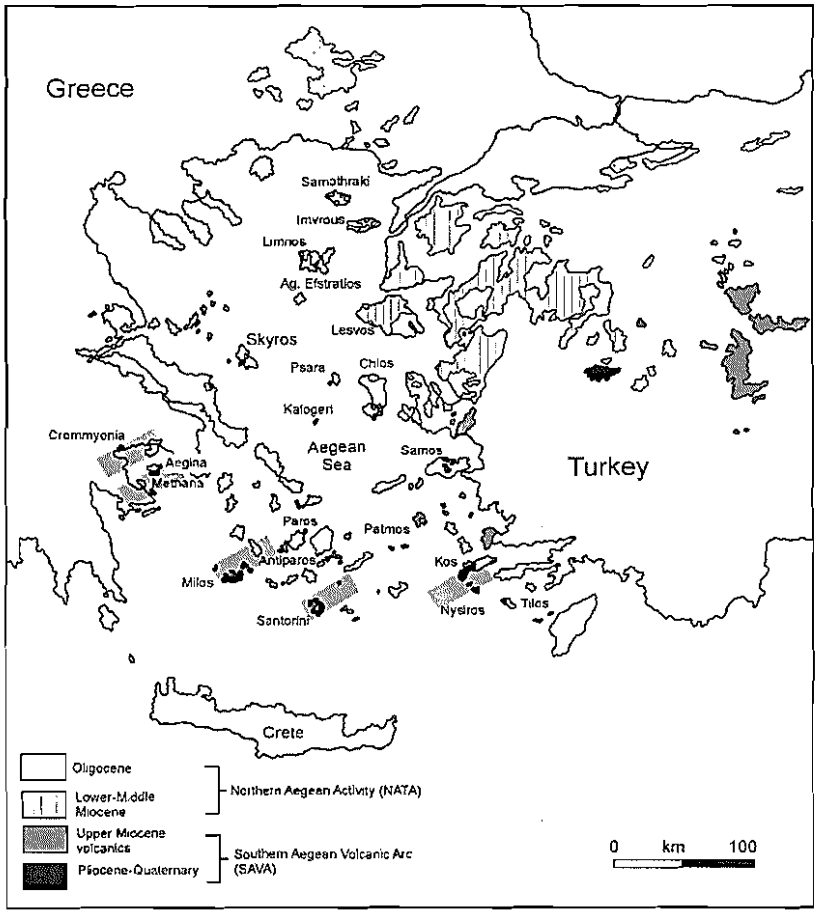

Figure 2.4 Distribution of volcanic products from the Oligocene to present in the Aegean, after Fytikas et al. (1984). Several volcanic centres lie on NE-SW trending fault zones (grey) marked by concentrations of shallow to intermediate depth earthquakes (Papazachos and Panagiotipoulos 1993).

The outer arc volcanoes lie above a Benioff Zone at 130-150 km depth, about 200 km from the Hellenic Trench (Keller 1982; Dewey and Sengör 1979). Fault-plane solutions for earthquakes along the arc are normal in character (McKenzie 1978; Jackson et al. 1982). Therefore, despite the compressive stress regime associated with subduction, the arc has developed in an extensional environment.

The position of the volcanic centres along both arcs is strongly controlled by five NE-SW lithospheric fault zones (Papzachos and Pangiotopoulos 1993). Lava dome complexes occur in the western part of the arc (Aegina, Methana and Milos; Western Aegean Block). In comparison, calderas and composite volcanoes occur in the central and eastern sectors of the arc (Santorini, Kos and Nisyros; Eastern Aegean-Anatolian Block). The variations from east to west along the volcanic arc have been interpreted as an effect of the differences in the lithospheric stress field in the various sectors of the

arc (Fytikas et al. 1984). The local stress field is related to the geometry of the convergent system: the main convergence direction is oblique to parallel to the arc in the central and eastern sectors, respectively, whereas it is orthogonal to the arc in the western sector.

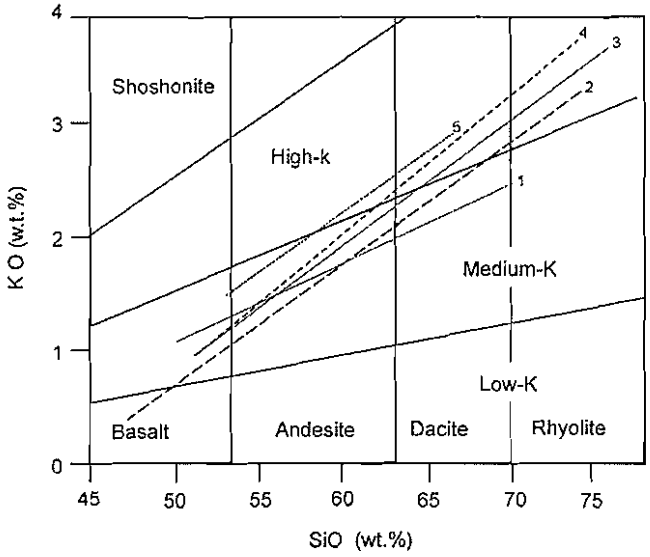

Figure 2.5 K_2O v. SiO_2 diagram for SAVA volcanic centers. Data from Innocenti et al. (1981) for different volcanic centres are represented by best-fit lines. 1-Methana; 2-Milos; 3-Santorini; 4-Nisyros; 5-Aegina.

The volcanic products are calc-alkaline, and range continuously in composition from basalt to rhyolite, although dacite is dominant (Fytikas et al. 1976; Innocenti et al. 1979; Fytikas et al. 1984; Clift and Bluseztajn 1999). The mafic rocks of the SAVA are enriched in Al_2O_3 (>18 wt. %), TiO_2 (>0.9 wt. %), and depleted in K_2O (<4 wt. %; Innocenti et al. 1981). Intermediate and silicic rocks have medium to high K_2O (1.6-4.5 wt. %).

Although lavas within single volcanic centres have trace element ratios consistent with fractional crystallisation, between-island variations in trace element abundances suggest that the subcontinental lithosphere beneath the southern Aegean is rather complex (Mitropoulos et al. 1987). Lavas from the eastern (Nisyros, Kos) and western (Milos, Paros, Aegina, Methana) parts of the arc have higher abundances of Ba and Sr, but lower Th, K and Rb concentrations than Santorini in the centre of the arc (Keller 1982; Mitropoulos et al. 1987).

2.5 Summary

The Aegean region is situated on the small, rapidly moving continental Aegean microplate (McKenzie 1970; Le Pichon and Angelier 1979; Jackson 1994). The main Tertiary phase of collision between the Eurasian and African continental plates was followed by a period of lithospheric fragmentation (Dewey et al. 1973), and numerous microplates were formed. From the Miocene up to the present, these microplates have undergone independent evolution producing a complex neotectonic framework (McKenzie 1972, 1978). The Alpine metamorphic rocks (Cycladic Crystalline Complex) were exhumed during this extension. Granitoids were intruded in the Middle Miocene, during the later stages of extensional exhumation (Lee and Lister 1992; Pe-Piper et al. 2002) and are related to early subduction of the African plate beneath the Aegean microplate (Fytikas et al. 1976).

Widespread volcanic activity has occurred in the Aegean region and western Anatolia since the Oligocene (Fytikas et al. 1984). The first voluminous volcanic activity occurred during the Oligocene in northern Greece (NATA). Subsequently it migrated south-westward through the northern Aegean islands (Early Miocene volcanism) and Cyclades (Miocene I-type plutonism) to the younger SAVA (Pliocene -Quaternary).

The SAVA (no more than 20 km wide) is one of the dominant tectonic features of the Aegean region. The volcanic island of Milos is situated in the central part of the modern SAVA (Figure 2.1), which extends from the Greek mainland in the west, through to the islands of Kos and Nisyros in the east. The products of this arc volcanism are a typical calc-alkaline association which displays a continuous evolution from basalt to rhyolite.

Chapter 3
Regional geology of Milos: an overview

3.1 Introduction

The small archipelago of Milos, which includes the islands of Kimolos, Polyegos and Antimilos, is situated in the central part of the modern Southern Aegean Volcanic Arc. The volcanic succession on Milos was first documented and described by Sonder (1924). The most recent of several attempts (Fytikas and Marinelli 1976; Angelier et al. 1977) at establishing the volcanic stratigraphy on Milos is the systematic study of Fytikas et al. (1986), based on mapping of the island at 1:25 000 scale (Fytikas et al. 1977).

The Milos volcanic succession covers approximately 151 km^2, and has a maximum thickness of 700 m (Figure 3.1; Fytikas and Marinelli 1976). The succession is characterised by submarine and subaerial, calc-alkaline volcanic and submarine sedimentary rocks (Fytikas et al. 1986). The volcanic rocks are predominantly rhyolite and dacite with subordinate andesite and basaltic andesite (Fytikas et al. 1986) and dominated by lava domes and syn-volcanic intrusions interleaved with thick volcaniclastic and sedimentary units. The stratigraphy exposed on Milos shows an upward progression from submarine to subaerial (Fytikas et al. 1986). Locally, the succession hosts epithermal gold ores. These ore deposits occur within a variety of volcanic and sedimentary facies, however, all ores occur at a similar stratigraphic level (Chapter 7).

Although there are strong links between the timing and style of volcanism, and mineralisation on Milos, the internal stratigraphy and distribution of lithostratigraphic groups are poorly constrained. This chapter provides an outline of current interpretations of the volcanic stratigraphy of Milos and a review of the structure, geochronology, mineralisation and geochemistry.

3.2 A review of the existing stratigraphy of Milos

The stratigraphic scheme proposed by Fytikas et al. (1986) is similar to those of Sonder (1924), Fytikas (1977) and Angelier et al. (1977). Most workers agree with this relatively straightforward stratigraphic pattern; however, many refinements have been presented

for particular parts of the stratigraphy (e.g. Campos Venuti and Rossi 1996; Rinaldi and Campos Venuti 2003; Stewart and McPhie 2003; Stewart and McPhie in press), regional inter-island correlations (e.g. Fytikas and Vougioykalakis 1993), and timing of deformation (e.g. Angelier et al. 1977; Kondopoulou and Pavlides 1990).

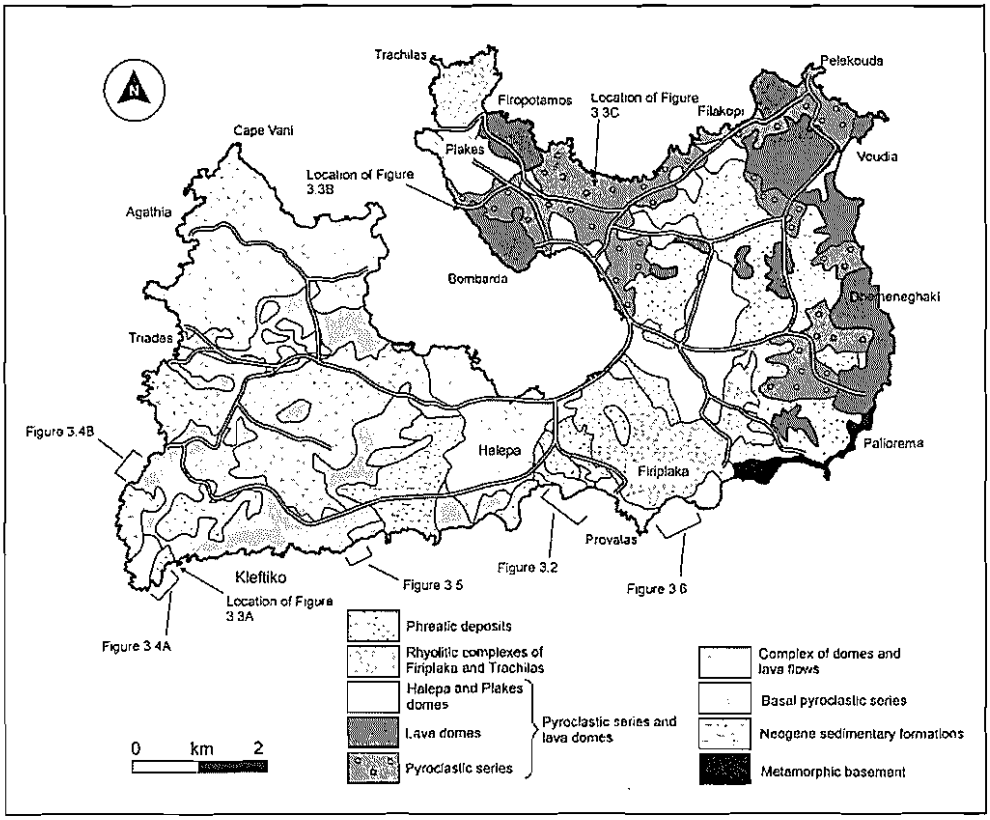

Figure 3.1 Simplified geological map of Milos Island, showing the distribution of the seven major stratigraphic units of Milos, after Fytikas et al. (1986).

The simple seven-fold regional stratigraphy defined by Fytikas et al. (1986) consists of (Figure 3.1): the Mesozoic metamorphic group, the Neogene sedimentary group, the basal pyroclastic series (Middle-Late Pliocene), the complex of domes and lava flows series (Late Pliocene), the pyroclastic series and lava domes (Early Pleistocene), the acid complex of Firiplaka and Trachilas series (Late Pleistocene) and the products of phreatic activity (Late Pleistocene to present).

Collectively, the four Pliocene to Pleistocene volcanic units comprise compositionally and texturally diverse submarine and subaerial calc-alkaline volcanic and submarine sedimentary rocks. The volcanic units display significant lateral and vertical facies variations that are further complicated by locally strong hydrothermal alteration and post-

depositional faults, some of which have vertical displacements of several hundred metres. Following is a summary of the formal stratigraphy defined by Fytikas et al. (1986). However, the results of this research suggest that revision of this stratigraphy is necessary (Chapter 8).

Mesozoic metamorphic group

The Mesozoic metamorphic group (Cycladic Crystalline Complex) is exposed along the southern and southeastern coast of the island (Figure 3.1). The unit forms the basement to the volcanic units and consists principally of chlorite, actinolite and glaucophane schists and metapelites of greenschist and blueschist facies (Fytikas and Marinelli 1976; Fytikas et al. 1986). The various metamorphic lithologies on Milos have been described in detail by Kornprost et al. (1979) and Hoffmann and Keller (1979).

Neogene sedimentary group

The Neogene sedimentary group was initially defined by Fytikas and Marinelli (1976) as a submarine "transgressive" sedimentary succession, comprising distinctive brown to red limestone intercalated with conglomerate, breccia and sandstone (Figure 3.2). The Neogene sedimentary group is exposed along the southern and southeastern coast of the island (Figure 3.1). The group displays an extremely variable internal stratigraphy and detrital units are composed of clasts mostly derived the underlying metamorphic complex. Volcanic clasts are totally absent (Fytikas et al. 1986). The group has a maximum measured stratigraphic thickness of 180 m.

Figure 3.2 View looking east across along Provatas beach. Most of the foreground consists of the Neogene sedimentary group (Nsg). Mesozoic schist (Msc) is exposed at the point. Photograph location on Figure 3.1.

On the basis of microfossils, the group is no older than Miocene (D'Erasmo 1924). The group unconformably overlies the Mesozoic metamorphic basement and is interpreted to reflect a progression from shelf to shallow marine environments (Fytikas and Marinelli 1976). It is overlain both conformably and unconformably by the volcanic succession.

The basal pyroclastic series

The lowermost basal pyroclastic series (equivalent to the 'Old Tuffs' of Fytikas 1977) has a minimum stratigraphic thickness of 120 m, and dominates the southwestern sector of Milos (Figure 3.1). The true thickness of the succession is poorly constrained, due to structural complexities and alteration. A section at Kleftiko was described by Fytikas (1986; Figure 3.3A).

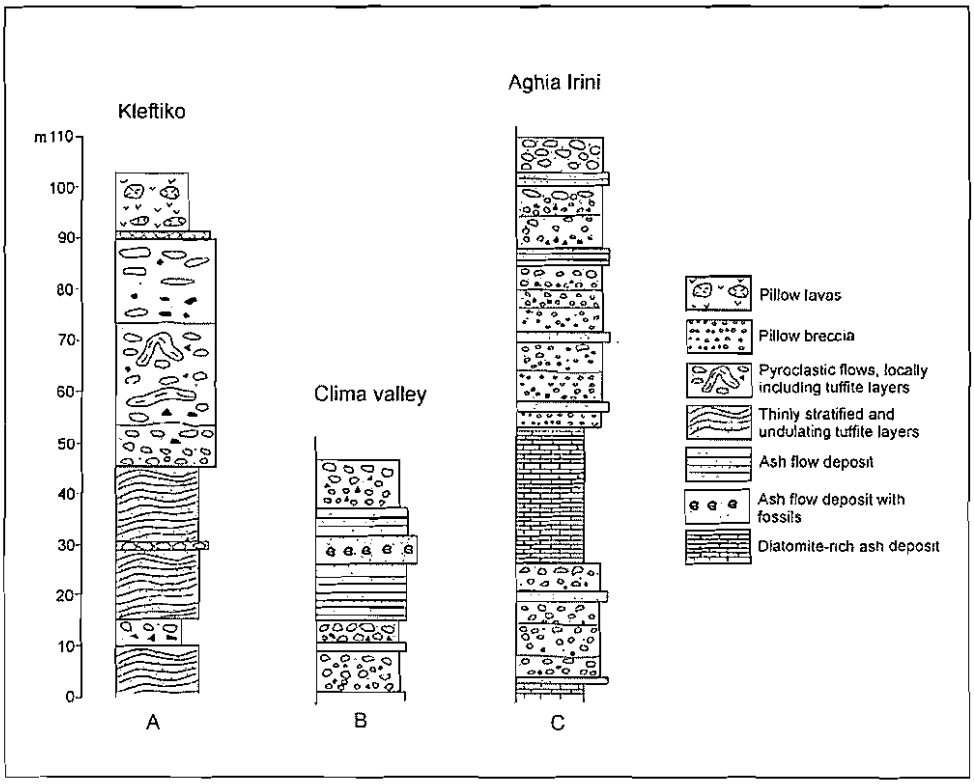

Figure 3.3 Generalised stratigraphic columns for the basal pyroclastic series at Kleftiko (**A**), and the pyroclastic series and lava domes at Clima valley (**B**) and Aghia Irini (**C**). From Fytikas et al. (1986). Location of stratigraphic sections on Figure 3.1.

The basal pyroclastic series consists mainly of a mixed volcanic and sedimentary succession dominated by submarine "pyroclastic flow, tuffs pumice flows, pillow lavas and pillow breccias" (Figure 3.3A; Fytikas et al. 1986). The thick submarine pyroclastic units

(Figure 3.4A) are generally massive, locally graded and characterised by coarse pumice clasts (over 1 m in diameter). Bedforms in the volcaniclastic units and abundance of macrofossils (mainly lamellibranches and echinoids) provide evidence for emplacement in a submarine setting (Fytikas and Marinelli 1976). Mafic dykes and sills are abundant towards the top of the basal pyroclastic series. The dykes are basaltic andesite and associated with "pillow lavas, pillow breccias and subordinate hyaloclastite" (Figure 3.4B; Fytikas et al. 1986).

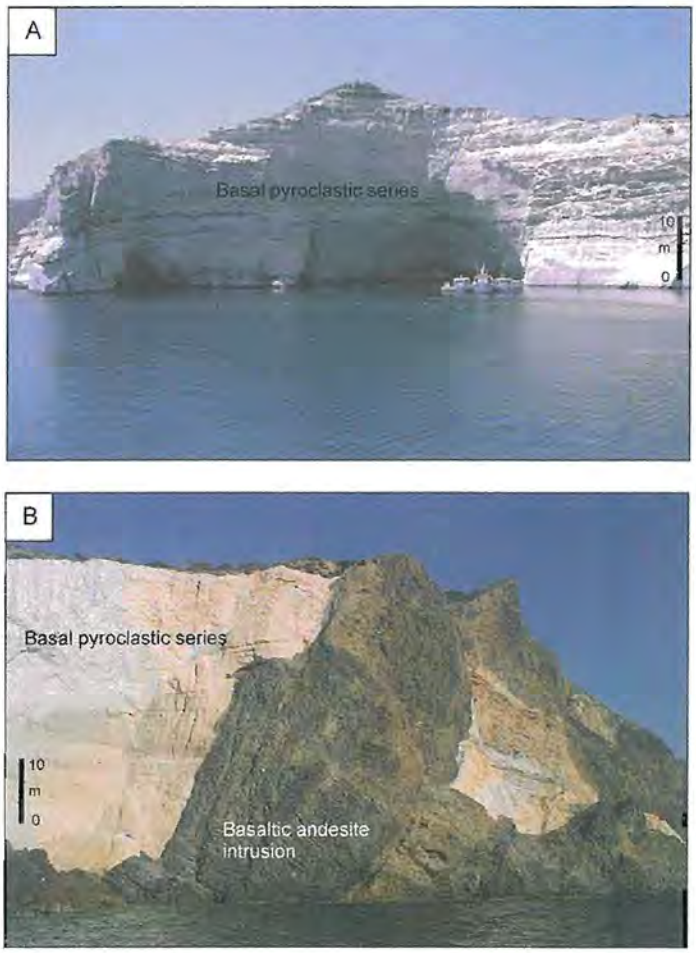

Figure 3.4 A Basal pyroclastic series of southwest Kleftiko headland. Most of the headland consists of the basal pyroclastic series. **B** Basal pyroclastic series at Sikia (southwest) intruded by several basaltic andesite dykes. Photograph locations on Figure 3.1.

Locally, the succession was thought to be capped by thick (up to 150 m thick), "welded and non-welded subaerial ignimbrites" (Fytikas et al. 1986). The ignimbrite units are separated by palaeosols and record intermittent explosive subaerial volcanism prior to eruption of the overlying complex of domes and lava flows series (Fytikas and Marinelli 1976).

Complex of domes and lava flows

The complex of domes and lava flows is composed of massive and flow-banded dacite and andesite and breccia, mostly forming domes and lavas which are typically 100-150 m thick (Figure 3.5; Fytikas and Marinelli 1976). The effusive activity was accompanied by explosive episodes from small central volcanoes located along NNE or NE striking faults (Fytikas et al. 1986). Fytikas et al. (1986) did not define the boundary between the complex of domes and lava flows series and the younger pyroclastic and lava domes series, although interpreted it as conformable.

Figure 3.5 Complex of domes and lava flows, showing the Krotiraki dome. Outer contact of a dacite dome with the basal pyroclastic series (white). The contact is highly irregular and discordant, truncating the local bedding. Photograph location on Figure 3.1.

The pyroclastic series and lava domes

The pyroclastic series and lava domes has an extremely variable internal stratigraphy and thickness (50-200 m thick). The group is dominated by rhyolitic lavas and domes and pumiceous volcaniclastic units (Fytikas et al. 1986) that are restricted to the eastern and northern parts of the island (Figure 3.1). The pyroclastic series and lava domes has been loosely subdivided into three units: the lower pyroclastic series, lava domes and upper Halepa and Plakes domes (Figure 3.1; Fytikas et al. 1986).

The pyroclastic series comprise thick intervals (up to 110 m; Figure 3.3B and C) considered to be subaqueous pyroclastic deposits (Fytikas and Marinelli 1976). Fytikas et al. (1986) identified minor intercalated andesitic pillow lavas and breccia. Fytikas et al. (1986) interpreted felsic facies at Bombarda and Demenegaki (Figure 3.5) as coalesced (100-150 m) thick lavas and domes with intercalated autoclastic breccia aprons. The

upper lava part of the series includes the large and laterally extensive, thick rhyolitic lava complexes of Halepa and Plakes in the middle part of the island (Figure 3.6).

Significant thickness variations (50-200 m) were interpreted to reflect infilled, fault-bounded basins or constructional features (Fytikas et al. 1986). The boundary between the pyroclastic series and lava domes and overlying rhyolitic complexes of Firiplaka and Trachilas was interpreted as conformable (Fytikas et al. 1986).

The rhyolitic complexes of Firiplaka and Trachilas

Firiplaka and Trachilas are two subaerial rhyolitic volcanic centres at Firiplaka (Campos Venuti and Rossi 1996) in the south and Trachilas in the north (Figure 3.1). Products of the volcanic centres range in thickness from 120 m in the proximal zones to several metres thick in distal parts (Figure 3.6). Each volcanic centre consists of distinctive quartz-biotite-phyric rhyolitic lava and pumiceous pyroclastic deposits (Fytikas et al. 1986; Campos Venuti and Rossi 1996). The pyroclastic beds are dominated by juvenile volcanic components but also contain basement-derived schist clasts (Fytikas et al. 1986). Detailed facies analysis by Campos Venuti and Rossi (1996) indicated that the products of both centres are characterised by an initial phreatic stage that evolved to a cone-building phreatomagmatic episode represented by surge deposits. Later eruptions produced ash-fall deposits and lavas.

The products of phreatic activity

The products of phreatic activity are the youngest primary pyroclastic units exposed on Milos. The deposits mainly occur in the southeastern sector of the island although there are minor exposures in the north that are spatially associated with several structural depressions (Figures 3.1 and 3.6; Fytikas et al. 1986). The deposits have lateral extents up to 50 m and have a maximum thickness of 30 m. Deposits are typically coarse grained, poorly sorted, matrix-supported lithic breccias which show only minor lateral variation in thickness, geometry, internal organization and grain size (Fytikas and Marinelli 1976). Primary phreatic deposits are locally intercalated with reworked sequences (Fytikas et al. 1986).

In the southeastern area, the products of phreatic activity interfinger with, and conformably overlie, the felsic pyroclastic deposits of Firiplaka. In the north around Triovassalos, phreatic units disconformably and conformably overlie the Trachilas complex and the pyroclastic series and lava domes (Fytikas et al. 1986).

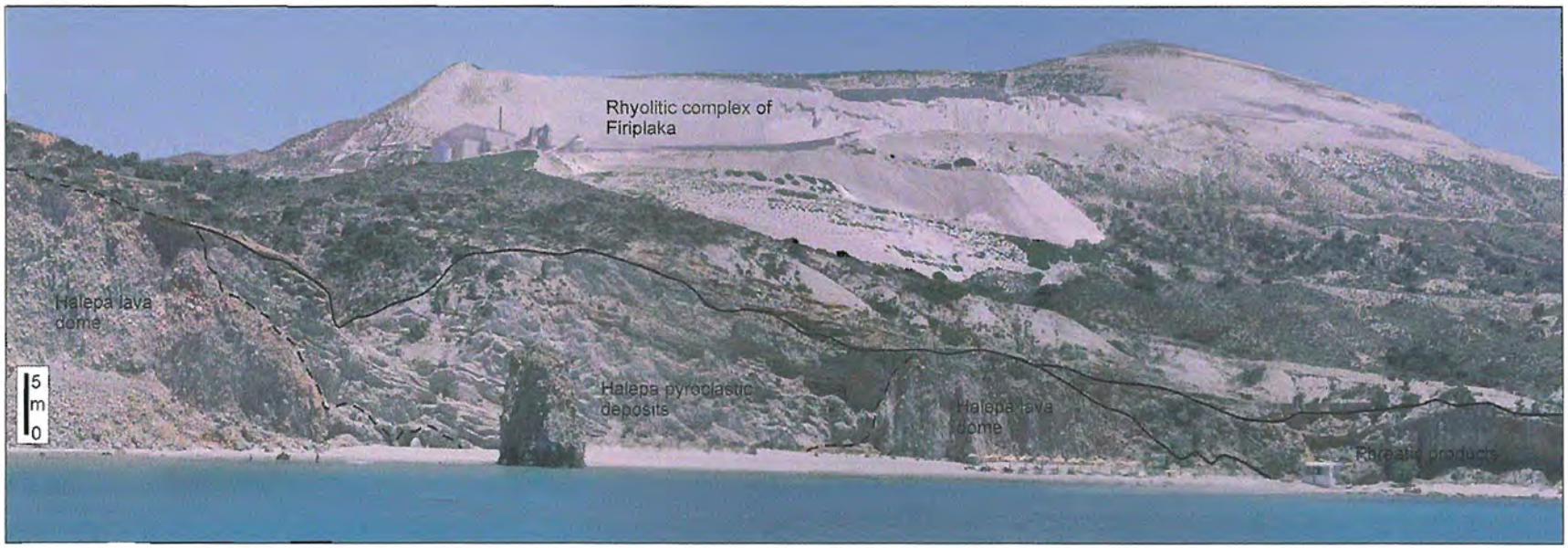

Figure 3.6 Firiplaka Beach on the southern coast of Milos, looking northeast. Rhyolitic autobreccia and pyroclastic deposits of the Halepa rhyolite are overlain by a red palaeosol and a phreatic deposit. A palaeosol separates the rhyolitic complex of Firiplaka the phreatic products. Photograph location on Figure 3.1.

Quaternary sedimentary formations

The Quaternary sedimentary units are scarce and typically restricted the Zefiria plain (Figure 3.1). The deposits are relatively thin (tens of metres). In geothermal exploration wells at Zefiria, they consist of unconsolidated sand, silt and minor conglomerate (Fytikas and Marinelli 1976).

3.3 The volcanic products of the neighbouring islands

Kimolos and Polyegos

The two neighbouring islands of Kimolos and Polyegos are composed of submarine and subaerial, calc-alkaline volcanic and submarine sedimentary rocks that are broadly similar to those on Milos (Fytikas et al. 1986). The volcanic rocks are predominantly rhyolite and dacite, with subordinate andesite and basaltic andesite (Fytikas et al. 1986), and dominated by lavas and domes, which on Kimolos and Polyegos are interleaved with thick volcaniclastic and sedimentary units. Each succession records a transition from a relatively shallow but dominantly below-wave-base submarine setting to a subaerial one (Fytikas et al. 1986). The successions on Kimolos and Poliegos (Figure 3.7) host a few base metal massive sulfide ores.

Both Kimolos and Polyegos display extremely variable internal stratigraphies (Figure 3.7), consisting of a poorly exposed, thick succession of rhyolitic to dacitic pumiceous units, volcanic breccias, and minor lavas intercalated with bioturbated and fossiliferous sedimentary units (e.g. Lower lavas, Kastro Ignimbrite, Prassa Ignimbrite; Fytikas and Vougioykalakis 1993). These rhyolitic to dacitic pumiceous basal units are thought to represent regional correlates of the basal pyroclastic series on Milos (Fytikas and Vougioykalakis 1993). The pumiceous units are conformably overlain by a diverse succession of rhyolitic, dacitic or andesitic lavas which include the domes of Polyegos, the Geronikikola lavas of Kimolos, and the lava domes and pyroclastic deposits of Psathi (Fytikas and Vougioykalakis 1993).

Antimilos

The island of Antimilos is dominated by dacitic and andesitic lavas, and minor pyroclastic units. Massive and flow-banded feldspar-phyric lavas dominate the basal part of the island, whereas the upper parts are characterised by feldspar-hornblende-phyric lavas. Antimilos is thought to represent the uppermost part of a polygenetic composite volcano (Marinos 1960; Fytikas et al. 1986).

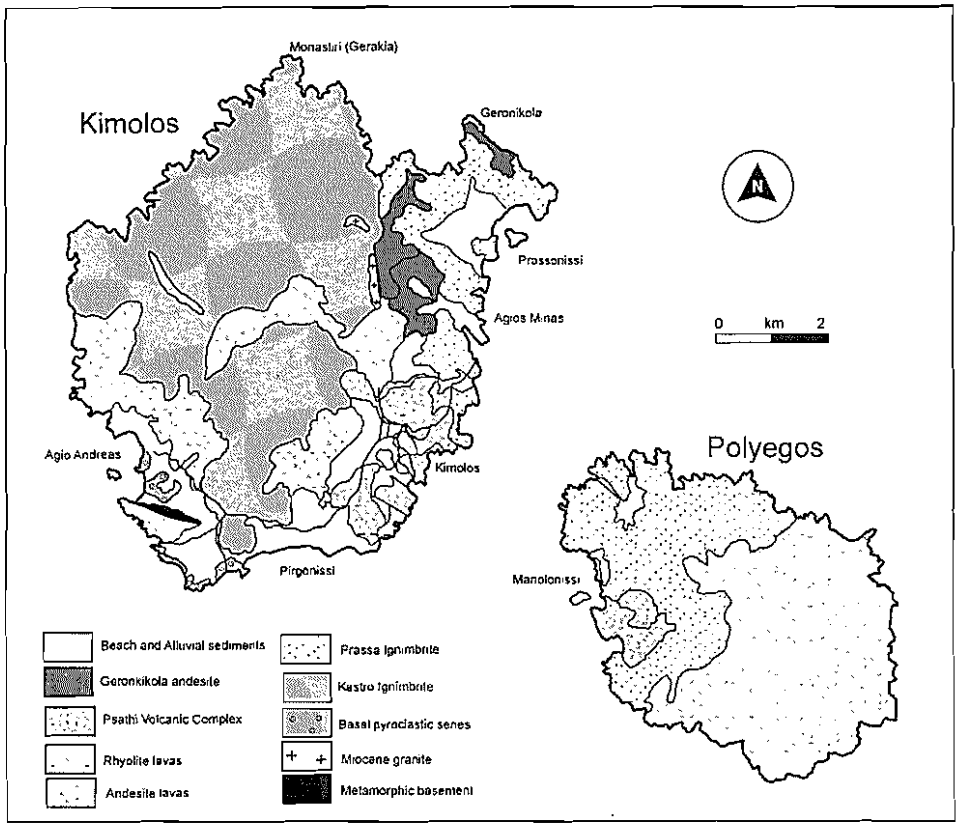

Figure 3.7 Simplified geological map of Kimolos and Polyegos, showing the distribution of the major lithostratigraphic units. Geological maps of Kimolos and Polyegos are modified after Fytikas and Vougioykalakis (1993).

3.4 Age relationships

A variety of dating techniques has been applied to the basement units and five volcanic units on Milos (Table 3.1): K-Ar radiometric dating of biotite and amphibole (Fytikas et al. 1976; Angelier et al. 1977; Fytikas et al. 1986), fission track dating of felsic glasses (Bigazzi and Radi 1981), ^{14}C measurements on Roman pot fragments (Traineau and Dalabakis 1989; Principe et al. 2002). The results indicate that volcanic activity on Milos began during the Late Pliocene (~3 Ma) and has continued to relatively recent times (200 BC-200 AD; Figure 3.8).

The age of the basal pyroclastic series is relatively poorly constrained, as it is dominated by volcaniclastic facies and lacks coherent lava facies, which makes dating difficult. The series contains marine fossils that are consistent with a Late Pliocene age (c.f. Fytikas et al. 1977). A K-Ar date on a rhyolite clast from the base of the series suggests a maximum age of 3.08 ± 0.14 Ma (Fytikas et al. 1986; Figure 3.8).

Table 3.1 Age data for stratigraphic units on Milos

Stratigraphic Group	Lithology	Age*	Dating Method
Phreatic Group			
	Phreatic mud flow deposit	200 BC-200 AD	^{14}C on Roman pot fragments[6]
	Phreatic breccia (known in the literature as Green Lahar)	27.000 ± 0.03 ka	^{14}C on wood remains[7]
Rhyolitic complexes of Firiplaka and Trachilas			
	Firiplaka Rhyolite	0.09 ± 0.02	K-Ar in biotite[5]
	Firiplaka Rhyolite	0.14 ± 0.03	K-Ar in biotite[5]
	Firiplaka Rhyolite	0.48 ± 0.05	K-Ar in biotite[1]
	Trachilas Rhyolite	0.37 ± 0.09	K-Ar in biotite[5]
Pyroclastic series and lava domes			
	Plaka Dacite	0.97 ± 0.06	K-Ar in biotite[5]
	Halepa Rhyolite	0.95 ± 0.08	K-Ar in biotite[2]
	Halepa Rhyolite	1.13 ± 0.10	K-Ar in biotite[3]
	Demengak Rhyolite	0.88 ± 0.18	K-Ar whole rock[1]
	Demengak Rhyolite	1.84 ± 0.05	K-Ar in biotite[2]
	Koraki Andesite	1.59 ± 0.25	K-Ar in biotite[5]
	Bombarda Rhyolite	1.47 ± 0.05	K-Ar whole rock[1]
	Bombarda Rhyolite	1.50 ± 0.28	K-Ar in biotite[4]
	Bombarda Rhyolite	1.71 ± 0.05	K-Ar in biotite[5]
	Bombarda Rhyolite	1.91 ± 0.44	K-Ar in biotite[4]
	Bombarda Rhyolite	2.15 ± 0.08	K-Ar in biotite[2]
	Clast in Sarakiniko Pumice Breccia	1.85 ± 0.10	K-Ar in biotite[5]
Complex of domes and lava flows			
	Adamas Dacite	2.03 ± 0.06	K-Ar in biotite[5]
	Agathia Dacite	2.38 ± 0.10	K-Ar in biotite[5]
	Mavro Vouni Dacite	2.50 ± 0.08	K-Ar in hornblende[2]
	Kleftiko Basaltic-andesite	3.50 ± 0.14	K-Ar in hornblende[5]
Basal pyroclastic series			
	Rhyolite breccia	3.08 ± 0.14	K-Ar in biotite[5]
Mesozoic metamorphic group			
	Chlorite schist	33.20 ± 1.03	K-Ar in muscovite[1]
	Glaucophane schist	64.20 ± 6.50	K-Ar in glaucophane[1]

Data from [1]Fytikas et al. (1976); [2]Angelier et al. (1977); [3]Fytikas (1977); [4]Bigazzi and Radi (1981); [5]Fytikas et al. (1986); [6]Traineau and Dalabakis (1989); [7]Principe et al. (2002).

Two dacite lava domes, the Agathia dome in the west and the Adamas dome in the north (Figure 3.8), have yielded K-Ar dates of 2.38 ± 0.10 and 2.03 ± 0.06 Ma (Table 3.1; Fytikas et al. 1986) respectively. In terms of stratigraphic position, both domes occur towards the top of the series. One K-Ar age obtained for basaltic andesite dykes on the southwestern coast (around Kleftiko) is 3.5 ± 0.14 Ma (Fytikas et al. 1986), which is significantly older than ages from the rocks they intrude (basal pyroclastic series, Fytikas et al. 1986), and therefore considered inaccurate. Hence, the complex of domes and lava flows is taken to be around 2 Ma (Late Pliocene) and to conformably overlie the basal pyroclastic series.

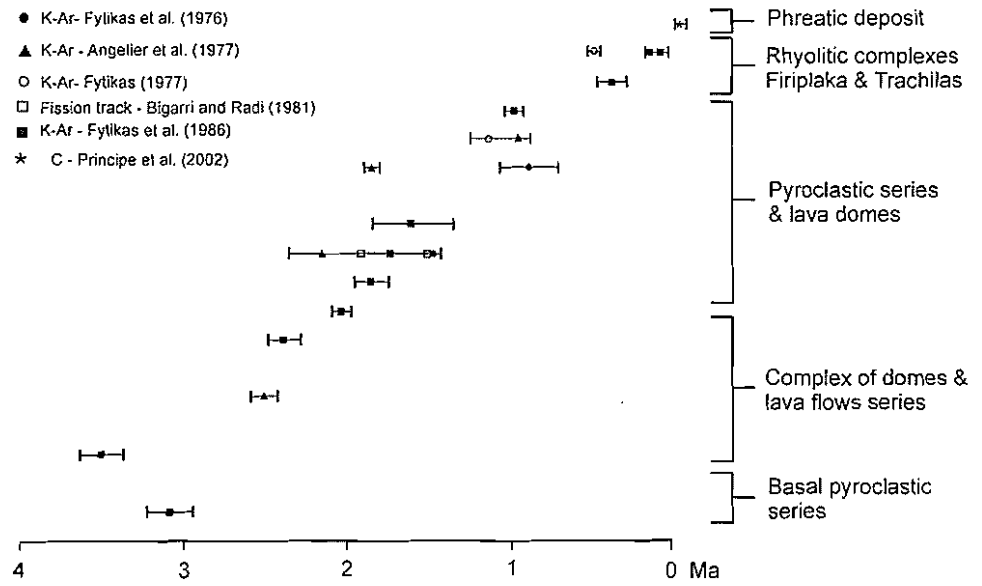

Figure 3.8 Summary of data for the volcanic succession on Milos. Bars give the 1 σ error on measurements. New U-Pb in zircon SHRIMP dates determined in this study are reported in Chapter 8.

The K-Ar dates of units within in the pyroclastic series and lava domes series are consistent with an Early Pleistocene age (<1.5 Ma; Angelier et al. 1977; Fytikas et al. 1986). K-Ar dates dating of biotite have further constrained the age of the pyroclastic series and lava domes series. Within the Halepa area on south coast of Milos, rhyolite lava (Halepa lava) from the stratigraphic top of the series has been dated at 0.95 ± 0.08 Ma (Figure 3.8).

3.5 Structure of Milos

The volcanic succession of Milos is only gently deformed. Bedding in volcaniclastic and sedimentary formations on Milos is generally flat-lying or gently dipping. The succession is mainly disrupted by normal faults, some of which have displacements up to several hundred metres (Fytikas et al. 1986), and numerous syn-volcanic intrusions. The subvertical normal faults (Figure 3.9) interacted during periods of extension to produce horsts and grabens (Fytikas and Marinelli 1976). Three main episodes of deformation are recognised in the Late Pliocene-Pleistocene (Fytikas 1989).

The earliest episode of extension is characterised by ENE-WSW striking normal faults that controlled uplift of Mesozoic and Neogene basement in the southwest. The faults

may have controlled emplacement of dacite domes and lavas (complex of domes and lava flows series; Figure 3.9). A second episode resulted in several NE-SW- and N-S-striking normal faults predominantly in the central and eastern sector of the island (Figure 3.9). These faults formed the Zefiria Graben, and probably influenced emplacement of volcanic centres associated with the pyroclastic series and lava domes (Fytikas 1989). The final extensional phase produced NW-SE-striking faults that define the Milos Gulf in the centre of the island (Figure 3.9). The volcanic centres of Firiplaka and Trachilas occur at either end of the Milos Gulf graben. Four young phreatic centres occur in the central part of the island (Figure 3.9). Based on the presence active fumaroles and solfataras (Botz et al. 1996; Stüben and Glasby 2001) and the seismic activity of March 1922 (with focal depths between 1-4 km, Papazachos 1990; Papanikolaou et al. 1993), this central area is considered structurally active (Fytikas 1989).

In places, syn-volcanic intrusions have disturbed the succession (Chapter 5) and locally caused up-doming of overlying clastic units. However, deformation is generally restricted to within a few several hundred metre from the margins of the intrusions.

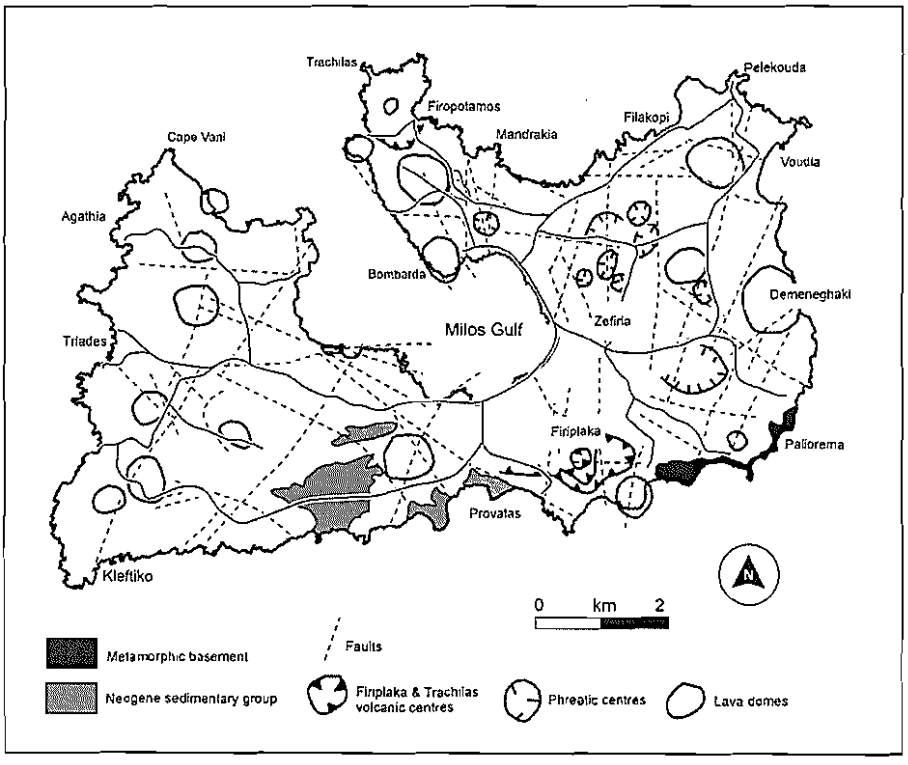

Figure 3.9 Structural sketch map of Milos taken from Fytikas et al. (1986).

3.6 The Milos geothermal system

Milos has one of the best-known geothermal fields in Europe. The high-enthalpy field is considered among the most promising and important in Greece (Fytikas et al. 1976). The field includes numerous active and extinct hot springs, hot grounds, fumaroles, phreatic explosion craters and submarine gas escapes concentrated in the central and eastern parts of the island (Figure 3.10A; Fytikas et al. 1976; Fytikas 1989; Botz et al. 1996; Stüben and Glasby 2001).

In 1976, the island became the focus of an extensive multinational research project, which was financed by the Commission of the European Communities (Fytikas 1989). Five boreholes were drilled between 1973 and 1976 around Zefiria to depths of 1000-1400 m. The five boreholes encountered a production zone at about 1000 m depth within the metamorphic basement (temperatures of 300-320^0 C, producing a two-phase fluid flow rate of 50-120 x 10 m^3/h; Fytikas et al. 1976). The system could support a 25 MW power unit, whereas the total potential of the island was estimated to be 120 MW (Fytikas et al. 1989).

The high salinity of the fluids caused difficulties in exploration. The borehole casings corroded, and were rapidly blocked by the deposition of salts, gypsum and carbonates. Despite these technical problems, exploration continued until 1986, but ceased in response to public outcry. The release of large amounts of CO_2 and H_2S from some of the boreholes caused health concerns.

3.7 Mineralisation

The presence of mineralisation on Milos has been known since ancient times (Renfew and Wagstaff 1982). There has been a 10 000-year-long history of mining on the island. Commodities such as obsidian, salt, mill stone, sulfur, pozzolan, pumice, alunite, kaolinite, bentonite, copper, silver, manganese and lead were all mined during antiquity (Figure 3.10B, C and D). Milos is actively exploited for various natural resources and industrial minerals which include perlite, pozzolanic earths, kaolite, silica, bentonite and barite (Christidis and Scott 1997; Christidis et al. 1995; Ericsson et al. 1992; Hauck 1983). The island is currently the second biggest producer of bentonite and perlite in the world.

Figure 3.10 **A** Hot grounds east of Adamas, and the discarded material of an experimental geothermal plant. **B** Old sulfur mines at Paliorema. **C** Cape Vani silver-manganese mines. **D** Ancient alunite mines of Langada. **E** The active Agena bentonite pit. **F** Chondro Vouno epithermal gold-silver prospect.

Milos also contains a number of economically significant epithermal gold deposits including the Profitis Illias deposit (5.5 Mt grading 4.4g/t Au and 43 g/t Ag), Chondro Vouno deposit (3.3 Mt grading 4.2 g/t Au) and Triades deposit (1.2 Mt grading 1g/t Au and 124 g/t Ag), and one sub-economic base metal deposit (Cape Vani, 2.1 Mt of manganese ore). Studies by Liakopoulos (1987), Hauck (1988), Spartali (1994), Sillitoe (1995), Christanis and Seymour (1995), Vickery (1995), Vavelidis and Melfos (1998), Kilias et al. (2001), and Liakopoulos et al. (2001) have focussed on various aspects of the ore and alteration assemblages, fluid chemistry and origin of mineralisation in this epithermal district.

The main characteristics of the Au-Ag and some minor base metal ore deposits are summarised in Chapter 7, with emphasis on the relationships between the ores and their host rocks. There is a strong stratigraphic control on mineralisation on Milos, and all epithermal ores occur within and near the top of the basal pyroclastic series.

3.8 Petrography and geochemistry

The volcanic rocks of Milos are mainly porphyritic, although some rhyolites and dacites are entirely glassy. In the most mafic rocks (basaltic andesite) , phenocrysts (<10 vol. % phenocrysts <0.5 mm in length) are dominated by clinopyroxene, plagioclase and orthopyroxene; olivine and hornblende are rare (Fytikas et al. 1986). The groundmass is typically glassy. In the andesites, the most common phenocrysts (10-15 vol. % phenocrysts, <3 mm in length) are plagioclase, hornblende, orthopyroxene; minor biotite and embayed quartz are present (Fytikas et al. 1986). The groundmass is generally glassy. Most felsic units on Milos are characterised by plagioclase and embayed quartz phenocrysts, with minor amounts of biotite (10-20 vol. % phenocrysts, <3 mm in length). Sanidine is present in the rhyolitic lavas from Trachilas and Firiplaka (Fytikas et al. 1986). The groundmass is typically totally glassy.

Innocenti et al. (1981) and Fytikas et al. (1986) analysed major elements from the four main volcanic groups on Milos (Figure 3.11). An additional forty-five least-altered samples representing the four principal volcanic groups were analysed during this research for major and trace elements using XRF at the University of Tasmania (Appendix A). The scattered distribution of the more mobile elements (e.g. Na and K) on variation diagrams (Figure 3.11), local albitisation of plagioclase, and presence of secondary silica and clay minerals (e.g. kaolinite, alunite) provide abundant evidence for partial hydrothermal alteration of the volcanic units. Given the likelihood that some major element abundances are not pristine, the following discussion is based mainly on the high-field-strength elements (HFSE) considered to remain reasonably immobile during alteration processes (Figures 3.12 and 3.13B; Pearce and Cann 1973).

The four main volcanic groups on Milos contain greater than 54.15 wt. % SiO_2, and range up to 75.15 wt. % SiO_2 in the (Figure 3.11). The intermediate and felsic rocks on Milos show well-defined trends on Harker variation diagrams (Figure 3.11). On an FeO vs. MgO vs. total alkalis diagram (Figure 3.13A), the samples display a calc-alkaline

character, as reported by earlier workers (e.g. Barton et al. 1983; Fytikas et al. 1986). The succession is mildly enriched in K_2O (>1.57 wt. %), Al_2O_3, and large-ion lithophile elements (LILE) [Rb]. All have low Nb/Y (<1) and Zr/TiO_2 ratios (Figure 3.13B), which increase markedly from andesite to rhyolite. This is characteristic of rocks of calc-alkaline affinities (Winchester and Floyd 1977). The rhyolites have slightly higher Zr/TiO_2 ratios, but similar Nb/Y to intermediate units (Figure 3.13A) and fall in the calc-alkaline dacite-rhyolite field (Figure 3.13B).

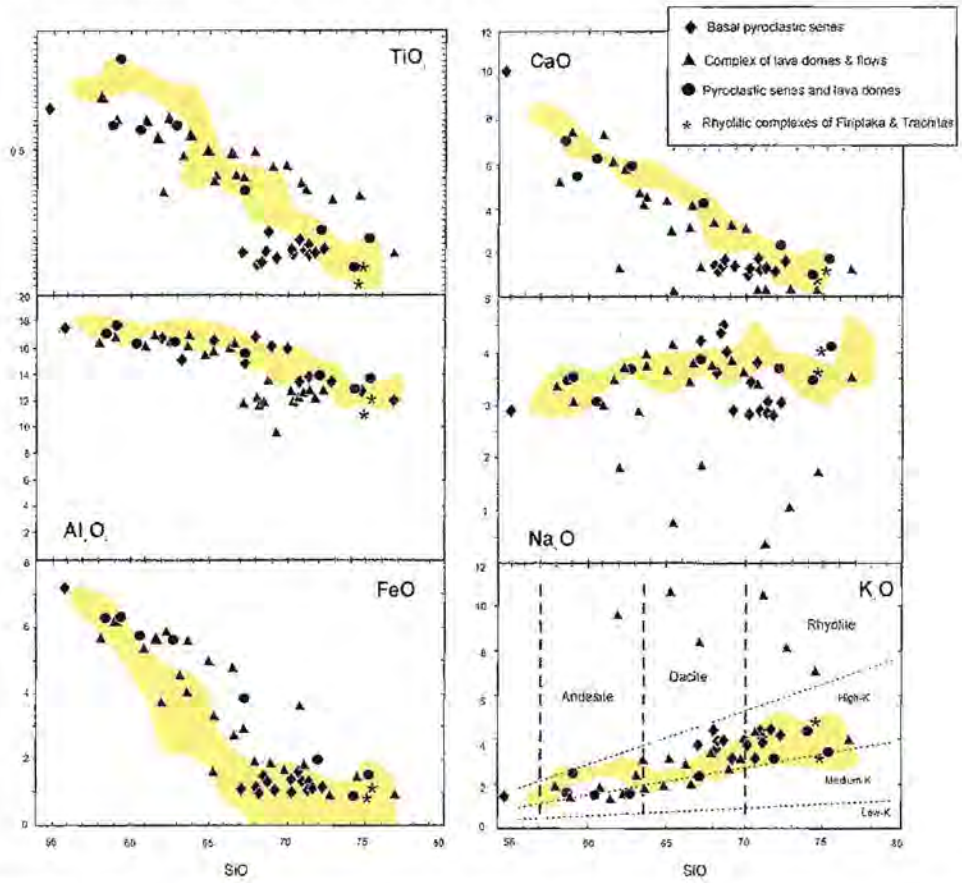

Figure 3.11 Selected major element abundances (wt. %) in the four volcanic units of Milos shown plotted against SiO_2. XRF analysis calculated anhydrous with all iron as FeO. Yellow shade represents data taken from Innocenti et al. (1981) and Fytikas et al. 1986. Subdivision of the volcanic rocks into High-K and Shoshonite series from Le Maitre (1989). The new geochemical data are presented in full in Appendix A.

The Zr/TiO_2 vs. Nb/Y discrimination diagram (Figure 3.13B) shows that the samples from the basal pyroclastic series are dominantly rhyolites and dacites with a broad range of Nb/Y values. The complex of domes and lava flows and pyroclastic series and lava domes samples (Figure 3.13B) include andesites, dacites and rhyolites. The Firiplaka and Trachilas samples are rhyolites.

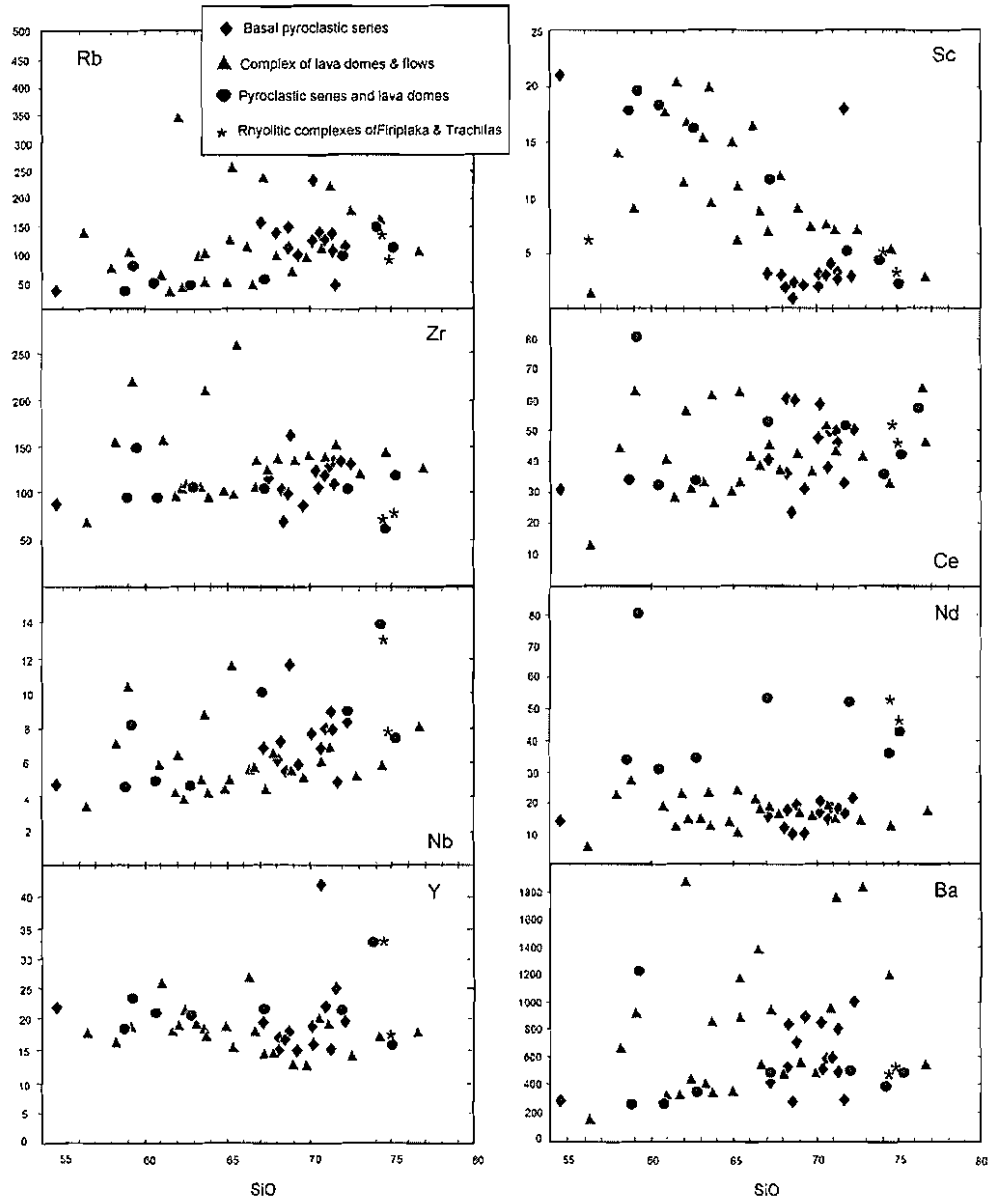

Figure 3.12 Selected trace element (ppm) abundances for the four volcanic stratigraphic units on Milos shown plotted against SiO_2. Symbols same as Figure 3.11. The new geochemical data are presented in full in Appendix A.

Previously published $^{87}Sr/^{86}Sr$ ratios for Milos range from 0.7038 to 0.7076 (Barton et al. 1983; Briqueu et al. 1986). Barton et al. (1983) proposed that high ^{87}Sr / ^{86}Sr values (relative to MORB) of Milos samples reflect minor amounts of assimilation of continental crust and concurrent fractional crystallization, but that an unusual mantle source composition may also have been involved. Briqueu et al. (1986) suggested that the least-evolved lavas of Milos are the most contaminated, and they related this attribute to the geodynamic evolution of the SAVA subduction zone. Phases of tectonic extension resulted in the eruption of rhyolites formed either by anatexis of LILE-depleted crust, or

by mixing crustal melts with mantle-derived magmas. Compressive episodes led to the formation of hotter, more mafic magmas that remained in crustal magma chambers for longer, and so assimilated more crust.

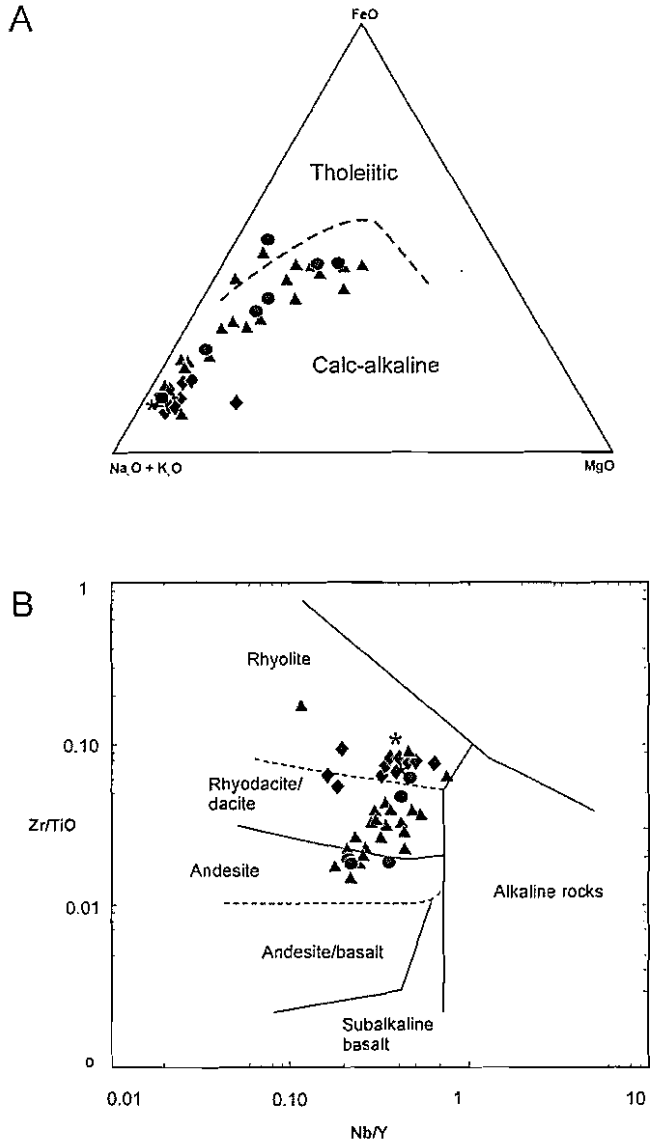

Figure 3.13 A FeO vs. MgO vs. total alkalies diagram. The volcanic rocks show a calc-alkaline character. **B** Zr/TiO_2 versus Nb/Y diagram (after Winchester and Floyd, 1977). The Milos rocks volcanic are andesites, dacites and rhyolites. All the rocks are subalkaline, based on the Nb/Y ratio. Symbols as in Figure 3.11.

3.9 Summary

The small archipelago of Milos, Antimilos, Kimolos and Polyegos is situated in the central part of the active SAVA, Greece. Lithostratigraphic units comprise compositionally

and texturally diverse submarine and subaerial calc-alkaline volcanic rocks and submarine sedimentary rocks. On Milos, there are seven main stratigraphic units, consisting of Mesozoic metamorphic basement rocks, Neogene sedimentary formations and five volcanic formations. The oldest date for volcanic rocks on Milos is 3.5 Ma, during the Upper Pliocene, and volcanic activity has continued until 200 BC-200 AD. The structure of Milos is dominated by subvertical normal faults that produced horsts and grabens. The volcanic succession ranges in composition from basaltic andesite to rhyolite (54.15 wt. %-75.15 wt. % SiO_2,) and displays typical calc-alkaline trends.

Chapter 4

Submarine volcanic and sedimentary facies and facies associations of Milos

4.1 Introduction

Of particular interest in research on the architecture of felsic volcanic islands is the identification and interpretation of the submarine facies associations. In many such volcanic successions, these sections are poorly understood. This neglect has arisen mainly due to their complexity, arising from the interplay of volcanic and sedimentary processes, contemporaneous erosion, and complicated fluctuations in sea level due to volcano-tectonic uplift/subsidence. In addition, modern observations and records of island-building eruptions and their products are extremely restricted (e.g. Tuluman Island, Reynolds et al. 1980; Myojinsho volcano, Fiske et al. 1998; Kavachi volcano, McConachy and McInnes 2001). It is only recently that various aspects of felsic seamounts have been examined with the assistance of modern sea-floor survey equipment. Never-the-less, even the most detailed bathymetric surveys of seafloor topography (e.g. Yuasa et al. 1991; Wright and Gamble 1999; Fiske et al. 1998; Fiske et al. 2001; Wright et al. 2003) cannot examine the internal facies characteristics. As a result, volcanic facies architecture studies rely instead on ancient successions that have been uplifted to subaerial settings (e.g. Horikoshi 1969; de Rosen-Spence et al. 1980; Busby-Spera 1986; Allen 1992; Allen et al. 1996; Doyle and McPhie 2000; Ayres and Peloquin 2000; Brown et al. 2002). However, in ancient successions the depositional setting may be ambiguous, and preservation and exposure are commonly incomplete.

This chapter focuses on description and interpretation of the Upper Pliocene-Pleistocene submarine volcanic facies of Milos. The identification of facies and their genetic interpretation are based on systematic field mapping and core logging. The available exposures and textural preservation are generally excellent, the exceptions be-

ing relatively small areas of intense hydrothermal alteration. In addition, coastal outcrops in particular provide almost three-dimensional information on facies geometry, a rarely met circumstance. This research provides new data on the facies architecture of felsic arc volcanoes that have high potential as hosts for precious and base metal ore deposits.

4.2 Terminology for volcanic textures

Volcanic terminology used throughout this study follows that of Cas and Wright (1987) and McPhie et al. (1993). In most cases, descriptive, non-genetic terminology has been used to name facies and facies associations. Bed thickness terms are those outlined in Ingram (1954).

The term 'facies' is used for a distinct body of rock or 'association' of rocks that can be defined and distinguished from others by a set of distinctive characteristics that include composition, texture, volcanic or sedimentary structures, contact relationships, and geometry (Selley 1978).

Pumice breccia and *scoria breccia* are descriptive terms for volcaniclastic deposits or rocks and used to indicate grainsize (>2 mm), angular grain shape, and the dominance of pumice and scoria clasts, respectively.

Pyroclasts are fragments (pumice, scoria, shards, crystals and lithic fragments) produced by explosive eruptions (Fisher 1960, 1966).

Pyroclastic facies are primary pyroclastic deposits, composed of particles generated by explosive eruptions (magmatic, phreatomagmatic and phreatic) and deposited by primary volcanic processes (fallout, hot-gas-supported pyroclastic density currents).

Syn-eruptive facies are those which are genetically related to and contemporaneous with

active volcanism and, in submarine settings, typically involve a blend of volcanic and sedimentary processes (McPhie et al. 1993). These facies comprise clasts initially created by volcanic eruptions but ultimately deposited via sedimentary processes. The syn-eruptive category may include deposits from eruption-fed currents (c.f. White 2000) where clasts by-pass initial deposition as primary pyroclastic or autoclastic deposits, and are delivered directly to sedimentary transport and deposition systems. This category also includes facies that result from rapid redeposition after brief storage during eruptions. Unlike post-eruptive facies, syn-eruptive facies comprise texturally unmodified clasts of uniform composition and clast type. The facies characteristics of syn-eruptive facies vary due to the differences in eruption style, eruption volume, and vent and depositional (subaerial or submarine) setting.

4.3 Criteria used to recognise submarine facies

Few single facies are independently diagnostic of eruptive or depositional environments. Three main criteria have been implemented for identifying submarine volcanic and sedimentary facies on Milos: (1) presence of marine ichnofacies and/or marine fossils in sedimentary facies; (2) presence of sedimentary facies showing structures characteristic of subaqueous deposition, in particular tabular, massive to graded beds typical of deposits from water-supported particulate gravity currents, angle-of-repose cross-stratification and ripple cross-lamination; and (3) presence of juvenile volcanic clasts with quenched margins and volcaniclastic aggregates interpreted to be the products of quench fragmentation.

4.4 Facies associations and organisation

Twenty-two principal volcanic, sedimentary and intrusive facies have been identified, and arranged into seven compositionally and texturally distinct facies associations (Table 4.1). The volcanic facies associations have genetic significance with respect to volcano type, eruption style, proximity to source, emplacement processes, provenance and depositional setting: (1) the rhyolite facies association comprises coherent rhyolite and sediment-matrix rhyolite breccia; (2) the dacite facies association comprises coher-

ent dacite, non-stratified and stratified monomictic dacite breccia and sediment-matrix dacite breccia; (3) the andesite facies association comprises coherent andesite, non-stratified and stratified monomictic andesite breccia and sediment-matrix andesite breccia; (4) the basaltic andesite facies association comprises coherent basaltic andesite and sediment-matrix basaltic andesite breccia; (5) the pumice breccia facies association consists of coarse pumice breccia, stratified pumice breccia, lithic-pumice breccia, and graded pumice breccia; (6) the scoria-rich breccia facies association consists of cross-stratified scoria breccia, massive andesitic breccia and fine scoria sandstone. The seventh facies association comprises graded sandstone, thickly bedded to laminated mudstone, and polymictic breccia-conglomerate collectively referred to as the sandstone-conglomerate facies association. The distinguishing characteristics of the twenty-two main facies are summarised below.

Phenocryst assemblages have been used to discriminate among the facies associations and also provide a good indication of facies composition. The rhyolites in the succession have 10-15 vol. % phenocrysts and are either feldspar-quartz-phyric, biotite-feldspar-quartz-phyric or biotite-quartz-phyric. The quartz (8-10 vol.%), feldspar and biotite phenocrysts are mainly in the 1-3 mm size range. The majority of dacites comprise 8-20 vol. % phenocrysts of feldspar, biotite and quartz (<5 vol.%) mainly in the 0.5-2 mm size range. The andesites contain 10-20 vol. % phenocrysts, including 1-2 mm euhedral plagioclase (10-15 vol. %) and 1 mm prismatic hornblende (5-8 vol. %). Basaltic andesites are feldspar-pyroxene-phyric (10-15 vol. % phenocrysts). Plagioclase phenocrysts are <1 mm and pyroxene phenocrysts (<5 vol. %) are up to 0.5 mm. These field terms have been confirmed by major and trace element analyses by XRF at the University of Tasmania (Appendix A), and each compositional group displays only slight variations in major- and trace-element abundances.

The distribution, associations, and interrelationships of facies are shown in Figures 4.1, 4.2, 4.3, 4.4 and 4.5. For brevity, facies that differ only in mineralogical and chemical composition are combined under the same facies group in Table 4.1. However, several facies were routinely mapped and subdivided to a further order of detail. For example, most rhyolite and dacite facies have a second-order subdivision according to the phenocryst assemblages. This method of subdivision is similar to that of Allen et al. 1996 and has enabled identification of single emplacement units of each facies type.

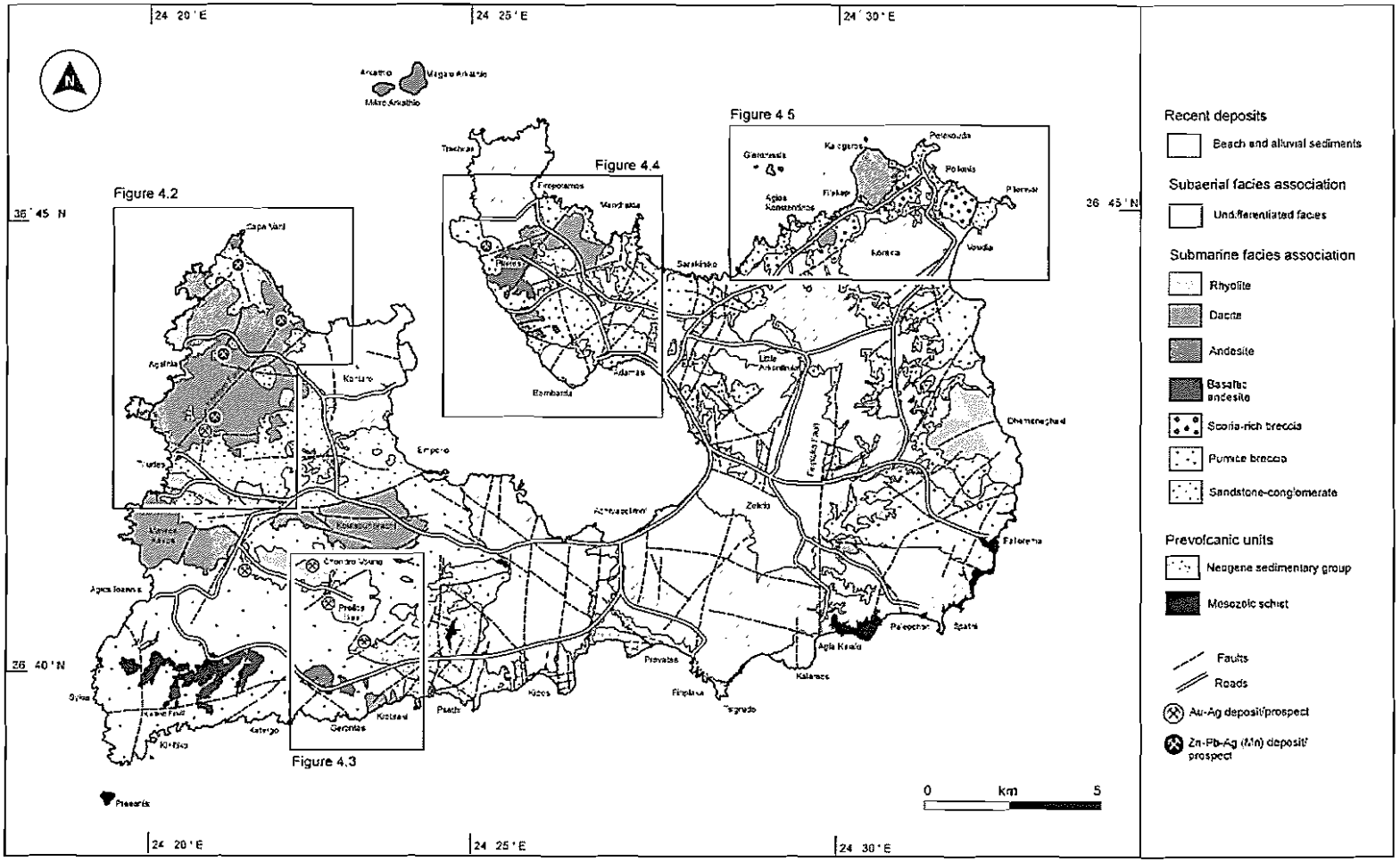

Figure 4.1 Simplified geological map of Milos Island, also showing the locations of the major ore deposits. (Modified after Fytikas 1977).

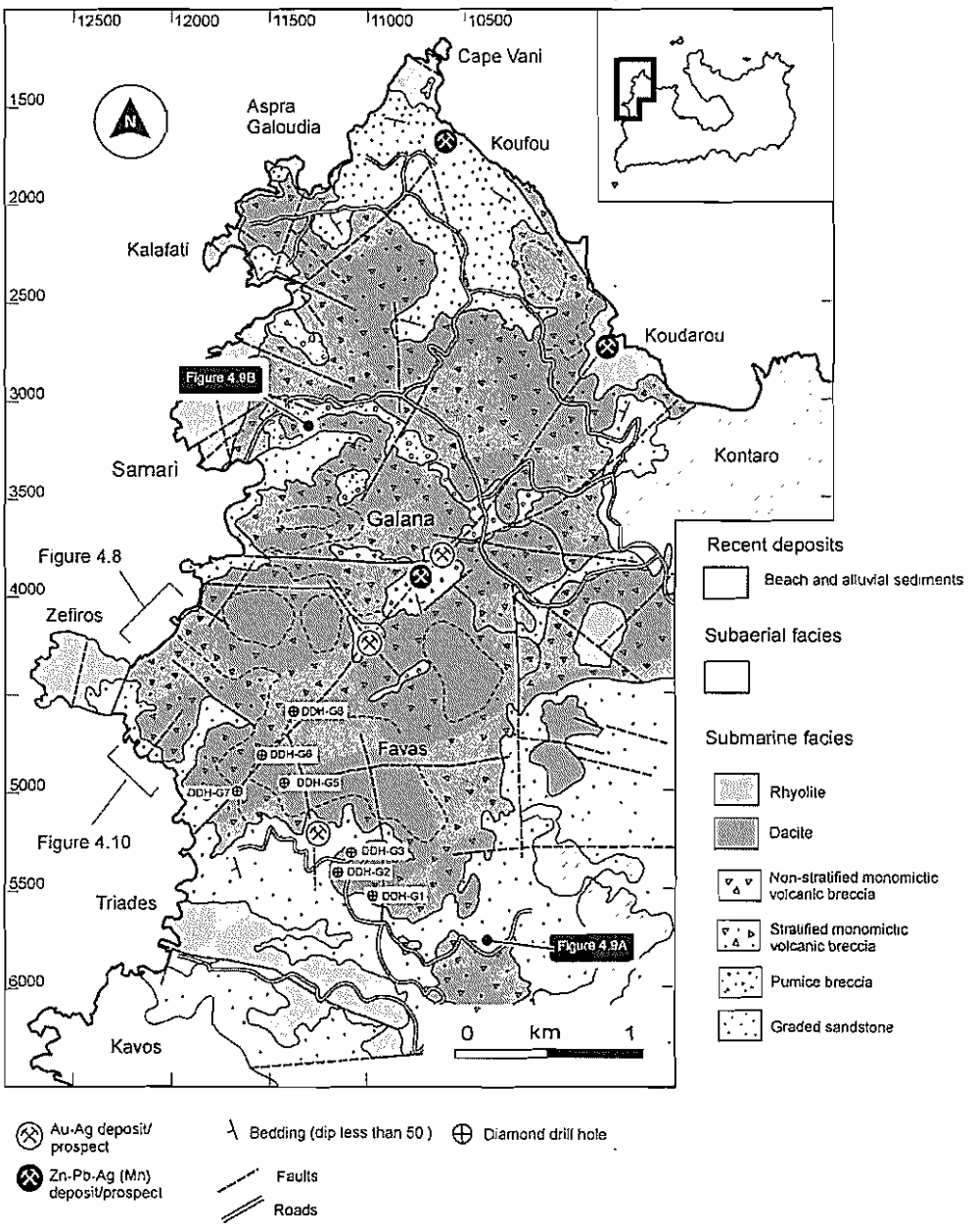

Figure 4.2 Geological map of the Triades area (inset) showing the distribution of the main volcanic facies, structure and ore deposits, modified after Fytikas (1977) and Vickery (1995). Local grid from 1:5000 scale Greek topographic maps.

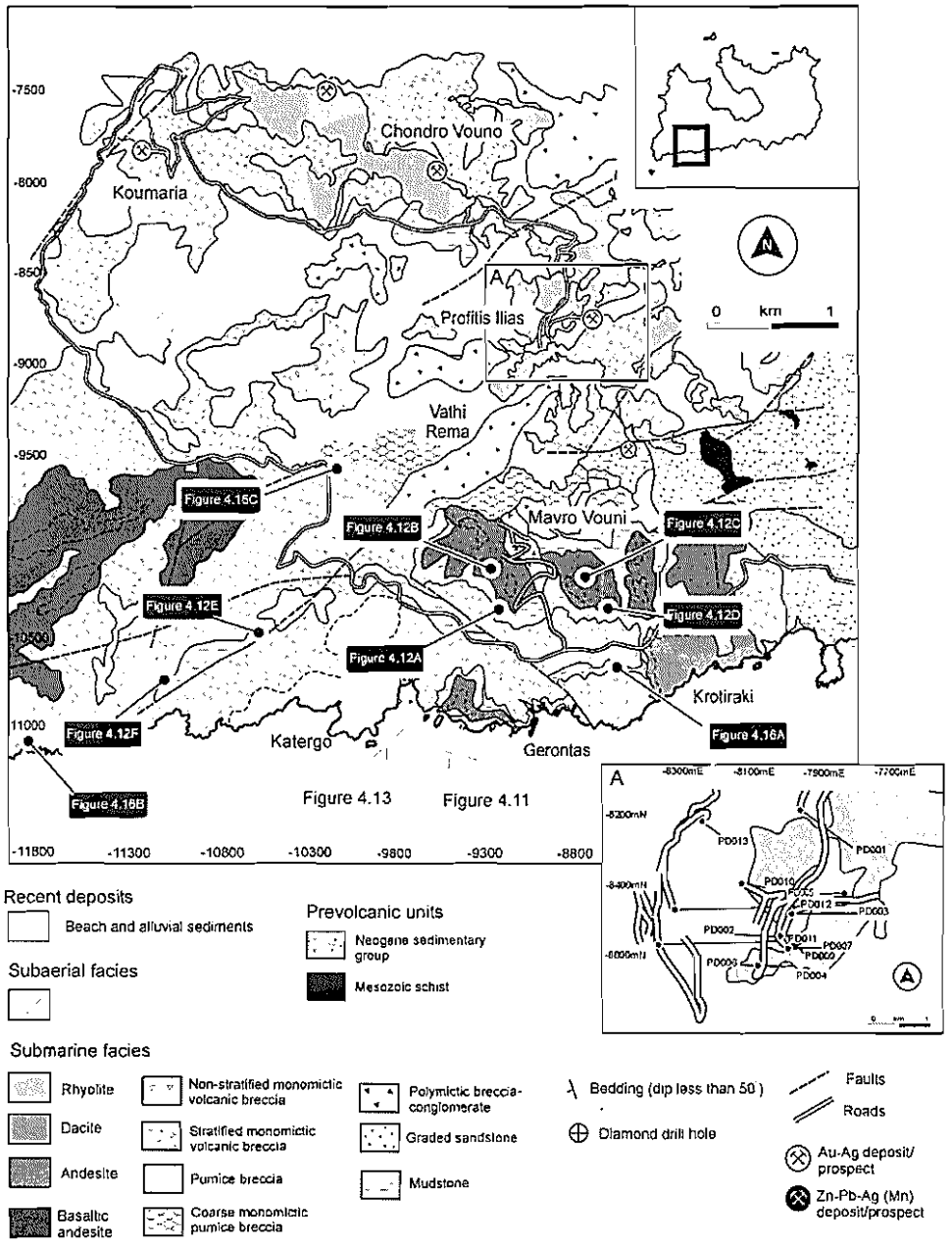

Figure 4.3 Geological map of the Profitis Illias area (inset) showing the distribution of the main volcanic facies, structure and ore deposits, modified after Fytikas (1977). Map (**A**) shows the location of diamond drill holes. Local grid from 1:5000 scale Greek topographic maps.

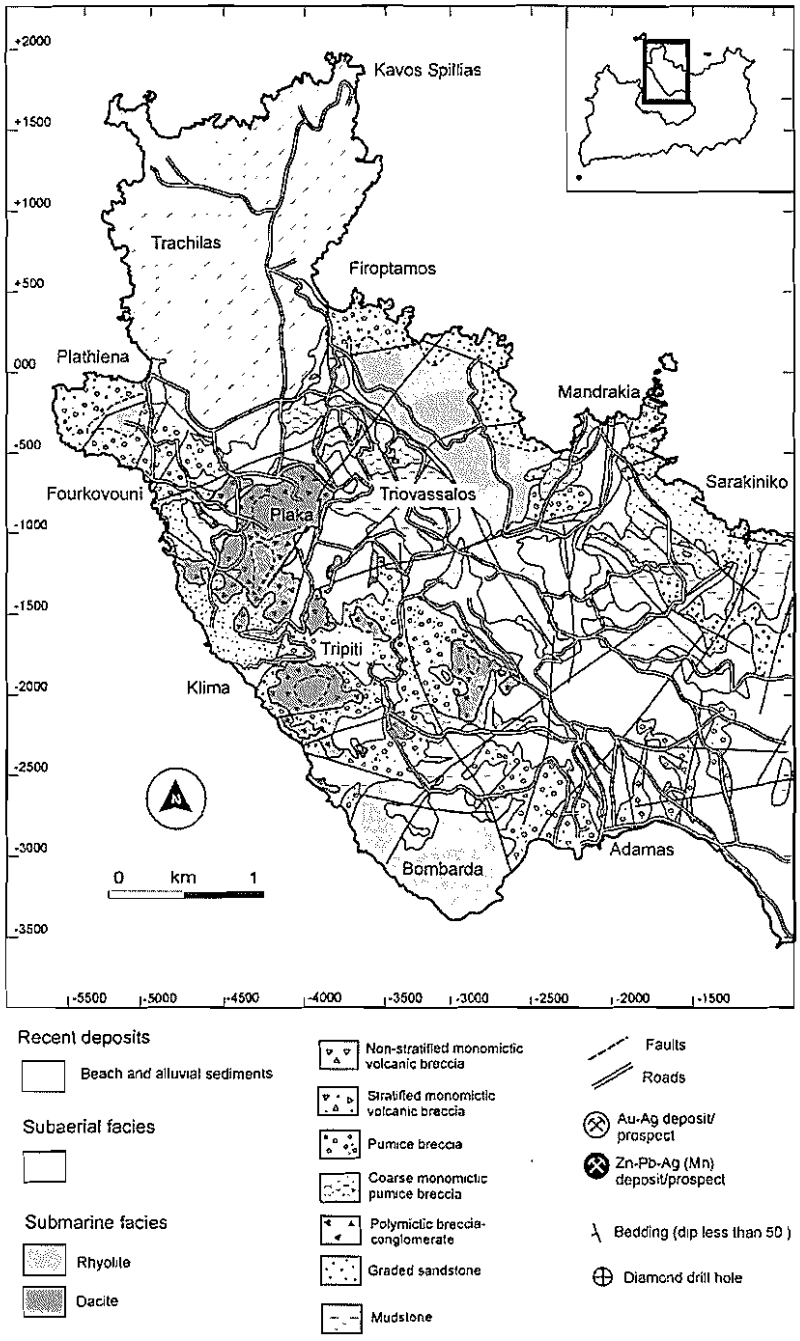

Figure 4.4 Geological map of the Bombarda area (inset) showing the distribution of the main volcanic facies, structure and ore deposits, modified after Fytikas (1977). Local grid from 1:5000 scale Greek topographic maps.

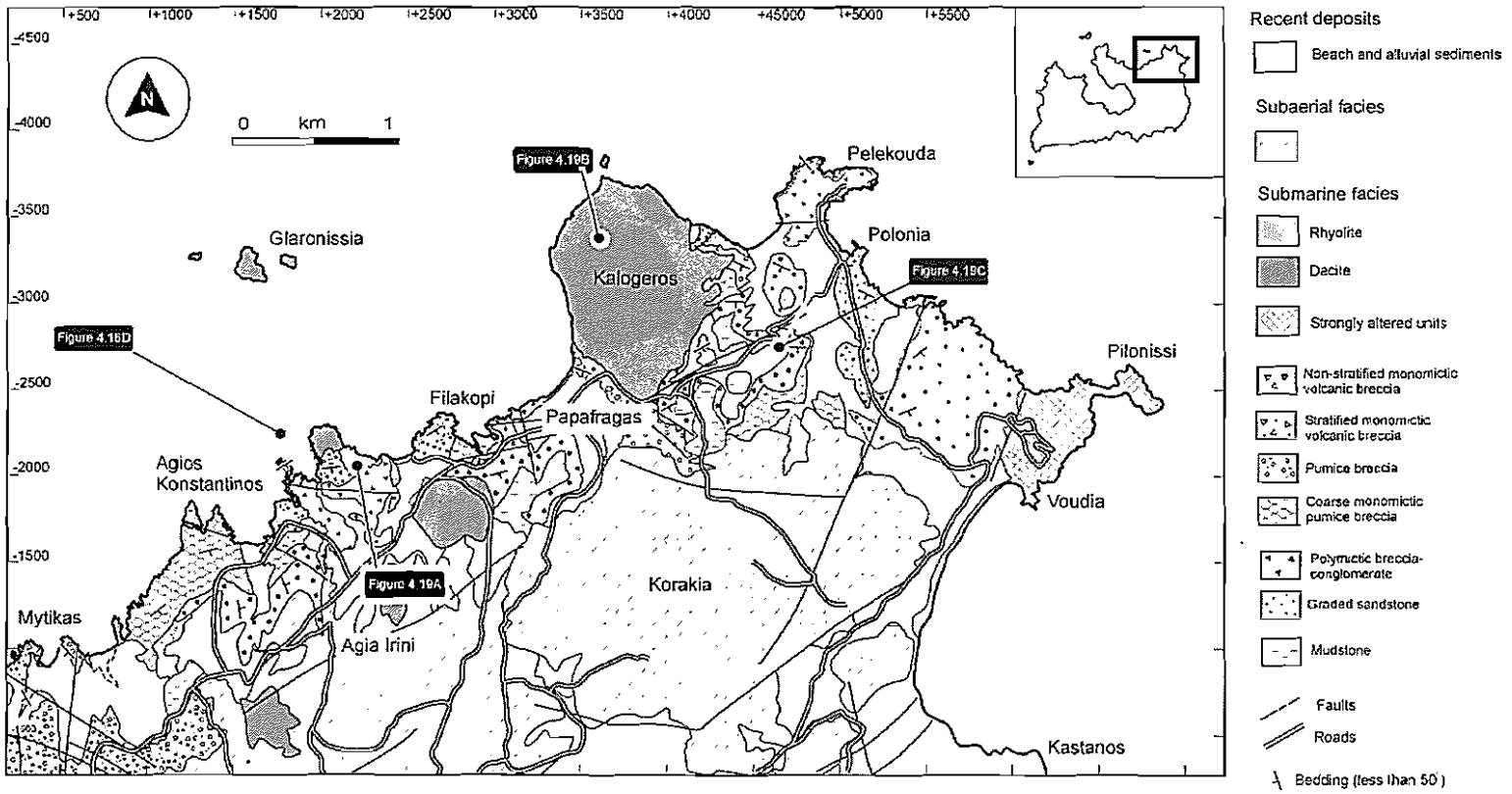

Figure 4.5 Geological map of the Filakopi area (inset) showing the distribution of the main volcanic facies, structure and ore deposits, modified after Fytikas (1977). Local grid from 1:5000 scale Greek topographic maps.

Table 4.1 Summary of the principal submarine facies on Milos

Facies	Description	Interpretation
	Rhyolite facies association	
1. Coherent rhyolite	Evenly porphyritic (10-15 vol. %), euhedral quartz ± feldspar or biotite phenocrysts (<3 mm), groundmass perlitic or microcrystalline, weakly to non-vesicular, columnar joints, massive, flow banded. Thickness x extent: 5-300 m thick x 0.2-1.5 km.	Coherent facies of lavas, domes and intrusions
2. Sediment-matrix rhyolite breccia facies	Non-stratified, poorly sorted, clast- to matrix-supported, jigsaw-fit texture, gradational contacts with coherent rhyolite facies. Thickness x extent: 0.1-10 m x <50 m. Clasts: 1 cm to 15 cm (outsized clasts up to 1.5 m across), blocky to polyhedral rhyolite clasts. Matrix: minor, quartz ± feldspar and biotite crystals and crystal fragments, pumice (<1 mm).	Intrusive hyaloclastite
	Dacite facies association	
3. Coherent dacite	Evenly porphyritic (8-20 vol. %), euhedral plagioclase (1-3 mm), biotite and quartz phenocrysts (0.5-1 mm), groundmass perlitic or microcrystalline, weakly to non-vesicular, columnar joints, massive, flow banded. Thickness x extent: 10-350 m x <3.5 km.	Coherent facies of lavas, domes and intrusions
4. Non-stratified monomictic dacite breccia facies	Monomictic, non-stratified, poorly sorted, clast- to matrix-supported, jigsaw-fit and clast-rotated texture, gradational contacts with coherent dacite. Thickness[a] x extent: <30 m x <1 km. Clasts: 1-40 cm, blocky to polyhedral. Matrix: minor, same as clasts, crystals and crystal fragments (<2 mm).	In situ hyaloclastite
5. Stratified monomictic dacite breccia facies	Monomictic, reversely or normally graded, poorly sorted, clast- to matrix-supported, diffusely stratified sandstone tops or bases, gradational contacts with non-stratified monomictic dacite breccia. Thickness x extent: 0.9–4 m x <0.5 km. Clasts: 2 mm–1.5 m, angular to subangular. Matrix: minor, dacite clasts (<5 cm), crystals and crystal fragments (<2 mm).	Redeposited hyaloclastite
6. Sediment-matrix dacite breccia facies	Non-stratified, poorly sorted, clast- to matrix-supported, jigsaw-fit texture, gradational contacts with coherent dacite facies. Thickness x extent: 0.1-5 m x <25 m. Clasts: 1 cm-15 cm, blocky, polyhedral. Matrix: minor, quartz ± feldspar, biotite crystals and crystal fragments, pumice(<1 mm).	Intrusive hyaloclastite

Facies	Description	Interpretation
	Andesite facies association	
7. Coherent andesite	Evenly porphyritic (10-20 vol. %), euhedral plagioclase (1-2 mm), hornblende (<1 mm) ± pyroxene (<1 mm) phenocrysts, groundmass perlitic or microcrystalline, weakly to non-vesicular, columnar joints, massive, flow banded. Thickness x extent: 60-200 m x <3.5 km.	Coherent facies of lavas, domes and intrusions
8. Non-stratified monomictic andesite breccia facies	Monomictic, non-stratified, poorly sorted, clast- to matrix-supported, jigsaw-fit and clast-rotated texture, gradational contacts with coherent andesite. Thickness x extent: 5-30 m x <1 km. Clasts: 2-40 cm, blocky, polyhedral. Matrix: minor, same as clasts, crystals and crystal fragments (<2 cm).	In situ hyaloclastite
9. Stratified monomictic andesite breccia facies	Monomictic, reversely or normally graded, poorly sorted, clast- to matrix-supported, diffusely stratified sandstone tops, gradational contacts with non-stratified monomictic andesite breccia. Thickness[a] x extent: 1.5–8 m x <0.5 km. Clasts: 2 cm-1.2 m, angular to subangular, coarse clasts (>64 mm) normal joints at their margins and internal polyhedral joints (pseudo-pilliow texture). Matrix: minor, same as clasts, crystals, crystal fragments (<2 cm).	Redeposited hyaloclastite
10. Sediment-matrix andesite breccia facies	Non-stratified, poorly sorted, clast- to matrix-supported, jigsaw-fit texture; gradational contacts with coherent andesite facies. Thickness x extent: 0.1-5 m x <40 m. Clasts: 1 cm-15 cm, blocky, polyhedral. Matrix: plagioclase, hornblende ± pyroxene crystals and crystal fragments, pumice minor.	Intrusive hyaloclastite
	Basaltic andesite facies association	
11. Coherent basaltic andesite facies	Evenly porphyritic (10-15 vol. %), euhedral plagioclase and pyroxene phenocrysts, groundmass perlitic or microcrystalline, weakly to non-vesicular, columnar joints, massive, fractured intervals-polyhedral blocks 0.9-1.5 m in length (pseudo-pillows). Thickness x extent: 20 m thick x <1 km.	Coherent facies of dykes
12. Sediment-matrix basaltic andesite breccia facies	Non-stratified, poorly sorted, clast- to matrix-supported, jigsaw-fit texture; gradational contacts with coherent basaltic andesite facies. Thickness x extent: 0.1-5 m x <25 m. Clasts: 5-20 cm, blocky, polyhedral. Matrix: plagioclase, pyroxene crystals and crystal fragments (<1 mm), pumice (<2 cm).	Intrusive hyaloclastite

Facies	Description	Interpretation
	Pumice breccia facies association	
13. Coarse pumice breccia facies	Reversely graded, poorly sorted, grain-supported, upper contacts with enclosing units are planar and sharp, lower contacts are gradational. Thickness[a] x extent: 1-20 m x >2 km. Clasts: 64 mm–8.5 m, prismatic, pumice, no lithic clasts. Matrix: internally graded, base fine (1–2 cm) pumice clasts and top shard-rich mud.	Water-settled pumice produced by a submarine explosive eruption
14. Stratified pumice breccia facies	Massive or diffusely stratified, poorly sorted, normal grading of dense lithic clasts, and reverse grading of coarse pumice clasts. Thickness[a] x extent: 0.9–4 m x >2 km. Clasts: 2 cm–1.5 m in diameter, angular to subrounded pumice, obsidian, lithic clasts (<1-50 vol. %). Matrix: same as clasts (>50 %), crystals, crystal fragments and cuspate shards.	Pumiceous gravity current deposit produced by a submarine explosive eruption
15. Lithic-pumice breccia facies	Massive, fines-poor, poorly sorted, grain-supported, lower contacts erosional and upper contacts gradational. Thickness[a] x extent: <8 m x <1 km. Clasts: 1 cm-20 m, angular to subangular rhyolite, dacite and andesite (may be hydrothermally altered), minor juvenile clasts (2–5 vol. %). Matrix: minor, same as clasts, crystals and crystal fragments. (<2 cm).	High-particle-concentration, lithic clast-rich, gravity current deposit produced by a submarine explosive eruption
16. Graded pumice breccia facies	Normally graded, clast- to matrix-supported, diffusely stratified sandstone tops. Thickness[a] x extent: 10 cm-4 m x <1 km. Clasts: 2-10 cm, equant to ragged tube pumice, crystal fragments, glass shards, dacite, andesite. Matrix: minor, same as clasts, crystals and crystal fragments (<2 cm).	Pumiceous gravity current deposit produced by a submarine explosive eruption
	Scoria-rich breccia facies association	
17. Cross-stratified scoria breccia facies	Internally diffusely stratified or high-angle cross-stratification or gradded. Thickness[a] x extent: 5 cm-2 m x 1-2 km. Clasts: 2-10 mm-andesitic scoria (40–70 vol. % vesicles), 0.5-1.5 m andesitic fluidal clasts (20–50 vol. % vesicles), minor lithic clasts (<1 %). Matrix: minor, plagioclase and ferromagnesian crystals and crystal fragments (<1 mm).	Gravity current and traction current deposits produced by strombolian-type explosive eruption
18. Massive andesitic breccia facies	Massive or normally graded, laterally discontinuous, clast- to matrix-supported. Thickness[a] x extent: 5 m-10 m x <0.5 km. Clasts: non-vesicular andesitic clasts, andesitic scoria. Matrix: minor, plagioclase and ferromagnesian crystals and crystal fragments (<1 mm).	High-particle-concentration, clast-rich, gravity current deposit

Facies	Description	Interpretation
19. Fine scoria sandstone facies	Normally graded or high-angle cross stratification. Thickness x extent: 30 cm-2 m x 1-2 km. Clasts: <1 to 5 cm scoria. Matrix: whole and broken plagioclase and ferromagnesian crystal fragments (1-3 mm).	Submarine gravity current and traction current deposits produced by strombolian-type explosive eruption
	Sandstone-conglomerate facies association	
20. Graded sandstone facies	Normally graded, grain-supported, high-angle angle bedding truncations, diffusely planar-stratified. Thickness[a]: 30 cm-2 m. Components: broken quartz and feldspar crystal fragments ± rhyolite, dacite, andesite, sedimentary and schist clasts.	Deposits from low- and high-concentration turbidity currents and traction currents
21. Thickly bedded to laminated mudstone	Laminated to thickly bedded, white to brown, laterally continuous. Thickness[a]:<1-40 cm. Components: feldspar (dominantly plagioclase), quartz and white mica crystal fragments, and glass shards, sparse large (>1 m) pumice clasts.	Predominantly suspension sedimentation; in part water-settled ash and pumice
22. Polymictic breccia-conglomerate facies	Massive to weakly normally graded, laterally discontinuous beds, intercalated graded sandstone or mudstone beds. Thickness[a]: 1-40 m. Clasts: 1-10 cm, subangular to rounded, rhyolite, dacite, andesite and sedimentary clasts. Matrix: whole and broken plagioclase and ferromagnesian crystal fragments (1-3 mm).	Fragments stored and reworked in high-energy environment; final transport by high-concentration sediment gravity flows

[a]Thickness ranges of facies refer to beds.

4.5 Rhyolite facies association

The rhyolite facies association consists of two spatially related facies: coherent rhyolite and sediment-matrix rhyolite breccia. Distinction between these two facies in outcrop and core can be difficult due to the pervasive hydrothermal alteration. Contacts between the two facies are gradational and the breccia facies typically occurs along the upper contacts of the coherent facies.

Coherent rhyolite facies

Coherent rhyolite is common in the western part of Milos, at Profitis Illias and Chon-

dro Vouno (Figure 4.3), and in the north at Bombarda and between Firopotamos and Mandrakia (Figures 4.4, 4.7A and 4.7B). In cross-section, intervals of coherent rhyolite are broadly semi-circular and range from 300 m to several tens of metres in thickness (Figure 4.6). This facies consists of pale purple to grey, massive or flow-banded rhyolite (Figure 4.7C) and may be weakly vesicular (<10 vol. %) near contacts. The competent and siliceous nature of this facies makes it resistant to weathering and erosion and it commonly caps hills in the field area (e.g. Profitis Illias and Chondro Vouno).

The mineralogy, abundance and distribution of phenocrysts are, in most cases, uniform within a single unit. Intervals of coherent rhyolite are typically weakly quartz-feldspar-phyric and less commonly biotite-feldspar-quartz-phyric (10-15% phenocrysts). Phenocrysts (<3 mm) are euhedral and set in a groundmass which is microcrystalline or perlitic and contains spherulites. Quartz phenocrysts are commonly highly embayed. Feldspar phenocrysts are euhedral, 0.2-3 mm and dominantly plagioclase, which is typically partially to completely altered to fine-grained sericite.

Units of coherent rhyolite commonly cross-cut stratigraphy, although in many instances, contact relationships are ambiguous or poorly exposed. Thick intervals are characterised by regular well-developed columnar joints (Figure 4.7D). Column axes are generally subvertical, or radiating regularly from the core towards the margins of single units. The columns typically have pentagonal, hexagonal or quadrangular outlines in cross-section. Flow banding occurs in some units, particularly along margins (Figure 4.7C). Where present, the flow bands are approximately parallel to the outer contacts of the units. Single bands vary in thickness, being narrow (mm scale) to relatively wide (cm-m scale) and are generally discontinuous, with lateral extents in the order of tens of metres. The flow banding is overprinted by columnar joints.

Sediment-matrix rhyolite breccia facies

Intervals of the sediment-matrix rhyolite breccia facies occur at the margins of coherent rhyolite (Figure 4.7E). Contacts between the sediment-matrix rhyolite breccia facies and coherent rhyolite facies are gradational to sharp. This breccia facies is limited in extent, forming discontinuous lenses (<50 m in length) that range in thickness from a few tens of centimetres to several tens of metres (Figure 4.6, PD009).

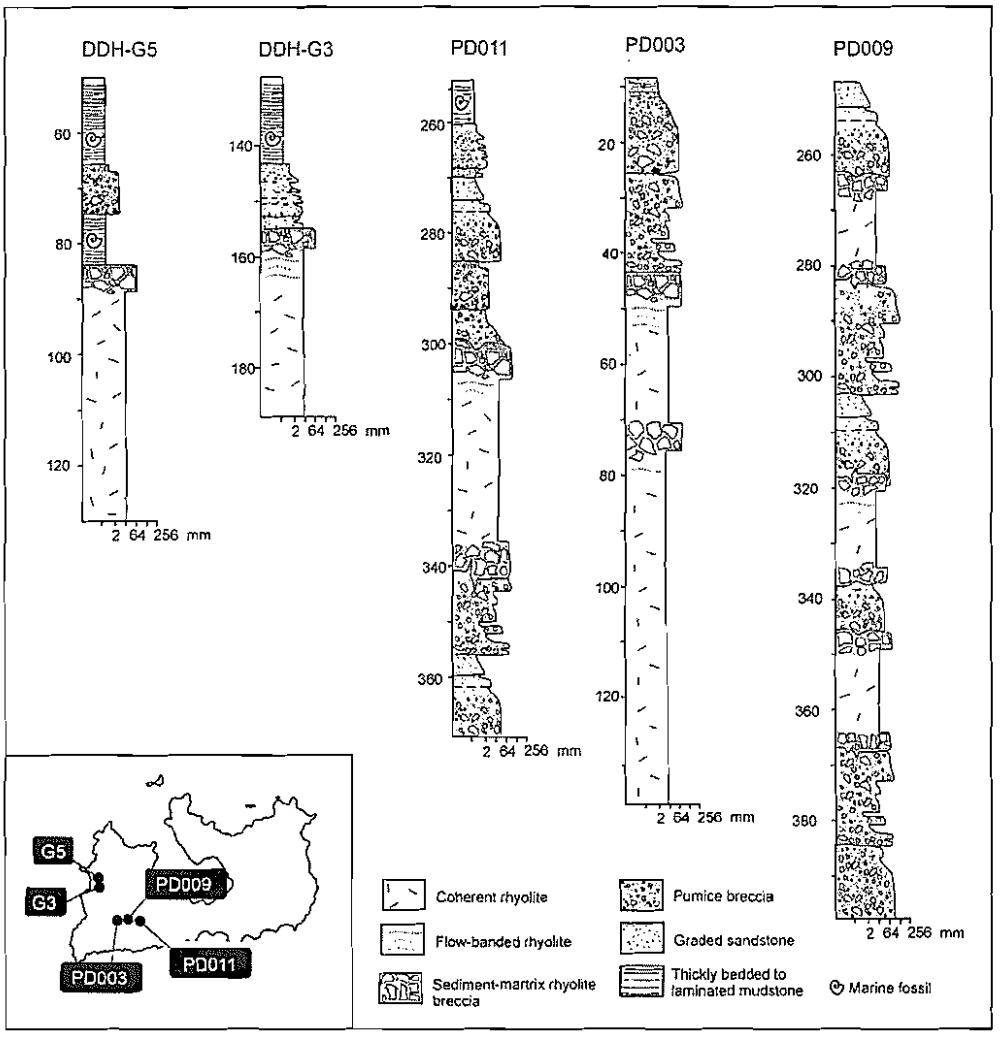

Figure 4.6 Graphic logs for key parts of diamond drill holes at several locations (inset) showing important textures, structures and contact relationships of the two main facies comprising the rhyolite facies association. Diamond drill holes DDH-G5 and DDH-G3 are vertical holes (location in Figure 4.2). Diamond drill holes PD011, PD003 and PD009 are angled holes (location in Figure 4.3) and the logs show the calculated true thickness.

The sediment-matrix rhyolite breccia facies is massive and consists of blocky to polyhedral rhyolite clasts. The sediment-matrix rhyolite breccia units vary from clast-supported jigsaw-fit texture to matrix-supported aggregates of rotated clasts (Figure 4.7F). The breccia is dominated by clasts 1 cm to 15 cm in diameter, with some rare outsized clasts up to 1.5 m across. Rhyolite clasts comprise approximately 45-75 vol. % of the breccia. The clasts are mineralogically identical to the coherent rhyolite facies and are typically slightly more vesicular (up to 20 vol. % vesicles). The breccia is commonly poorly sorted and local groups of clasts define jigsaw-fit textures, or else, may be dispersed in the sediment matrix. In many places, clasts within the breccia decrease in size approaching the outer contacts of such intervals. Rhyolite clasts are separated by a pale

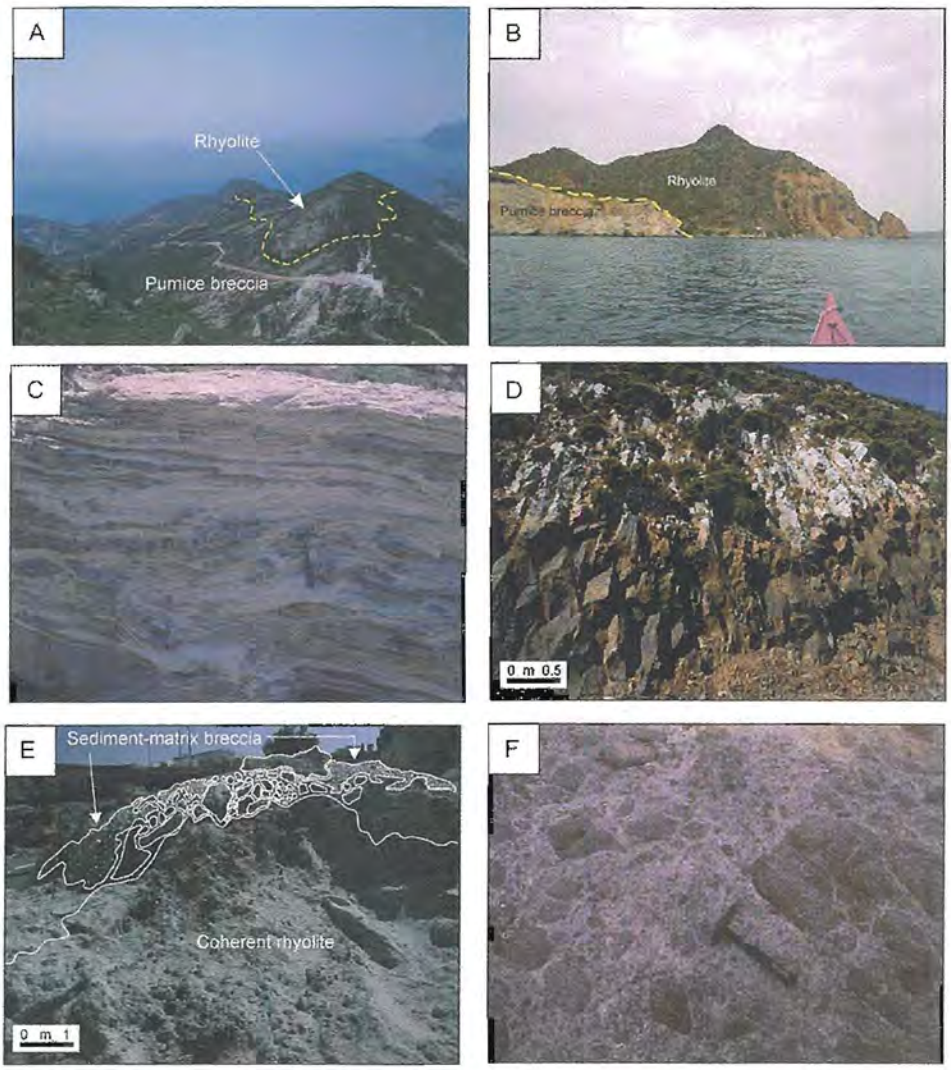

Figure 4.7 **A** Outcrop of the rhyolite facies association at Chondro Vouno, looking towards the west from Profitis Illias. Most of the foreground consists of altered pumice breccia. The top of the mountain is dominated by coherent rhyolite. Intervals of the sediment-matrix rhyolite breccia facies occur at the margins of coherent rhyolite and the pumice breccia facies. **B** The Bombarda rhyolite crosscuts the host formation (pumice breccia) along a highly irregular, discordant contact that truncates local bedding. **C** Close-up view of the flow-banded rhyolite of Dhemeneghaki dome (Figure 4.1). Single bands are uneven in thickness and generally laterally discontinuous; no systematic variations in band thickness are evident. **D** Dark green to grey, massive, non-vesicular coherent rhyolite facies, characterised by well-developed columnar joints, at Chondro Vouno. **E** Outer margin of a rhyolite intrusion at Mandrakia (Figure 4.4). Coherent rhyolite passes into sediment-matrix rhyolite breccia. **F** The sediment-matrix rhyolite breccia at Triades (Figure 4.2) comprises blocky to polyhedral rhyolite clasts. The breccia includes domains of jigsaw-fit breccia and clast-rotated breccia.

grey matrix consisting dominantly of blocky rhyolite clasts <2 cm and millimetre- to sub-millimetre-sized crystals and crystal fragments and felsic pumice. The fine rhyolite clasts have the same phenocryst assemblage and texture as other rhyolite clasts in the breccia, but are less vesicular.

Gradations between coherent rhyolite and sediment-matrix rhyolite breccia are common at the margins of coherent rhyolite intervals. The sediment-matrix rhyolite breccia typically has gradational contacts with pumice breccia, sandstone or mudstone. Bedding in the adjacent sedimentary facies is generally disrupted and contorted. Bedding rarely extends into the sediment-matrix breccia facies. Coherent rhyolite facies typically grades into clast-supported sediment-matrix rhyolite breccia. The abundance of sediment intervals increases towards the outer contacts of units.

Interpretation

The spatial association, compositional similarity and gradational contacts of intervals of coherent rhyolite and sediment-matrix rhyolite breccia indicate that the two facies are different but genetically related parts of a single lava or intrusion.

Gradational contacts between intervals of coherent rhyolite and sediment-matrix rhyolite breccia are consistent with clasts within breccia facies being derived from disintegration of the coherent rhyolite. The abundance of jigsaw-fit texture within the sediment-matrix rhyolite breccia indicates that fragmentation was more or less in situ. The polyhedral shape of the rhyolite clasts suggests that brittle fracture occurred in response to contraction during rapid cooling on contact with wet sediment at the outer margin of the rhyolite (c.f. Pichler 1965; Yamagishi and Dimroth 1987), and the sediment-matrix rhyolite breccia is thus interpreted to represent intrusive hyaloclastite (e.g. Hanson and Wilson 1993). The wet sediment (mainly pumice breccia) invaded the fractures in the rhyolite, probably in response to pressure reduction as the fractures opened (e.g. Kokelaar 1982; Brooks 1995).

Textures and contact relationships of the rhyolite facies association on Milos are consistent with cryptodomes and syn-volcanic sills (e.g. Horikoshi 1969; de Rosen-Spence et

al. 1980; Cas et al. 1990; Allen 1992; Hanson and Wilson 1993; Hamasaki 1994; Allen et al. 1996; Goto and McPhie 1998).

4.6 Dacite facies association

The dacite facies association consists of four spatially related facies: coherent dacite, non-stratified monomictic dacite breccia, stratified monomictic dacite breccia and sediment-matrix dacite breccia. In Chapter 5, a particularly well exposed example of this facies association (the Kalogeros cryptodome) is described and interpreted in detail. Thus, the following descriptions and interpretations are based on other examples of the dacite facies association on Milos.

Coherent dacite facies

Intervals of coherent dacite are well exposed in the Triades-Kontaro area (Figure 4.1), especially in the cliffs at Triades (Figures 4.2 and 4.8). They also occur sporadically through the northern part of the island (Figures 4.4 and 4.5). Units of coherent dacite are thick (10 to 350 m; Figure 4.9), massive, weakly to non-vesicular, columnar jointed and dark grey to purple in colour. They have lateral extents up to 3.5 km. The coherent dacite at Triades has gradational contacts with thick (up to 50 m) non-stratified and stratified monomictic dacite breccia (Figure 4.8).

The coherent dacite facies is generally poorly to moderately porphyritic, containing 8-20 vol. % euhedral phenocrysts, including 1-3 mm plagioclase (5-10 vol. %), 1 mm biotite (2-5 vol. %) and 0.5-1 mm quartz phenocrysts (2-5 vol. %) in a microcrystalline or glassy perlitic groundmass. The groundmass is dominated by microlites of plagioclase and opaque phases (65 vol. %) in black glass (20 vol. %). Plagioclase microlites are moderately aligned and define a weak flow texture. Regular columnar joints characterise some thick intervals of massive coherent dacite and margins are locally flow banded parallel to the outer contact. At the margins of single units, especially along the upper contacts, the coherent dacite facies merges into several-metre-wide intervals of non-stratified monomictic dacite breccia and sediment-matrix dacite breccia.

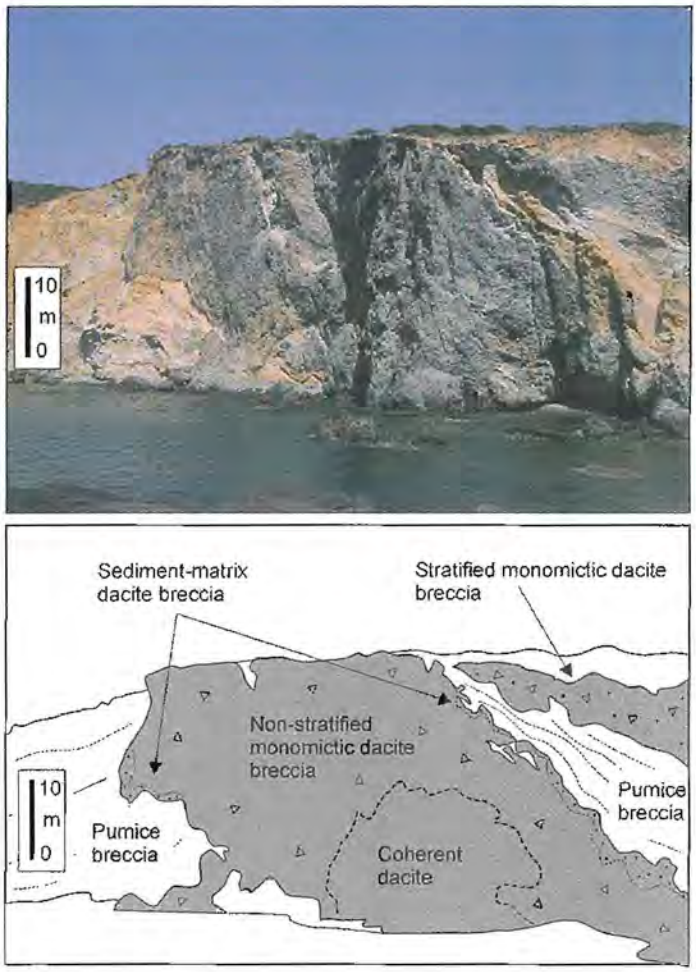

Figure 4.8 Dacite facies association. A north-south section of the Favas partially extrusive dacite cryptodome, at Triades (Figure 4.2), shows the context and contact relationships of the main facies of the dacite facies association. The intrusive facies (coherent dacite, non-stratified monomictic dacite breccia and sediment-matrix dacite breccia) cross-cut local bedding in the host pumice breccia formation (white) along a highly irregular, discordant contact. The extrusive facies (stratified monomictic dacite breccia) is interbedded with pumice breccia facies.

Non-stratified monomictic dacite breccia

Intervals of non-stratified monomictic dacite breccia typically occur at the margins of or within coherent dacite (Figure 4.9, DDH-G3). Contacts between non-stratified monomictic dacite breccia facies and coherent dacite facies are gradational (Figure 4.8). Intervals of non-stratified monomictic dacite breccia facies are limited in lateral extent and thickness (typically less than 10 m thick).

The non-stratified monomictic dacite breccia facies consists of blocky to polyhedral dacite clasts (1-40 cm in diameter) and is characterised by domains of jigsaw-fit and

clast-rotated breccia (Figure 4.10A). The dacite clasts within the breccia are poorly to moderately porphyritic, containing 8-20% plagioclase, biotite and quartz phenocrysts and may be flow banded and weakly vesicular (up to 20 vol. % vesicles). Vesicles are mostly amoeboid to slightly elongate in shape (2-3 mm across and 3-8 mm long).

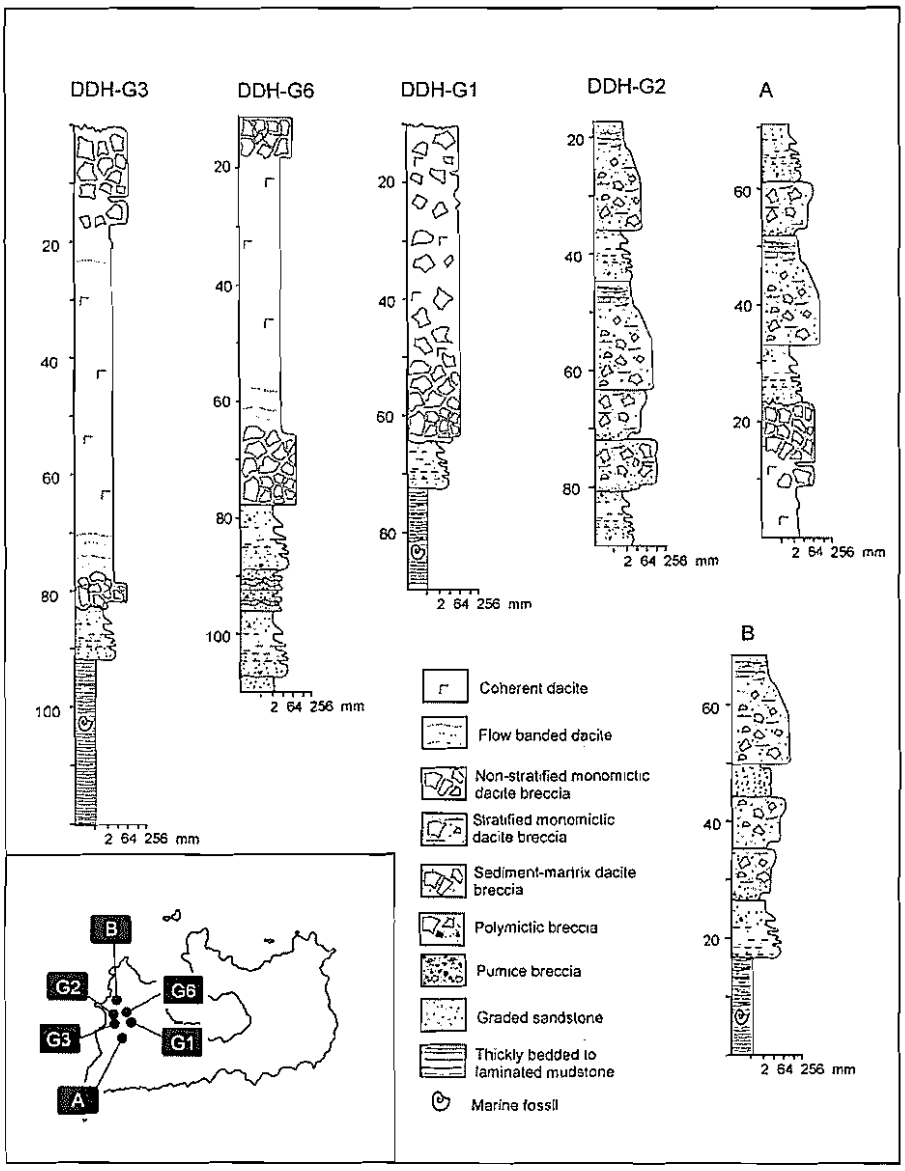

Figure 4.9 Graphic logs for key parts of diamond drill holes and outcrops at several locations (inset) showing important textures, structures and contact relationships of the four main facies comprising the dacite facies association. Diamond drill holes DDH-G3, DDH-G6, DDH-G2 and DDH-G1 are vertical holes (location in Figure 4.2).

Only very minor matrix is present in most of the non-stratified dacite breccia facies. However, clasts in this facies are locally separated by a pale grey matrix consisting of fine (<2 mm), non- to weakly vesicular (up to 20 vol. % vesicles), dominantly blocky

dacite clasts (Figure 4.10B). The fine dacite clasts have the same mineral assemblage and textures as other dacite clasts in the non-stratified monomictic dacite breccia facies, but are less vesicular. Commonly, the matrix is poorly sorted, although some groups of fine dacite clasts define jigsaw-fit textures.

Stratified monomictic dacite breccia facies

The stratified monomictic dacite breccia facies is exposed along the coast north of Triades (Figure 4.8). It contains clasts with morphologies, textures and compositions identical to clasts in the non-stratified monomictic dacite breccia, with which it has gradational contacts. Intervals of this facies are typically less than 50 m thick, although they extend laterally up to 0.5 km.

Intervals of this facies comprise several internally diffusely stratified, moderately to poorly sorted, very thick (0.9–4 m), reversely or normally graded beds of breccia with diffusely stratified sandstone tops or bases. Bed contacts are poorly defined. Wavy, diffuse stratification within the beds is defined by alignment of coarse dacite clasts. The breccia is mainly composed of weakly vesicular, angular to subangular dacite clasts (2 cm–1.5 m in diameter) bound by planar to curviplanar or irregular margins, in grain- or matrix-support (Figure 4.10C). The stratified monomictic dacite breccia is characterised by domains of clast-rotated breccia (Figure 4.10C). Flow-banded clasts are randomly oriented, indicating clast rotation. The matrix consists of a poorly sorted mixture of angular, non- to weakly vesicular (up to 10 vol. % vesicles), dacite clasts (<5 cm) and non-vesicular black glass shards (<2 mm).

Sediment-matrix dacite breccia facies

Intervals of sediment-matrix dacite breccia range in thickness from a few tens of centimetres to several metres (Figure 4.8). The sediment-matrix dacite breccia has gradational contacts with thick intervals of coherent and non-stratified monomictic dacite breccia facies. The facies occurs as discontinuous lenses (<25 m in length) associated with the basal margins of coherent dacite units or intermixed with the non-stratified monomictic dacite breccia facies (Figure 4.9, DDH-G6). The sediment-matrix dacite breccia facies is texturally similar to the sediment-matrix rhyolite breccia facies.

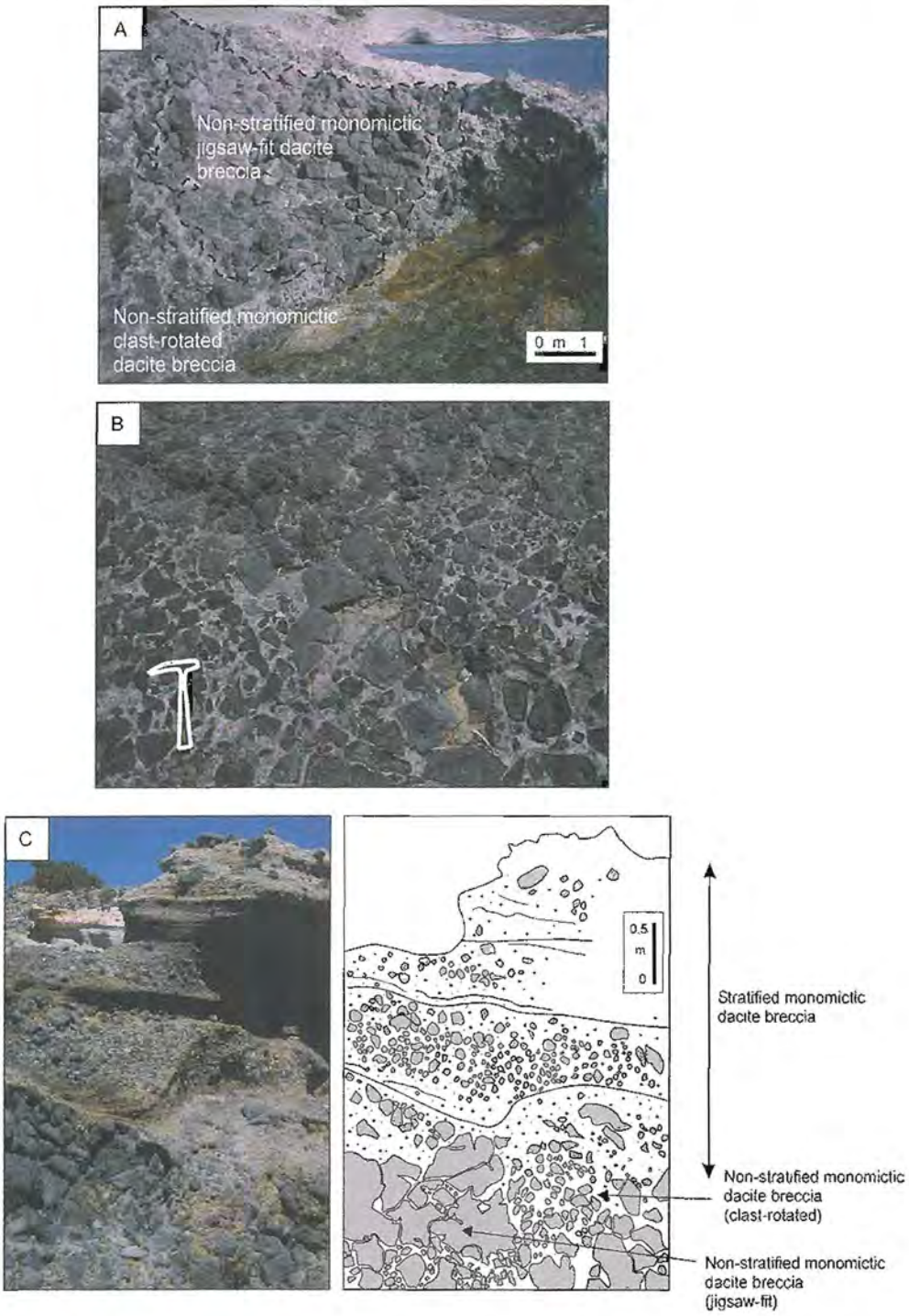

Figure 4.10 Dacite facies association at Triades (Figure 4.2). **A** The non-stratified monomictic dacite breccia facies includes domains of jigsaw-fit (centre of photo) and clast-rotated matrix-rich breccia (separated by dashed black line). **B** Non-stratified monomictic dacite breccia facies comprises blocky to polyhedral dacite clasts 1-40 cm in diameter. **C** Stratified monomictic dacite breccia consists of moderately to poorly sorted, reversely graded beds with diffusely stratified sandstone bases. The beds are mainly composed of blocky dacite clasts bound by planar to curviplanar or irregular margins.

Interpretation

The coherent dacite, non-stratified monomictic dacite breccia, stratified monomictic dacite breccia and sediment-matrix dacite breccia facies are all closely spatially associated and mineralogically similar, and may have gradational contacts, indicating that these facies are genetically related and were probably produced by single eruptive or intrusive events.

The polyhedral shapes of the dacite clasts in the non-stratified monomictic dacite breccia are the result of brittle fracture, possibly in response to contraction during rapid cooling on contact with wet sediment or seawater (c.f. Pichler 1965; Yamagishi and Dimroth 1987). Hence, this facies is interpreted to represent in situ hyaloclastite. Fragmentation may have also been induced by dynamic stressing due to continued movement of adjacent less-viscous dacite lava (e.g. Brooks et al. 1982; Kokelaar 1986; Griffiths and Fink 1993).

The stratified monomictic dacite breccia facies contains clasts that are compositionally identical to those in the non-stratified monomictic dacite breccia, but edge-modified. The poor sorting, reverse to normal grading and tabular bed geometry are consistent with rapid deposition from high-particle-concentration gravity currents (c.f. Lowe 1976; Postma 1986). Hence, this facies is interpreted to represent redeposited hyaloclastite.

The sediment-matrix dacite breccia occurs at the gradational contacts between coherent facies and pumice breccia, sandstone and mudstone facies. The composition and textures in this facies are consistent with the interpretation that it is a variety of intrusive hyaloclastite (c.f. Hanson and Wilson 1993). Intrusive hyaloclastite provides evidence for intrusion of magma into wet unconsolidated sediment, and is commonly found at the contacts of shallow intrusions, or along the basal contacts of lavas with underlying sediments.

Facies characteristics, facies geometries and contact relationships in the dacite facies association are consistent with its interpretation as submarine lavas, domes, cryptodomes and partially extrusive cryptodomes (c.f. de Rosen-Spence et al. 1980; Cas et al.

1990; Allen 1992; Kano et al. 1991; Goto and McPhie 1998; Doyle and McPhie 2000). The association of redeposited hyaloclastite (stratified monomictic dacite breccia facies) with some intervals of coherent dacite indicates at least partial extrusion of dacite as lavas, domes, and partially extrusive cryptodomes. Dacite lavas and domes on Milos are strongly constructional, and dominated by central domains of coherent dacite surrounded by variable amounts of in situ hyaloclastite. In contrast, the presence of intrusive hyaloclastite (sediment-matrix dacite breccia) along upper contacts of some intervals is consistent with the interpretation that they are shallow syn-volcanic cryptodomes.

4.7 Andesite facies association

The andesite facies association consists of four spatially related facies: coherent andesite, non-stratified monomictic andesite breccia, stratified monomictic andesite breccia and sediment-matrix andesite breccia.

Coherent andesite facies

Coherent andesite occurs in the Mavro Vouni area in the western part of Milos. There are excellent examples exposed in the southern cliffs at Gerontas (Figures 4.3 and 4.11). Single intervals of coherent andesite are typically very thick (60 to 200 m, Figure 4.12), massive, weakly to non-vesicular and dark brown or purple in colour. They have lateral extents of several kilometres.

Intervals of coherent andesite facies are generally poorly to moderately porphyritic, containing 10-20 vol. % phenocrysts, including 1-2 mm euhedral plagioclase (10-15 vol. %), 1 mm prismatic hornblende (5-8 vol. %), and 1 mm clinopyroxene (<1 vol. %), in a microcrystalline or glassy perlitic groundmass. Regular columnar joints characterise some thick intervals of massive coherent andesite. The margins of such intervals are locally flow banded parallel to the contacts. At the margins of single units, especially along the upper contacts, the coherent andesite facies merges into several-metre-wide intervals of non-stratified monomictic andesite breccia.

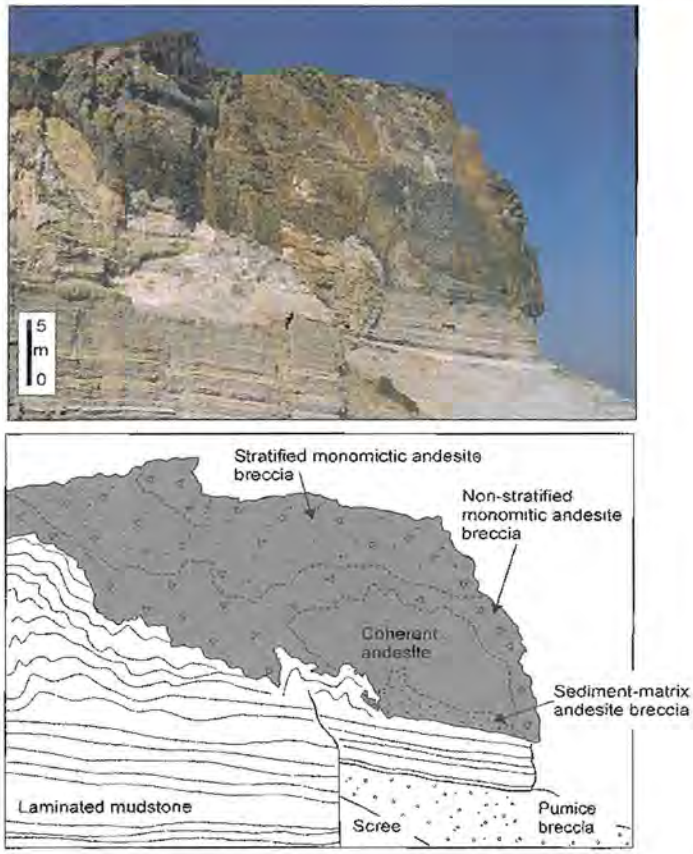

Figure 4.11 Andesite facies association. A cliff section at Gerontas (Figure 4.3) shows an irregular interval of coherent andesite and gradational relationships with non-stratified monomictic andesite breccia facies and sediment-matrix andesite breccia facies, particularly along the lower and upper contacts. Note the soft-sediment deformation in laminated and thinly bedded mudstone underlying the andesite facies association.

Non-stratified monomictic andesite breccia facies

Non-stratified monomictic andesite breccia typically occurs at the margins of or within coherent andesite. Contacts between non-stratified monomictic andesite breccia facies and coherent andesite facies are sharp or gradational (Figures 4.11 and 4.12).

The non-stratified monomictic andesite breccia facies consists of blocky to polyhedral andesite clasts (2-40 cm in diameter) and is characterised by domains of jigsaw-fit and clast-rotated breccia. Only very minor matrix is present in most of the non-stratified andesite breccia facies. However, at the margins of such intervals of non-stratified andesite breccia, clasts in the breccia are separated by a pale purple matrix consisting of fine (<2 cm), non- to weakly vesicular (up to 20 vol. % vesicles), dominantly blocky andesite clasts. Andesite clasts may be massive or flow banded. The fine andesite clasts

have the same phenocryst assemblage and textures as other andesite clasts in the non-stratified monomictic andesite breccia facies. Commonly, the matrix is poorly sorted, although some groups of andesite clasts define jigsaw-fit textures.

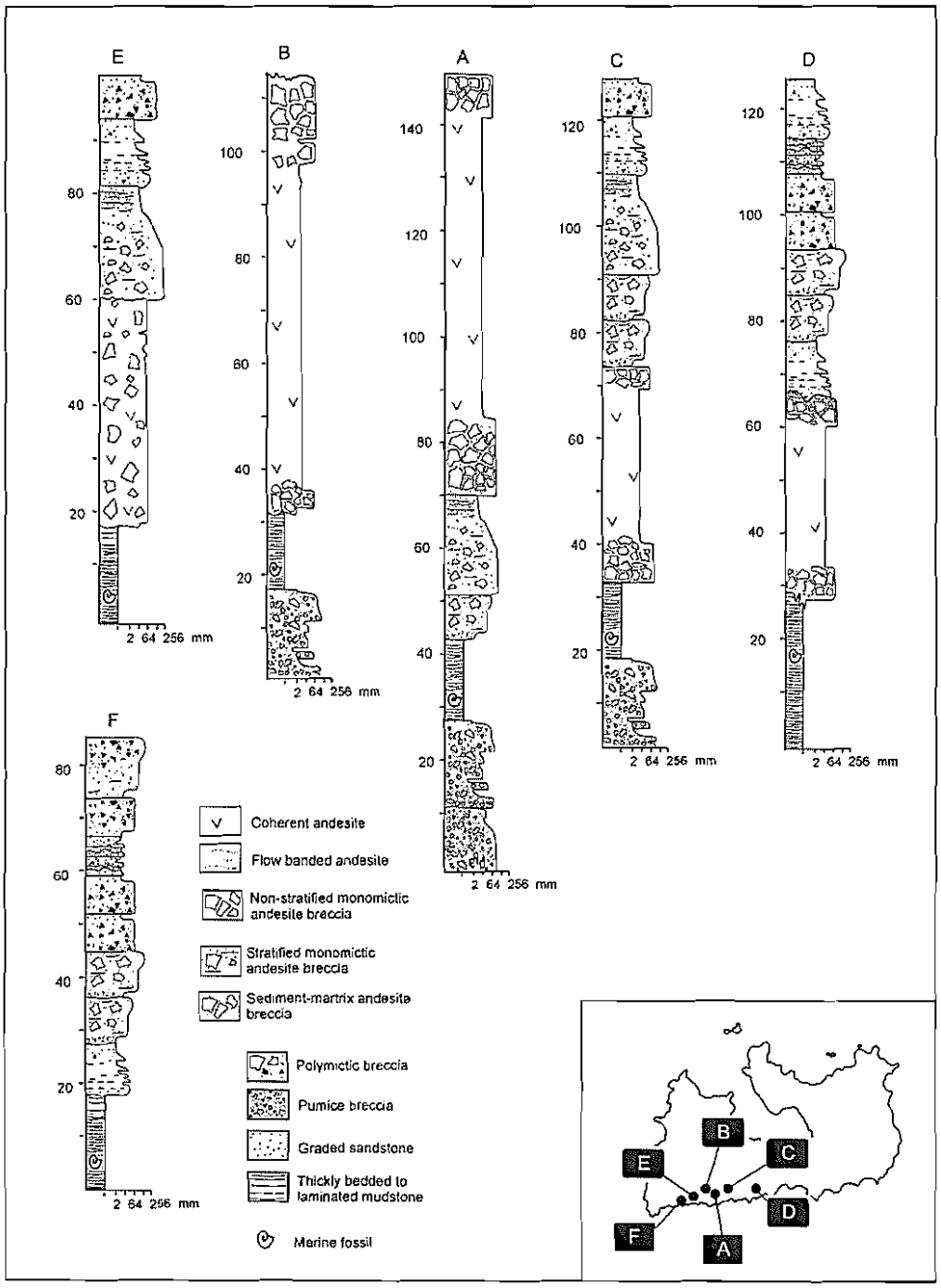

Figure 4.12 Graphic logs for key parts of outcrops at several locations (inset), showing important textures, structures and contact relationships of the four main facies comprising the andesite facies association. Locations of sections on Figure 4.3.

The non-stratified andesite breccia facies is texturally similar to non-stratified dacite breccia facies and is spatially associated with coherent andesite, sediment-matrix andesite breccia and stratified monomictic andesite breccia.

Stratified monomictic andesite breccia facies

This facies is commonly spatially associated with coherent andesite and non-stratified andesite breccia facies (Figure 4.11). Intervals of this facies are typically less than 50 m thick, although they extend laterally up to 0.2 km (Figure 4.13A).

Beds of this facies are very thick (1.5-8 m thick) and either internally massive, graded or diffusely stratified. These beds generally consists of poorly to moderately sorted, clast-supported, monomictic breccia composed of massive or flow-banded andesite clasts (Figure 4.13B). Clasts range from 2 mm to 1.2 m, and are generally subangular and blocky with curviplanar margins. The coarse andesite clasts (>64 mm) have normal joints at their margins whereas clast interiors exhibit polyhedral joints (Figure 4.13C). Clasts are typically randomly oriented, however, some jigsaw-fit texture is present. The matrix consists of smaller (<1 mm to 2 cm) andesite fragments (Figure 4.13C).

The lower contacts of beds are sharp and vary from passive and depositional to strongly erosional. The upper contacts of intervals of the stratified monomictic andesite breccia are diffusely stratified and gradational into sandstone (Figure 4.12).

Sediment-matrix andesite breccia facies

Intervals of sediment-matrix andesite breccia range in thickness from a few tens of centimetres to several metres. Intervals of this facies occur as discontinuous lenses (<40 m in length) associated with the basal margins of coherent andesite units or intermixed with the non-stratified monomictic andesite breccia facies (Figure 4.11). The sediment-matrix andesite breccia facies is similar texturally to the sediment-matrix dacite breccia facies.

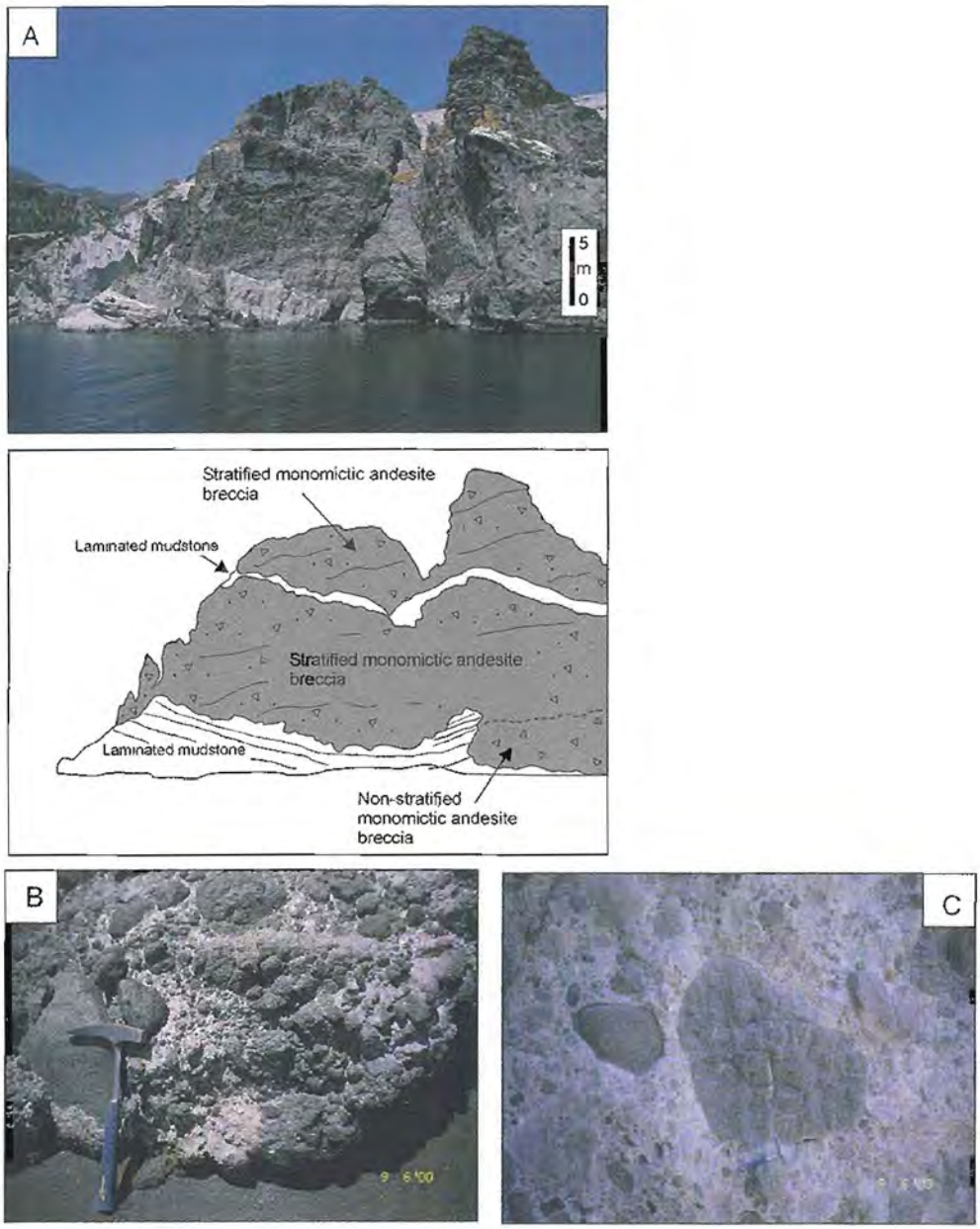

Figure 4.13 Stratified monomictic andesite breccia. **A** Cliff section at Gerontas (Figure 4.3), showing a very thick sequence of stratified monomictic andesite breccia facies. **B** The stratified monomictic andesite breccia facies (at Gerontas, Figure 4.3) comprises blocky to polyhedral andesite clasts (1-40 cm in diameter) in grain- or matrix-support. **C** Many coarse andesite clasts (>64 mm) have normal joints at their margins (pseudo-pillow texture, Watanabe and Katsui 1976; Yamagishi 1991), whereas clast interiors exhibit polyhedral joints. Same location as 4.13B.

Interpretation

The andesite facies association is similar to the dacite facies association, differing only in composition, and is interpreted in the same way to comprise submarine lavas, domes, cryptodomes and partially extrusive cryptodomes (c.f. De Rosen-Spence et al. 1980; Kokelaar 1982; Cas et al. 1990; Kano et al. 1991; Doyle and McPhie 2000). The non-stratified monomictic andesite breccia facies is interpreted as in situ hyaloclastite, the stratified monomictic breccia is interpreted as redeposited hyaloclastite and the sediment-matrix andesite breccia facies is interpreted as intrusive hyaloclastite, and all three clastic facies are related to and derived from the coherent andesite facies.

4.8 Basaltic andesite facies association

The basaltic andesite facies association consists of two spatially related facies: coherent basaltic andesite and sediment-matrix basaltic andesite breccia. Contacts between the two facies are gradational. The breccia facies typically occurs along the outer contacts of the coherent facies.

Coherent basaltic andesite facies

Coherent basaltic andesite occurs in the southwestern part of Milos, west of Mavro Vouno (Figure 4.3). The coherent basaltic andesite facies is volumetrically dominant (80 vol. %) in this association, and occurs in elongate and laterally continuous intervals that range up to 20 m in thickness (Figure 4.14A). Units of coherent basaltic andesite commonly cross-cut stratigraphy and consist of dark grey to black, massive and non- to weakly vesicular basaltic andesite.

The coherent basaltic andesite facies is typically aphyric or feldspar-pyroxene-phyric (10-15 vol. % phenocrysts). Phenocrysts (<1 mm) are euhedral and distributed evenly throughout a microcrystalline or glassy perlitic groundmass. Feldspar phenocrysts (8-10 vol. %) are dominantly strongly zoned plagioclase. Minor clinopyroxene (<5 vol. %) up to 0.5 mm, and sparse olivine and hornblende (<2 vol. %) are also present. The groundmass (85-90 vol. %) is characterised by microlites of plagioclase and opaque phases (65 vol. %) in pale brown perlite (20 vol. %).

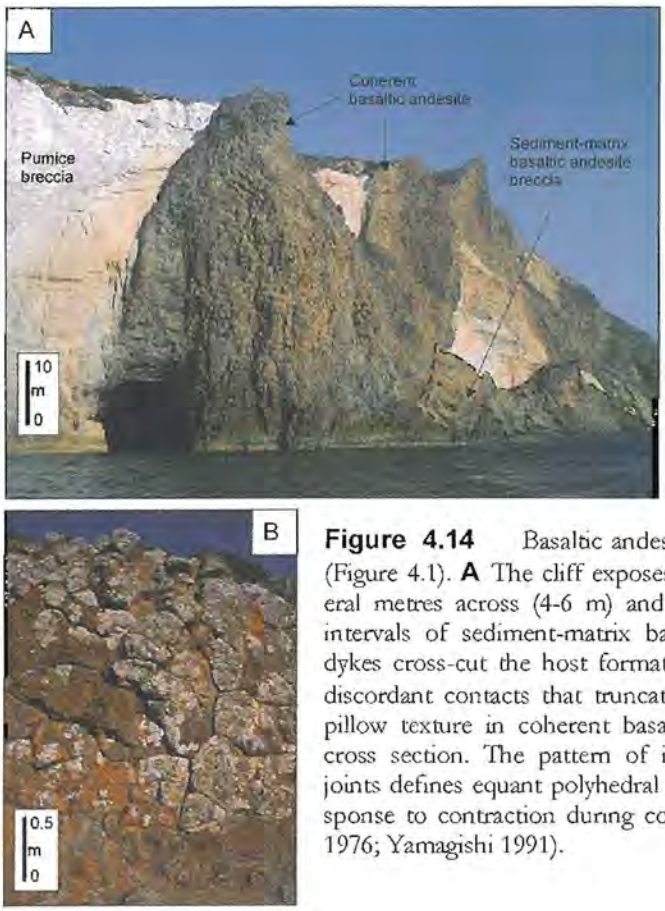

Figure 4.14 Basaltic andesite facies association at Sikia (Figure 4.1). **A** The cliff exposes basaltic andesite dykes several metres across (4-6 m) and separated by discontinuous intervals of sediment-matrix basaltic andesite breccia. The dykes cross-cut the host formation along a highly irregular, discordant contacts that truncate local bedding. **B** Pseudo-pillow texture in coherent basaltic andesite shown here in cross section. The pattern of intersecting, broadly curving joints defines equant polyhedral blocks, which develop in response to contraction during cooling (Watanabe and Katsui 1976; Yamagishi 1991).

Thick intervals (15-20 m) of basaltic andesite are characterised by regular, well-developed columnar joints (Figure 4.14A). Column axes are generally perpendicular to the margins of single units. Near contacts with host facies, the coherent facies merges into several-metre-wide intervals of blocky jointing and platy jointing. Intersecting joints outline polyhedral blocks 0.9-1.5 m in length (pseudo-pillows, Watanabe and Katsui 1976; Yamagishi 1991, Figure 4.14B).

A gradual outward transition occurs from closely columnar-jointed basaltic andesite into the sediment-matrix basaltic andesite breccia facies, particularly along upper contacts with volcaniclastic and sedimentary facies (Figure 4.14A).

Sediment-matrix basaltic andesite breccia facies

Intervals of the sediment-matrix basaltic andesite breccia occur at the margins of coherent basaltic andesite intervals, creating a discontinuous selvage between the coherent

basaltic andesite and the host sedimentary formations, ranging in thickness from a few centimetres to several metres (Figure 4.14A). Contacts between the sediment-matrix basaltic andesite breccia facies and coherent basaltic andesite facies are gradational to sharp.

The sediment-matrix basaltic andesite breccia facies consists of blocky to polyhedral basaltic andesite clasts and varies from clast-supported jigsaw-fit texture to matrix-supported aggregates of rotated clasts. The facies is dominated by clasts 5-20 cm across, with some rare outsized clasts up to 50 cm across. Clasts are separated by small amounts of millimetre- to sub-millimetre-sized matrix composed of plagioclase, clino-pyroxene and olivine crystals and crystal fragments, fine (<2 cm) non-vesicular, dominantly blocky basaltic andesite clasts and rhyolitic pumice. The fine basaltic andesite clasts have the same mineral assemblage and textures as other basaltic andesite clasts in the sediment-matrix basaltic andesite breccia facies. Commonly, the matrix is poorly sorted.

Interpretation

The coherent basaltic andesite facies and sediment-matrix basaltic andesite breccia facies are closely spatially associated and mineralogically similar and may have gradational contacts, indicating that these facies are genetically related. The abundance of jigsaw-fit texture within the sediment-matrix basaltic andesite breccia indicates that fragmentation was more or less in situ. The polyhedral shape of the basaltic andesite clasts suggests that brittle fracture occurred in response to contraction during rapid cooling on contact with wet sediment at the outer margin of the basaltic andesite (c.f. Pichler 1965; Yamagishi and Dimroth 1987), and the sediment-matrix basaltic andesite breccia is thus interpreted to represent intrusive hyaloclastite (e.g. Hanson and Wilson 1993).

The volumetrically dominant, texturally uniform coherent basaltic andesite intervals are dissected by a network of intersecting, gently curved fractures at their margins. This distinctive polyhedral fracture pattern is typical of the rapidly chilled parts of subaqueous lavas, domes and shallow intrusions (c.f. pseudopillows, Watanabe and Katsui 1976; Yamagishi 1991). The gradational change from columnar-jointed basaltic andesite to fractured basaltic andesite probably reflects a transition from regular, stable iso-

therms in the interior to highly irregular, shifting isotherms at the rapidly cooled outer margin of an intrusion or lava.

All contacts of the basaltic andesite facies association are intrusive, highly irregular and cross-cut bedding in the host volcaniclastic formations. Therefore, the coherent basaltic andesite facies is inferred to occupy dykes with outer selvages of intrusive hyaloclastite (e.g. Yamagishi 1987; Yamagishi 1991; Kano 2002).

4.9 Pumice breccia facies association

The pumice breccia facies association is the most voluminous facies association on Milos (Figure 4.1). The association comprises four facies: coarse pumice breccia, diffusely stratified pumice breccia, lithic-pumice breccia and graded pumice breccia. In Chapter 6, a particularly well exposed example of this facies association (the Filakopi Pumice Breccia) is described and interpreted in detail. Only a brief summary is presented here, together with a discussion of variations shown by other examples.

There are four main types of juvenile clasts in the pumice breccia facies association: (1) pumice (85-90 vol. %); (2) non- to poorly vesicular, glassy, relatively phenocryst-rich clasts (<2 vol. %); (3) black, perlitic obsidian clasts (<<1 vol. %); and (4) glass shards. All analysed juvenile clasts are rhyolitic and dacitic (67.13-72.25 wt. % SiO_2), and juvenile clasts in single units show only slight variations in major- and trace-element abundances (Appendix A). The pumice clasts generally contain 1-5 vol. % phenocrysts of quartz (up to 1 mm in diameter), biotite and plagioclase. The pumice clasts are moderately to highly vesicular (50–80 vol. % vesicles) and vesicles are spherical to elongate (several mm long and less than 1 mm diameter). Coarse (>64 mm) pumice clasts are prismatic to tabular and have normal joints at their margins and internal polyhedral joints. Finer (<64 mm) pumice clasts are generally blocky or polyhedral, and subangular to subrounded. Phenocryst-rich, glassy, non- to poorly vesicular (0-30 vol. % vesicles) clasts contain 5–8 % phenocrysts of quartz or plagioclase (up to 1 mm in diameter) and biotite. Vesicles show transitions from ovoid to elongate morphologies. The perlitic obsidian clasts are aphyric and typically less than a few millimetres in diameter. The glass shards are generally <0.5 mm across and cuspate in shape.

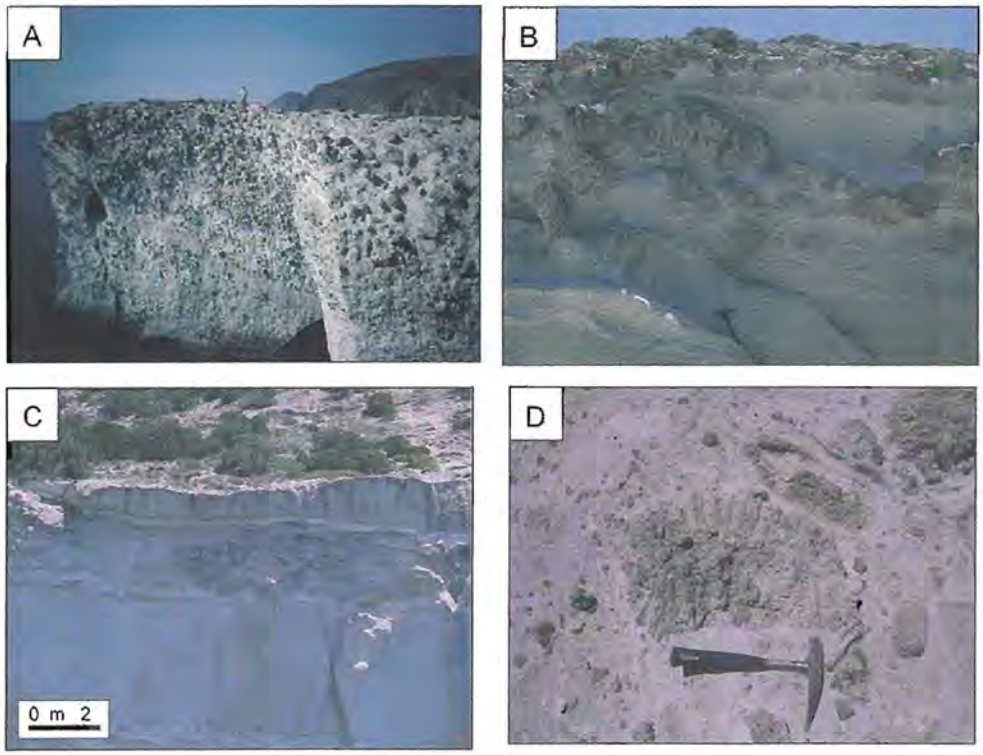

Figure 4.15 Pumice breccia facies association. **A** A very thick (17 m) interval of coarse pumice breccia exposed in Filakopi headland (location Figure 4.5). The coarse-grained pumice breccia is reversely graded and dominated by large (64 mm–8.5 m) prismatic pumice clasts in a much finer matrix. A person at the top of the unit for scale. **B** A laterally uneven and discontinuous interval of coarse pumice breccia facies. The fine pumice matrix is diffusely stratified with internally massive beds composed of well-sorted, angular to subangular pumice clasts in grain support. **C** A tabular bed of coarse pumice breccia facies enclosed by massive stratified pumice breccia units at Kleftiko. The bed is overlain by 30 cm of laminated, white, shard-rich mud. **D** Prismatic pumice clast with normal joints along the margins and internal polyhedral joints in the basal part of a interval of coarse pumice breccia facies.

Coarse pumice breccia facies

Beds of coarse pumice breccia (e.g. unit C in Chapter 6) occur throughout the submarine succession on Milos, and are best exposed in the cliffs at Filakopi (Figures 4.5, 4.15A and 4.15B). They also occur sporadically through the southern part of the island (Figures 4.3 and 4.15C). Tabular beds of coarse pumice breccia are typically very thick (1–20 m), reversely graded and grain-supported. The most striking features of this facies are the extreme range in grain size, and the lack of dense lithic clasts. Intervals of this facies are dominated by very large (64 mm–8.5 m) prismatic pumice clasts in a much finer matrix (Figures 4.15D). The matrix within single beds grades internally upward through the bed from fine (1–2 cm) pumice clasts at the base to shard-rich mud at the top (Figure 4.16). The upper contacts with enclosing units are planar and sharp, whereas lower contacts are gradational.

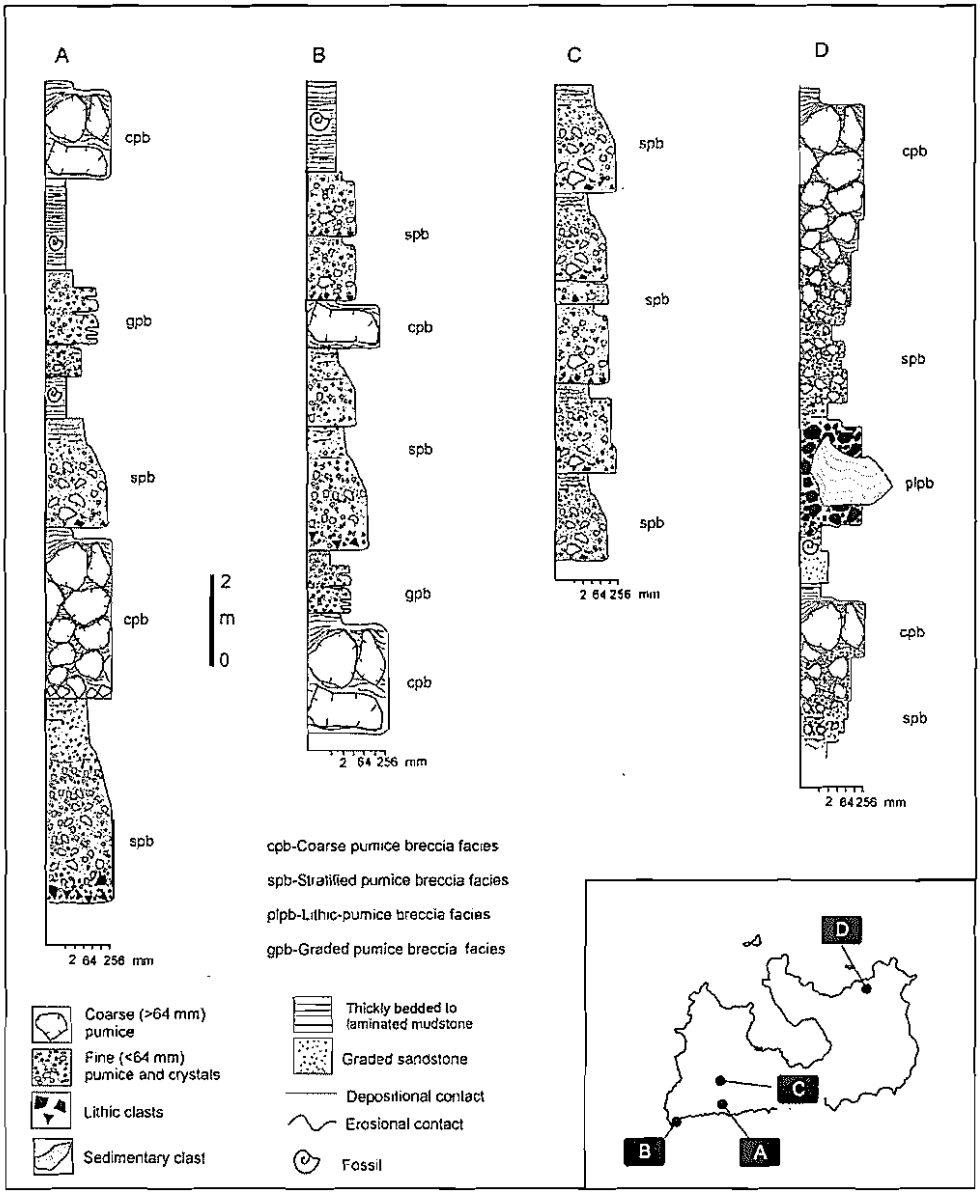

Figure 4.16 Graphic logs for key parts of outcrops at several locations (inset), showing important textures, structures and contact relationships of the four main facies comprising the pumice breccia facies association. Graphic log D shows part of the FPB (Chapter 6). Location of sections on Figures 4.2 and 4.4.

Stratified pumice breccia facies

Intervals of stratified pumice breccia facies (e.g. unit B in Chapter 6) are well exposed in the cliffs at Filakopi (Figures 4.5 and 4.17A). They also occur sporadically through the southern part of the island, including a very thick interval (up 300 m thick) at Profitis Illias (Figures 4.3 and 4.16). Intervals of stratified pumice breccia facies are typically massive or diffusely stratified, poorly sorted and comprise very thick (0.9–4 m) beds

(Figure 4.17A). Single beds of this facies are generally poorly defined and mainly composed of angular to subangular pumice clasts (2 cm–1.5 m in diameter) in grain support, with scattered non- to poorly vesicular, glassy, crystal-rich clasts and obsidian clasts (Figure 4.17B). Single beds display normal grading of dense lithic clasts, and reverse grading of coarse pumice clasts.

Lithic-pumice breccia facies

Intervals of lithic-pumice breccia facies (e.g. unit A in Chapter 6) are well exposed in the cliffs at Pollonia and Agios Konstantinos (Figures 4.5 and 4.17C). They also occur sporadically through the southern part of the island. The lithic-pumice breccia facies occurs as fines-poor, poorly sorted, polymictic, grain-supported lithic breccia beds (Figure 4.17C). Single beds are typically tabular and generally less than 8 m thick and comprise lithic clasts from centimetres to a several metres in diameter, most of which are fresh or hydrothermally altered dacite or andesite. Other lithic clasts include schist, Neogene limestone and sedimentary clasts (mudstone and sandstone). Coarse lithic clasts (>20 cm in diameter) are generally subrounded, whereas smaller lithic clasts are angular. Juvenile clasts are minor (2–5 vol. %) and typically coarse (~40 cm in diameter) non- to poorly vesicular, glassy rhyolitic or dacitic clasts.

Graded pumice breccia facies

Intervals of graded pumice breccia facies are well exposed in the cliffs at Sarakiniko (Figures 4.4 and 4.17D). They also occur sporadically through the southern part of the island. Beds of graded pumice breccia are normally graded with massive or diffusely bedded sandstone tops. A few beds have thin reverse-graded sandstone bases overlain by normally graded breccia or sandstone. The sandstone is composed of quartz and plagioclase crystals, crystal fragments and fine (<5 mm) subangular pumice. Single beds of graded pumice breccia are tabular, ranging from 10 cm to 4 m thick, and laterally discontinuous (Figure 4.17D). The breccia is mainly composed of angular to subangular pumice clasts (2-10 mm) in grain support, with scattered lithic clasts (<5 vol. %) that range in size from 1-30 cm diameter. The lithic clast population can include rhyolite, dacite, andesite, sedimentary clasts and basement-derived schist. Outsized, sparsely distributed pumice clasts (up to 0.5 m in diameter) occur in some intervals of graded pumice breccia (Figure 4.17D). The coarse prismatic pumice clasts have normal joints at

their margins, whereas clast interiors exhibit polyhedral joints. The upper and lower contacts of beds range from gradational to sharp.

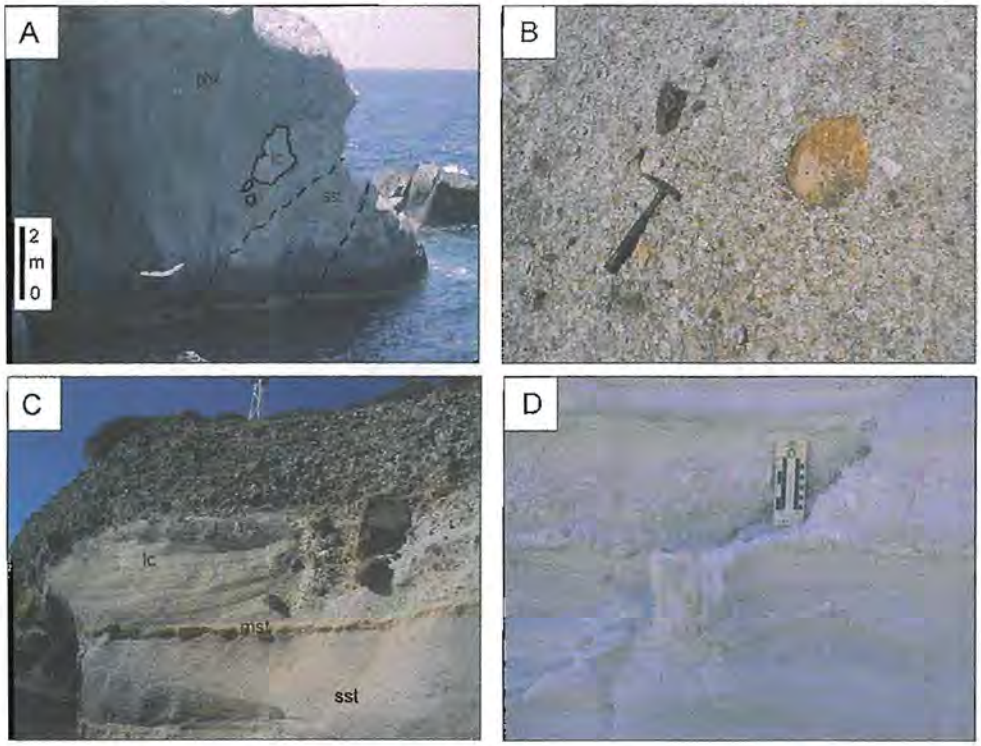

Figure 4.17 Pumice breccia facies association. **A** A very thick bed of stratified pumice breccia facies. The unit has an erosional contact with the underlying sandstone (sst). A large clast (lc) derived from sandstone (sst) occurs at the base. **B** Close-up of the stratified pumice breccia. The bed is composed of poorly sorted, angular to subrounded pumice clasts in grain support with minor, hydrothermally altered, lithic clasts . **C** Reversely to normally graded interval of lithic-pumice breccia facies at Pelekouda Point (Figure 4.4). The breccia has a sharp, planar contact with the underlying fossiliferous and bioturbated mudstone (mst). A large clast (lc) derived from sandstone (sst) occurs at the base. Two parts of the coarse lithic breccia are visible: a lower, 1.5-2-m-thick, finer grained, pumiceous part and an upper, 5 m-thick, coarser grained, lithic clast-rich part which includes andesitic and dacitic clasts up to 2.5 m in diameter. **D** An interval of graded pumice breccia facies at Sarakiniko (Figure 4.4) containing an outsized (40 cm) prismatic pumice clast.

Interpretation

This facies association is interpreted to be the product of explosive eruptions from submarine vents because: (1) highly vesicular, glassy, felsic pumice clasts are the dominant component; (2) although very coarse pumice and lithic clasts are present, most are relatively small (<2 cm) and, in some beds, ash is abundant; (3) coarse pumice clasts (>64 mm) are common and have complete quenched margins; (4) overall, the facies association shows good hydraulic sorting.

The facies characteristics of the coarse pumice breccia facies are consistent with deposition of the coarse pumice clasts from suspension, creating a framework that was progressively infilled by fine pumice clasts from contemporaneous traction currents, and then by water-settled ash. The bed forms in the stratified pumice breccia, lithic-pumice breccia and graded pumice breccia suggest deposition from submarine gravity currents. The abundance of thick intervals (up to 300 m) of this association and the widespread distribution (tens of kilometres) suggest aggradation was rapid and syn-eruptive, involving suspension and large-volume, pumiceous, submarine gravity currents.

Variations within the pumice breccia facies association

The oldest parts of the submarine succession are dominated by the pumice breccia facies association. This association displays little in internal heterogeneity. Although the FPB (Chapter 6) is representative of the pumice breccia facies association, there are obvious variations in the geometry of single facies within the Milos succession. To a large extent, these variations depend on a number of factors, including proximity to source (vent), and inferred eruption magnitude and intensity (c.f. Allen and Stewart, in press). Single-event, small- to moderate-volume eruptions (e.g. Filakopi Pumice Breccia, Chapter 6) produced basal, poorly sorted, lithic-rich gravity current deposits overlain by pumiceous gravity current deposits, both of which are fines-poor (stratified pumice breccia and lithic-pumice breccia). Density-sorted pumiceous and vitric ash deposited by water-settled fall are also a common product (coarse pumice breccia). Larger volume eruptions produced thick, breccia units comprising normally graded dense lithic clasts and reversely graded pumice clasts, overlain by successively finer and thinner, graded beds (e.g. Profitis Illias, Figure 4.16C), all of which were deposited from syn-eruptive gravity currents. These deposits are texturally similar to the Wadaira Tuff, Japan (Fiske and Matsuda 1964) also considered as the product of submarine explosive eruptions. Small volume, lower intensity eruptions (e.g. Bombarda pumice breccia, Rinaldi and Campos Venuti 2003) produced thick, fines-poor, laterally confined facies dominated by water-settled coarse pumiceous fallout and their resedimented equivalents (graded pumice breccia).

4.10 Scoria-rich breccia facies association

The scoria-rich breccia facies association is volumetrically minor and limited to the northeastern sector of Milos. This facies association is best exposed in the coastal cliffs of Papafragas (Figures 4.4 and 4.18A) and comprises three facies: cross-stratified scoria breccia, massive andesitic breccia and fine scoria sandstone (Figure 4.19). The scoria-rich breccia facies association is dominated by andesitic clasts (~95 vol. %; ~56 wt % SiO_2). The pristine state, abundance and uniform composition suggest that the andesitic clasts were freshly erupted and they are considered to be juvenile. The remainder (<5 vol. %) consists of non-juvenile clasts, primarily comprising subangular to rounded felsic pumice, and non- to poorly vesicular, plagioclase-phyric, glassy dacite and andesite. Some are strongly hydrothermally altered. Other non-juvenile lithic clasts include basement-derived metamorphic (schist) and sedimentary rocks.

The juvenile andesitic clasts can be divided into three principal types according to vesicularity and shape: (1) scoria clasts (5-10 cm in diameter); (2) large (>64 mm), black, fluidal clasts; (3) poorly vesicular clasts. The scoria clasts (type 1) are typically aphyric and glassy or contain 1-5 vol. % phenocrysts of plagioclase (up to 1 mm in diameter). Black to dark grey scoria is moderately to highly vesicular (40–70 vol. % vesicles) and vesicles are elongate to spherical (several mm long and less than 1 mm diameter). The black fluidal clasts (type 2) contain <1 vol. % phenocrysts of plagioclase set in a glassy groundmass. The fluidal clasts are moderately vesicular (20–50 vol. % vesicles) and vesicles are highly elongate. The poorly vesicular (0-5 vol. % vesicles) clasts (type 3) contain 2-5 vol. % plagioclase phenocrysts (0.5-2 mm in length) and rare pyroxene (<1 vol. %).

Cross-stratified scoria breccia facies

This facies mainly consists of thick (2-3 m) sets of angle-of-repose cross-stratified scoria breccia composed of angular to subangular, scoria clasts (> 85%, 2-10 mm), black, fluidal clasts (13%, 1.5 m in diameter) and subordinate lithic clasts (<2%). The cross-stratified beds are poorly sorted and, clast supported (Figures 4.18B and 4.18C). Diffusely stratified intervals characterised by high-angle bedding truncations are also presented. Contacts of this facies with adjacent facies vary from sharp to diffuse. Intervals

of this facies range from 10 m to 45 m in thickness. Foresets in cross-stratified beds, are defined subtle grain-size variations, and are planar and inclined at 25-30^0 to the bed base. Cross-bed foresets display unidirectional dips (toward the southeast).

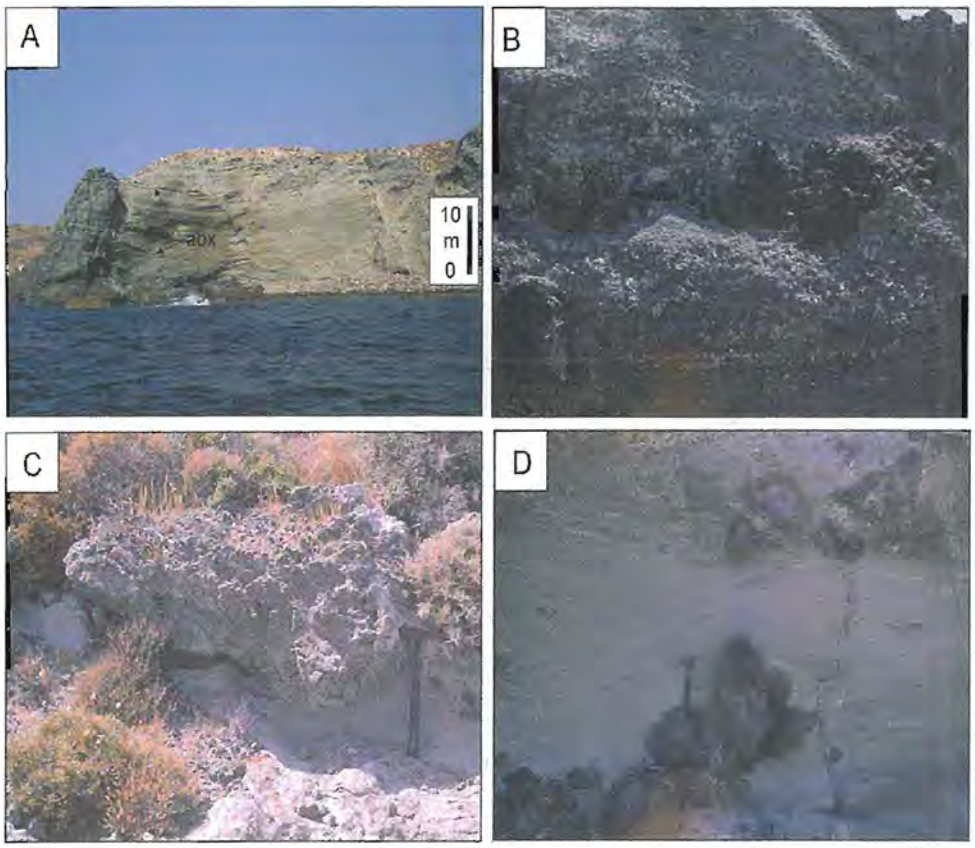

Figure 4.18 Scoria breccia facies association. **A** A thick interval (25-30 m) of cross-stratified scoria breccia and massive andesitic breccia at Papafragas (Figure 4.5). Beds of massive andesitic breccia (abx) are wedge-shaped and laterally discontinuous. **B** A thick interval of cross-stratified scoria breccia containing large fluidal andesite clasts at Papafragas. **C** A very coarse fluidal clast at Papafragas. **D** Fine scoria sandstone facies. The beds vary in thickness from 5 to 10 cm. Large fluidal clasts are oriented perpendicular to bedding, at Papafragas.

The fragment population are elongate to ellipsoidal or sub-spherical in shape with smooth, or curviplanar margins. The larger fluidal clasts (up to 1.5 m in diameter; Figure 4.18C) are typically elongate and characterised by irregular, contorted, glassy margins, 1-2 cm thick. Large (>64 mm) fluidal clasts are characterised by normal joints at their margins and internal polyhedral joints. Sparse lithic clasts (2-8 cm in diameter) include rounded quartz-phyric rhyolitic pumice and angular to subangular schist clasts, and hydrothermally altered dacite and andesite clasts. The facies shows only minor lateral variation in thickness, geometry, internal organization and grain size.

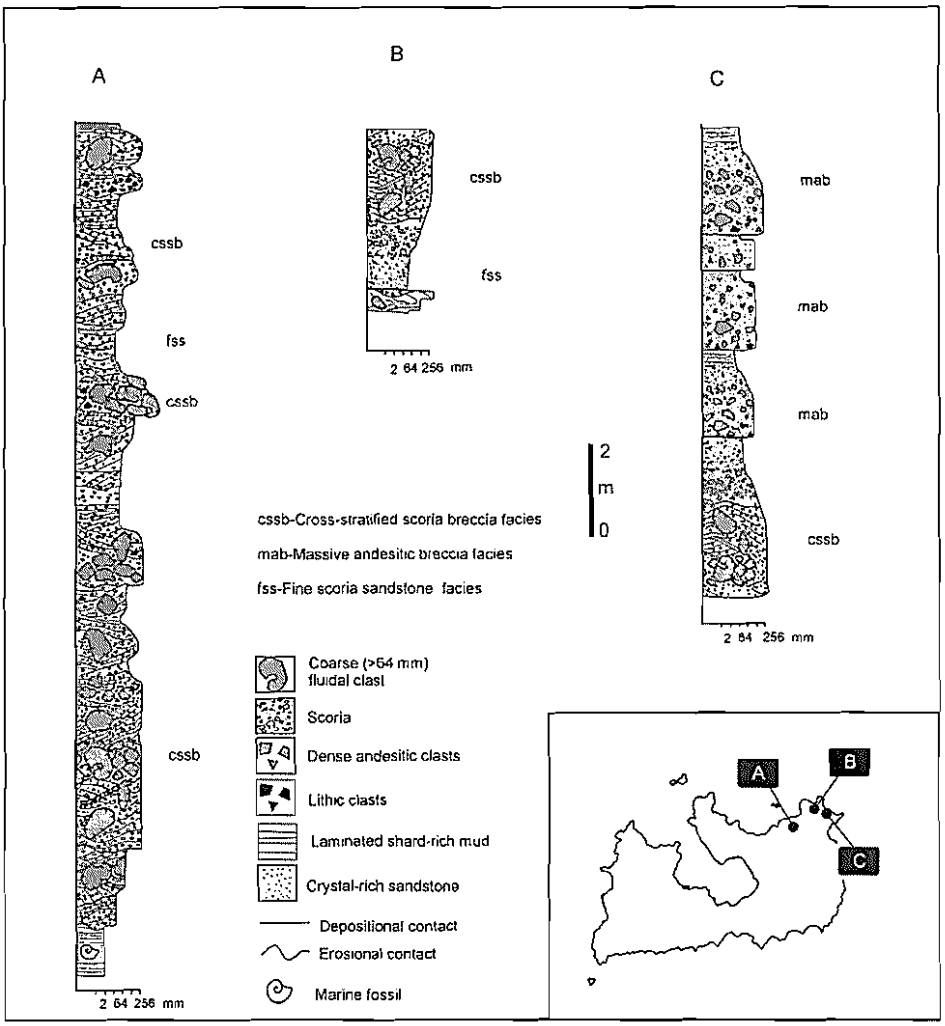

Figure 4.19 Graphic logs for key parts of outcrops at several locations (inset), showing important textures, structures and contact relationships of the three main facies comprising the scoria-rich breccia facies association. Location of sections on Figure 4.4.

Massive andesitic breccia facies

The massive andesitic breccia beds are monomictic, fines-poor and moderately to poorly sorted. Intervals of this facies range from 5-10 m in thickness. Single beds are thick (0.5-3.5 m), massive or diffusely stratified, wedge-shaped and mainly composed of angular to subangular, dense, feldspar-phyric andesitic clasts (95%, 10 to 90 cm in size) in grain support. Scoria clasts identical to those in the cross-stratified scoria breccia are a minor component (~5%). Andesite clasts are mostly blocky and angular to subangular. Clasts have poorly vesicular, glassy rinds 5 to 10 mm thick. The bases of beds are sharp and vary from passive and depositional to strongly erosional. The upper contacts of the massive andesitic breccia intervals are gradational and marked by diffuse stratification and an upward increase in the proportion of scoria clasts.

Fine scoria sandstone facies

The fine scoria sandstone facies consists of thickly bedded, cross-bedded and planar laminated dark grey sandstone. Weakly defined, planar cross-beds occur in 30-cm to 2-m-thick sets with sharp bases. Foresets are planar or asymptotic and inclined at less than 18^0 to the bed base. In addition to low-angle cross-stratification unidirectional bedforms such as dunes, climbing ripples and chute-and-pool structures are also present.

Cross-bedded intervals occupy broad (~2-3 m) shallow (1.5-2 m) channels. Contacts of this facies with adjacent facies range from sharp to gradational. Intervals of this facies range from 0.5 m up to 4 m in thickness. The sandstone consists of whole and broken feldspar (plagioclase) and ferromagnesian crystals (hornblende). Scoria clasts comprise approximately 5-10 vol. % of the facies. Large fluidal clasts (up to 1.5 m in diameter) identical to those in the cross-stratified scoria breccia facies are sporadically distributed through the facies (<5 vol. %). Rare lithic clasts (<1 vol. %) include rounded white felsic pumice, basement-derived schist and sedimentary clasts.

Interpretation

The spatial association, compositional similarity and gradational contacts among intervals of cross-bedded scoria breccia, massive andesitic breccia and fine scoria sandstone suggest that the three facies are genetically related.

The large volume of highly vesicular juvenile clasts is interpreted to be the product of explosive, magmatic-volatile-driven eruptions. The grain size (≤2 cm) and vesicularities of the scoria clasts are similar to those found in subaerial strombolian scoria deposits (Walker and Croasdale 1972; Walker 1973; Self et al. 1974). The fluidal clasts resemble bombs and fluidal lapilli formed by tearing apart of relatively low-viscosity lava ribbons jetted upward from vents during strombolian-style eruptions (Macdonald 1972). However, outer glassy margins and internal fracture patterns of the fluidal clasts suggest they were probably quenched in a submarine environment.

The fine scoria sandstone facies is finer and more crystal-rich than the cross-stratified scoria breccia facies but otherwise similar in componentry and bedforms. In both facies, the presence of cross-bedding diffuse stratification and edge-modified, subangular scoria clasts, indicate lateral transport. The sedimentary structures are consistent with deposition from unidirectional traction currents. At single locations, the unidirectional bedforms in the two facies imply similar transport directions, and hence, similar sources. These two facies may be the product of weaker (fine scoria sandstone facies) versus stronger (cross-stratified scoria breccia) traction current transport from a single source. That source was most likely an active scoria cone subject to syn-eruptive mass-wasting events that resulted in mass-flow and traction current resedimentation of loose scoria. The coarse fluidal clasts in both facies have intact quenched margins and it is likely that their transport differed from that of the smaller, edge-modified scoria clasts and crys. They were probably initially suspended in the water column and may then have settled from suspension up-current and been collected by the gravity currents, and/or settled directly into the active currents. Given the relatively shallow-water depositional setting, it is plausible that the vent could have been either subaerial or submarine.

In the massive andesitic breccia facies, clasts are edge-modified. However, the polyhedral shape of the dense feldspar-phyric andesitic clasts and their glassy rims imply that they were formed by brittle fracture in response to contraction during rapid cooling (c.f. Pichler 1965; Yamagishi and Dimroth 1987).The poor sorting, and wedge-shape geometry are consistent with rapid deposition high-particle-concentration, clast-rich gravity currents (c.f. Lowe 1976; Postma 1986). Lateral variations in internal organisation of single beds over a few metres to a few tens of metres is consistent with non-uniform currents. This facies could be a variety of redeposited hyaloclastite from a wholly or partly submarine andesitic lava generated by the same, or one nearby, that also produced the cross-bedded scoria breccia and fine scoria sandstone facies. The scoria-rich breccia facies association on Milos is similar to the successions found on the outer submarine flanks of scoria cone volcanoes (e.g. Staudigel and Schmincke 1984; Cas et al. 1989; Houghton and Landis 1989; Dolozi and Ayres 1991; Kano 1998).

4.11 Sandstone-conglomerate facies association

The sandstone-conglomerate facies association comprises graded sandstone, thickly bedded to laminated mudstone and polymictic breccia-conglomerate that have mixed volcanic and non-volcanic provenance. Facies in this association are also characterised by polymictic clast assemblages, rounded particles, relatively thin sedimentation units and the presence of marine fossils. Units of this association are intercalated with most of the other submarine facies associations although they are more abundant towards the base of the succession.

Graded sandstone facies

This facies is common in the Triades (Figure 4.2) and Sarakiniko (Figure 4.4) areas, and consists principally of thickly bedded (30 cm-2 m), normally graded, coarse to fine sandstone. Between Mandrakia and Sarakiniko, intervals of this facies range in thickness from ~40-60 m. Contacts of this facies with adjacent facies vary from sharp to gradational. Some beds display basal scours and flame structures.

Sandstone beds are dominantly planar, and high-angle bedding truncations are common (Figure 4.2A). Low-angle, unidirectional cross-stratification also occurs in intervals of graded sandstone, and typically comprises 1-m-thick sets. Foresets defined by grain-size variations are planar and inclined at less than 15^0 to the bed base. Graded sandstone beds are characterised by a lower division of massive to graded sandstone, which passes up into a thin, diffusely planar-laminated, finer sandstone division. The principal components of the sandstone beds are angular quartz and feldspar crystal fragments, and felsic volcanic fragments, including felsic pumice. Sparse lithic clasts (30 cm-1.5 m) occur throughout many sandstone beds; their size and abundance (<2 %) increase towards the bases of single beds. Most lithic clasts are subangular to subrounded rhyolitic, dacitic or andesitic clasts and felsic pumice clasts. Other lithic clasts include schist, Neogene limestone and sedimentary clasts (mudstone and sandstone).

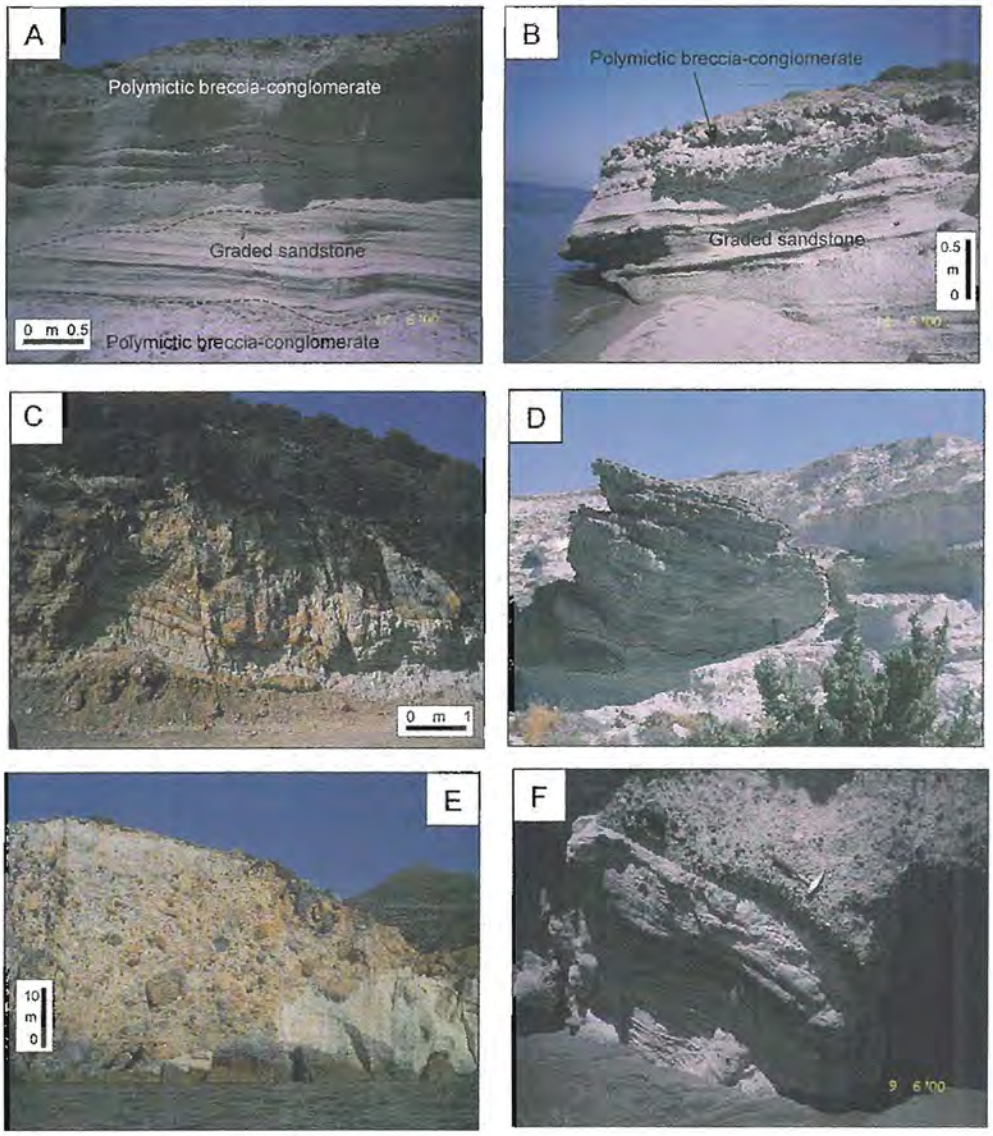

Figure 4.20 Sandstone-conglomerate facies association. **A** Graded sandstone interbedded with thin (<0.5 m) intervals of polymictic breccia-conglomerate at Sarakiniko (Figure 4.4). Note the high-angle truncation of bedding (above the hammer) . **B** Graded sandstone interbedded with stratified monomictic dacite breccia at Triades (Figure 4.2). **C** Thickly bedded, alternating white and brown mudstone east of Sarakiniko. Single beds display ripples and wavy bedforms; some contain intact bivalves. **D** A very large (5 x 3.5 m) pumice clast set in fossiliferous mudstone, east of Sarakiniko (Figure 4.4). **E** A very coarse (clasts up to 15 m in diameter), clast- to matrix-supported polymictic breccia south of Agios Ioannis. **F** Normally graded, clast-supported polymictic breccia. The contact with underlying laminated mudstone is sharp to planar.

Thickly bedded to laminated mudstone

The thickly bedded to laminated mudstone facies is white to brown, massive and laterally continuous in outcrop (Figure 4.20C). Some mudstone beds contain marine fossils that indicate a submarine depositional setting. The mudstone consists of feldspar

(dominantly plagioclase), quartz and white mica crystal fragments, and cuspate glass shards. Feldspar and quartz crystal fragments are mostly angular but a few grains are subrounded. Single beds range in thickness up to tens of centimetres but are generally less than 1 cm, and commonly show ripples and wavy bedforms. Sparsely distributed outsized pumice clasts (up to 10 m in diameter) occur in some intervals of mudstone that overlie pumice breccia beds. The coarse prismatic pumice clasts have normal joints at their margins, whereas clast interiors exhibit polyhedral joints.

Polymictic breccia-conglomerate facies

The polymictic breccia-conglomerate facies occurs in moderately sorted, normally or reversely graded, beds (generally 1-40 m thick), intercalated with intervals of graded sandstone or mudstone (Figure 4.20B). The breccia beds are clast- to matrix-supported and some lower contacts are erosional surfaces. Most beds are dominated by clasts measuring 1-10 cm in diameter, but some intervals include clasts up to 15 m in diameter (Figure 4.20E). The clast population can include rhyolite, dacite, andesite and sedimentary clasts (Figure 4.20F). Coarse lithic clasts (>20 cm in diameter) are generally subrounded, whereas smaller lithic clasts are angular to subrounded. Lithic clasts are separated by a grey matrix consisting of dominantly angular to subangular lithic clasts (<2 cm) and millimetre- to sub-millimetre-sized crystals and crystal fragments.

Interpretation

Most volcanic detritus contained in the graded sandstone facies is angular to subangular, suggesting that the grains have not been significantly reworked. Some crystal fragments, however, are rounded, indicating that have they undergone a higher degree of reworking prior to final deposition, possibly indicating two sources. Traction-current structures, such as large-scale cross bedding, indicate deposition in near- or above-wave base environments (e.g. Bull and Cas 1989). Diffuse contacts between beds are interpreted to reflect deposition from moderate- to high-concentration turbidity currents. The combination of angular grains and massive beds reflects relatively continuous sediment supply. Reworking by storm-generated traction currents could have generated the cross-stratified beds.

The thickly bedded to laminated mudstone beds contain volcanic fragments (principally

glass shards, crystal fragments and isolated coarse pumice clasts) which are mixed with non-volcanic components (white mica and microcrystalline quartz). Most volcanic grains are angular, suggesting the grains have not been significantly reworked. The bed-forms and internal organisation of the mudstone facies suggest an origin through a combination of background hemipelagic sedimentation and water-settling of pyroclasts. The sparse, irregular, large pumice clasts enclosed by mudstone are interpreted to have settled from suspension (e.g. Reynolds et al. 1980; Mahood 1980; Clough et al. 1981; Wilson and Walker 1985), and presumably record near-contemporaneous, explosive eruptions from distal submarine vents.

The polymictic breccia-conglomerate beds are laterally discontinuous and associated with graded sandstone and mudstone. Rounding of clasts implies reworking in high-energy environments prior to final deposition, suggesting the source areas were subaerial to shallow marine. Final deposition is interpreted to have been from coarse-clast-rich gravity currents, possibly debris flows, in a submarine environment below wave-base.

4.11 Summary

The submarine volcanic and sedimentary succession on Milos comprises twenty-two principal volcanic, sedimentary and intrusive facies, which have been arranged into seven compositionally and texturally distinct facies associations. The submarine facies and facies associations comprise the intercalated products of intrusive, effusive and explosive eruptions, and post-eruptive resedimentation.

Intercalations of bioturbated and fossiliferous mudstone indicate that this part of the succession was deposited in a submarine environment. The in situ and intact bivalve shells and burrows in these beds imply deposition in a relatively shallow-water environment, up to a few hundred metres water depth being most likely.

The syn-volcanic intrusions consist of coherent and minor autoclastic facies (intrusive hyaloclastite). Contacts of the syn-volcanic intrusions show varying effects of quench-

ing and of interaction with the poorly consolidated, water-saturated host sequence. Intrusions are commonly associated with domes and minor lavas. The domes are characterised by thick autoclastic facies (in situ hyaloclastite and autobreccia). Among the volcaniclastic facies, there is a wide range of textural characteristics, including facies generated by coeval explosive or effusive eruptions and facies that exhibit evidence for reworking prior to deposition. The syn-eruptive facies are characterised by a dominance of unmodified juvenile clasts. There are three main types present: (1) very thick (tens of metres), massive or diffusely stratified, rhyolitic to dacitic pumice breccias. This facies consists of particles produced by explosive fragmentation, but transported and deposited by water-supported gravity currents; (2) very thick andesitic scoria breccia, related to the construction of a submarine or partly emergent scoria cone; (3) stratified and graded, monomictic dacitic or rhyolitic breccias. This facies was generated as a by-product of lava or dome effusion (resedimented hyaloclastite).

Chapter 5

Internal structure and emplacement of an Upper Pliocene dacite cryptodome

The following chapter has been published in the Journal of Volcanology and Geothermal Research. In order to keep with the chapter format of the thesis the introduction of the original manuscript has been modified and the abstract removed.

5.1 Introduction

Lava domes form when high-viscosity, typically felsic magma piles up above and around a vent, whereas cryptodomes are high-level intrusions of similar shape and composition that cause up-doming of overlying sediments or rocks (Minakami et al. 1951). The emplacement style, morphology and internal structure of lava domes are relatively well understood, largely because of comprehensive observations of historic eruptions (e.g. Soufrière dome at St. Vincent, Huppert et al. 1982; Mount St. Helens dome, Swanson and Holcomb 1990). In addition, lava domes have been simulated in laboratory experiments and numerically (e.g. Blake 1990; Iverson 1990; Fink and Griffiths 1990; Griffiths and Fink 1993) and examined by means of satellite infrared image analysis (e.g. Kaneko et al. 2002). In contrast, little is known about cryptodomes, even though they are common, especially in subaqueous, intermediate-felsic, volcanic successions (Allen 1992; McPhie et al. 1993; Doyle and McPhie 2000). This neglect has arisen mainly because intrusion is impossible to observe directly and probably also because cryptodomes in ancient dissected successions can easily be mistaken for extrusive domes.

Although most modern cryptodomes occur in subaerial settings (e.g. Usu volcano, Katsui et al. 1985), the few documented ancient examples are in submarine successions (e.g. Snyder and Fraser 1963; Goto and McPhie 1998; Doyle and McPhie 2000). At present, understanding of the internal structures and growth mechanisms of cryptodomes depends entirely on such studies. In addition, cryptodomes that occur in submarine successions can be spatially and temporally associated with the formation of volcanic-

terpreted to have occurred in a storm- and tide-dominated shallow marine environment.

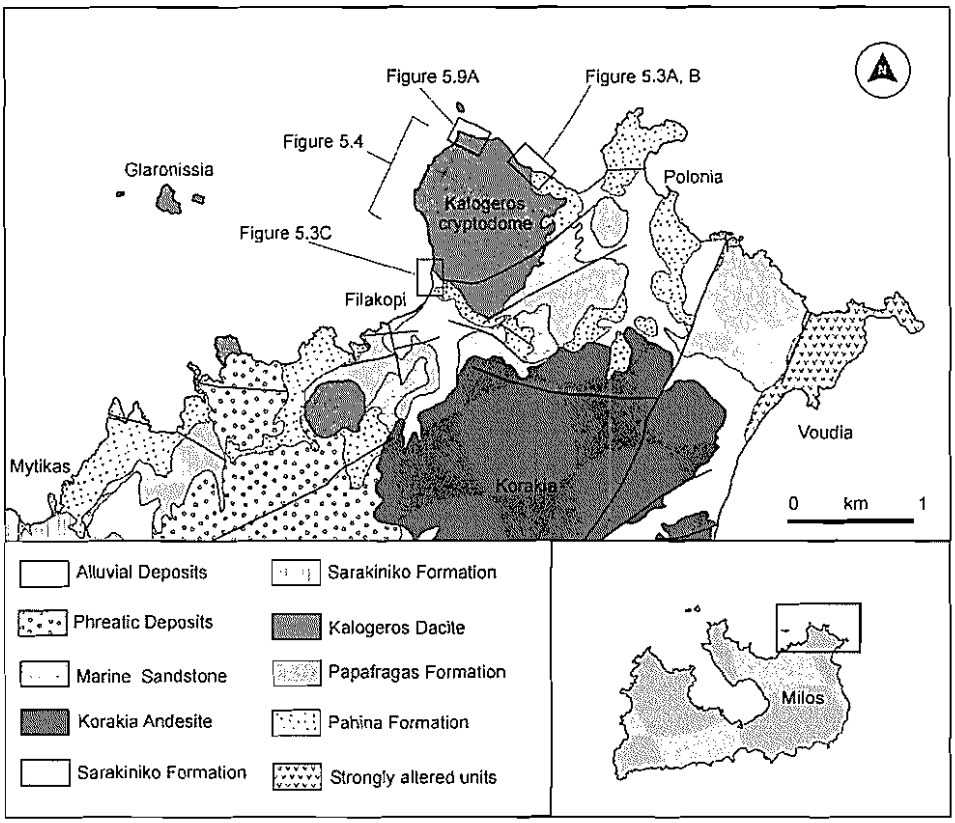

Figure 5.1 Geological map showing the location of the Kalogeros cryptodome (modified after Fytikas 1977).

The Korakia Andesite (pyroclastic series and lava domes) is 30-35 m thick and occurs east of the Sarakiniko Formation. It includes coherent andesite and andesitic autobreccia together with subordinate pyroclastic units. Locally, Korakia Andesite is unconformably overlain by a thin interval (~5 m) of brown bioclastic sand. A palaeosol separates the young phreatic deposits (up to 5 m thick) at the top from the underlying succession.

Contact relationships and lithofacies characteristics of the Kalogeros Dacite at Kalogeros suggest that it was entirely intrusive: (1) all contacts of the Kalogeros dacite crosscut the host formations along highly irregular, discordant contacts that truncate bedding (Figure 5.3A), (2) it is entirely surrounded by the Pahina and Papafragas Formations, and adjacent units are highly deformed and locally intermixed or dismembered (Figure 5.3B), and (3) no dacite clasts or dacite-derived clastic facies are present in the adjacent younger parts of the succession (Figure 5.3C). Therefore, the dacite at Ka-

logeros is inferred to be a cryptodome (c.f. Minakami et al. 1951). The other Kalogeros Dacite bodies are probably also intrusions but their contacts are not exposed and/or not definitive.

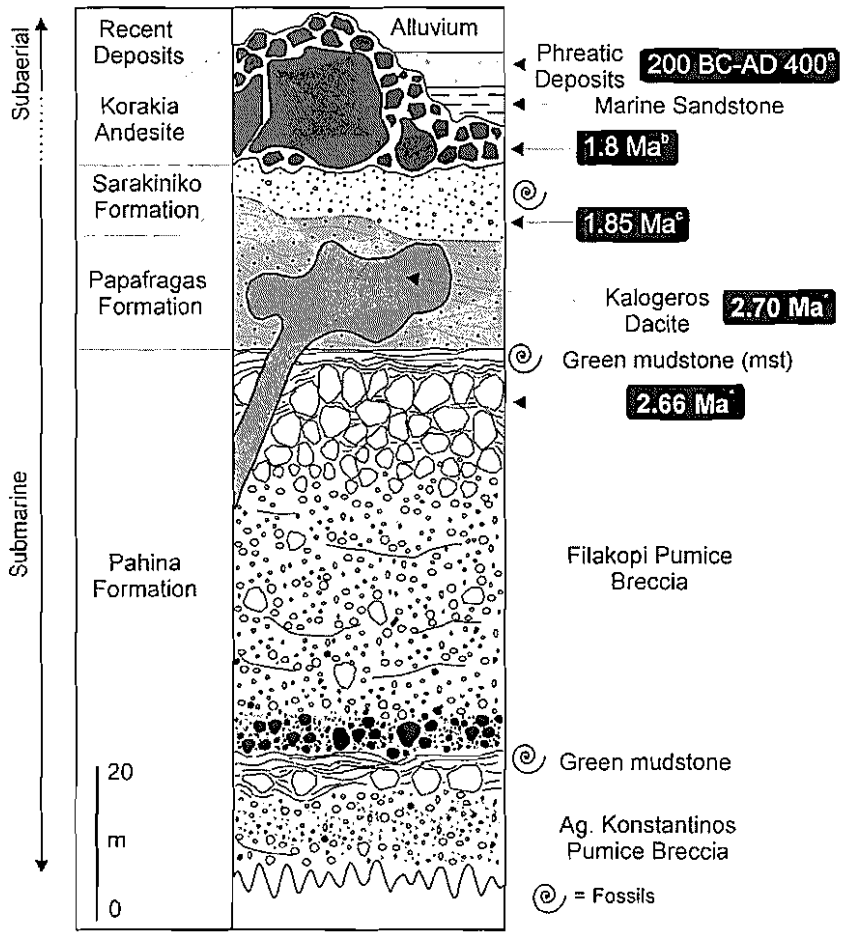

Figure 5.2 Generalised stratigraphic section through the volcanic succession exposed on northeastern Milos. The sequence records an upward progression from submarine to subaerial depositional environments. Ages are based on: [a]14 C measurements on pot fragments within phreatic deposits (Traineau and Dalabakis 1989); [b]Paleomagnetic polarity from the Korakia Andesite (Kondopoulou and Pavaides 1990); [c]K-Ar dates on biotite from a dacite pumice clast (Fytikas et al. 1986); and [d] U-Pb dating of zircons (Chapter 8).

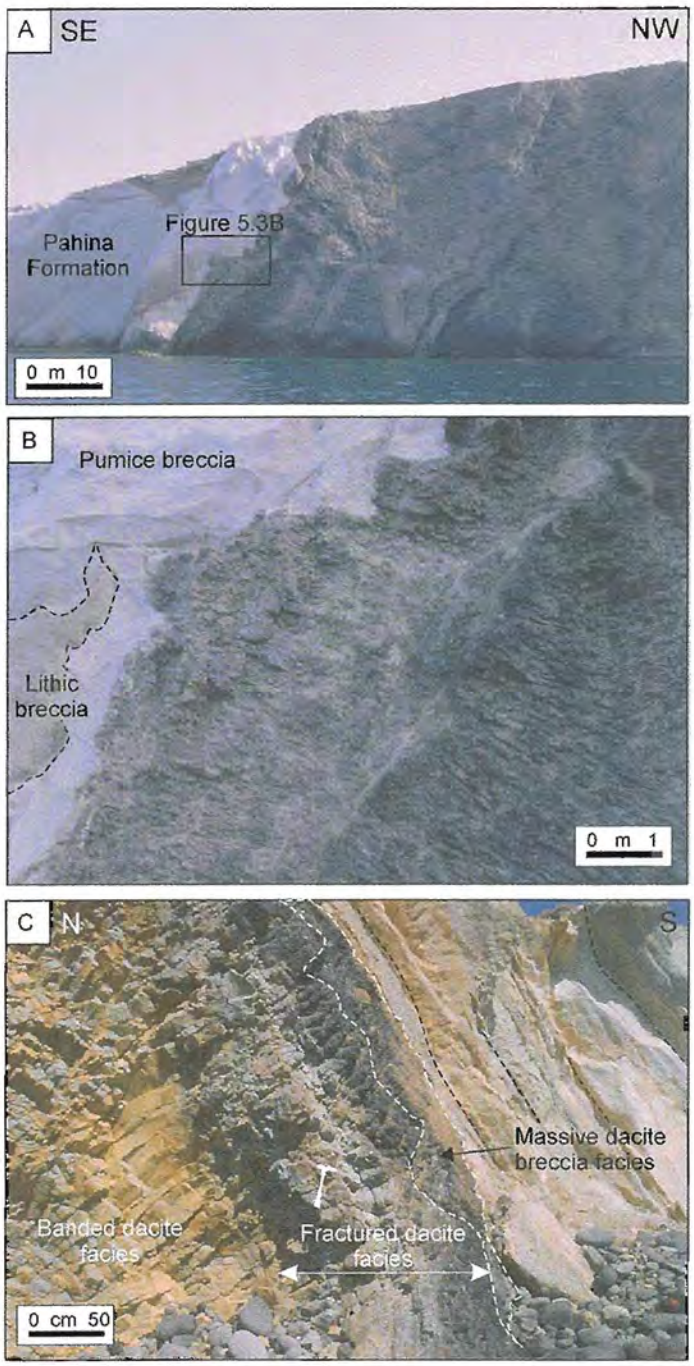

Figure 5.3 Contact relationships. **A** Eastern contact of the Kalogeros cryptodome with Pahina Formation (white). The Kalogeros cryptodome crosscuts the host formation along a highly irregular, discordant contact that truncates local bedding. **B** Close-up of the eastern contact with the Pahina Formation, showing local soft-sediment deformation adjacent to the contact. Note that the lithic breccia layer within the pumice breccia has been strongly disturbed. **C** Western contact of the Kalogeros cryptodome with Pahina Formation. The contact is sharp, and marked by highly fractured dacite (massive dacite breccia facies). Note the steep southerly dip of adjacent pumice breccia of the Pahina Formation (dashed black lines mark bedding). Photograph locations are given on Figure 5.1.

5.3 The Kalogeros cryptodome and host formation

The Kalogeros cryptodome has been partly exhumed and is well exposed in three-dimensional continuous coastal cliffs. In plan view, the cryptodome is oval, ranging in diameter from 800 m (east-west) to 1300 m (north-south). In cross section (Figure 5.4), the cryptodome is broadly semi-circular with very steep sides and an exposed height of 120 m. The Kalogeros cryptodome has a minimum bulk volume of 0.12 km^3. It is mainly surrounded by and in contact with the Upper Pliocene Pahina Formation (Figures 5.1 and 5.2). Bedding within the host formations is generally flat lying or gently dipping to the south. In places, the Pahina Formation is disrupted by numerous NNE- to NE-striking normal faults, some of which have displacements up to several tens of metres. The Kalogeros cryptodome and related dacitic units have also locally disturbed the host succession.

The coarse pumiceous units of the Pahina Formation have been described in detail in Chapter 6 and principally comprise, white-cream pumice breccia interbedded with thick intervals of laminated, bioturbated, pale green mudstone and subordinate lithic breccia (Figure 5.2). The juvenile components of the pumice breccia include highly vesicular, biotite-plagioclase-phyric rhyolitic pumice (~85%; 68-71 wt.% SiO_2), aphyric obsidian clasts (<1%) of the same composition, and glass shards (~10%). The remainder (<5%) consists of plagioclase-phyric andesitic lithic clasts. The pumice breccia occurs in medium to very thick beds that are internally massive, diffusely stratified or normally and reversely graded.

5.4 Lithofacies and internal structure

The Kalogeros cryptodome consists of five lithofacies: coherent dacite, banded dacite, fractured dacite, massive dacite breccia, and stratified dacite breccia. The phenocryst assemblage (plagioclase, quartz and trace amounts of biotite, clinopyroxene and opaque phenocrysts) and XRF analyses indicate that all lithofacies are dacitic (63.68-65.33 wt.% SiO_2; Appendix B). The distinguishing characteristics of the five main facies are summarised below.

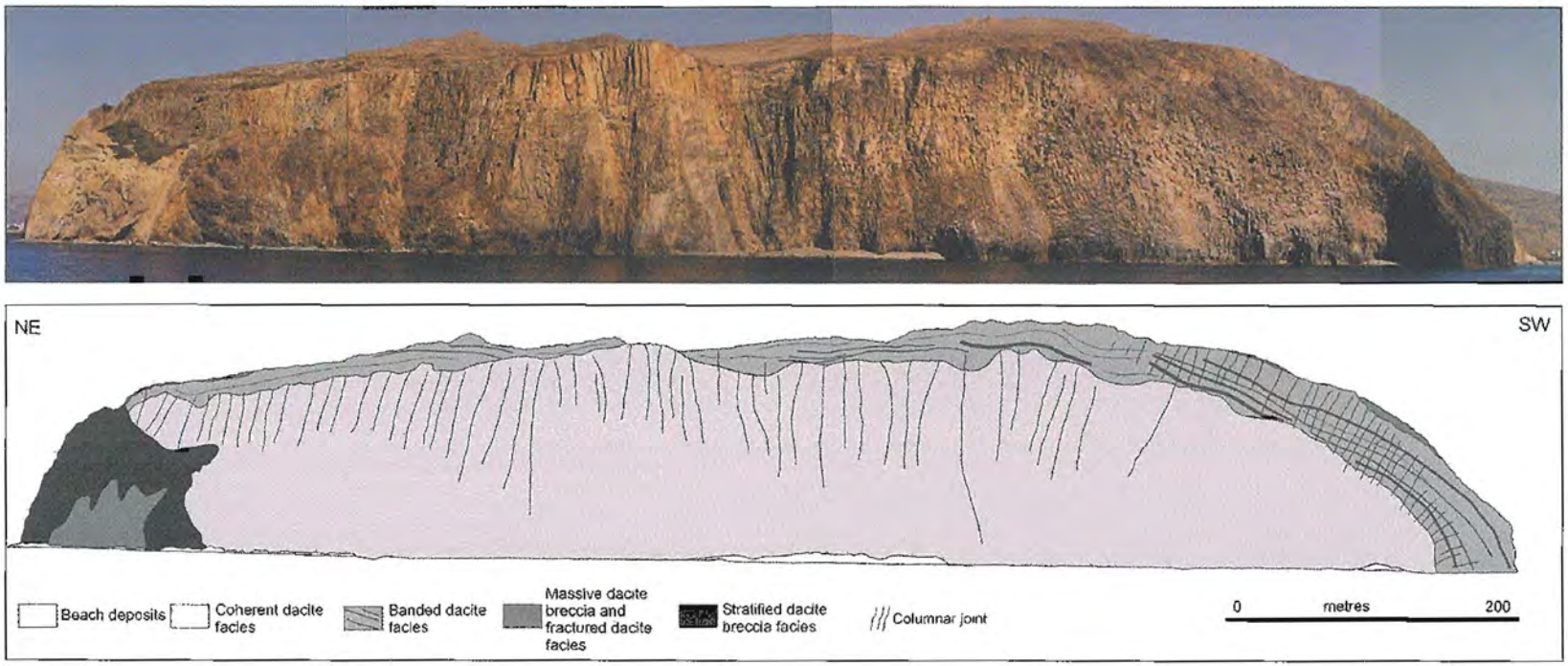

Figure 5.4 Northeast-southwest section of the Kalogeros cryptodome, showing the lithofacies.

Coherent dacite facies

The coherent dacite facies is volumetrically dominant (80 vol.%), being 1000 m wide and up to 100 m high (Figure 5.4). It consists of dark green to grey, massive, non-vesicular dacite that is characterised by regular, well-developed columnar joints. Column axes are generally subvertical and perpendicular to the cryptodome margins, radiating regularly from the core outward. The columns have pentagonal and, in some cases, hexagonal or rectangular outlines in cross section (Figure 5.5A) and decrease in width outward from 150-250 cm in the centre to 100-150 cm at the margin. The coherent facies passes gradually outward into the banded facies toward the outer surface of the cryptodome. The contact between the two facies is gradational and commonly poorly defined.

The coherent dacite is evenly porphyritic, containing euhedral phenocrysts (10-15 vol.%) of plagioclase, quartz, biotite, clinopyroxene and opaque phases up to 2 mm across (Figure 5.5B). The groundmass is dominated by microlites of plagioclase and opaque phases (65 vol.%) in black glass (20 vol.%). Although no flow banding is present in the coherent facies, some plagioclase microlites are moderately aligned and define a weak flow texture. The coherent dacite facies contains abundant green, fluidally shaped microcrystalline enclaves (Figure 5.5C) that comprise fine (<1 mm) plagioclase, clinopyroxene and opaque phases.

Banded dacite facies

The banded dacite facies forms a broad, 30-40-m-thick sheath that encircles the inner coherent facies (Figure 5.4). It comprises alternating bands of pale grey and black dacite. Boundaries between the bands are gradational through intervals of a few to several centimetres. The bands range in thickness from 0.5 to 4 m (Figure 5.6A), and lie approximately parallel to the outer surface of the cryptodome. Single bands vary in thickness and are generally discontinuous, with lateral extents in the order of tens of metres. The bands show no systematic variation in thickness outward. The banding is overprinted by columnar joints (Figure 5.6B). The columns in the banded facies are pentagonal or hexagonal in cross section, similar to those in the coherent facies. They also continue the trend of decreasing diameter outward, from 100-150 cm at the inner part of the banded dacite facies to 10-20 cm at the outer edge of the cryptodome.

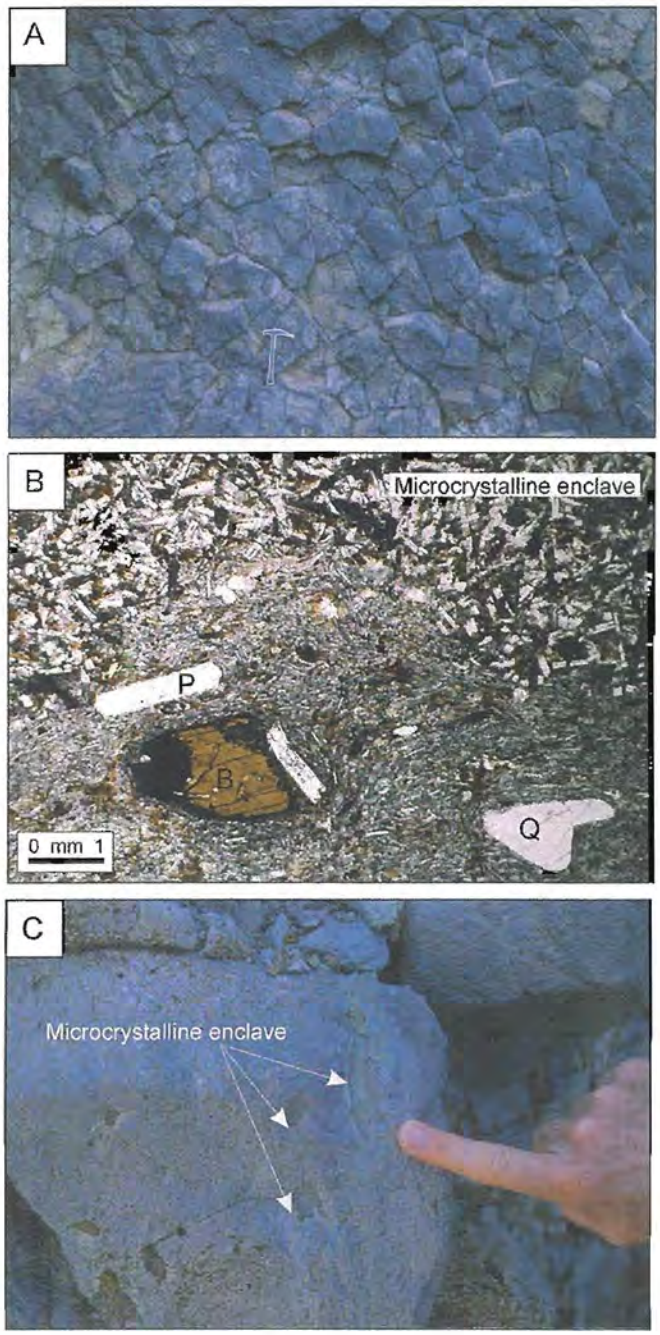

Figure 5.5 Coherent dacite facies. **A** Dark green to grey, massive, non-vesicular dacite that is characterised by well-developed columnar joints. The columns have pentagonal, hexagonal rectangular outlines in cross-section. **B** Photomicrograph of evenly porphyritic coherent dacite facies, containing euhedral phenocrysts of plagioclase (P), quartz (Q), biotite (B) and opaque phases up to 2 mm across. The groundmass is dominated by microlites of plagioclase and opaque phases (65 vol.%) set in black glass (20 vol.%). The upper half of the field of view shows an equigranular, microcrystalline enclave composed of plagioclase, clinopyroxene and opaque phases. **C** The massive coherent facies contains abundant, green, fluidally shaped, microcrystalline enclaves.

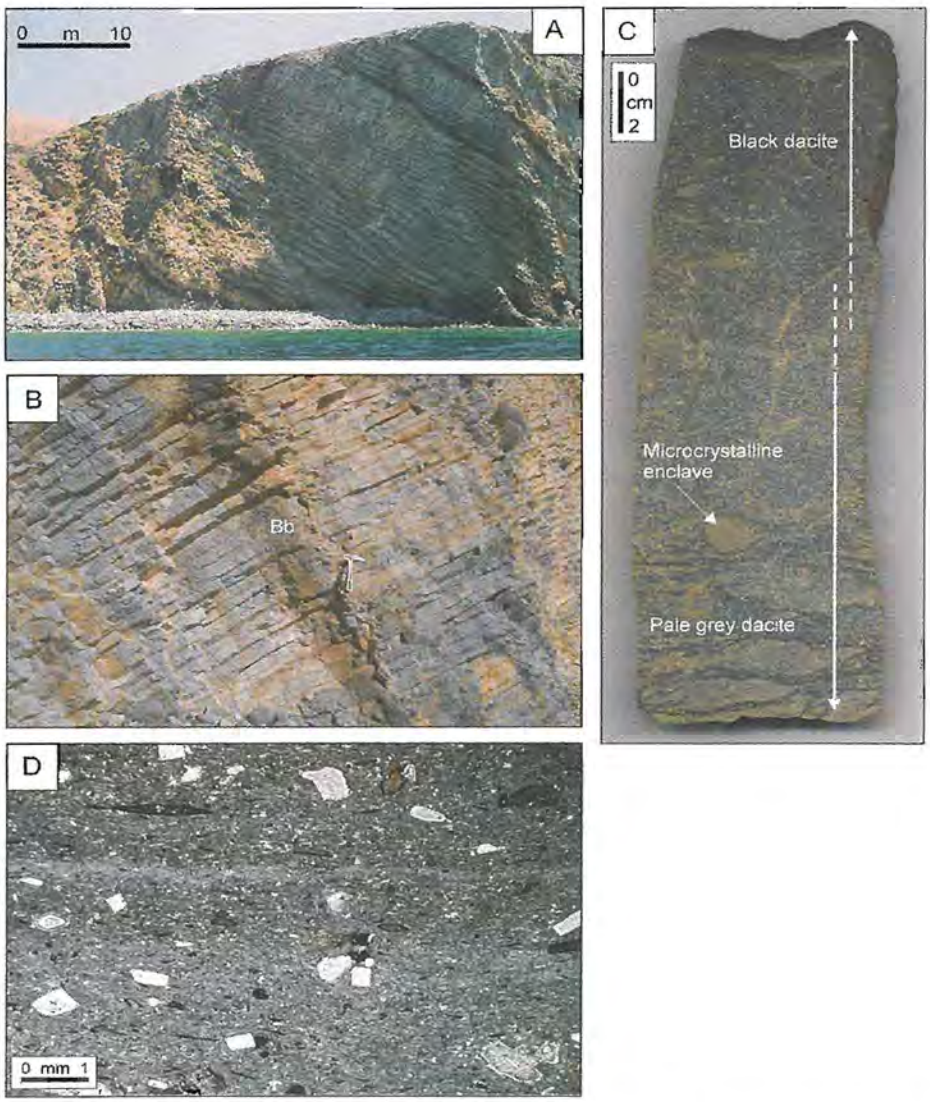

Figure 5.6 Banded dacite facies. **A** The banded facies consists of alternating bands of pale grey dacite and black dacite. **B** Close-up view of the banded facies. Single bands are uneven in thickness and generally laterally discontinuous; no systematic variations in band thickness are evident. **C** Polished slab showing the transition from black (top) to pale grey dacite (bottom). The pale grey bands display an internal anastomosing foliation. **D** Photomicrograph of pale grey dacite in the banded dacite facies, containing euhedral aligned phenocrysts (<10 vol.%) of plagioclase, quartz, biotite (black) and opaque phases up to 2 mm across.

The dacite of the banded facies has an identical phenocryst population, (mineralogy, size and abundance) to that of the coherent dacite facies. However, the pale grey bands display distinct internal foliation and are weakly vesicular (~5 vol.% vesicles). The internal foliations are slightly darker grey and range from 2 mm to 20 mm in width. They are parallel to the outer surface of the cryptodome, commonly laterally discontinuous and branch or merge, defining lens- and rhomb-shaped domains (Figure 5.6C). The vesicles are amoeboid to elongate in shape (1-2 mm across and 2-5 mm long), with the long axes generally parallel to the large flow bands. The groundmass (85-90 vol.%) of the

pale grey dacite (Figure 5.6D) is characterised by microlites of plagioclase and opaque phases (65 vol.%) in black glass (20 vol.%). The plagioclase microlites are strongly aligned parallel to the outer surface of the cryptodome. The black bands differ from the pale grey bands in that they are non-vesicular (<1 vol.% vesicles) and slightly less porphyritic (8-10 vol.% phenocrysts) than the pale grey bands (Figure 5.6C).

Fractured dacite facies

A gradual outward transition occurs from closely columnar-jointed banded dacite facies into the fractured dacite facies (Figure 5.3C and 5.4). The fractured dacite facies (<1 vol.%) forms an irregular zone 1-3 m thick at the outer margin of the cryptodome. Within the fractured dacite facies, multiple sets of irregular fractures become more closely spaced toward the outer surface of the cryptodome. The fracture pattern is crudely polygonal and dominated by first-order fracture sets that outline equant polyhedral blocks, ranging from 30 to 60 cm in diameter (Figure 5.7A and B). Extending in from the first-order fractures are sets of narrowly spaced fractures, which define a net-like pattern and divide the rock into small (<5 cm) cuboid shapes.

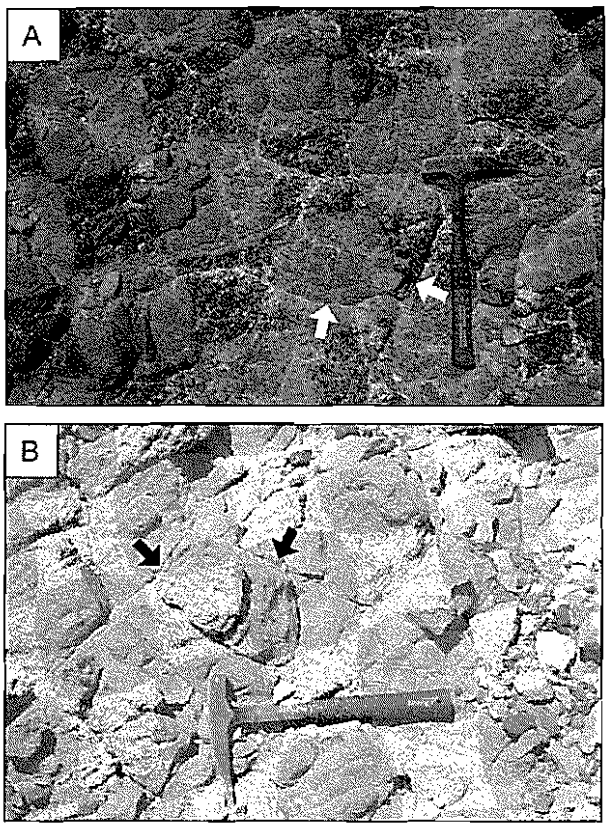

Figure 5.7 Fractured dacite facies. The fractured dacite facies displays the same banding of black **A** and pale grey **B** as the banded dacite facies. The fracture pattern is crudely polygonal, dominated by first-order fractures (arrows) that outline equant polyhedral blocks.

The dacite of the fractured dacite facies is identical to that of the banded dacite facies; it displays the same banding of pale grey and black dacite with the same phenocryst populations (mineralogy, size and abundance). The fractured dacite facies passes gradationally outward into the massive dacite breccia facies at the outer margin of the cryptodome.

Massive dacite breccia facies

The massive dacite breccia facies forms a carapace at the margin of the cryptodome (Figure 5.3C and 5.4), creating a narrow selvage between the fractured dacite facies and the host formation ranging in thickness from a few centimetres to several metres. The massive dacite breccia facies consists of blocky to polyhedral dacite clasts (1-40 cm in diameter) and is characterised by domains of jigsaw-fit (Figure 5.8A) and clast-rotated breccia (Figure 5.8B). In many places, clasts within the breccia decrease in size approaching the outer contacts of the cryptodome. The clasts within the breccia are a combination of black glassy and pale grey dacite that are identical to the black and pale grey dacites, respectively, in the banded and fractured dacite facies. However, the clasts in the massive dacite breccia facies are slightly more vesicular (up to 10 vol.% vesicles). Vesicles are mostly amoeboid to slightly elongate in shape (2-3 mm across and 3-8 mm long).

Only very minor matrix is present in most of the massive dacite breccia facies. However, near the outer contacts with the host formation, clasts in the massive breccia facies are separated by a pale grey matrix consisting of fine (<2 cm) non- to moderately vesicular (up to 10 vol.% vesicles), dominantly blocky dacite clasts and rhyolitic pumice (Figure 5.8C). The fine dacite clasts have the same mineral assemblage and textures as other dacite clasts in the massive dacite breccia facies, but are less vesicular. Commonly, the matrix is poorly sorted, although some groups of dacite clasts define jigsaw-fit textures. A 10-20-cm-wide, gradational contact separate matrix-rich dacite breccia and adjacent pumice breccia of the Pahina Formation.

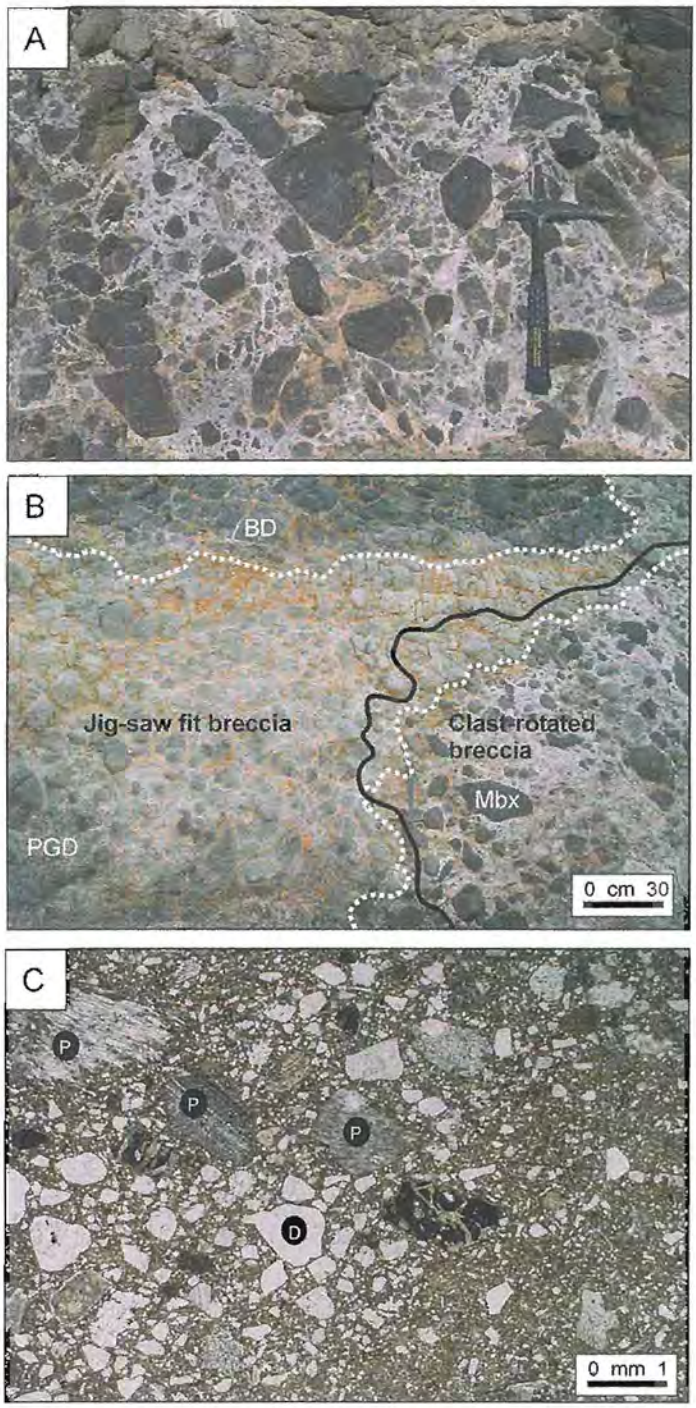

Figure 5.8 Massive dacite breccia facies. **A** The massive dacite breccia facies comprises blocky to polyhedral dacite clasts 1-40 cm in diameter. **B** The massive breccia facies includes domains of jigsaw-fit and clast-rotated matrix-rich breccia (separated by solid black line). Domains within the massive breccia facies may comprise only black glassy dacite clasts (BD), only pale grey dacite clasts (PGD), or a mixture (Mbx) of the two types of dacite. **C** Photomicrograph of the matrix in the massive dacite breccia facies at the outer margin of the cryptodome. The matrix contains fragments of rhyolitic pumice (P), derived from the host Pahina Formation, and blocky fine dacite clasts (D), identical to the large dacite clasts. The matrix commonly shows variations in the abundance of fine dacite clasts; for example, dacite clasts are much less abundant toward the bottom right hand corner of the photomicrograph.

Stratified dacite breccia facies

This facies consists of monomictic, diffusely stratified to massive, poorly sorted breccia that forms an irregular domain within the northeastern sector of the Kalogeros cryptodome (Figure 5.4). Contacts of the stratified dacite breccia facies are subvertical, striking NNE, and about 15 m apart (Figure 5.9A). The eastern (ESE) contact is sharp and sheared (Figure 5.9B), and truncates large columnar joints in the coherent dacite facies.

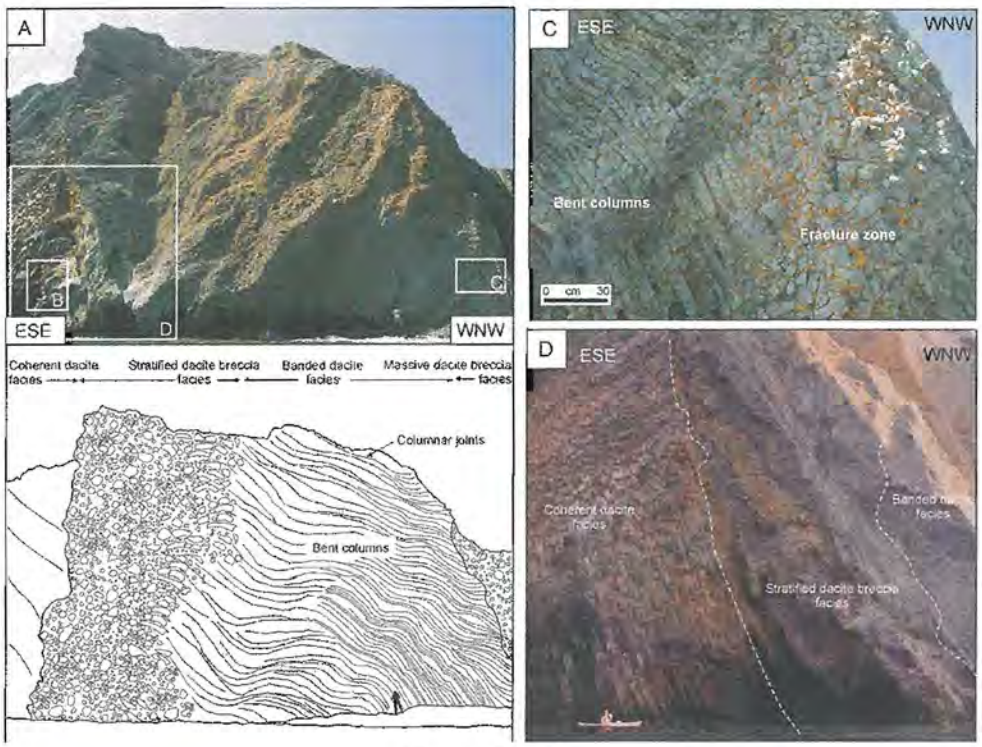

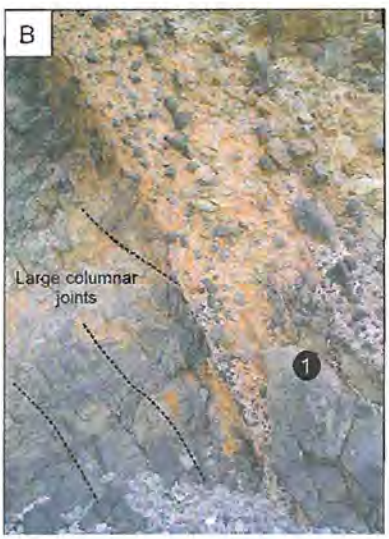

Figure 5.9 A West-northwest cliff exposure showing the context of the stratified dacite breccia facies. The breccia has a maximum width of 15 m (person for scale) and separates coherent dacite (left) from banded dacite (right). **B** Stratified, matrix- to clast-supported, poorly sorted breccia. Clasts range from several centimetres to metres in diameter. Single clasts are typically polyhedral with smooth surfaces. The larger clasts have internal polyhedral joints (1). The eastern (ESE) contact is sheared, and truncates large columnar joints in the coherent dacite facies (dashed black lines mark column orientations). **C** Columns in the adjacent banded dacite facies are bent (left hand side) and locally ruptured along narrow subvertical fracture zones. The fracture zones are generally 10-15 cm wide and have gradational boundaries with columnar-jointed banded dacite facies. **D** Steeply dipping, diffusely stratified or massive, dacite breccia. Beds show major lateral variations in thickness, geometry, internal organization and grain size. Kayak (bottom left) is 4.5 m long.

Platy clasts adjacent to the subvertical shear surface form irregular domains along the contact, and many clasts are aligned parallel to the contact. In contrast, the western (WNW) contact with the outer banded dacite facies is gradational. The columns in the adjacent banded facies are bent, sharply 'kinked' and locally ruptured along narrow (<0.5 m), irregular, anastomosing fracture zones (Figure 5.9A and C) parallel to the interval of stratified dacite breccia.

Bedding in the stratified dacite breccia is steep to subvertical and typically parallel to the eastern contact. Single beds are internally diffusely stratified or massive but not graded, very thick (0.5-3.5 m) and show marked lateral variations in thickness, geometry, internal organization and grain size (Figure 5.9D). Bed contacts are diffuse. Wavy, diffuse stratification within the facies is defined by alignment of coarse dacite clasts.

This facies contains dacite clasts that range from several centimetres to several metres in diameter (Figure 5.9B). Most clasts are weakly vesicular (up to 10 vol.%), angular and polyhedral, with smooth, planar to curviplanar surfaces; some clasts are subangular. The larger clasts (>20 cm) generally have internal polyhedral joints. The composition, texture and mineralogy of the dacite clasts within the stratified breccia facies closely resemble those in the massive dacite breccia facies. The matrix consists of a poorly sorted mixture of angular, non- to weakly vesicular (up to 10 vol.% vesicles), pale grey and black dacite clasts (<5 cm) and non-vesicular black glass shards (<2 mm). The matrix is similar to the matrix in the massive dacite breccia facies, but lacks rhyolitic pumice.

5.5 Facies architecture of the Kalogeros cryptodome

The Kalogeros cryptodome consists of five facies dominated by compositionally and mineralogically identical dacite and separated by gradational or sheared boundaries. In addition, a single set of radial columnar joints is continuous through two dominant facies (coherent and banded dacite facies). These features indicate that the five facies are different but genetically related parts of a single discrete cryptodome. The volumetrically dominant, texturally uniform, coherent dacite facies is characterised by columnar joints with the largest diameter and by the highest groundmass crystallinity. Columnar joints result from contraction during cooling of stagnant lavas and intrusions in which isotherms are parallel or concentric (Grossenbacher and McDuffie 1995). Faster cooling rates produce narrower columns (Long and Wood 1986; Graff et al. 1989). Like-

wise, groundmass crystallinity relates directly to cooling rate, with slow cooling favouring more complete crystallization. The coherent dacite facies occurs in the centre of the cryptodome, where cooling of the magma was slowest.

The 30-40-m-thick, banded dacite facies broadly encircles the coherent dacite facies and is characterised by alternating bands defined by variations in colour, groundmass crystallinity and vesicularity. Pale grey bands alternating with black bands are similar to large-scale flow bands formed during laminar shear in highly viscous silicic lavas and intrusions (e.g. Snyder and Fraser 1963; Christiansen and Lipman 1966; Goto and McPhie 1998). The large-scale flow bands in the Kalogeros cryptodome are overprinted by columnar joints and therefore formed before the cooling contraction that formed the joints. The banded facies in the Kalogeros cryptodome is thus interpreted to be a large-scale, flow-banded domain that developed close to the margin during ductile flow accompanying intrusion and growth.

The fractured dacite facies is dissected by a network of intersecting, gently curved fractures. This distinctive polyhedral fracture pattern is typical of the rapidly chilled parts of subaqueous lavas and shallow intrusions (c.f. pseudopillows, Yamagishi 1987, 1991; Yamagishi and Goto 1992). The fractures cut both pale grey and black dacite and hence post-date the formation of the large-scale flow bands (banded dacite facies). The gradational change from columnar-jointed banded dacite to fractured (banded) dacite probably reflects a transition from regular, stable isotherms in the interior to highly irregular, shifting isotherms at the rapidly cooled outer margin of the cryptodome.

The jigsaw-fit texture in the massive dacite breccia facies implies that brecciation was in situ. The polyhedral shape of the dacite clasts suggests that brittle fracture occurred in response to contraction during rapid cooling on contact with wet sediment at the outer margin of the intrusion. Fragmentation may have also been induced by dynamic stressing of the thick, already solid margin due to continued movement of the less viscous core (e.g. Brooks et al. 1982; Kokelaar 1986; Griffiths and Fink 1993). The wet sediment invaded the fractures in the dacite, probably in response to pressure reduction as the fractures opened (e.g. Kokelaar 1982; Brooks 1995).

The stratified dacite breccia facies contains bedding and edge-modified clasts that imply lateral transport. However, transport can only have been very minor, as one contact (with the banded dacite facies, Figure 5.9A and D) is gradational. Because the other

contact is a sharply defined shear surface, we consider that the principal fragmentation mechanism was brittle fracture in response to shear. The most intense shear, sufficient to produce cataclasite, was mainly focussed close to the ESE contact but died out toward the gradational contact with the banded facies. Shear failure and variable movement produced both the crude stratification roughly parallel to the shear direction, and the edge-modified clasts.

The shear failure responsible for the stratified dacite breccia facies probably accompanied the final stages of solidification, when the dacite passed through the ductile-brittle transition. Columnar joints in the adjacent banded facies preserve evidence for ductile (bent columns), transitional ('kinked' columns) and brittle (fracture zones) responses to shear (Figure 5.9). The stratified dacite breccia facies is inferred to represents an additional step in this progression, involving brittle failure and formation of cataclasite. This facies is located at a boundary between the coherent dacite facies and banded dacite facies that was evidently mechanically weak.

5.6 Timing and environment of cryptodome emplacement

The margins of the cryptodome have been quench fragmented (massive dacite breccia facies) and locally mixed with the host pumice breccia (Pahina Formation), indicating that the pumice breccia was poorly consolidated and wet at the time of cryptodome emplacement. The Pahina Formation was deposited in a shallow submarine environment (dominantly below wave base) in water up to 200 m deep. The Pahina and Papfragas Formations were deformed by the cryptodome, whereas the overlying formations (Sarakiniko Formation and Korakia Andesite) were apparently unaffected. The overlying units of Sarakiniko Formation thicken appreciably east and west of the Kalogeros cryptodome and record a transition from a relatively shallow, but dominantly below-wave-base, setting to a storm- and tide-dominated shallow marine environment. Thus, we infer that the intrusion of Kalogeros cryptodome formed a seafloor topographic high, after deposition of the Pahina and Papafragas Formations and probably before deposition of the Sarakiniko Formation.

The position of the palaeoseafloor at the time of intrusion has not been recognised in the overlying stratigraphy, and the pumiceous breccia cover may have been as little as a few tens of metres. Neither is the water depth at the time of intrusion known, although

it cannot have been more than the few hundred metres maximum depth inferred for the depositional setting of the host formations. In addition, the dacite of the outer margins of the cryptodome is vesicular, implying a relatively low confining pressure.

5.7 Mode of emplacement of the Kalogeros cryptodome

The broadly concentric arrangement of the lithofacies of the Kalogeros cryptodome, combined with the gradational contacts between them, indicates that growth involved steady injection of magma in a single, more-or-less continuous episode (e.g. Momo-Iwa cryptodome, Goto and McPhie 1998). Either episodic magma supply or multiple injections of magma would have resulted in a more complex internal structure marked by more variable flow banding orientations and more complicated joint patterns (e.g. Izumiyama cryptodome, Hamasaki 1994). This style of growth is endogenous, involving addition of new lava into the dome interior (Fink et al. 1990; Fink 1993)

Formation of the Kalogeros cryptodome initially involved injection of dacitic magma into a thick sequence of unconsolidated, wet pumiceous sediments in a shallow submarine environment (1 in Figure 5.10A). The margins of the intrusion were rapidly cooled on contact with wet pumice breccias, producing in situ and clast-rotated intrusive hyaloclastite (massive dacite breccia facies) (2 in Figure 5.10A). The chilled carapace would have been an effective insulator, so that the interior retained sufficient heat to remain ductile. Expansion of the cryptodome in response to continued supply of magma into the interior (3 in Figure 5.10B) was accommodated by deformation and displacement of the surrounding weak, wet pumice breccia. As the cryptodome inflated, laminar shear affected the cooler, more viscous, outer part, generating large-scale flow banding (banded dacite facies) (4 in Figure 5.10B). Progressive inward propagation of quench fractures generated a domain composed of fractured dacite (fractured dacite facies) adjacent to the intrusive hyaloclastite. The final magma injected into the core of the cryptodome cooled slowly and solidified in a setting unaffected by laminar shear (coherent dacite facies). The radial columnar joints of the Kalogeros cryptodome are very regular in arrangement and gradually decrease in width outward from the core to the margin (5 in Figure 5.10C), suggesting that the isothermal surfaces were concentric and parallel to the outer contact.

The stratified dacite breccia facies is likely to have formed during final solidification of

the Kalogeros cryptodome when the cryptodome had just passed though the ductile-brittle transition. This facies is a variety of cataclasite resulting from brittle fracture of coherent dacite in response to shear affecting the northeastern segment of the cryptodome (6 in Figure 5.10D). Contraction during this stage may have been uneven, producing local high-strain zones, especially near margins of the cryptodome.

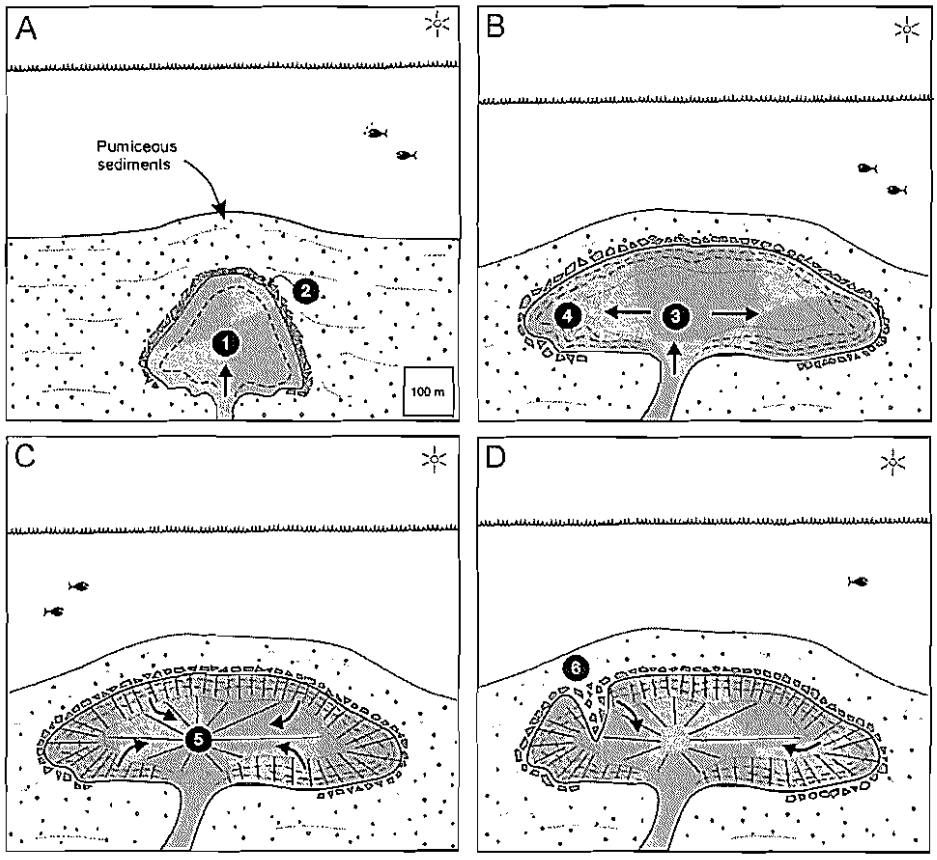

Figure 5.10 Cartoon of the emplacement of the Kalogeros cryptodome. **A** Dacite magma was injected (1) into unconsolidated, wet pumiceous sediments in a shallow submarine environment. The margins of the intrusion were quenched, producing in situ and clast-rotated intrusive hyaloclastite (massive dacite breccia facies) and intensely fractured domains (fractured dacite facies) (2). **B** Continued supply of magma into the interior resulted in inflation of the cryptodome (3). As the cryptodome expanded, large-scale flow banding developed along the inner margins of the intrusion (4). **C** The final magma injected into the core of the cryptodome (coherent dacite facies) cooled slowly and solidified in a setting that was unaffected by laminar shear. The radial columnar joints of the Kalogeros cryptodome are very regular in arrangement and gradually decrease in width outward from the core to the margin (5). **D** During the final stage of solidification when the dacite was at the ductile-brittle transition, shear locally affected dacite near the margin of the cryptodome, producing an interval of cataclasite (stratified dacite breccia facies) (6).

5.8 Characteristics of felsic submarine cryptodomes

The Kalogeros cryptodome is larger than many other cryptodomes in ancient subaqueous settings (e.g. Doyle and McPhie 2000; Hanson and Wilson 1993; Horikoshi 1969; Hamasaki 1994; Goto and McPhie 1998; Table 5.1), although very similar in dimensions to a Devonian cryptodome in the Boyd Volcanic Complex (Cas et al. 1990). All examples are, however, relatively small-volume (<<1 km^3), high-aspect-ratio bodies dominated by non- to poorly vesicular, massive or columnar-jointed coherent facies. Some cryptodomes, such as the Kalogeros and Momo-Iwa cryptodomes, show a distinctive concentric distribution of internal textural domains, comprising a largely crystalline, massive, coherent core, rimmed by a more glassy flow-banded zone and an outer fragmental carapace (Figure 5.11A). This internal zonation presumably reflects the regular shape of the isotherms within a cooling cryptodome. In addition, contacts of syn-sedimentary cryptodomes show varying effects of quenching (intrusive hyaloclastite) and interaction with poorly consolidated, wet sediments (peperite).

Submarine felsic lava domes formed by endogenous growth have morphologies, facies characteristics, and internal structure that are broadly similar to those of equivalent cryptodomes (Figure 5.11). With few exceptions, however, submarine lava domes are associated with both in situ and redeposited autoclastic facies (e.g. Punta del Papa dome, Ponza, Scutter et al. 1998; Figure 5.11B). In contrast, submarine cryptodomes are dominated by coherent facies with well-developed concentric textural zones, and entirely lacking in redeposited autoclastic facies (Figure 5.11A). The intrusive setting of cryptodomes evidently limits autoclastic fragmentation and prevents redeposition.

One facies of the Kalogeros cryptodome, the stratified dacite breccia facies, is similar to redeposited autoclastic facies in being monomictic, stratified and gradational into coherent facies (banded dacite facies). The context and contact relationships strongly suggest that this facies is cataclasite. However, in the absence of such constraints, interpretation as redeposited autoclastic breccia would seem entirely plausible. The mistake is not trivial, as the latter interpretation implies derivation from an extrusion, which, in this case, is incorrect. It is note that the convergence in characteristics of genetically different clastic facies in submarine felsic dome-cryptodome associations can result in flawed interpretations.

Table 5.1 Characteristics of selected felsic cryptodomes in submarine volcanic successions.

Locality	Age	Composition	Dimensions (m)*	Thickness (m)	Depositional setting of host sediments	Reference
Kalogeros dacite, Milos Island, Greece	Upper Pliocene	Dacite	800 x 1300	>120	Shallow marine	this study
Momo-Iwa, Rebun Island, Japan	Miocene	Dacite	200-300	190	Shallow marine	Goto and McPhie (1998)
Kosaka district, Honshu, Japan	Miocene	Dacite	(M4) 400 x 220	200	Deep marine	Horikoshi (1969)
			(M6) 800 x 400	200		
			(M8) 340	>50		
			(M9) 200-600	150		
Izumiyama intrusion, Saga, Japan	Miocene	Rhyolite	(R1) 300 x 250	>200	Shallow marine/subaerial	Hamasaki (1994)
			(R2) 150 x 100			
			(R3) 200 x 150			
			(R4) ~350 x 200			
			(R5) 150 x 50			
			(R6) 50 x 25			
Ultima Esperanza district, Chile	Jurassic	Rhyolite	> 3 km²	> 300	Deep marine (below wave base)	Hanson and Wilson (1993)
Boyd Volcanic Complex, Australia	Devonian	Rhyolite	1300	180	Shallow marine	Cas et al. (1990)
Mount Windsor Volcanics, Queensland, Australia	Cambro-Ordovician	Rhyolite-Dacite	(D1) 250 x 300	> 300	Deep marine (below wave base)	Doyle and McPhie (2000)
			(R2) 175 x 275	50-100		
			(R2) > 100 x >125	120-170		
			(R3) 175 x > 150	20-100		
			(R9) > 350	> 225		

* Dimensions are lengths, widths (m) or areas (km²)

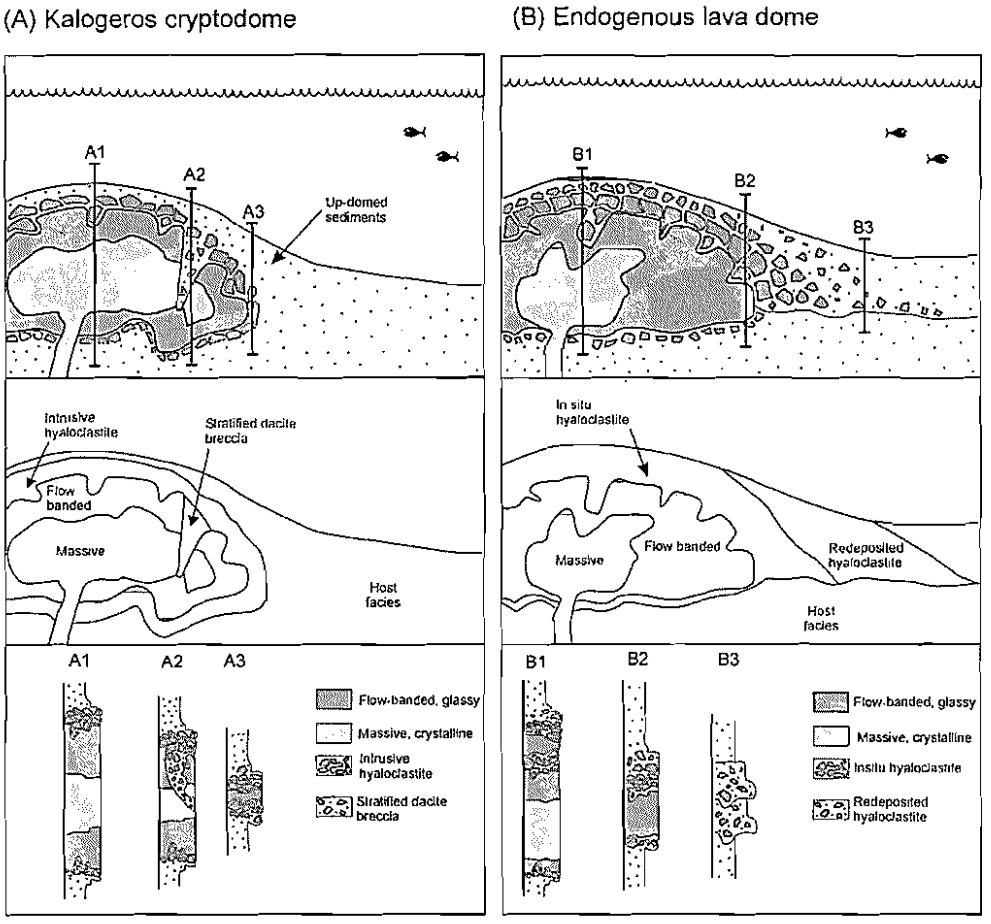

Figure 5.11 Character and arrangement of facies in the Kalogeros cryptodome **A**, and in a submarine lava dome **B** (modified from McPhie et al. 1993). Submarine cryptodomes and endogenous lava domes may show a similar internal arrangement of flow-banded, glassy or partly glassy and massive, crystalline facies. However, in cryptodomes, any autoclastic facies will be subordinate to coherent facies and exclusively in situ.

5.9 Summary

The Kalogeros dacite is a cryptodome which formed from intrusion of dacite magma into poorly consolidated, low density, wet pumiceous sediments deposited in a relatively shallow submarine environment. The cryptodome grew mainly by steady inflation as magma was supplied continuously during a single intrusive phase. The margins of the intrusion were quench fragmented, forming domains of intensely fractured dacite and intrusive hyaloclastite. The near-solid outer carapace insulated the hotter, less viscous interior. Laminar shear accompanying inflation generated large-scale flow banding around the outer part of the core. Once stagnant, regularly concentric isotherms were established within the cryptodome and controlled the orientation of columnar joints.

The columnar joints also reflect the cooling rate, having wider diameters in the centre (slower cooling) and narrower diameters at the margins (faster cooling). Local shear failure formed cataclasite breccia, possibly in response to final cooling-induced contraction of the cryptodome.

Chapter 6
An Upper Pliocene coarse pumice breccia generated by a shallow submarine explosive eruption

The following chapter has been accepted in the Bulletin of Volcanology. In order to keep with the chapter format of the thesis the introduction of the original manuscript has been modified and the abstract removed.

6.1 Introduction

The products of submarine explosive eruptions are poorly known compared to their subaerial counterparts, despite their probable abundance in modern oceans and in ancient volcanic terrains. These eruptions are difficult to observe so records are extremely restricted (e.g. 1953–1957 Tuluman eruption, Reynolds et al. 1980; 1952-1953 Myojinsho eruption, Fiske et al. 1998; 1989 eruption Teishi Knoll, Izu Peninsula, Yamamoto et al. 1991). As a result, volcanological studies rely instead on submersible surveys (e.g. Fiske et al. 2001) or ancient successions that have been uplifted to subaerial settings (e.g. Fiske 1963; Fiske and Matsuda 1964; Cashman and Fiske 1991; Kokelaar and Busby 1992; Kano 1996; Kano et al. 1996). However, in ancient successions the depositional setting may be ambiguous, and preservation and exposure are commonly incomplete.

The Filakopi Pumice Breccia (FPB) on Milos, Greece, is exceptional in that the submarine depositional setting is very well constrained. Furthermore, componentry, lithofacies and context strongly suggest that the vent was also submarine and that the eruption was explosive. In this chapter, the FPB is described and interpreted. The results extend current understanding of eruptive and depositional processes involved in shallow-submarine explosive eruptions. We also compare the FPB with pyroclastic deposits generated by subaerial explosive eruptions.

6.2 Stratigraphy of northeastern Milos

Sections that include the FPB are well exposed on the northeastern coast of Milos and southwestern Kimolos (Figures 6.1 and 6.2). The lowest unit is the Pahina Formation (basal pyroclastic series), which has a thickness of 70 m. This formation includes at least two pumice breccia members, the lower dacitic Agios Konstantinos Pumice Breccia, and the upper rhyolitic FPB, separated by a 4-m-thick interval of green mudstone characterised by burrows, intact bivalves and calcareous nodules. The most extensive and best exposed of the two pumice breccias is the 45-m-thick FPB. The FPB is conformably overlain by an 0.2–1.5-m-thick interval of green mudstone (Figure 6.3) that is similar to the underlying bioturbated and fossiliferous mudstone, but also contains sparse, large (1.5 m) pumice clasts. The upper mudstone is massive to laminated, and commonly shows ripples and wavy bed forms.

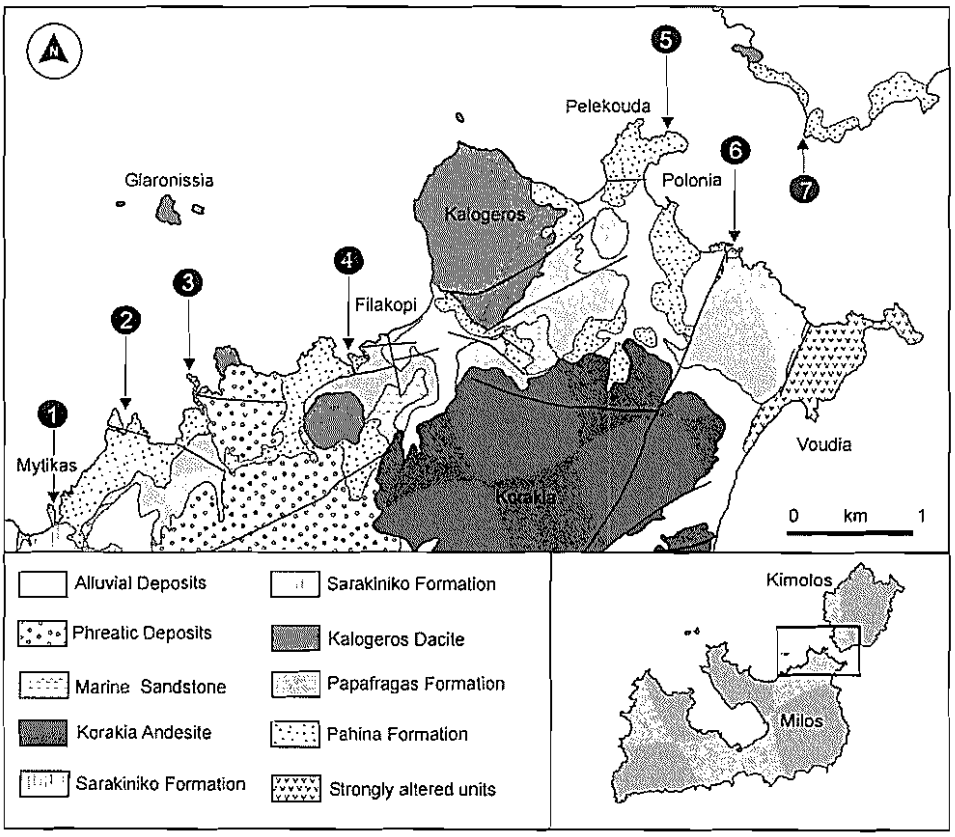

Figure 6.1 Geological map showing the distribution of the FPB and location of logged sections (1–7 shown in Figure 6.5) (modified after Fytikas 1977, Fytikas and Vougioykalakis 1993).

The upper green mudstone is conformably overlain by the 10–45-m-thick Papafragas Formation (complex of domes and lava flows), which comprises thickly to very thickly bedded, generally graded, andesitic scoria and pillow-fragment breccias. The formation is intruded by several cryptodomes of the Kalogeros Dacite(complex of domes and lava flows). The Papafragas Formation thins to the east and is gradationally overlain by the Sarakiniko Formation (~50 m thick). The Sarakiniko Formation consists primarily of thickly bedded sandstone, intercalated with beds of pumice breccia, which grade upward into fossiliferous mudstone. The Korakia Andesite (pyroclastic series and lava domes) consists of lavas, intrusions and subordinate pyroclastic facies about 30–35 m thick. Locally the Korakia Andesite it is unconformably overlain by an interval (~5 m) of brown unconsolidated bioclastic sand. A palaeosol separates this interval from phreatic deposits (up to 5 m thick) that form the youngest unit of the section.

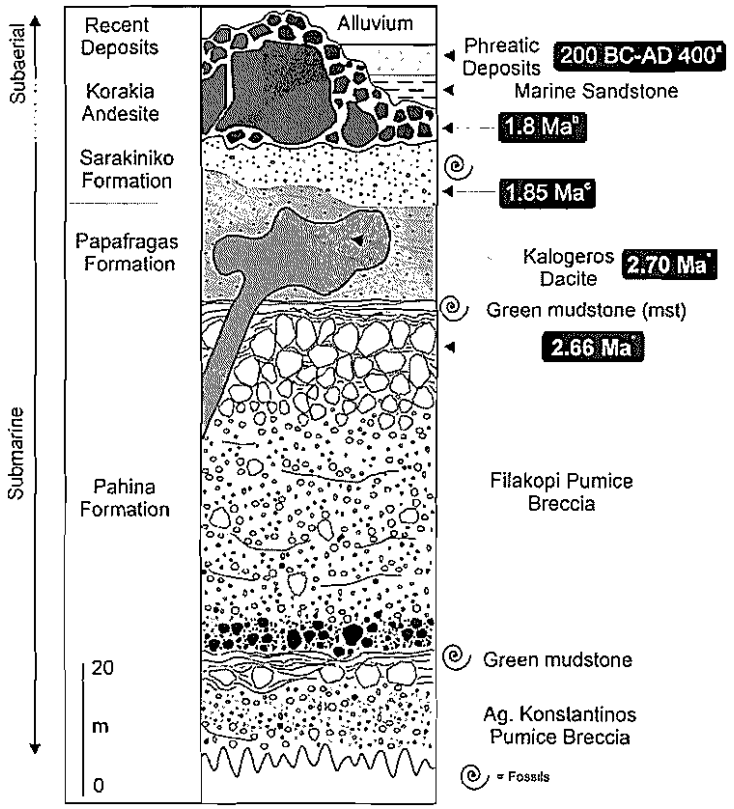

Figure 6.2 Generalised stratigraphic section through the volcanic succession exposed on northeastern Milos and southwestern Kimolos. The succession changes upward from submarine to subaerial. Ages are based on: [a] ^{14}C measurements on pot fragments within phreatic deposits (Traineau and Dalabakis 1989); [b] paleomagnetic polarity (Matyama) for the Korakia Andesite (Kondopoulou and Pavaides 1990), [c] K-Ar dates on biotite from a dacite pumice clast (Fytikas et al. 1986); and [d] U-Pb dating of zircons (Chapter 8).

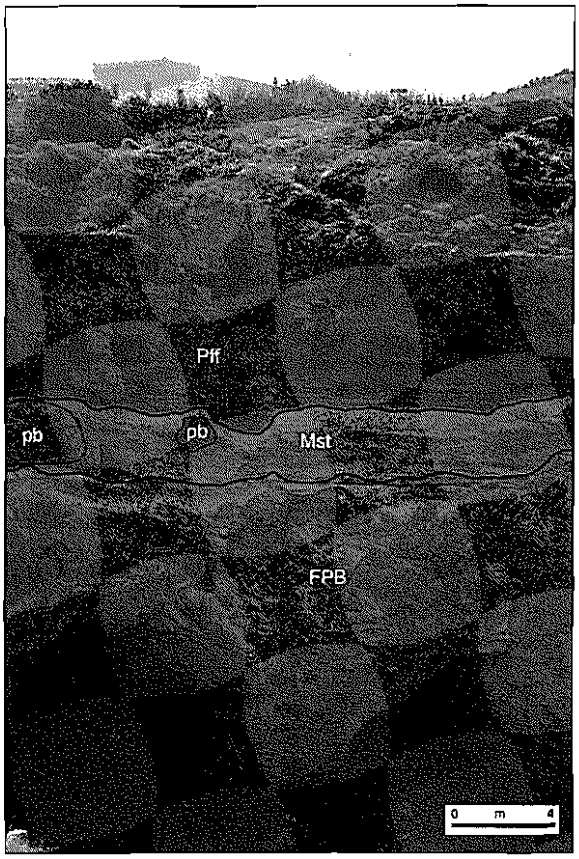

Figure 6.3 The upper contact of the FPB. The FPB is conformably overlain by fossiliferous and bioturbated mudstone (Mst), which contains isolated large pumice clasts (pb). The Papafragas Formation (Pff) overlies the mudstone and comprises thickly bedded, andesitic scoria breccia.

The Filakopi Pumice Breccia

The FPB is exposed in steep coastal outcrops east of Mytikas, and in limited outcrops on the southwestern coast of Kimolos (Figure 6.1). It covers approximately 18 km$_2$, and has a minimum bulk volume of 1 km$_3$. An additional but indeterminate volume is concealed by younger units and by the sea. Bedding is generally flat-lying or gently dipping to the south. The succession is disrupted by several normal faults, some of which have displacements up to 60 m, and by cryptodomes of the Kalogeros Dacite.

Seven sections through the FPB were logged at a scale of 1:100. Features measured and recorded included: clast types and proportions, clast shape, grain size, the longest dimension of the maximum and three largest pumice clasts (MP and MP3, respectively), the longest dimensions of the largest lithic clasts (ML), bed forms and bed thickness. Single juvenile and non-volcanic lithic clasts were sampled for geochemistry and petrography. Pumice breccia is a descriptive term that we use to indicate the dominance of pumice and angular shape of the clasts. Bed thickness terms are those outlined in Ingram (1954).

6.3 Components and composition of the FPB

The dominant component of the FPB is glassy rhyolitic pumice (~85 vol. %). The pristine state, abundance and uniform composition (Figure 6.4, Table 6.1) suggest that the pumice clasts were freshly erupted and they are considered to be juvenile. Minor aphyric obsidian clasts (<1 vol. %) of the same composition and glass shards (~10 vol. %) are probably also juvenile. The remainder (<5 vol. %) consists of non-juvenile lithic clasts.

Juvenile clasts

There are five main types of juvenile clasts in the FPB: (I) white, biotite-plagioclase-phyric pumice (85-90 vol. %); (II) white-grey aphyric pumice (5 vol. %); (III) grey, non- to poorly vesicular, glassy, crystal-rich clasts (<2 vol. %); (IV) black, perlitic obsidian clasts (<<1 vol. %); and (V) glass shards. All analysed juvenile clasts are rhyolitic (70.31-72.25 wt. % SiO_2), and show only slight variations in major- and trace-element abundances (Figure 6.4). The biotite-plagioclase-phyric pumice (type I) contains 1-5 % phenocrysts of platy biotite (up to 1 mm in diameter), plagioclase, pyroxene and quartz. This pumice is moderately to highly vesicular (50-80 vol. % vesicles) and vesicles are elongate to spherical (several mm long and less than 1 mm diameter). The white-grey aphyric pumice (type II) contains <1 vol. % phenocrysts of plagioclase, biotite and quartz. The white-grey aphyric pumice is highly vesicular (65-80 vol. % vesicles), and vesicles are elongate with very low aspect ratios, imparting a 'woody' appearance. Coarse (>64 mm) pumice clasts (types I and II) are prismatic to tabular with normal joints at their margins and internal polyhedral joints. Finer (<64 mm) pumice clasts are generally blocky or polyhedral, and subangular to subrounded. Crystal-rich, glassy, non- to poorly vesicular (0-30 vol. % vesicles) clasts (type III) contains 5-8 % phenocrysts of biotite (up to 1 mm in diameter), plagioclase and quartz. Vesicles show transitions from ovoid to elongate morphologies. The perlitic obsidian clasts (type IV) are typically less than a few millimetres in diameter. The glass shards are generally <0.5 mm across, non-vesicular and cuspate in shape.

Non-juvenile clasts

Non-juvenile lithic clasts are mostly non- to poorly vesicular, plagioclase-phyric, glassy

dacite and andesite (Figure 6.4). Some are strongly hydrothermally altered. Other non-juvenile lithic clasts include basement-derived metamorphic (schist and gneiss) and sedimentary rocks. In addition, sporadic dark grey pumice clasts are present. These pumice clasts have identical mineralogy and texture to pumice clasts in the lower Agios Konstantinos Pumice Breccia. These clasts are rounded, and are also interpreted to be non-juvenile. The non-juvenile lithic clasts are dominantly small (<5 cm) but locally up to 2.6 m diameter, and are angular to subangular.

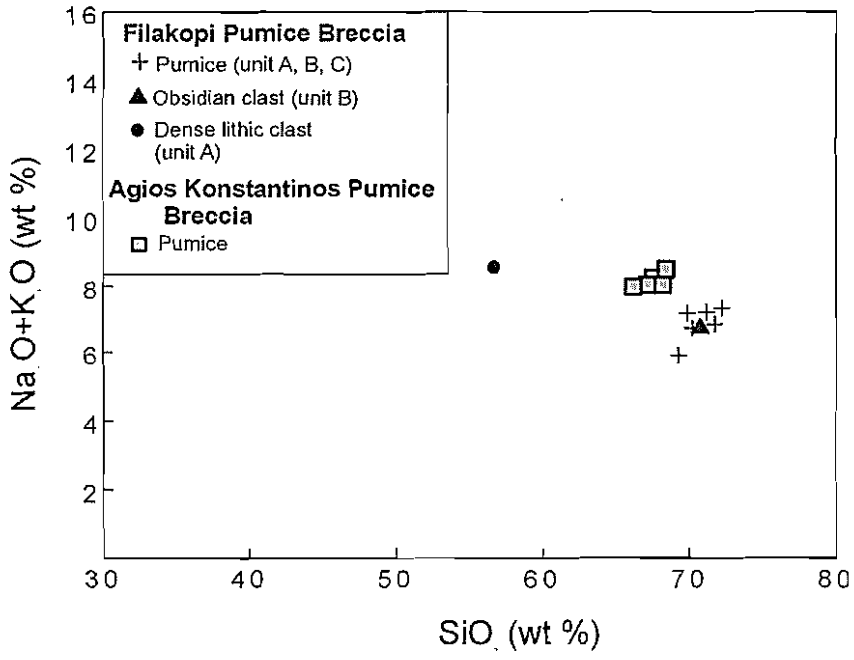

Figure 6.4 Na_2O+K_2O vs. SiO_2 (wt.%) from whole-rock XRF analyses. The juvenile pumice clasts in the FPB are compositionally distinct from those in the underlying Agios Konstantinos Pumice Breccia, being slightly more silicic.

6.4 Internal stratigraphy of the FPB

The FPB consists of three main units that display distinctive textures and lithofacies characteristics (Table 6.1): (A) basal lithic breccia (4–8 m); (B) stratified pumice breccia (12–17 m); and (C) coarse pumice breccia at the top (6.5–20 m). The three units are conformable and contacts among them are gradational.

Table 6.1 Characteristics of the three units in the FPB. Grain size: L-non-vesicular juvenile and accessory lithic clasts.

Unit	Grain shape	Grain size (cm)	Components	Lithofacies
C 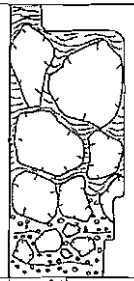	prismatic quenched margins internal polyhedral joints	MP3: 303 MP: 650	Vol% L: < 0.1 all pumice types present	Thickness 6.5-20 m Laterally extensive, very thick, tabular bed. Contacts: lower gradational, upper relatively sharp, planar. Fabric: coarse pumice clasts set in a fine pumice breccia to shard-rich mud, lithic poor.
B 	subangular-subrounded mixture of prismatic large clasts and with subordinate polyhedral clasts	MP3: 240 MP: 110 ML: 90	Vol% L: 2-5 part of Section 5) all pumice types present	Thickness 12-17 m Wedge-shaped, internally massive or diffusely stratified, very thick beds Sharp upper and lower contacts Fabric: fines poor, poorly sorted, grain-grain supported
A 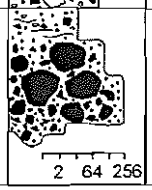	Subangular-subrounded lithic clasts together with subordinate rounded pumice clasts	MP3: 25 MP: 150 ML: 250	Vol% L: 95 (~70 in the basal part of section 5) Dark grey, dense poorly vesicular andesite and dacite	Thickness 4-8 m Laterally extensive, very thick (up to 8 m), tabular bed. Contacts: lower strongly erosional to sharp, upper gradational with overlying pumiceous units Fabric: Fines poor, poorly sorted, inversely to normally graded, grain-supported

Grain size: L = non-vesicular juvenile and lithic clasts; MP3=longest dimensions of the three largest pumice clasts;
MP=longest dimensions of the largest pumice clast; ML=longest dimensions of the largest lithic clast

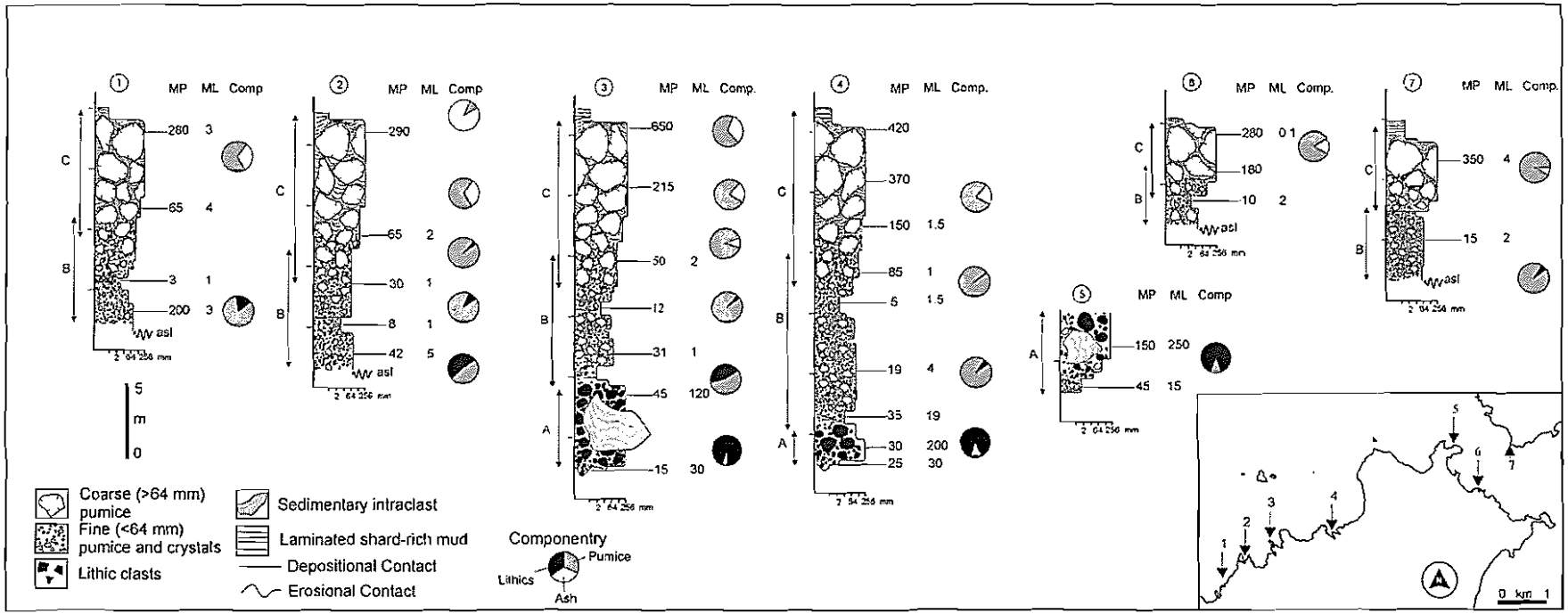

Figure 6. 5 Graphic logs of key FPB outcrops at locations 1-7 (insert) showing the three main units (A, B, C). The width of the units in the logs reflects the grain size of the pumice and lithic clasts. MP - longest dimensions in cm of the largest juvenile pumice clast, ML - longest dimensions in cm of the largest lithic clast, asl – average sea level. Componentry (Comp.) data are averages of all measured exposures on Milos and Kimolos.

Unit A

Unit A is present in three sections (3, 4 and 5, Figure 6.5), and is a fines-poor, poorly sorted, grain-supported lithic breccia (Figure 6.6A). It occurs as a tabular bed, generally less than 8 m thick. Unit A shows only minor lateral variation in thickness, geometry, internal organization and grain size. It is coarsest and thickest (8 m) at the northeastern end of Milos (section 5, Figure 6.5). The basal 0.2–0.5 m of the unit is reversely graded, whereas the rest of the unit is normally graded with a diffusely stratified upper part. The unit includes lithic clasts from centimetres to a several metres in diameter, most of which are fresh or hydrothermally altered dacite. Other lithic clasts include schist, Neogene limestone and sedimentary clasts (mudstone and sandstone). Coarse lithic clasts (>20 cm in diameter) are generally subrounded, whereas smaller lithic clasts are angular. Juvenile clasts are minor (2–5 vol. %) and typically coarse (~40 cm in diameter) type III clasts.

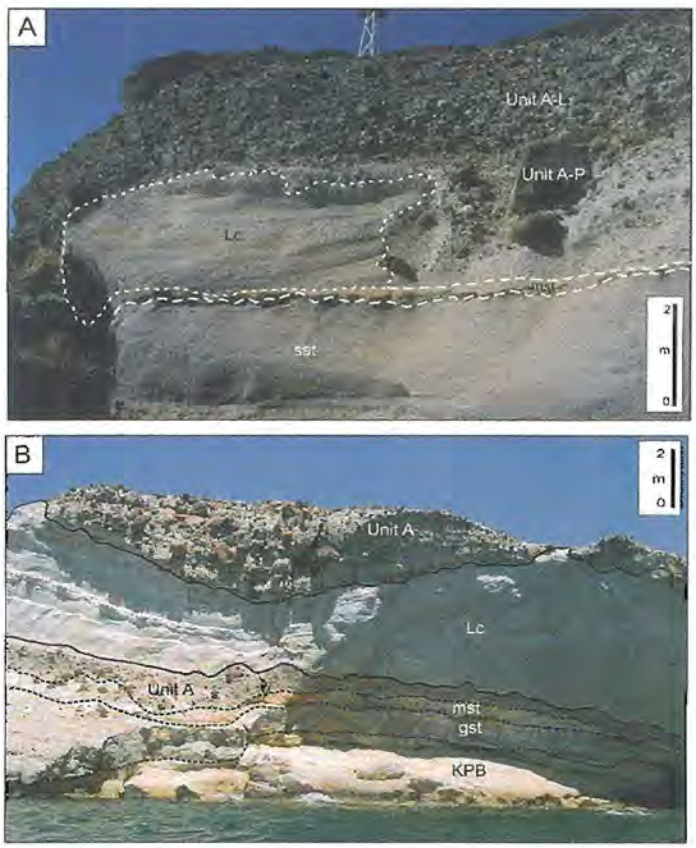

Figure 6.6 **A** Reversely to normally graded coarse lithic breccia (unit A) at the northeastern end of Milos (section 5, Figure 6.1). The breccia has a sharp, planar contact with the underlying green fossiliferous and bioturbated mudstone (mst). A large clast (Lc) derived from sandstone (sst) occurs at the base. Two parts of the coarse lithic breccia are visible: a lower, 1.5–2-m-thick, finer grained, pumiceous part (unit A-P); and an upper, 5-m-thick, coarser grained, lithic clast-rich part which includes andesitic and dacitic lithic clasts up to 2.5 m in diameter (unit A-L). **B** The coarse lithic breccia (unit A) at section 3 (Figure 6.1) includes a large sedimentary intraclast

(Lc), 20 m across and 3.5 m high. Bedding in the intraclast is deformed but still preserved. The lithic breccia overlies green fossiliferous and bioturbated mudstone (mst) with a sharp, locally erosional contact. The Agios Konstantinos Pumice Breccia (KPB) and a coarse sandstone (gst) unit occur lower in the section.

The lower contact is sharp and varies from passive and depositional to strongly erosional. Very large clasts derived from immediately underlying sedimentary units are present near the base. These intraclasts have been partly disaggregated and deformed, and were probably poorly consolidated. The largest recorded (20 x 3.5 m) intraclast occurs in section 3 (Figure 6.6B). In section 5, the lithic breccia has a finer grained basal part up to 2.5 m thick which is rich in type III juvenile clasts (Figure 6.6A). This finer interval is internally massive and highly irregular in thickness. The upper contact of the lithic breccia with unit B is gradational and marked by diffuse stratification and an upward increase in the proportion of pumice clasts and a decrease in the proportion of lithic clasts.

Unit B

The most distinctive features of unit B are the dominance of pumice and the poor sorting. It comprises several internally massive or diffusely stratified, very thick (0.9-4 m), poorly defined beds (Table 6.1, Figure 6.7). The beds are mainly composed of angular to subangular pumice clasts (2 mm-1.5 m in diameter; Figure 6.8A) in grain support, with scattered obsidian clasts. Within unit B, dense lithic clasts show an upward decrease in abundance from 10-50 vol. % (ML=30 cm) at the base to <1 vol. % (ML=5 cm) at the top (Figure 6.5). Pumice clasts up to 2.5 m across occupy 50-98 vol. % (Figure 6.5). The coarse pumice clasts (>64 mm) have normal joints at their margins, whereas clast interiors exhibit polyhedral joints (Figure 6. 8B, C). Smaller pumice clasts (<64 mm) are polyhedral, with smooth, planar to curviplanar surfaces that crosscut vesicles. The compositions and textures of the pumice (dominantly type I and III, and minor type IV) and lithic clasts in the pumiceous breccia closely resemble those in the underlying lithic breccia (unit A).

The beds are dominantly wedge-shaped. Parallel to wavy, diffuse stratification is commonly defined by alignment of coarse pumice clasts, especially in the lower parts of beds. Single beds display normal grading of dense lithic clasts, and reverse grading of coarse pumice clasts. Bed contacts vary laterally from sharp to diffuse. The unit shows

only minor variation in thickness, geometry, internal organization and grain size. It is coarsest and thickest (17 m) at the northeastern end of Milos (section 4, Figure 6.5), and particularly poorly sorted.

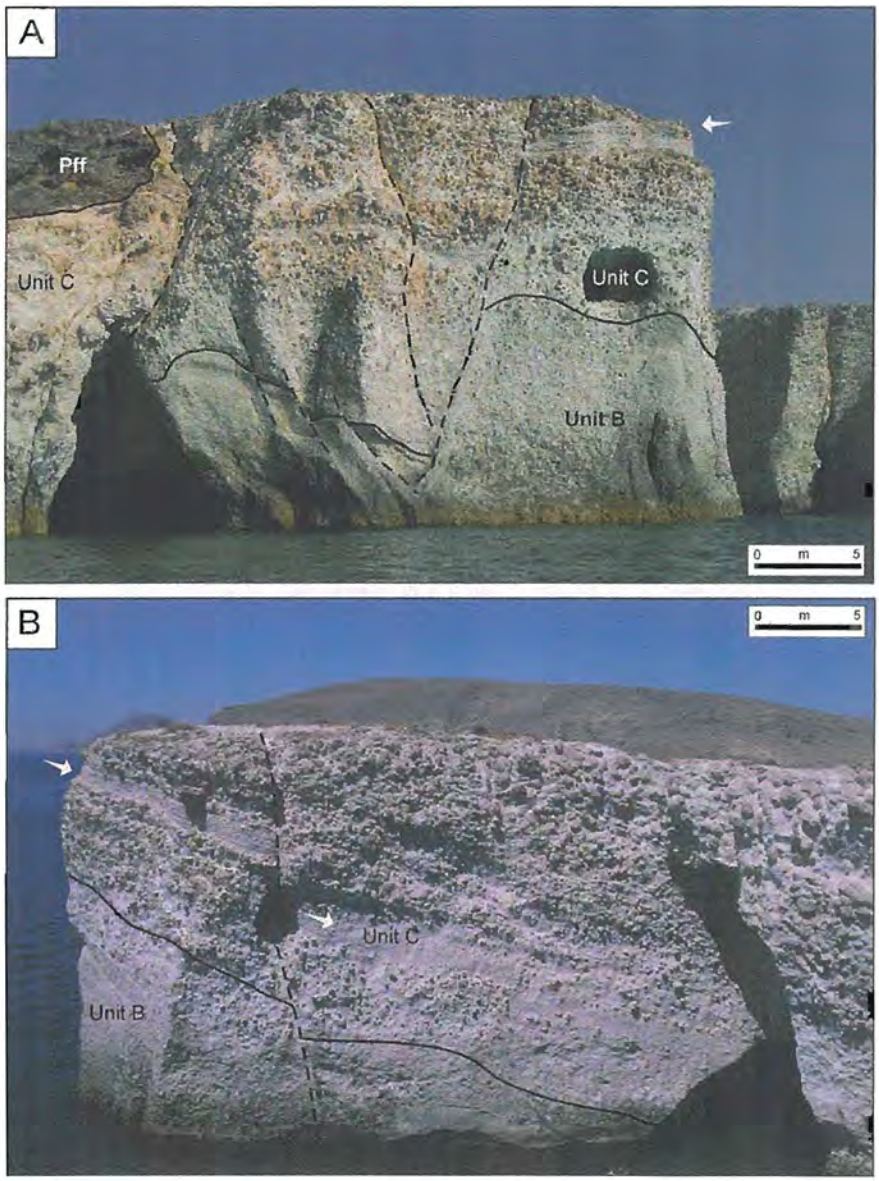

Figure 6.7 Units B and C exposed in Filakopi headland, near section 4. The view in **A** (to the south) is approximately perpendicular to the view in B (to the east). Diffusely stratified, poorly sorted unit B at the base is conformably overlain by the coarse grained, reversely graded unit C. Seven metres above the base of unit C is a discontinuous, stratified interval that lacks the coarse pumice clasts (arrow). Dashed lines indicate normal faults and solid lines are unit boundaries. **B** Wedge-shaped beds of unit B at the base are overlain by the tabular, upward coarsening unit C that dips gently to the south. The stratified interval that lacks the coarse pumice clasts is marked by arrows.

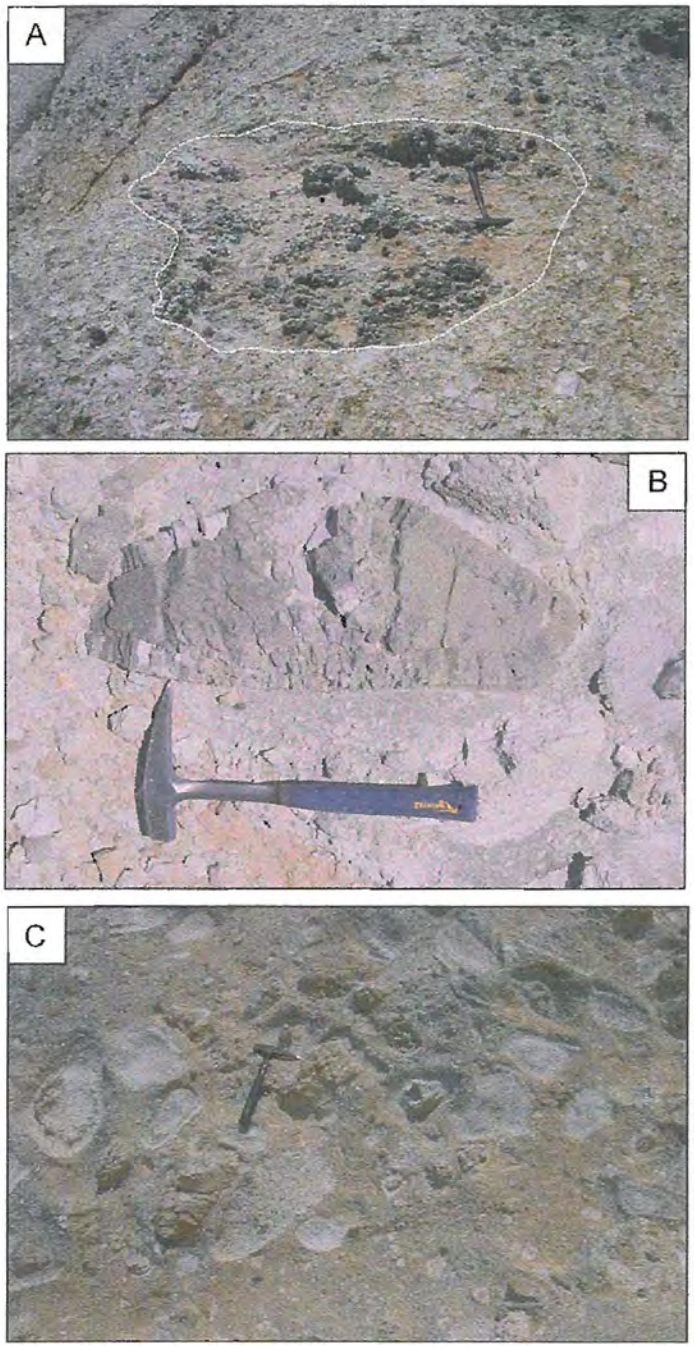

Figure 6.8 Unit B in the FPB at section 4 (Figure 6.1). **A** A bed composed of poorly sorted, angular to subrounded pumice clasts in grain support with minor scattered non-juvenile lithic clasts. A large prismatic pumice clast (white outline) occurs at the top of the bed. **B** Prismatic pumice clast with normal joints along the margins and internal polyhedral joints. **C** Mixture of prismatic pumice clasts in a fine pumiceous matrix at the top of unit B. The pumice clasts are subangular and polyhedral in shape and in grain support.

Unit C

The most striking features of unit C are the extreme range in grain size, and the lack of dense lithic clasts. It is dominated by coarse (64 mm-6.5 m) prismatic pumice clasts in a much finer matrix (Figure 6.9A). The coarse pumice clasts are reversely graded, relatively well sorted, and in grain-to-grain contact throughout a single, tabular, very thick bed (Table 6.1, Figure 6.5). Normal joints occur along the margins of the pumice clasts (dominantly type I, and minor type II and IV), and clast interiors exhibit polyhedral joints, similar to the largest pumice clasts in unit B.

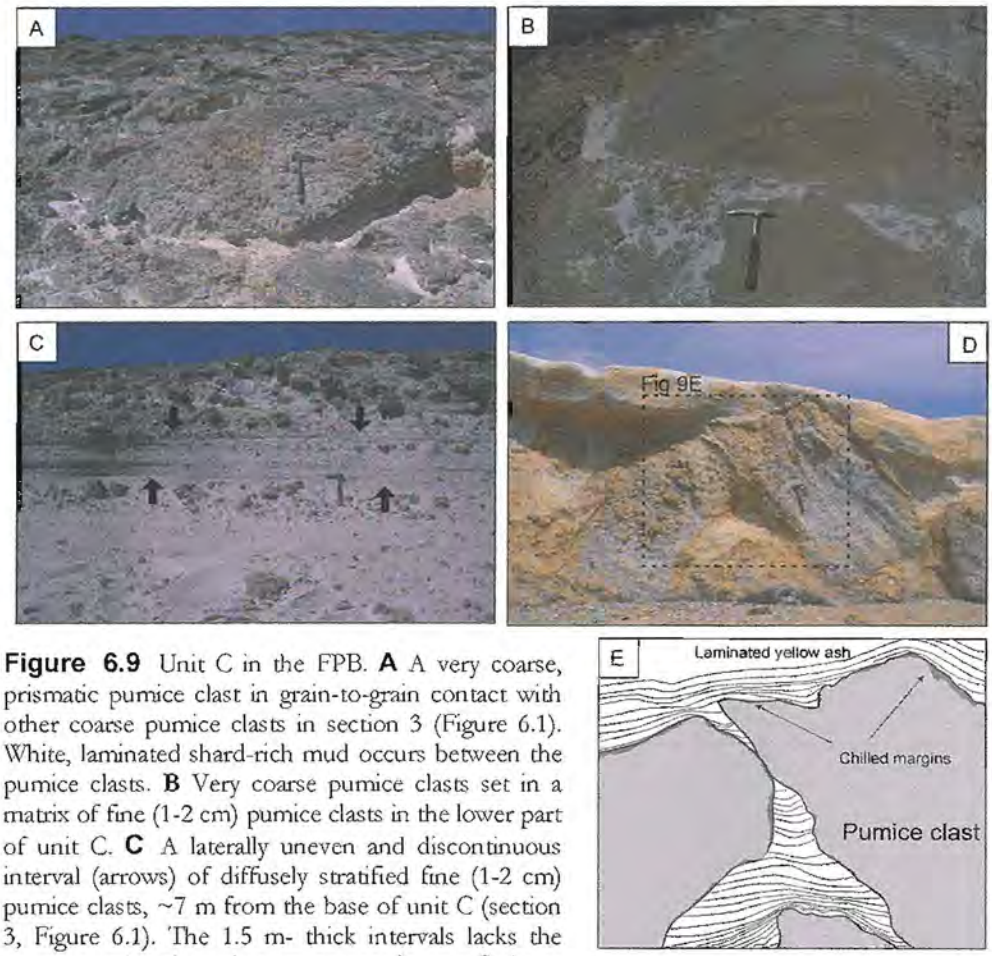

Figure 6.9 Unit C in the FPB. **A** A very coarse, prismatic pumice clast in grain-to-grain contact with other coarse pumice clasts in section 3 (Figure 6.1). White, laminated shard-rich mud occurs between the pumice clasts. **B** Very coarse pumice clasts set in a matrix of fine (1-2 cm) pumice clasts in the lower part of unit C. **C** A laterally uneven and discontinuous interval (arrows) of diffusely stratified fine (1-2 cm) pumice clasts, ~7 m from the base of unit C (section 3, Figure 6.1). The 1.5 m- thick intervals lacks the coarse pumice clasts that are present in unit C above and below. **D** Coarse prismatic pumice clasts at the top of section 7, overlain by 30 cm of laminated, white, shard-rich mud. The coarse pumice clasts are randomly oriented, and most likely settled from suspension. Insert **E** shows a schematic sketch of the yellow laminated shard-rich mud matrix, with the laminae draping coarse pumice clasts. Single laminae are laterally even in thickness, and show minor low angle bedding truncations when draping coarse pumice clasts.

The interstitial matrix grades internally upward through the bed from fine (1-2 cm) pumice clasts at the base to shard-rich mud at the top. The fine pumice matrix occurs

in the lower 25-30 % of the total thickness of unit C and is diffusely stratified with internally massive beds composed of well-sorted, angular to subangular pumice clasts in grain support. The fine pumice matrix is transitional from unit B, however, the beds are much thinner and finer and they lack lithic clasts. Seven metres above the base of the unit is a laterally uneven (0.2-1.5m) and discontinuous interval (Figure 6.7A, 6.7B 6.9C), which is dominated by the diffusely stratified, fine pumice matrix, and contains only sparse, isolated, coarse pumice clasts. The yellow shard-rich mud matrix (Figure 6.9D) in the upper part is laminated, with the laminae contorted around pumice clasts. Single laminae are laterally even in thickness (Figure 6.9E), and show minor low-angle bedding truncations where draping coarse pumice clasts. Glass shards (<1 mm) are the dominant component, with lesser amounts of crystal (<1 mm) and fine pumice (<2 mm) fragments. At the top of unit C, there is an interval approximately 20-90 cm thick of shard-rich mud that lacks the coarse pumice clasts.

The upper contact with the overlying green fossiliferous and bioturbated mudstone is planar and sharp. The thickest and coarsest examples of unit C (~20 m) occur in sections 3 and 4 (Figure 6.5). The unit thins markedly to the east and west of these two sections.

6.5 Depositional setting of the FPB

The presence of bioturbated and fossiliferous mudstone above and below the FPB indicates that it was deposited in a submarine environment. The in situ and intact bivalve shells and burrows in these beds imply deposition in a relatively shallow-water environment, up to a few hundred metres water depth being most likely (Johnson and Baldwin 1986). The presence in the FPB of tabular, massive to graded beds typical of deposits from sediment gravity currents, and the absence of sedimentary structures indicative of wave action (e.g. oscillatory ripples or hummocky cross-stratification) are consistent with a setting below wave base. Sedimentary and volcanic formations overlying the FPB record a transition from this relatively shallow, but dominantly below-wave-base setting to a subaerial environment. Rinaldi and Campos-Venuti (2003) concluded that a pumice breccia unit in the order of 100 m stratigraphically above the FPB, was deposited in water about 50 m deep. Traction-current structures, such as large-scale cross bedding, within both the Papafragas and Sarakiniko Formations indicate deposition above wave

base, and the young phreatic deposits are subaerial.

6.6 Location and character of the FPB source

Given the relatively shallow-water depositional setting, it is plausible that the vent could have been either subaerial or submarine. There are no exposed vent structures nor any obvious bathymetric expressions of a possible submerged vent. Nevertheless, depositional structures, clast textures, and grain-size and thickness variations indicate that the source was submarine and located offshore to the north of the exposures on the north-eastern coast of Milos.

Palaeocurrent indicators (imbricated clasts) measured in units A and B show consistent north-to-south transport directions (Figure 6.10A). The joint pattern in the coarse pumice clasts in units A and B - normal joints along outer margins and internal polyhedral joints - is typical of hot juvenile clasts that have been quenched (e.g. Yamagishi and Dimroth 1985; Kano 1996; Kano et al. 1996). The preservation of quenched margins on the coarse pumice clasts indicates that there was minimal abrasion during transport and deposition, and suggests that the eruption environment and vent were also wholly submarine. The lithic clasts within unit A are significantly coarser in section 5 (Figure 6.1, 6.5 and 6.10B) than elsewhere, regardless of unit thickness or pumice clast size, strongly suggesting that the Pelekouda Peninsular section was closer to the source than other sections. The thickness and maximum pumice clast size of unit C show a different pattern: both increase to a maximum at some distance from the inferred source and then decrease (Figure 6.10C).

Given the palaeocurrent and textural data, we infer that the FPB was produced from a submarine vent. The water depth above the vent is uncertain, but must have been shallower than the ~200 m depth of the depositional setting indicated by contemporaneous sedimentary units. The andesitic and dacitic lithic clasts within the FPB amount to at least 0.1 km^3, perhaps indicating the former presence of a small, lava- and/or dome-dominated, submarine volcanic edifice at the source.

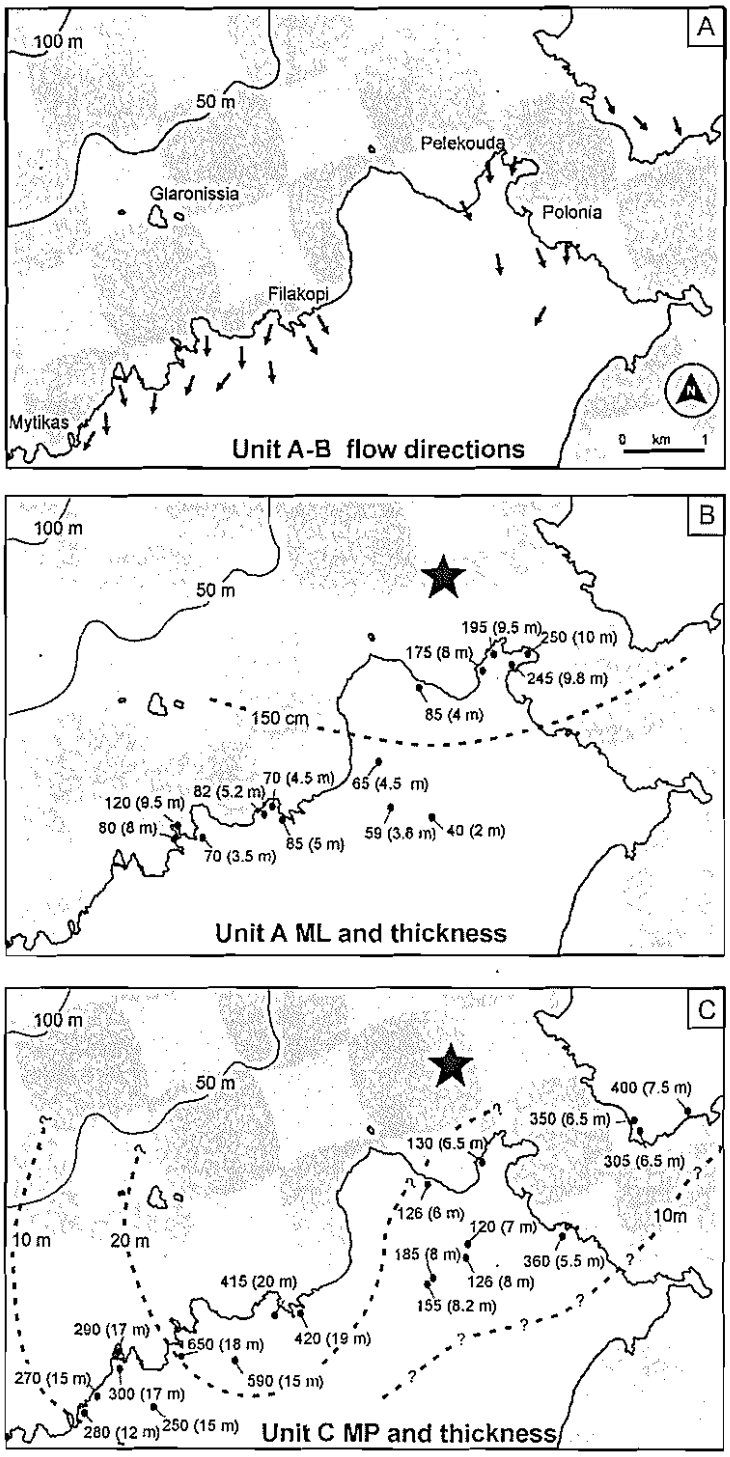

Figure 6.10 Thickness and ML-MP data for selected units of the FPB. All diagrams are at the same scale. **A** Flow direction data for Unit A based on traction structures and imbricated pumice clasts. **B** Unit A bed thickness (m) and ML (cm). **C** Bed thickness (m) and MP (cm) for Unit C. Inferred position for the centre of the FPB source area (black star) based on a combination of thickness and clast size variations for units A and B.

6.7 Origin of pumice clasts in the FPB

The FPB comprises a large volume of juvenile pumice clasts and a small amount of fine (<0.5 mm) glass shards. Felsic pumice can be generated by both explosive and effusive eruptions in subaqueous settings. Submarine felsic domes and lavas are commonly partly pumiceous (e.g. Kato 1987; Scutter et al. 1998). Effusive pumice is, however, typically small in volume (<<1 km^3) and much of that volume is coherent pumiceous lava or else very coarsely fragmented. Only the coarser pumice clasts (up to 6.5 m) in the FPB are comparable in size to pumice clasts produced by spalling (e.g. 8.5 m at Sierra La Primavera, Mexico, Mahood 1980, Clough et al. 1981; up to several metres in diameter from the Tuluman eruption, Reynolds et al. 1980; up to 6 m from the 186 AD Taupo eruption, Wilson and Walker 1985) or explosive submarine eruptions (e.g. 2 m in the Tayu Volcaniclastic Bed E, Kano et al. 1996; ~1 m from the 1952-1953 Myojinsho eruption, Tsuya et al. 1953, Fiske et al. 1998). For effusive pumice, there is in addition a close association with dense to poorly vesicular, coarse clastic and coherent facies of the same composition. In contrast, the coarse pumice clasts in the FPB occur together with a large volume of fine pumice clasts (<64 mm) and glass shards (<0.5 mm), and all three grain sizes were being generated more or less simultaneously. Furthermore, the pumice-rich units of the FPB are intimately associated with coarse lithic breccia that has no parallels in the facies produced by lava or dome eruptions. Hence, we infer that the pumice in the FPB was generated by an explosive, rather than effusive, submarine eruption.

This conclusion is further supported by the vesicularity of the pumice clasts and by lithic clast types in the FPB. The pumice vesicularity (abundance and morphology) is similar to that of pumice clasts produced by magmatic-volatile-driven explosive eruptions (e.g. Houghton and Wilson 1989). The lithic clast population is dominated by lithologies that are not present immediately below the FPB but that occur deeper in the volcanic succession and in the basement. Such clasts are likely to be vent- and conduit-derived accessory pyroclasts generated by explosive disintegration of partly hydrothermally altered, dacitic and andesitic domes and/or lavas at the vent and the underlying metamorphic basement rocks.

The prismatic shapes and subplanar fracture surfaces of pumice clasts in the FPB are distinctive and imply brittle fragmentation. Given the high vesicularities (up to 80 vol. %) of the pumice clasts, brittle fracture could have occurred in response to overpressure in the vesicles (e.g. Sparks 1978; Houghton and Wilson 1989). Unlike the coarse pumice clasts, the finer pumice clasts (<64 mm) lack preserved quenched margins, probably because they were too small for significant differences in temperature to exist between clast margins and core. It is also plausible that many of the fine pumice clasts were generated by explosive or passive disintegration of coarse pumice clasts (e.g. Reynolds et al. 1980; Kano et al. 1996; Allen and McPhie 2000).

The dimensions of the coarse pumice clasts in the FPB exceed those typical of pumice pyroclasts in subaerial pyroclastic deposits (generally <64 mm; e.g. Walker 1971; Sparks 1976). The large size is inferred to reflect the important influence of the submarine setting. Coarse pumice clasts erupted into seawater would be much more likely to survive than those erupted in a subaerial setting. Seawater would greatly reduce the effects of collision and impacts following fragmentation, and during transport and deposition. Also, subaqueous eruption columns may be less energetic than their subaerial counterparts (Cashman and Fiske 1991), diminishing the effects of clast interaction and abrasion within the column. Thus, both the coarse and fine pumice clasts can be accounted for fully by magmatic-volatile-driven explosions.

6.8 Transport and depositional mechanisms

Contact relationships and lithofacies characteristics suggest that the coarse lithic breccia (unit A) and the overlying thickly bedded pumice breccia (unit B) were closely related. First, the coarse lithic breccia grades vertically into the pumice breccia. Second, the pumice and lithic clast types are the same in both units, even though the relative proportions differ markedly. Finally, bed forms in both units imply deposition from laterally moving, high-particle-concentration, gravity currents.

In unit A, pumice and lithic clasts are edge-modified, and very large intraclasts occur at the base. The poor sorting reverse to normal grading and tabular geometry are consistent with rapid deposition of unit A from a high-particle-concentration, lithic-clast-rich gravity current (c.f. Lowe 1976; Postma 1986). Reverse grading at the base could have

been by generated in a lithic clast-concentrated sheared layer, due to either dispersive pressure being greater for coarser clasts (Bagnold 1956) or finer clasts filtering downward between coarser clasts (Middleton 1970). Normal grading in the upper parts of the unit can be attributed to a combination of waning current competence and density-controlled fallout from the suspended load. In terms of geometry, stratigraphic position and thickness, unit A closely resembles coarse lithic breccias present at the base of some other submarine volcaniclastic deposits believed to have been generated directly from explosive eruptions (e.g. Shirahama Group, Cashman and Fiske 1991; Tayu Volcaniclastic Bed E, Kano 1996).

In unit B, the presence of wedge-shaped beds, low-angle truncations of bedding and edge-modified, subangular to subrounded smaller pumice clasts, indicate lateral transport. The poor sorting and division into multiple, very thick, pumice-rich beds that show basal concentrations of dense clasts are consistent with deposition from a series of pumiceous, probably stratified sediment gravity currents. In order for the pumice clasts to be transported by such currents, they must have been denser than water and hence, already waterlogged. Given that hot pumice is more rapidly waterlogged than cold pumice (c.f. Whitham and Sparks 1986; Kato 1987; Cashman and Fiske 1991; Kano et al. 1996), the juvenile character and uniform composition of the pumice, and the strong evidence for continuous aggradation, we conclude that the unit B pumiceous gravity currents were syn-eruptive.

The coarse pumice clasts in unit B have intact quenched margins and it is likely that their long-distance transport differed from that of the smaller, edge-modified pumice clasts. They were probably initially suspended in the water column. Being very hot, they could have generated their own steam carapace, which would have temporarily inhibited water absorption (c.f. Kano et al. 1996). In addition, being very large, water-logging would have been relatively slow. They may then have settled from suspension up-current and been collected by the gravity currents, and/or settled directly into the active currents. Once incorporated, the coarse clasts would have been preferentially affected by lift forces arising from the flow-velocity gradient (e.g. Kano and Takeuchi 1989; Kano 1996), leading to their concentration in the upper parts of beds.

The three distinct grain-size classes in unit C reflect different transport and depositional processes. The reversely graded, well-sorted, grain-supported framework of coarse pumice clasts with intact quenched margins was probably generated by passive settling through the water column. The hot coarse pumice clasts were apparently at least temporarily buoyant. The progressive upward increase in their size resulted from the slower waterlogging, and hence delayed settling, of the coarse pumice clasts relative to the fine pumice clasts. The discontinuous interval that lacks coarse pumice clasts probably represents a slight change in the dispersal direction rather than an interruption to either the supply or settling of the coarse pumice clasts.

The intermediate grain-size class of 1–2 cm pumice that form the matrix within the basal part of unit C are poorly sorted and diffusely stratified, reflecting deposition from relatively dilute, weak traction currents. It is likely that these currents were in fact the waning phase of the pumice-rich gravity currents that formed the thickly bedded pumice breccia of unit B. Hence, the lower part of unit C was generated by two simultaneous depositional processes: settling from suspension (coarse pumice clasts) and weak traction currents (pumiceous matrix). The finest grain-size class (shard-rich mud) in the upper part of unit C consists of very small (<0.5 mm) and low-density grains that would have easily been suspended in water Deposition of this grain-size fraction may have begun at the same time as settling of the coarse pumice clasts in the upper part of unit C and continued for some time after, as it infills interstices in the pre-existing framework of coarse pumice clasts and caps the unit. The combination of fine grain size, delicate laminations and uniform composition imply that no other particle types were available for deposition at this stage.

In subaqueous explosive eruptions, the finest pyroclasts can be incorporated in upwelling plumes of heated water and are typically separated from the coarse fraction by near-surface currents (e.g. Cashman and Fiske 1991; Fiske et al. 1998). The significant volume of shard-rich mud in unit C could indicate that deposition was relatively rapid, before ocean currents redistributed it. Settling of the finest pyroclasts through the water column may have been accelerated by convective instabilities in one or more high-particle concentration layers in the water column (c.f. Carey 1997), greatly reducing the residence time of the suspended load. It is also possible that the FPB was erupted from an area enclosed by islands, possibly a partly submerged caldera, that was sheltered

from both wind and ocean currents, allowing complete deposition of the suspended load.

6.9 The FPB eruption

The large volume of finely fragmented, highly vesicular pumice in the FPB is inferred to have been produced by a submarine explosive eruption driven primarily by vesiculation of the magma within the conduit. Although very little is known about the behaviour of submarine eruption columns, we present a model for eruption and emplacement of the FPB constrained by its textural and lithofacies characteristics and by comparisons with subaerial eruption columns.

The high percentage of vent- and conduit-derived lithic clasts, and narrow range of lithic clast types in unit A, indicate that the opening phase of the FPB submarine explosive eruption involved vent clearing and conduit erosion, probably of a single vent (Figure 6.11A). The eruption may have involved a low and wide basal gas-thrust region (1 in Figure 6.11A), driven by the expansion to ambient pressures of exsolved magmatic gases (c.f. Cashman and Fiske 1991). The gas thrust would have been suppressed by a combination of mixing with seawater and the confining pressure exerted by overlying water column (Cashman and Fiske 1991; Kano 1996). However, given the shallow water depth, it is highly likely that the plume, or at least the central portion of it, temporarily breached the ocean surface during peak discharge (2 in Figure 6.11A). The initial gravity currents were overloaded with dense lithic clasts derived from vent-clearing explosions (3 in Figure 6.11A) but later currents were pumiceous (4 in Figure 6.11B), reflecting open-vent explosivity and rapid waterlogging of abundant fine pumice clasts.

The largest hot pumice clasts would have been buoyant, at least temporarily, and entered a rising buoyant plume, along with the ash (5 in Figure 6.11B). The surfaces of the coarse pumice clasts quenched while their interiors cooled slowly. They may have accumulated at the water surface, forming a pumice raft (6 in Figure 6.11B) that drifted a short distance from the source. Waterlogging affected the finer pumice clasts first and eventually also the coarse pumice clasts, resulting in an upward-coarsening deposit. Initial fallout of coarse pumice was rapid and coincided with the waning stages of gravity-current deposition on the seafloor (7 in Figure 6.11C).

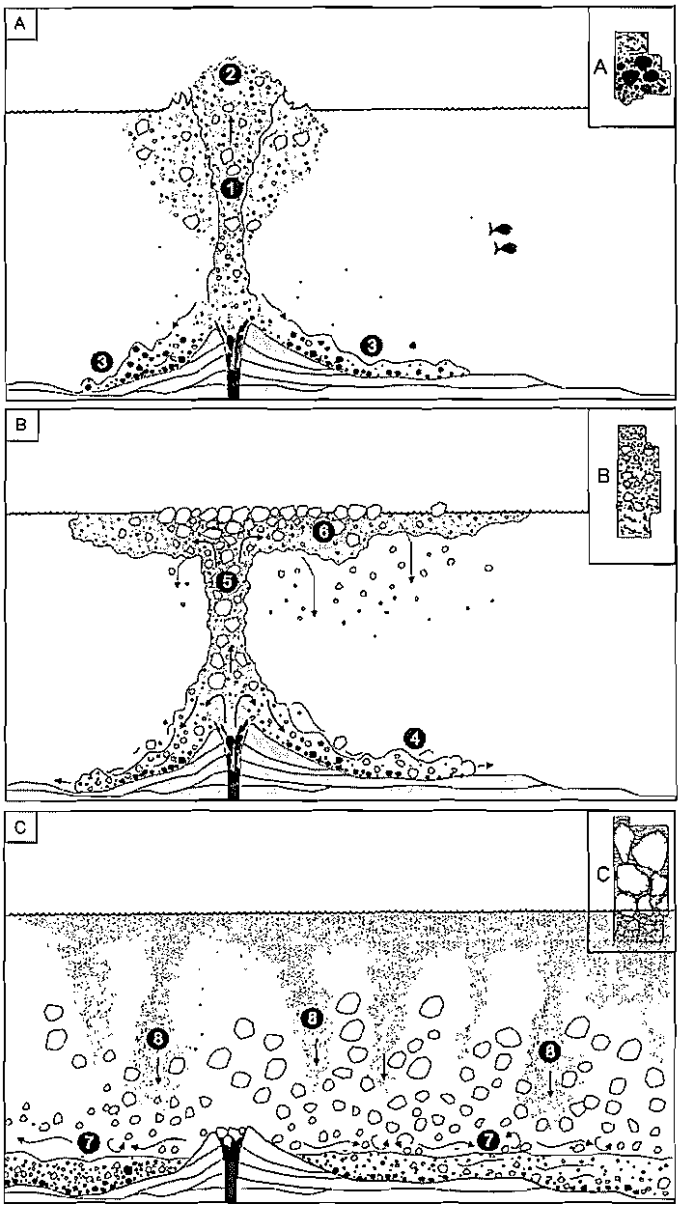

Figure 6.11 Cartoon of the eruption and emplacement of the FPB. The FPB has a minimum bulk volume of 1 km3. **A** Initiation of the submarine explosive eruption of the FPB. Formation of a buoyant plume of hot pumice and ash (1) that may have locally and temporarily breached the sea-air interface (2). Initial gravity currents (3) were lithic-rich, reflecting vent clearing and erosion within the conduit. Insert shows the main features of the coarse lithic breccia (unit A) generated at this stage. **B** Collapse of the pumice-rich eruption plume and formation of pumiceous gravity currents (4) that deposited very thickly bedded pumice breccia (unit B). The buoyant part of the plume (5) of hot pumice clasts and ash ascended to form pumice rafts and ash-laden layers in the water column (6). Insert shows the main features of unit B. **C** The eruption wanes and ends. Dilute traction currents (7) deposited fine (1–2 mm) pumice fragments simultaneously with initial fallout of the coarse pumice clasts. The coarsest pumice clasts settled last, accompanied by deposition of ash, perhaps accelerated by vertical gravity currents (8) that formed from high-particle concentration layers in the water column. Insert shows the main features of unit C.

Vertical gravity currents (8 in Figure 6.11C) may have formed in the water as a result of density-driven convective instabilities in regions or layers where pumice clasts and ash accumulated (c.f. Carey 1997). Downward fluxing of ash increased the effective settling velocities, greatly reducing the residence time of the ash in the water column. The ash would have progressively infilled and eventually covered the framework of freshly deposited coarse pumice clasts on the seafloor.

The lithofacies and textural variations within the FPB relate to a combination of hydraulic sorting and submarine eruption dynamics. The basal coarse lithic breccia (unit A) is coarsest in the more proximal area (section 5), reflecting proximity to vent and the rapid deposition of high-density lithic clasts. Farther from source, suspension settling became increasingly important. Unit C was primarily deposited by this process and it shows a markedly different pattern: the coarse pumice clasts actually increase in grain size and the unit thickness increases away from the source (Figure 6.10C). In this case, the coarsest clasts were the last, rather than the first, to be deposited.

6.10 Products of shallow submarine explosive eruptions

There are important similarities and contrasts between the products of submarine explosive eruptions such as the FPB and of comparable subaerial events (Figure 6.12). To a large extent, the contrasts result from the ambient fluid being seawater rather than air. One of the most conspicuous differences is the much larger size of juvenile pumice clasts in submarine products: in the FPB, these are very coarse (up to 6.5 m), presumably due to enhanced preservation of large pyroclasts erupted and deposited in water and also possibly because magmatic-volatile-driven fragmentation may be less efficient in a subaqueous setting, given the higher confining pressures and reduced rates of decompression.

The basal coarse lithic breccia (unit A) closely resembles the coarse lithic breccias associated with ignimbrites in grain size, componentry, sorting and stratigraphic position at the base of associated pumice-rich flow deposits (c.f. Druitt and Sparks 1982; Walker 1985; Wilson 1985; Allen and Cas 1998). However, unit A exhibits an overall better internal grading than most subaerial co-ignimbrite lithic breccias. Settling rates of dense

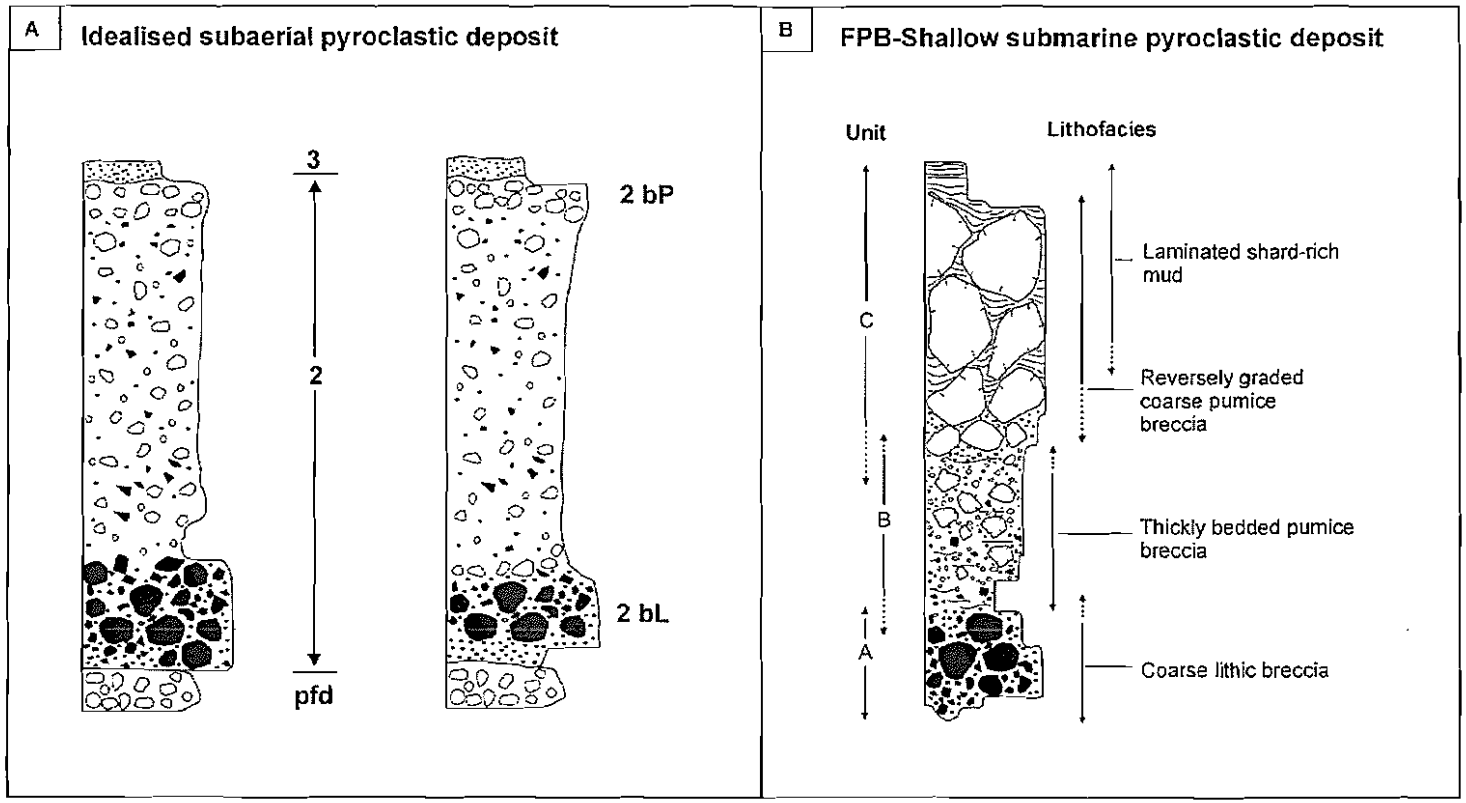

Figure 6.12 Schematic graphic logs comparing the internal organisation of non-welded subaerial pyroclastic deposits (**A**) based on Sparks et al. (1973) and Walker (1985), and the submarine FPB (**B**). Subaerial explosive eruptions commonly produce a pumice fall deposit (pfd) below, and ash fall deposit (layer 3) above, the associated ignimbrite (layer 2). In the FPB, water-settled coarse pumice and ash occur together at the top. Coarse lithic breccia that typically occurs near the base of a subaerial ignimbrite can include a ground layer or layer 2bL, and, in proximal areas, co-ignimbrite lag breccia. A similar pattern is evident in the FPB, the coarse lithic breccia (unit A) being overlain by pumice-rich, gravity-current deposits (unit B).

clasts will be somewhat slower in water-supported than in gas-supported currents, allowing time for separation of larger clasts from smaller clasts during fallout from the suspended load.

Subaerial pumiceous pyroclastic flow deposits (layer 2, Sparks et al. 1973; Figure 6.12A) are characteristically poorly sorted and may show normal grading in dense clasts (2bL) and reverse grading in pumice clasts (2bP), similar to unit B of the FPB. Unit B, however, is conspicuously depleted in ash (<2 wt. %) relative to most pumiceous ignimbrites (20–50 wt. % ash; Sparks 1976). Ash has evidently been separated from the unit B currents during submarine eruption and transport: in water-supported currents, ash can remain suspended much longer than in gas-supported currents, and hence, may be deposited separately from coarser and denser components. The fines-poor nature of unit A may have a similar significance, rather than reflecting current expansion (c.f. Walker 1985).

Another important difference between the subaerial and submarine products of explosive eruptions is the stratigraphic position and significance of fall deposits. In subaerial settings, pumice fall deposits (Figure 6.12A, pfd) reflect discrete periods of buoyant behaviour of the eruption column, in contrast to pyroclastic flow deposits generated during episodes of eruption column collapse. Most rhyolitic pumice is initially less dense than water and, in submarine settings, the deposition of early-erupted pumice will be delayed, with the length of the delay depending on the size, temperature and texture of the pumice (Whitham and Sparks 1986). The delay may result in the early- and late-erupted pumice being deposited together, during later stages of the eruption, and/or after the eruption has ceased. In the FPB (Figure 6.12B), the water-settled coarse pumice breccia (unit C) probably comprises coarse pumice clasts produced throughout the eruption, preferentially concentrated in one bed at the top because of delayed deposition from suspension. In addition, the coarsest and finest pyroclasts occur together in this water-settled fallout layer, in marked contrast to the typically unimodal character of subaerial fallout deposits. In a submarine setting, deposition from suspension of the finest pyroclasts may be accelerated by entrainment in descending particle-rich plumes (c.f. Carey 1997), especially in proximal areas where the water column is likely to be overloaded with suspended particles.

The coarse pumice clasts in unit C in the FPB show well-developed reverse grading. Reverse grading in subaerial pumice fall deposits is commonly attributed to an increase in eruption column height, in response to an increase in eruption intensity (e.g. Self et al. 1986). In submarine pumice-rich fall deposits, grading is not simply related to eruption column height because the fallout of coarse pumice clasts depends on them first being waterlogged and the time required for waterlogging is proportional to the clast size. Thus, reverse grading may be a hallmark of submarine pumice fall deposits, regardless of any trends in eruption intensity. Unit C also differs from subaerial pumice fall deposits in that the coarse pumice clasts become coarser and the unit thickens going from proximal to more distal sections.

6.11 Summary

The FPB was generated by an explosive rhyolitic eruption in a relatively shallow submarine environment. The uniform composition, presence of gravity-current-generated bed forms and lack of evidence of reworking indicate that submarine deposition was probably syn-eruptive. The FPB resembles subaerial pyroclastic deposits in being composed of pumice and lithic clasts and glassy ash, and in the presence of gravity-current and suspension fallout deposits. However, the pumice clasts in the FPB are much larger, and the sorting characteristics and internal stratigraphies differ, all of which reflect the influence of the ambient fluid being seawater rather than volcanic gas or air.

Vent-clearing and conduit erosion at the outset of the FPB eruption ejected a large volume of dense lithic clasts. The initial lithic clast-rich gravity currents generated a coarse lithic breccia (unit A) that is closely similar to co-ignimbrite lithic breccias. Subsequent gravity currents were pumice-rich and deposited a series of very thick, poorly sorted pumice breccia beds (unit B), broadly analogous to subaerial pyroclastic flow deposits. Most of the coarsest and finest pyroclasts were initially suspended in the water column. The coarse pumice clasts settled out of suspension according to size, with the largest clasts settling last because they took longest to become waterlogged. They formed a framework of coarse pumice clasts that was gradually infilled by water-settled, shard-rich ash. Although the water-settled coarse pumice and ash unit (unit C) occurs at the top of the FPB, it probably contains pyroclasts that were erupted throughout the eruption.

The FPB is not unique; several other formations (e.g. the Agios Konstantinos Pumice Breccia) in the submarine succession on Milos show a similar internal stratigraphy and include pumice clasts as large as those in the FPB. We conclude that shallow submarine, felsic explosive eruptions occurred repeatedly and that they generated distinctive facies and facies associations that can be taken as typical of both the setting and style of eruption.

Chapter 7

Subaerial volcanic facies and facies associations of Milos

7.1 Introduction

This chapter is devoted to description and interpretation of the subaerial volcanic facies and facies associations of Milos, in order to complete the facies analysis begun in Chapter 4. Although the subaerial part of the Milos succession is volumetrically minor (~30 vol. %), it is perhaps the best understood, given that significant parts have been the focus of detailed volcanological studies (e.g. Campos Venuti and Rossi 1996; Principe et al. 2002). Results from earlier investigations (e.g. Fytikas et al. 1986; Campos Venuti and Rossi 1996; Principe et al. 2002) are combined with new data on the character, geometry and distribution of the subaerial facies.

7.2 Criteria used to recognise subaerial facies

Three criteria have been implemented for identifying subaerial facies on Milos: (1) presence of palaeosols; (2) the presence of pyroclastic density current deposits (surge deposits and block-and-ash-flow deposits) and; (3) evidence of hot emplacement, such as thermal oxidation and/or carbonised wood and vegetation. In parts of the succession that lack both fossiliferous units (submarine) and palaeosols or pyroclastic density current deposits (subaerial), bedforms and sedimentary structures provide constraints on the setting. For example, very thick, graded sandstone, mudstone intervals containing outsized (>1.5 m) pumice clasts, ripple cross-laminated mudstone and high-angle cross-stratified sandstone have been taken to indicate submarine rather than subaerial depositional settings.

7.3 Facies associations and organisation

Twelve principal subaerial volcanic facies have been identified and arranged into five compositionally and texturally distinct facies associations (Table 7.1 and Figure 7.1). These associations have genetic significance with respect to depositional setting, volcano type, eruption style and proximity to source: (1) the biotite-quartz-phyric rhyolite facies association comprises coherent biotite-quartz-phyric rhyolite and clast-supported monomictic biotite-quartz-phyric rhyolite breccia; (2) the dacite facies association comprises coherent dacite, clast-supported monomictic dacite breccia and bedded monomictic dacite breccia; (3) the andesite facies association comprises coherent andesite and clast-supported monomictic andesite breccia; (4) the pyroclastic facies association comprises matrix-supported coarse breccia, cross-bedded lapilli-ash and bedded ash; (5) the mud-matrix lithic breccia facies association comprises massive schist-rich breccia and polymictic mud-matrix breccia.

Table 7.1 Summary of the principal subaerial facies on Milos

Facies	Description	Interpretation
	Biotite-quartz-phyric rhyolite facies association	
23. Coherent biotite-quartz-phyric rhyolite facies	Evenly porphyritic (10-20 vol. %), euhedral quartz (4 mm) and biotite ± plagioclase (<1 mm) phenocrysts, perlitic and spherulitic groundmass, weakly vesicular (5-10 vol. % vesicles), massive, flow banded, basal columnar joints. Thickness x extent: 40-150 m x 3-4 km.	Coherent facies of lavas
24. Clast-supported monomictic biotite-quartz-phyric rhyolite breccia facies	Monomictic, non-graded, poorly sorted, clast-supported, minor matrix (crystal fragments), gradational contact with coherent biotite-quartz-phyric rhyolite. Thickness x extent: <40 m x <100 m; Clasts: generally 64 mm-1.2 m, locally finer, locally abundant perlitic clasts, angular, equant or slabby clasts, jigsaw-fit and clast-rotated texture. Matrix: minor, rhyolite clasts, crystals and crystal fragments (<2 mm).	In situ autobreccia
	Dacite facies association	
25. Coherent dacite facies	Evenly porphyritic (8-20 vol. %), euhedral plagioclase, quartz and biotite phenocrysts, perlitic or microcrystalline, weakly to non-vesicular, columnar joints, massive, flow banded. Thickness x extent: 50-250 m x <3.5 km.	Coherent facies of lavas and domes

Facies	Description	Interpretation
26. Clast-supported monomictic dacite breccia facies	Monomictic, non-graded, poorly sorted, clast-supported, non-stratified, minor matrix, jigsaw-fit and clast-rotated texture, gradational contact with coherent dacite. Thickness x extent: <50 m x <0.5 km. Clasts: generally 64 mm-1.2 m, locally finer, locally abundant perlitic clasts, angular, equant or slabby clasts, jigsaw-fit and clast-rotated texture. Matrix: minor, dacite clasts, crystals and crystal fragments (<2 mm).	In situ autobreccia
27. Bedded monomictic dacite breccia facies	Monomictic, reversely graded or diffusely stratified, poorly to moderately sorted, clast-supported, , minor matrix, jigsaw-fit and clast-rotated texture, gradational contact with coherent dacite. Thickness[a] x extent: 1.5-8 m x <50 m; Clasts: 2 mm-3.5 m, outsized clasts up to 5 m, massive or flow-banded dacite clasts, mixture of clasts with different textures. Matrix: minor, dacite clasts, crystals and crystal fragments.	Talus breccia (redeposited auto breccia)
	Andesite facies association	
28. Coherent andesite facies	Evenly porphyritic (10-15 vol. %), euhedral plagioclase, hornblende ± pyroxene phenocrysts, groundmass perlitic or microcrystalline, weakly to non-vesicular, columnar joints, massive, flow banded. Thickness x extent: 60-150 m x <3.5 km.	Coherent facies of lavas and domes
29. Clast-supported monomictic andesite breccia facies	Monomictic, non-graded, poorly sorted, clast-supported, non-stratified, minor matrix, jigsaw-fit and clast-rotated texture, gradational contact with coherent andesite. Thickness x extent: 10-60 m x <0.5 km; Clasts: generally 64 mm-1.2 m, locally finer, locally abundant perlitic clasts, angular, equant or slabby clasts, jigsaw-fit and clast-rotated texture. Matrix: minor, andesite clasts, crystals and crystal fragments (<2 mm).	In situ autobreccia
	Pyroclastic facies association	
30. Matrix-supported coarse breccia facies	Non-welded, partly unlithified, polymictic, poorly sorted, basal and upper contacts sharp. Thickness[a]x extent: 0.4–6 m x <2.5 km. Clasts: 2 mm–2 m, angular to subangular, dacitic or andesitic clasts, pumice clasts, scattered lithic clasts (<5 vol. %). Matrix: <1 mm, crystal fragments (mostly feldspar, biotite and hornblende) and angular glass shards.	Block-and-ash-flow deposit

Facies	Description	Interpretation
31. Cross-bedded lapilli-ash facies	White-pale brown to pale purple, non-welded, partly unlithified, low-angle cross-beds, poorly sorted, contacts between beds are sharp and irregular. Thickness[a] x extent: <2 m x <100 m. Lapilli: quartz-biotite-phyric pumice (<15 mm), accretionary lapilli (<6 mm in diameter). Ash: Glass shards (<2 mm) and quartz, biotite crystals and crystal fragments (<1 mm).	Pyroclastic surge deposits
32. Bedded ash facies	White-pale brown to pale purple, non-welded, partly unlithified, massive or laminated, well sorted, mantle topography. Thickness[a] x extent: 10-50 cm x >1 km. Lapilli: clean biotite-quartz-phyric pumice (<10 mm). Ash: Glass shards (<0.5 mm) and quartz and biotite crystal fragments (<1 mm).	Pyroclastic fall deposits
	Mud-matrix lithic breccia facies association	
30. Massive schist-rich breccia facies	Polymictic, non-graded, poorly sorted, matrix- to clast-supported. Thickness[a] x extent: 15-17 m x 12 km^2. Clasts: 10 cm-2 m, hydrothermally altered, angular to subrounded, schist and volcanic clasts (non-juvenile). Matrix: <1 mm crystal fragments (quartz and mica).	Debris-flow deposit
31. Polymictic mud-matrix breccia facies	Polymictic, non-graded, poorly sorted, clasts hydrothermally altered, matrix-supported, tabular beds. Thickness[a] x extent: < 8 m x <1 km. Clasts: 10 cm-3 m, angular to subrounded, schist and volcanic clasts (non-juvenile), variably altered, Roman pot fragments. Matrix: <1 mm crystal fragments (anhydrite and microcrystalline quartz).	Phreatic fall

[a]Thickness ranges refer to beds.

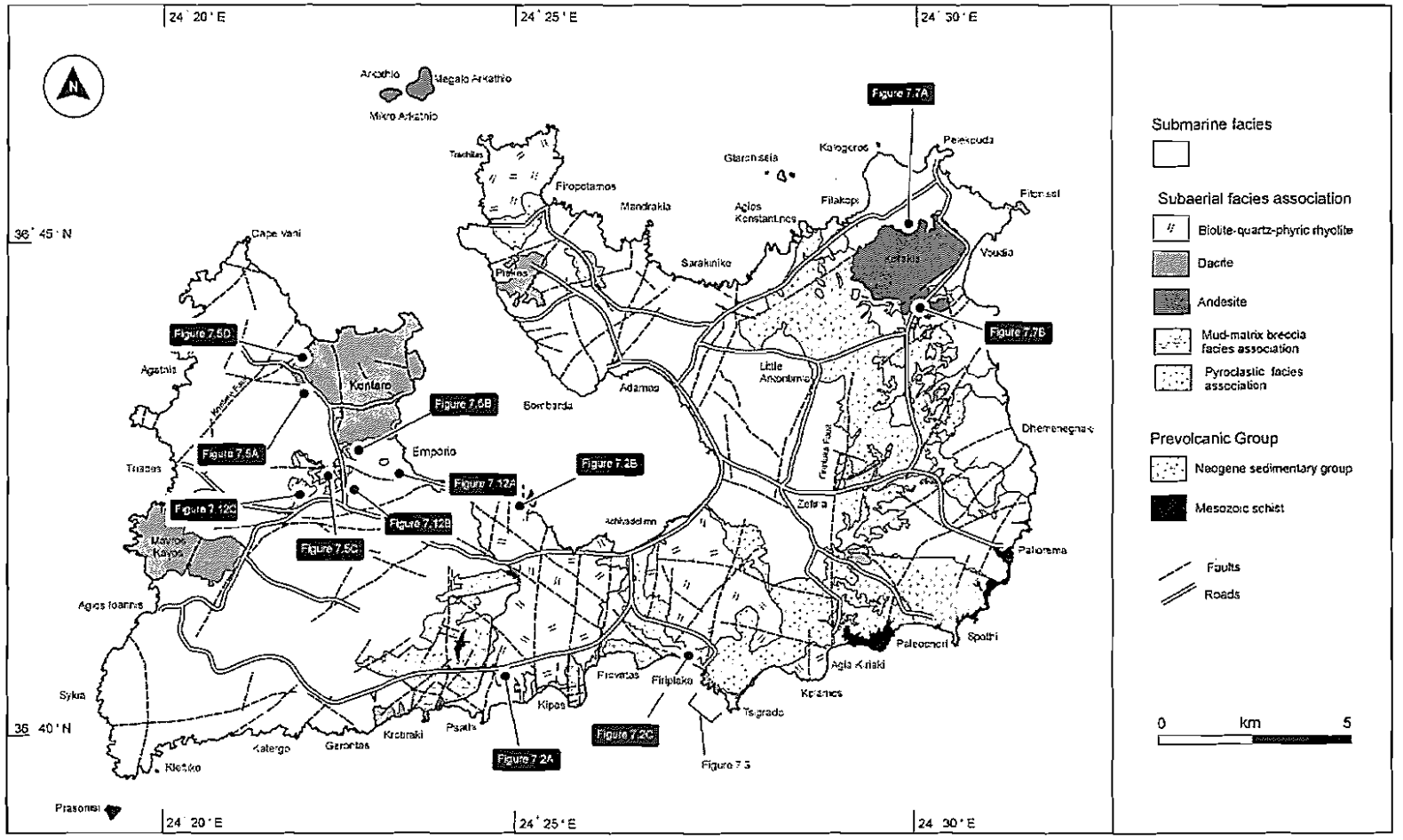

Figure 7.1 Simplified geological map of Milos Island, showing the distribution of subaerial volcanic facies associations. (Modified after Fytikas 1977).

7.4 Biotite-quartz-phyric rhyolite facies association

The biotite-quartz-phyric rhyolite facies association consists of two spatially related facies: coherent biotite-quartz-phyric rhyolite and clast-supported monomictic biotite-quartz-phyric rhyolite breccia. Contacts between the two facies are generally gradational and the breccia facies typically envelopes the coherent facies (Figure 7.2). The biotite-quartz-phyric rhyolite facies association is laterally equivalent to the cross-bedded lapilli-ash and bedded ash facies in the pyroclastic facies association.

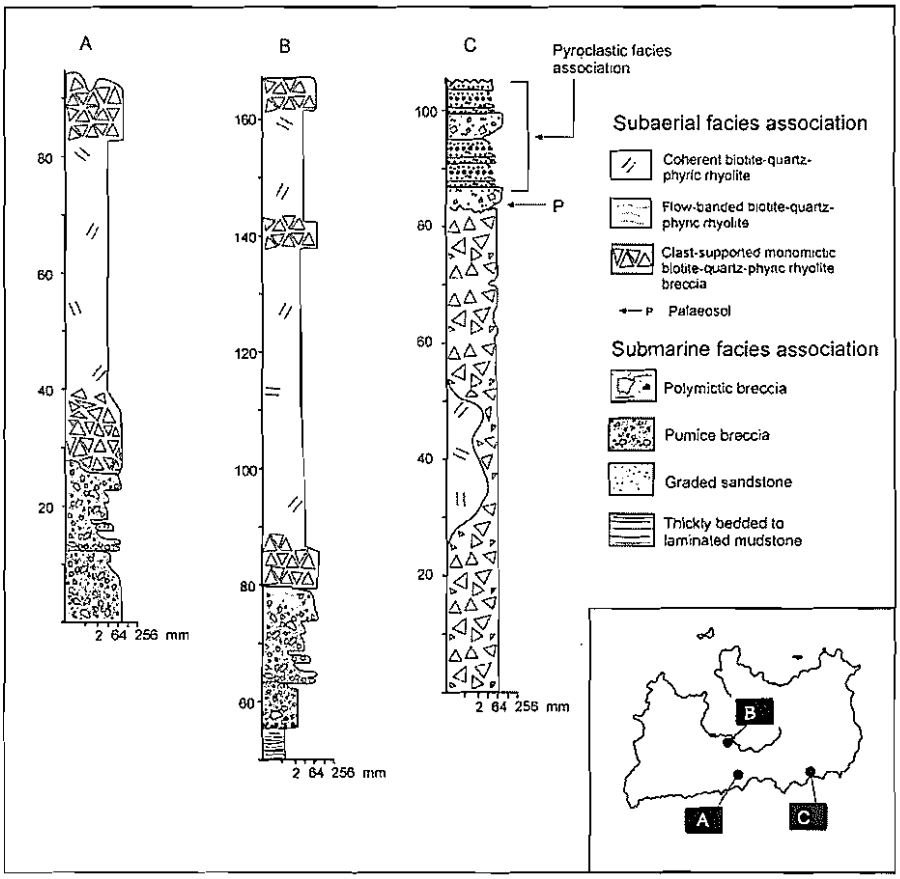

Figure 7.2 Graphic logs for key parts of outcrops at several locations (inset), showing important textures, structures and contact relationships of the two main facies comprising the biotite-quartz-phyric rhyolite facies association. Locations of section on Figure 7.1.

Coherent biotite-quartz-phyric rhyolite facies

Intervals coherent biotite-quartz-phyric rhyolite dominate the southern and northern parts of Milos and are best exposed around the coast of Trachilas and Firiplaka (Figure 7.1). The geometry of units of this facies is broadly tabular, and outcrops are laterally

continuous over an area of 8 km². Intervals of coherent biotite-quartz-phyric rhyolite are typically 40 m thick and range up to 150 m. Single units are thinner near their margins, but few are less than 40 m. The facies is composed of massive to flow-banded, perlitic, biotite-quartz-phyric rhyolite, which may be weakly vesicular (5-10 vol. %).

All the coherent biotite-quartz-phyric rhyolite units on Milos have similar mineralogy, abundance and distribution of phenocrysts, and groundmass characteristics. This facies is relatively coarse grained and characterised by an even distribution of quartz and biotite phenocrysts (10-20 vol. %), and trace amounts of plagioclase, sanidine, zircon and opaques. Quartz phenocrysts (<4 mm) are embayed and round. Biotite (up to 3 mm) and plagioclase (<1 mm) phenocrysts are euhedral. The groundmass is glassy, displaying well-developed classical and banded perlite, and scattered spherulites (<2 mm in diameter).

Figure 7.3 Biotite-quartz-phyric rhyolite facies association. A thick interval of coherent biotite-quartz-phyric rhyolite is enclosed in clast-supported monomictic biotite-quartz-phyric rhyolite breccia east of Tsigardo (location Figure 7.1). Clast-rotated breccia grades through in situ jigsaw-fit breccia into coherent biotite-quartz-phyric rhyolite. Note the well-developed subvertical to inclined joints (red lines) that divide units into elongate masses a few to several metres across. The joints propagate towards the unit interior from both the upper and lower surfaces.

Thick intervals of coherent rhyolite are characterised by well-developed, vertical or locally inclined joints that divide units into elongate bodies a few to several metres across (Figure 7.3), and are more conspicuous near the tops and margins of single units. Columnar joints are rare although they occur sporadically in the basal parts of some units. Tightly folded flow banding is present locally in the basal and marginal parts of coherent intervals. Single bands vary in thickness and are generally discontinuous, with lateral

extents in the order of tens of metres (Figure 7.4A). The bands show no systematic internal variation in thickness.

Figure 7.4 Biotite-quartz-phyric rhyolite facies association. **A** Coherent flow-banded biotite-quartz-phyric rhyolite in the basal part of the Trachilas lava (Figure 7.1). The flow-banded rhyolite is characterised by local, tightly folded, flow banding. **B** Marginal zones commonly consist of bulbous lobes (up to 15 in diameter) of coherent (jointed) rhyolite enclosed by intervals of monomictic biotite-quartz-phyric rhyolite facies at Firiplaka (Figure 7.1). **C** The clast-supported monomictic biotite-quartz-phyric rhyolite is poorly sorted (clasts ranging from centimetres to several metres in diameter) and contains only a very minor component of fine matrix at Firiplaka (Figure 7.1).

At the margins of single units, especially along the upper contacts, the coherent biotite-quartz-phyric rhyolite facies merges into several-tens-of-metre wide intervals of clast-supported monomictic biotite-quartz-phyric rhyolite breccia. These marginal zones are typically poorly defined, chaotic and laterally discontinuous.

Clast-supported monomictic biotite-quartz-phyric rhyolite facies

The clast-supported monomictic biotite-quartz-phyric rhyolite breccia facies envelopes (Figure 7.3), and/or occurs within, the larger units of coherent biotite-quartz-phyric rhyolite facies. Contacts between this breccia facies and the coherent biotite-quartz-

phyric rhyolite facies are highly irregular and vary from sharp to gradational. Thick intervals of clast-supported monomictic biotite-quartz-phyric rhyolite breccia may also include bulbous lobes (up to 15 m in diameter) of coherent (jointed) rhyolite (Figure 7.4B).

This facies is characteristically non-stratified, monomictic, clast-supported, poorly sorted (clasts range from centimetres to several metres in diameter, Figure 7.4C) and contains very little to no matrix. Intervals have a limited extent (up to 100 m) and thickness (typically less than 40 m). The clasts are evenly porphyritic and have the same mineral assemblage and textures as the coherent biotite-quartz-phyric rhyolite facies. The groundmass is glassy, displaying well-developed classical and banded perlite. Most clasts are weakly vesicular (up to 10 vol. %), angular, equant or slabby, and cobble- to boulder-sized (64 mm-1.2 m). The clasts lack normal joints along their margins. The larger clasts (>20 cm) are generally flow-banded.

Two principal breccia types are present within this facies. The first type is characterised by a jigsaw-fit texture, indicating clasts moved little following fragmentation. In the second type, the jigsaw-fit texture is disrupted and flow banding in adjacent clasts has different orientations, implying that rotation and separation of clasts have occurred. In most sections, clast-rotated breccia grades through in situ jigsaw-fit breccia into coherent biotite-quartz-phyric rhyolite. Flow banding in the coherent rhyolite may be continuous into the jigsaw-fit breccia (Figure 7.3).

Interpretation

The coherent biotite-quartz-phyric rhyolite and clast-supported monomictic biotite-quartz-phyric rhyolite breccia facies are closely related and may have gradational contacts. This suggests that these facies are genetically related.

The similarity and gradational contacts between intervals of clast-supported monomictic biotite-quartz-phyric rhyolite breccia and coherent biotite-quartz-phyric rhyolite are consistent with clasts in the breccia being derived from disintegration of coherent biotite-quartz-phyric rhyolite. The shapes and textures of clasts within the clast-supported

monomictic biotite-quartz-phyric rhyolite breccia and local jigsaw-fit are consistent with autobreccia, as documented in subaerial lavas or domes (e.g. Fink 1980; Bonnichsen and Kauffman 1987). Autobreccia results from non-explosive brittle fragmentation of the more viscous parts of a lava flow in response to locally higher strain rates (Fisher 1960).

Although clasts in the clast-rotated monomictic biotite-quartz-phyric rhyolite breccia have undergone separation and rotation, transport distances were clearly limited because the facies is neither stratified nor graded, and the clasts are angular. A gradation from jigsaw-fit to clast-rotated biotite-quartz-phyric rhyolite breccia adjacent to intervals of coherent biotite-quartz-phyric rhyolite indicates that rotation may have been the result of dynamic stressing of the thick, partially solid margin of the associated biotite-quartz-phyric rhyolite lava or dome due to endogenous growth (inflation) (c.f. Fink 1983).

Textures, contact relationships, and the broadly tabular geometry of the biotite-quartz-phyric facies association (covering an area of 8 km^2) are typical of subaerial rhyolitic lavas (c.f. Fink 1983, Bonnichsen and Kauffman 1987) comprising coherent and autobrecciated parts.

7.5 Dacite facies association

The dacite facies association consists of three spatially related facies: coherent dacite, clast-supported monomictic dacite breccia and bedded monomictic dacite breccia. Contacts between the three facies are gradational and the two breccia facies typically occur at the outer contacts of the coherent facies. The subaerial dacite facies association is spatially and temporally related to the submarine dacite facies association (Figure 7.5).

Coherent dacite facies

Intervals of coherent dacite are well exposed at Kontaro and Krotiraki (Figure 7.1). They also occur sporadically through the northern part of the island around Plakes

(Figure 7.1). The coherent dacite facies intervals are thick (50 to 250 m), massive, weakly to non-vesicular and dark grey to purple in colour. They have lateral extents of 5 km. The coherent dacite facies is texturally similar to the submarine coherent dacite facies (section 4.6) and has gradational contacts with the clast-supported monomictic dacite breccia and bedded monomictic dacite breccia facies (Figure 7.5).

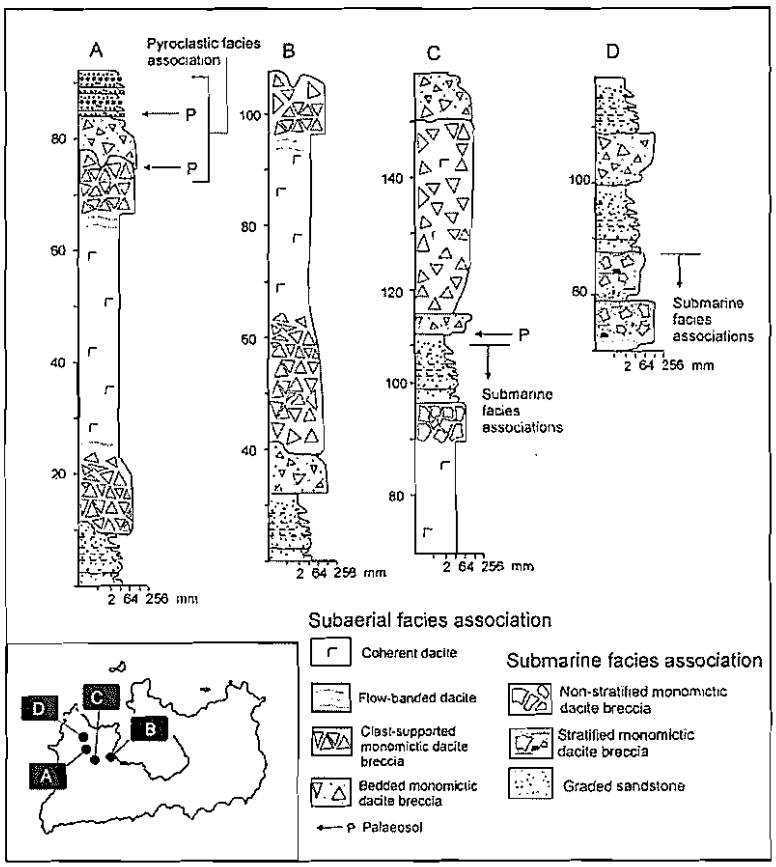

Figure 7.5 Graphic logs for key parts of outcrops at several locations (inset), showing important textures, structures and contact relationships of the three main facies comprising the dacite facies association. Locations of section on Figure 7.1.

The coherent dacite facies is generally moderately porphyritic, containing 8-20% plagioclase, biotite and minor quartz phenocrysts, mainly in the 0.5-2 mm size range. The groundmass is dominated by microlites of plagioclase and opaque phases (65 vol. %) in black glass (20 vol. %). Flow banding occurs in some units, particularly along margins (Figure 7.6A). Where present, the flow bands are approximately parallel to the outer contacts of the units. Single bands vary in thickness, being narrow (mm scale) to relatively wide (cm-m scale) and are generally discontinuous, having lateral extents in the order of tens of metres. At the margins of single units, especially along the outer contacts, the coherent dacite facies merges into several-metre-wide intervals of clast-supported monomictic dacite breccia.

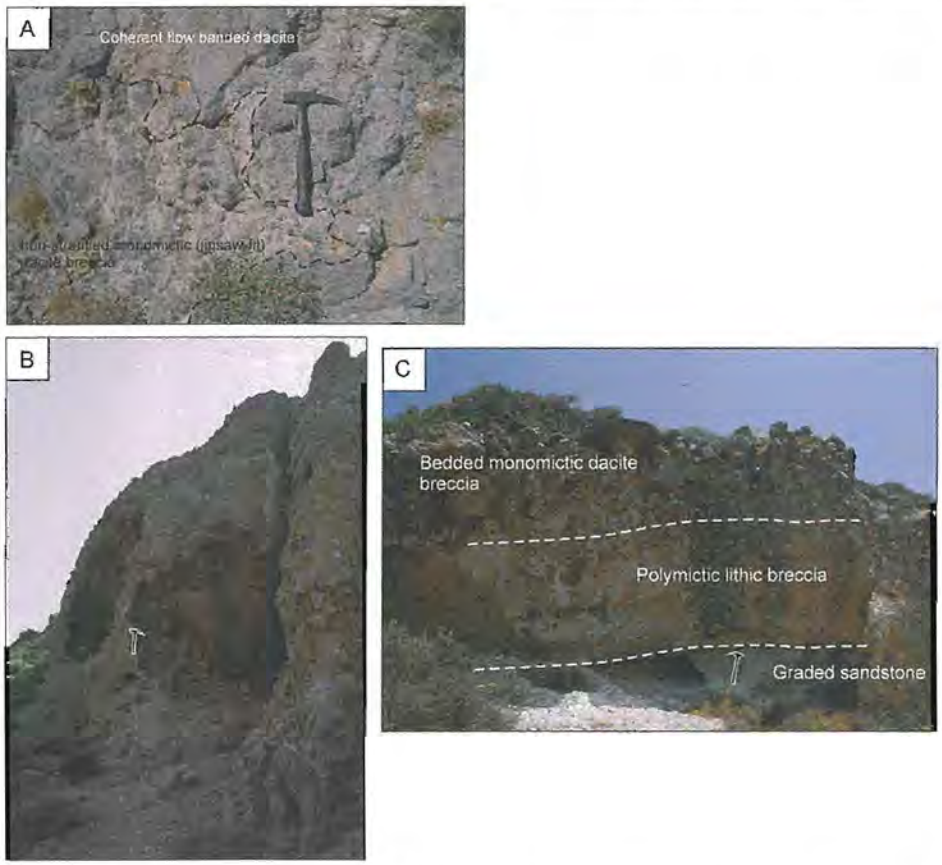

Figure 7.6 Dacite facies association. **A** Coherent flow-banded purple dacite grades into in situ jigsaw-fit clast-supported monomictic dacite breccia. Flow-banding in the coherent dacite is continuous into the clast-supported monomictic dacite breccia. Krotiraki lava dome (Figure 7.1). **B** Massive clast-supported monomictic dacite breccia facies comprises angular, equant or slabby clasts 1-40 cm in diameter. Kontaro (Figure 7.1). **C** Bedded, clast-supported, poorly sorted monomictic dacite breccia. Clasts range from several centimetres to metres in diameter.

Clast-supported monomictic dacite breccia facies

Clast-supported monomictic dacite breccia typically occurs at the margins of or within coherent dacite (Figure 7.6A). Contacts between clast-supported monomictic dacite breccia facies and coherent dacite facies are gradational. Units of this breccia facies are limited in extent (<0.5 km) and thickness (typically less than 50 m thick).

The clast-supported monomictic dacite breccia facies is texturally similar to clast-supported monomictic biotite-quartz-phyric rhyolite breccia facies (section 7.4). Intervals of clast-supported monomictic dacite breccia are massive, non-stratified and vary from clast-supported jigsaw-fit texture (Figure 7.6A) to clast-supported clast-rotated texture (Figure 7.6B). Clasts are evenly porphyritic, containing 8-20% feldspar, biotite

and quartz phenocrysts and may be flow banded and weakly vesicular (up to 20 vol. % vesicles). Compositionally, the fragments in the monomictic dacite breccia are the same as the coherent dacite facies. Clasts are angular, equant or slabby, and cobble- to boulder-sized. The larger clasts (>40 cm) are generally flow-banded. The clast-rotated breccia domains grade through jigsaw-fit breccia into coherent facies. Flow banding in the coherent dacite may be continuous into the jigsaw-fit clast-supported monomictic dacite breccia.

Bedded monomictic dacite breccia facies

This facies is commonly spatially associated with coherent dacite and clast-supported monomictic dacite breccia. The bedded monomictic dacite breccia facies contains clasts with morphologies, textures and compositions identical to clasts in the clast-supported monomictic dacite breccia, with which it has gradational contacts. Intervals of this facies are typically less than 20 m thick and may extend laterally up to 50 m.

Beds of this facies are very thick (1.5-8 m thick), internally diffusely stratified, massive or reversely graded, and wedge-shaped. Single beds consist of poorly to moderately sorted, clast-supported, monomictic dacite breccia composed of massive or flow-banded dacite clasts (Figure 7.6C), and contain a mixture of clasts with different textures. Clasts range from 2 mm to 3.5 m and less commonly up to 5 m and are generally subangular and equant or slabby. Flow-banded clasts are randomly oriented, indicating clast rotation. Basal contacts of beds are sharp or gradational. In a few cases, the facies is totally encased by graded sandstone.

Interpretation

The coherent dacite, clast-supported monomictic dacite breccia and bedded monomictic dacite breccia facies are all closely spatially associated and texturally similar and may have gradational contacts. This suggests that these facies are genetically related.

The shapes and textures of clasts, and local jigsaw-fit in the clast-supported monomictic breccia facies are features consistent with autobreccia which results from non-explosive

fragmentation of viscous lava (Fink and Manley 1987). Autobrecciation occurs due to the more viscous parts of a lava responding to locally higher strain rates by fragmenting into blocky slabs (Fink and Manley 1987).

The bedded monomictic dacite breccia facies contains edge-modified clasts that imply lateral transport. The presence of texturally variable clast types also suggests that some redistribution of clasts occurred following fragmentation. However, transport can only have been very minor, as intervals of this facies are laterally restricted (<50 m). The poor sorting and wedging bedforms are consistent with deposition from gravity-driven grain-flow processes. The bedded monomictic dacite breccia is considered to represent redeposited autobreccia (talus) breccia, analogous to clastic aprons that accumulate at the margins of lavas or domes, either during or following emplacement (c.f. Fink 1983). The presence of intercalated graded sandstone intervals associated with the bedded monomictic dacite breccia indicates that at least some breccias were deposited in a very shallow submarine setting. These breccias are volumetrically minor and represent redeposition of autobreccia initially produced subaerially. They have, therefore been included in the subaerial facies associations.

Facies characteristics, contact relationships and geometries in the dacite facies association are consistent with subaerial lavas and domes (c.f. Huppert et al. 1982; Bonnichsen and Kauffman 1987; Swanson and Holcomb 1990; Sohn 1995).

7.6 Andesite facies association

The andesite facies association consists of two spatially related facies: coherent andesite and clast-supported monomictic andesite breccia (Figure 7.7).

Coherent andesite facies

Coherent andesite is common in the northern part of Milos, at Korakia, and in the cliffs of the Arkadies islands, north of Milos Gulf (Figure 7.1). Single intervals of coherent andesite are typically very thick (60 to 250 m), massive, weakly to non-vesicular and

dark brown or purple in colour. They have lateral extents of several kilometres.

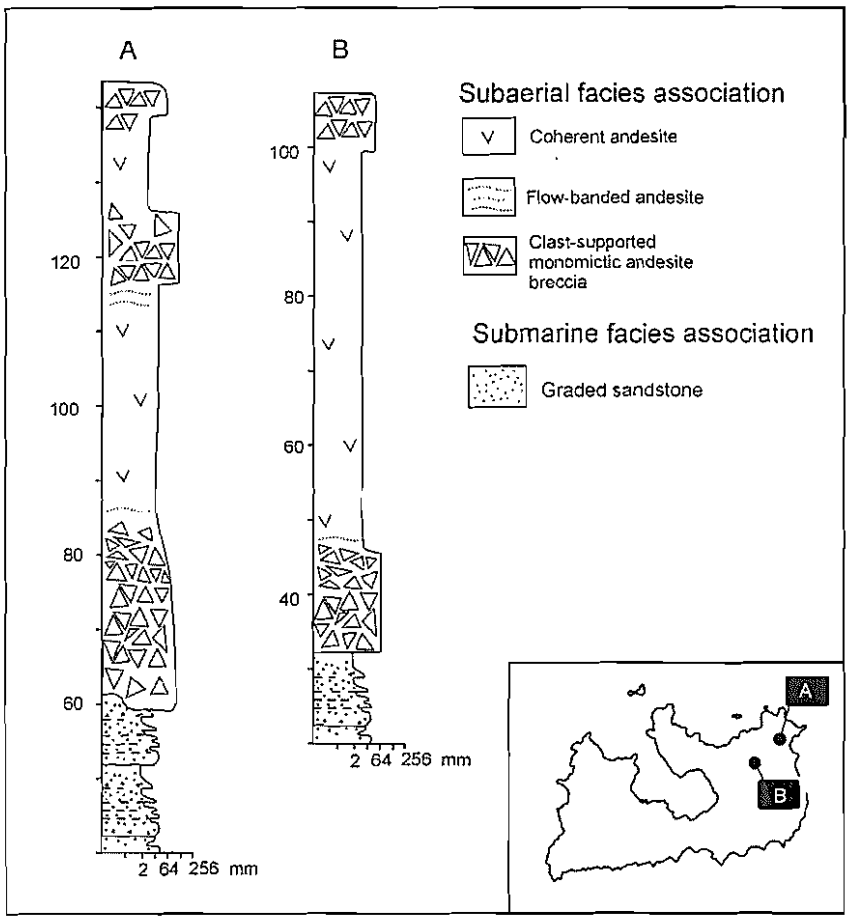

Figure 7.7 Graphic logs for key parts of outcrops at two locations (inset), showing important textures, structures and contact relationships of the two main facies comprising the andesite facies association. Locations of sections on Figure 7.1.

The mineralogy, abundance and distribution of phenocrysts are, in most cases, uniform within a single unit. Intervals of coherent andesite are typically porphyritic (15-20 vol. % phenocrysts). Phenocrysts (<3 mm) are euhedral and distributed evenly throughout a groundmass which is microcrystalline or perlitic. Plagioclase (0.2-3 mm; 10-12 vol. %) and hornblende (1 mm; 5-8 vol. %) phenocrysts are euhedral.

Regular columnar joints characterise thick intervals of massive andesite and margins of units are locally flow-banded parallel to the outer contact. At the margins of single units, the coherent andesite facies merges into several-metre-wide intervals of clast-supported monomictic andesite breccia.

Clast-supported monomictic andesite breccia

Clast-supported monomictic andesite breccia typically occurs at the margins of or within coherent andesite (Figure 7.8). Contacts between clast-supported monomictic andesite breccia facies and coherent andesite facies are sharp or gradational. The breccia facies forms thick (10-60 m) lenses up several hundred metres in length.

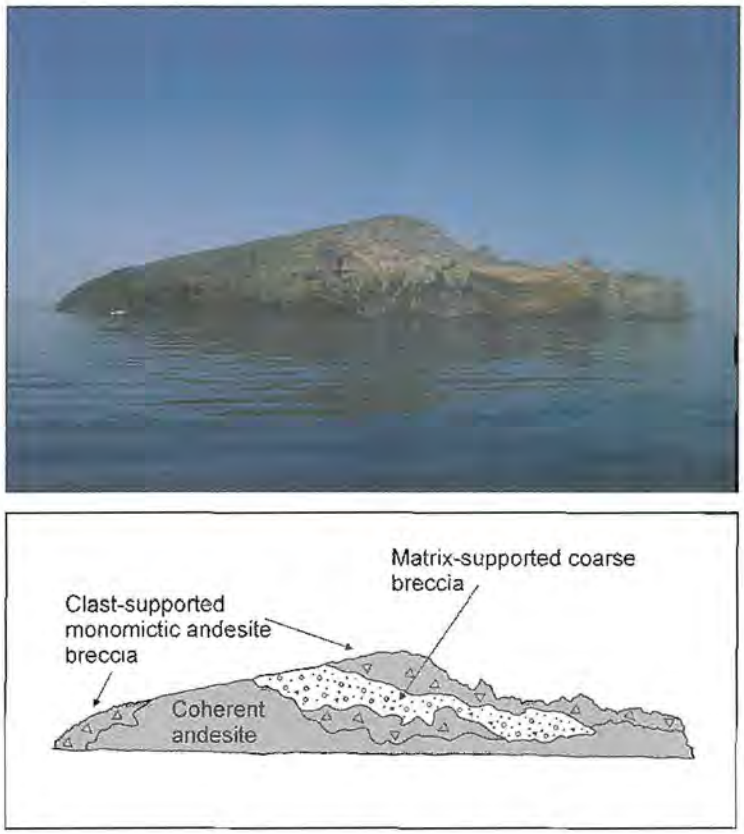

Figure 7.8 Cliff section exposed along the southern coast of Mikro Arkathios island (Arkathio) north of Milos Gulf (Figure 7.1), showing an irregular interval of coherent andesite and gradational relationships with a single thick bed of matrix-supported coarse breccia.

The clast-supported monomictic andesite breccia facies consists of angular, slabby clasts and is characterised by domains of jigsaw-fit and clast-rotated breccia. Only very minor matrix is present in most of the clast-supported monomictic andesite breccia facies. Clasts may be massive or flow-banded. The clast-supported andesite breccia facies is texturally similar to clast-supported monomictic dacite breccia facies and is spatially associated with coherent andesite.

Interpretation

The coherent andesite facies and clast-supported monomictic andesite breccia are closely spatially associated and mineralogically similar and may have gradational contacts, indicating that these facies are genetically related. The clast-supported monomictic andesite breccia facies is interpreted as autobreccia. Facies characteristics, contact relationships and geometries in the andesite facies association are consistent with subaerial lavas and domes (c.f. Walker 1973; Huppert et al. 1982; Swanson and Holcomb 1990).

7.7 Pyroclastic facies association

The pyroclastic facies association comprises some of the youngest volcaniclastic intervals on Milos. The association includes three facies: matrix-supported coarse breccia, cross-bedded lapilli-ash and bedded fine ash (Figure 7.9). The pyroclastic facies association is essentially composed of juvenile pyroclasts (angular, highly vesicular tube pumice clasts, non-vesicular juvenile clasts, glass shards and crystal fragments) generated during relatively small-volume explosive eruptions and/or as a by-product of dome extrusion. On Milos, the pyroclastic deposits occur intercalated with palaeosols, display evidence of thermal oxidation and the basal parts of some pyroclastic intervals contain charcoal fragments, implying hot emplacement and subaerial deposition. Intervals of the cross-bedded lapilli-ash and bedded ash facies are associated with the Firiplaka volcanic centre have been the subject of a detailed study by Campos Venuti and Rossi (1996).

Matrix-supported coarse breccia facies

Beds of matrix-supported coarse breccia facies are common in the northern part of Milos, at Kontaro, and on the islets of Arkadies (Figure 7.1). This facies comprises several non-welded, poorly sorted, very thick (up to 10 m) beds. Intervals of this facies extend laterally up to 2.5 km. Contacts between beds are sharp. Intervals of this facies may be interbedded with cross-bedded lapilli-ash facies, bedded ash facies and palaeosols. The beds are dominantly tabular.

This facies occurs as massive, graded or diffusely stratified, polymictic beds (Figures 7.10A and 7.10B). The main components are of angular to subangular, non- to weakly vesicular (up 30 vol. % vesicles) clasts (2 mm–3 m in diameter), pumice clasts (40-80 vol. % vesicles) and scattered lithic clasts (<5 vol.%) in matrix support. Within beds of this facies, non- to weakly vesicular clasts show an upward increase in size. Non- to weakly vesicular clasts are feldspar- and biotite-phyric, suggesting dacitic to andesitic compositions. Pumice clasts up to 0.9 m across occupy 10-15 vol. %. Pumice clasts are compositionally similar to the denser non- to weakly vesicular clasts and both are considered to be juvenile. Non- to weakly vesicular clasts comprise subangular, and strongly hydrothermally altered, dense plagioclase-phyric dacite and andesite. Other non-juvenile clasts include basement-derived metamorphic (schist) and sedimentary rocks. The matrix is composed of millimetre- to sub-millimetre-sized crystal fragments (mostly feldspar, biotite and hornblende) and angular glass shards. The basal parts of some beds contain charcoal fragments (4-10 mm in diameter).

Cross-bedded lapilli-ash facies

The unconsolidated cross-bedded lapilli-ash facies white to pale brown to pale purple in colour, and characterised by crudely to well defined, low-angle cross-beds and planar stratification. Intervals of this facies are typically less than 100 m thick, although they extend laterally up to several kilometres.

The cross-bedded lapilli-ash facies (Figure 7.10C), displays unidirectional bedforms, such as low-angle cross-stratification, dune bed forms, climbing ripples and chute-and-pool-structures. Single bed sets are <2 m thick. Dune-like bed forms are asymmetrical. Contacts between cross-bed sets are sharp and irregular (Figure 7.10D). In some cases, thin (2-15 cm) cross-laminated units are cyclically interbedded with thin (<10 cm), laterally continuous, beds of accretionary lapilli ash. The accretionary lapilli (<6 mm in diameter) have circular to oval cross-sections and are commonly scattered to closely packed within a matrix of structureless ash. Glass shards (<2 mm) are the dominant component of the cross-bedded lapilli-ash facies, with lesser amounts of quartz and biotite crystals (<1 mm) and fine quartz-biotite-phyric pumice lapilli (<15 mm). The beds also contain coarse, angular to subangular pumice clasts (up to 1.5 m in diameter), and scattered obsidian clasts. Pumice clasts are typically ragged and irregularly shaped.

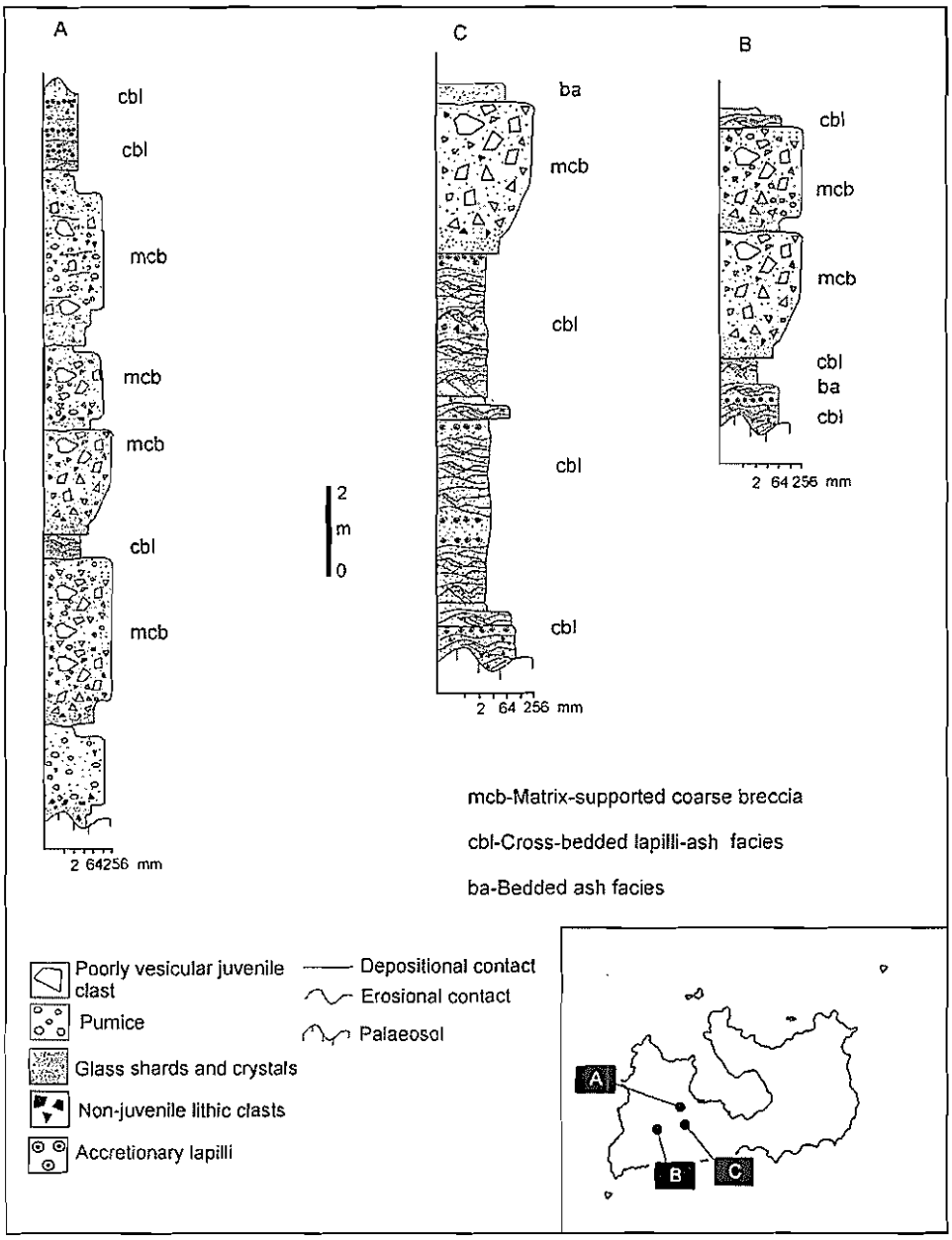

Figure 7.9 Graphic logs for key parts of outcrops at several locations (inset), showing important textures, structures and contact relationships of the three main facies comprising the pyroclastic facies association. Locations of sections on Figure 7.1.

Bedded ash facies

The bedded ash facies is best exposed around southwestern Milos, east of Firiplaka beach (Figure 7.1). This facies is characteristically unconsolidated, massive or planar stratified, well sorted and white to pale brown to pale purple in colour. Intervals of the facies are typically less than 10 m thick, although they extend laterally up to several kilometres (Figure 7.10C). Intervals of bedded ash mantle topography and in some locations, display internal wavy, irregular bedforms defined by pumice lapilli-rich laminae.

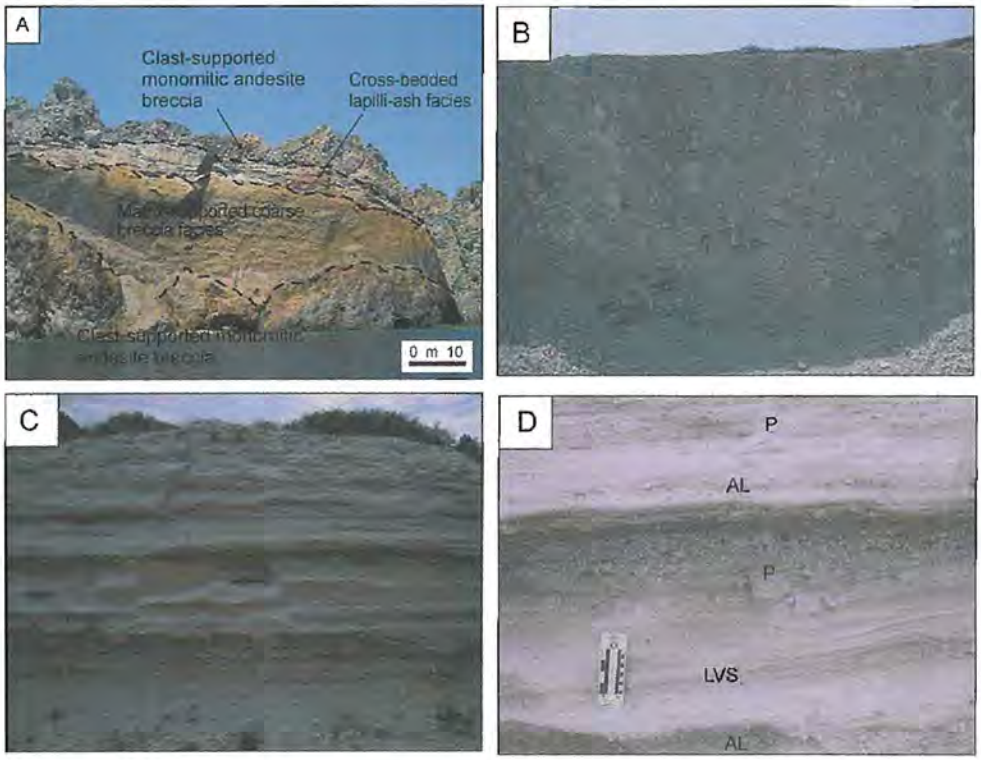

Figure 7.10 Pyroclastic facies association. **A** A thick (<15 m) bed of matrix-supported coarse breccia facies exposed on the eastern coast of Mikro Arkathio Island. The interval is intercalated with cross-bedded lapilli-ash facies and clast-supported monomictic andesite breccia that imply deposition was subaerial. Note the effects thermal oxidation (pink colour) towards the top of the interval. **B** Poorly sorted interval of matrix-supported coarse breccia at Firiplaka. The breccia is mainly composed of angular to subangular, juvenile rhyolite clasts (2 mm–1.5 m in diameter). **C** Outcrop of cross-bedded lapilli-ash and bedded ash facies north of Firiplaka. **D** Close-up view of cross-bedded lapilli-ash and bedded ash facies north at Firiplaka. Massive accretionary lapilli-rich layer (AL), pumice-rich layer (P) and planar bedded ash (LVS).

Glass shards (<0.5 mm) are the dominant component, with lesser amounts of quartz and biotite crystal fragments (<1 mm). Single beds (10-50 cm thick) of the bedded ash facies may also include fine pumice and lithic lapilli, and accretionary lapilli (Figure 7.10D). The fine pumice lapilli (<10 mm) are relatively clean, angular, ragged or blocky in shape, white to grey, biotite-quartz-phyric (<1 vol. % phenocrysts), and moderately to highly vesicular (50-80 vol. % vesicles). Vesicles are spherical to elongate (several mm long and less than 1 mm diameter).

Interpretation

The poorly sorted nature of the matrix-supported coarse breccia, along with the presence of charcoal and abundance of large (up to several metres in diameter), blocky and angular, poorly vesicular juvenile clasts, are features consistent with rapid deposition

from a high-particle-concentration, hot, probably gas-supported gravity current. In terms of texture, components, geometry, volume and thickness, beds of this facies closely resemble coarse block-and-ash flow deposits generated by gravitational collapse of unstable, active lava domes or by dome-related explosive eruptions (Lacroix 1904; Boudon et al. 1993; Yamamoto et al. 1993; Cole et al. 1998; Miyabuchi 1999). Small-volume, block-and-ash flows formed by dome collapse or dome-seated explosions are known to travel as highly concentrated pyroclastic avalanches.

The cross-bedded lapilli-ash facies is interpreted to mainly comprise base-surge deposits, being characterised by unidirectional cross bedding (e.g. Fisher and Waters 1970; Heiken 1971; Waters and Fisher 1971), and comprising glassy ash, pumice and accretionary lapilli units. Rare, thicker (>50 cm), massive, accretionary lapilli layers may represent more sustained periods of phreatomagmatic fallout. Campos Venuti and Rossi (1996) argued that the grain-size characteristics, bedforms, and abundance and morphology of finely fragmented juvenile clasts in this facies at Firiplaka are features consistent with clasts being derived from explosive phreatomagmatic eruptions at felsic subaerial vents.

Single beds of bedded ash are well sorted with mantling bedforms, wide distribution and sheet-like form. The ash shards are clean, angular and blocky in shape. Collectively, these characteristics indicate an explosive origin, and deposition primarily by subaerial fallout (e.g. Self and Sparks 1978; Walker 1983). Wavy, pumice lapilli-rich laminae may indicate wind– or surge-influenced fall. Depositional structures, clast compositions, and grain-size and thickness variations in the cross-bedded lapilli-ash facies and bedded ash facies indicate that the sources were primarily the centres of Firiplaka and Trachilas (Figure 7.1).

7.8 Mud-matrix breccia facies association

The mud-matrix breccia facies association is the youngest volcanic facies on Milos. The association includes two spatially and temporally related facies: massive schist-rich breccia and polymictic mud-matrix breccia. The mud-matrix breccia facies association

mainly occurs in the southeastern sector of the island although there are minor exposures in the north at Triovassalos (Figure 7.1).

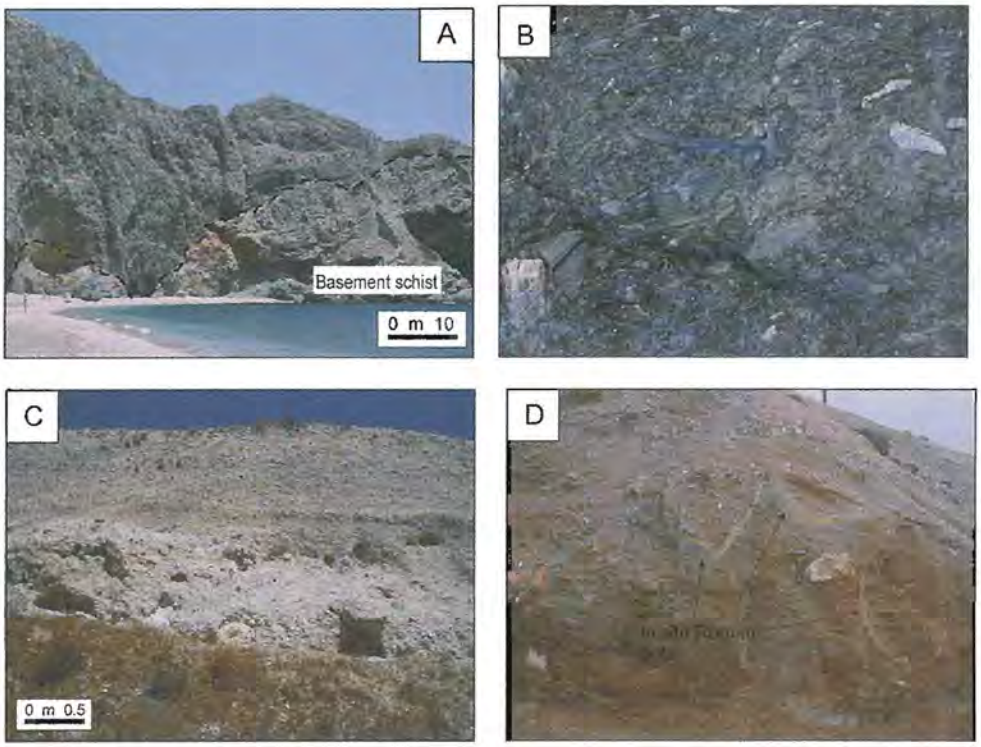

Figure 7.11 Mud-matrix lithic breccia facies association. **A** Spathi headland east of Paliochori Beach, showing the massive, thick (up 17 m), topographically controlled nature of the massive schist-rich breccia facies, southwestern Milos. **B** Close-up of the basal part of the massive schist-rich breccia at Spathi headland , consisting of 90% angular schist and buckey quartz fragments. The closed framework breccia is clast-supported. Principe et al. 2002 considered these outcrops to be the most proximal. **C** A coarse grained, poorly sorted, matrix- to grain-supported interval of polymictic mud-matrix breccia near Triovassalos. The tabular beds are generally less than 8 m thick, and laterally restricted (<1 km). **D** Outcrop of polymictic mud-matrix breccia at Agia Kiriaki beach. The massive, poorly sorted, matrix-supported breccia contains intact and in situ ancient Roman pots. ^{14}C measurements on the Roman pot fragments (Traineau and Dalabakis 1989) indicate that volcanic activity occurred between 200 BC-200 AD.

Massive schist-rich breccia facies

The massive schist-rich breccia facies (equivalent to the 'Green lahar' of Fytikas et al. 1986) is restricted to the southeastern part of Milos. The facies has recently been described in detail by Principe et al. (2002); only a summary is presented below.

This facies comprises a single internally massive, non-graded, poorly sorted, very thick (up to 17 m) bed and covers an area of 12 km^2. The massive schist-rich breccia facies is thickest in topographic lows. The clast- to matrix-supported breccia is mainly com-

posed of schist and buckey quartz fragments (90 vol. %), and minor strongly altered volcanic clasts (10 vol. %, Figure 7.11B). Clasts range in size from centimetres to a several metres in diameter. Coarse clasts (>20 cm in diameter) are generally subrounded, whereas smaller clasts are angular. The matrix is composed of sub-millimetre-sized crystal fragments (mostly quartz, and mica) derived from the basement schist.

The lower contact with the metamorphic basement schist is sharp, and with volcanic units, varies from passive and depositional to strongly erosional (Principe et al. 2002). Very large clasts derived from immediately underlying sedimentary units are present near the base. Basal (0.5-1 m) parts of the bed are finer grained and composed almost entirely of clasts derived from underlying units. The finer grained basal interval is internally massive and highly irregular in thickness. Principe et al. (2002) reported the presence of charcoal at the base of the most proximal sections (Paliochori Beach). The upper contacts of the massive schist-rich breccia are sharp and marked by diffuse stratification.

Polymictic mud-matrix breccia facies

Intervals of polymictic mud-matrix breccia facies are concentrated in the southwestern part of the island, and best exposed in the craters of Little Arkontimia and Anargiroi (Figure 7.1). This facies consists of coarse grained, poorly sorted, matrix-supported lithic breccia (Figure 7.11C and D). It occurs in wedge-shaped beds, generally less than 8 m thick, which are laterally restricted (<1 km). The massive polymictic mud-matrix breccia facies shows significant lateral variations in thickness, geometry, internal organisation and grain size. The facies includes clasts from centimetres to a several metres in diameter, most of which are hydrothermally altered volcanic clasts. Other clasts include schist, Neogene limestone, sedimentary clasts (mudstone and sandstone), opaline silica (sinter) and Roman pottery fragments. Coarse clasts (>20 cm in diameter) are generally subrounded, whereas smaller lithic clasts are angular. The matrix is typically strongly altered and components are often difficult to distinguish. In least-altered sections, the matrix is composed of sub-millimetre-sized crystal fragments of anhydrite and microcrystalline quartz.

Interpretation

The large-volume (covering 12 km^2), poorly sorted massive schist-rich breccia was interpreted by Principe et al. (2002) to represent a lithic-rich debris avalanche deposit. The abundance of hydrothermally altered clasts and absence of a juvenile component prompted Principe et al. (2002) to conclude that the breccia was derived from failure of the metamorphic basement triggered by phreatic explosions. Although the breccia clearly records a catastrophic mass-flow event, neither hummocky morphology nor mega-blocks are present (or preserved) and the internal organisation of the massive schist-rich breccia more closely resembles that of a debris-flow deposit.

The polymictic mud-matrix breccia facies is interpreted to be the product of steam-driven explosive eruptions from subaerial vents because: (1) non-juvenile, hydrothermally altered clasts are the dominant component; (2) hydrothermal mud and silica sinter clasts are common; (3) overall, the facies occurs in laterally restricted beds (<1 km) and comprises a very small volume; and (4) the facies is associated with well-preserved craters in the southwestern sector of the island, known to overlie an active geothermal system. Intact Roman pots (Figure 7.11D) indicate that the debris was emplaced with minimal lateral trajectory. In terms of geometry, volume and thickness, the polymictic mud-matrix breccia facies closely resembles fallout deposits generated directly from steam-driven (phreatic) explosions (c.f. Muffler et al. 1971; Nairn and Wiradiradja 1980; Hedenquist and Henley 1985; Mastin 1991).

7.9 Summary

The subaerial volcanic succession on Milos comprises twelve principal volcanic facies, which have been arranged into five compositionally and texturally distinct facies associations. Sparse palaeosols intercalated with the volcanic facies and the presence of in situ pyroclastic facies (surge and block-and-ash flow deposits) toward the top of the succession collectively constrain the depositional setting as subaerial.

The subaerial facies and facies associations comprise the intercalated products of effusive and explosive eruptions, and post-eruptive resedimentation. They are dominated

by massive, flow-banded and brecciated lavas and domes of rhyolitic to andesitic composition. Among the pyroclastic facies, facies generated by explosive and/or gravitational disintegration of active domes are dominant. The pyroclastic facies association also includes phreatomagmatic surge and fall deposits, and coarse near-vent deposits generated by steam-driven (phreatic) explosive eruptions.

Chapter 8

Volcanic and sedimentary facies architecture of Milos

8.1 Introduction

This chapter focuses on the facies architecture of the Upper Pliocene-Pleistocene volcanic succession of Milos, and is based on recognition of distinctive volcanic facies and facies associations (Chapters 4 to 7). Of importance is the identification of genetically related volcanic facies that represent the proximal, medial and distal parts of single volcanoes. The facies architecture serves as a framework for interpreting the styles of volcanism, types of volcanoes and their locations. This research builds on earlier studies of the stratigraphy, reinterpreting the position and nature of contacts between some of the main volcanic units. The results of this research significantly extend our present understanding of the facies architecture, internal structure and styles of volcanism associated with felsic volcanic islands in arc settings.

8.2 An evaluation of stratigraphic subdivisions and framework

Field mapping and core logging carried out by the author indicate that the previous stratigraphic scheme is broadly correct (Chapter 3). However, several problems with the published stratigraphy are now apparent in the light of the new mapping and SHRIMP U-Pb dates. The volcanic units described by Fytikas et al. (1986) display considerable internal variability and diverse contact relationships. The main stratigraphic units are reinterpreted to comprise one or more of the facies associations described in Chapter 4 and 7, and to have locally conformable, disconformable, and interfingering contacts. There are no mappable regional angular unconformities or disconformities within the volcanic succession and the continuous progression in volcanic construction evident in sections through the succession and from the age dating cannot easily be matched with the four "volcanic cycles" proposed by Fytikas et al.

(1986). Other important deductions from the new results are that some of the units are more widespread than previously considered (e.g. basal pyroclastic series) and that there is no simple west-to-northeast younging of volcanic units through time (Fytikas et al. 1986).

A revised, internally consistent time-stratigraphic framework (Figure 8.1) based on new SHRIMP dates (Figure 8.2) and numerous composite stratigraphic columns (Figure 8.3A-D) shows the geometry and spatial relationships of the volcanic units defined by Fytikas et al. (1986) and highlights the complexity of the stratigraphic relationships. Finally, although some submarine volcaniclastic facies were sourced from subaerial domes, most were generated by explosive and effusive eruptions from shallow submarine vents.

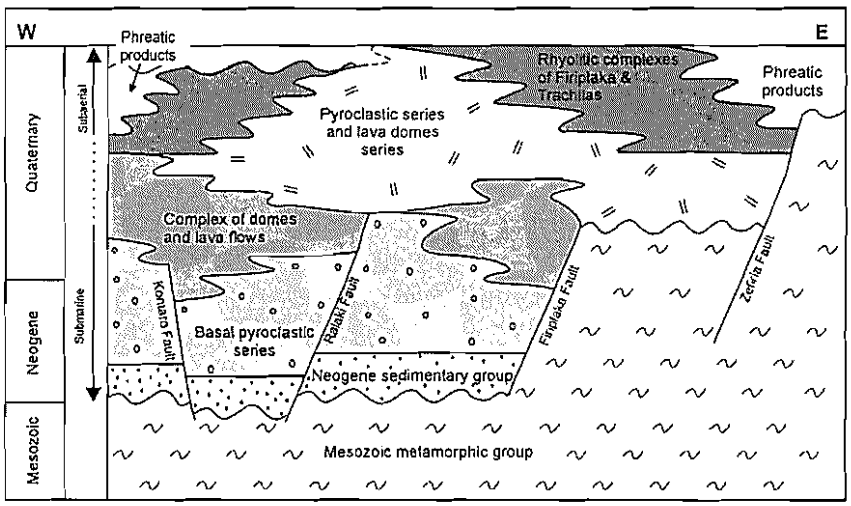

Figure 8.1 Regional time-stratigraphic relationships for the five main volcanic series identified by Fytikas et al. (1986) on Milos.

New SHRIMP U-Pb ages

Fytikas et al. (1976), Angelier et al. (1977), Fytikas et al. (1986), Bigazzi and Radi (1981), Traineau and Dalabakis (1989) and Principe et al. (2002) provided age constraints on the evolution of Milos. Their results indicated that volcanic activity on Milos began during the Late Pliocene (~3 Ma) and continued to relatively recent times (200 BC-200 AD, Chapter 3, Table 3.1, Figure 3.8). However, the timing of shallow submarine volcanism that produced the basal pyroclastic series and subsequent shoaling and subaerial volcanism are poorly constrained. This section presents new results from sensitive

high-resolution ion microprobe (SHRIMP II) analyses of $^{206}Pb/^{238}U$ in zircons undertaken during this study. This new information on the timing of volcanic processes underpins a more accurate geological framework for the volcanic evolution of Milos.

Geological context of samples

Zircon grains were separated and analysed from four samples (MIL 130, MIL 243, MIL 343 and MIL 365) taken from the basal, part of the succession on Milos (Figure 8.2). Sample MIL 130 is porphyritic dacite collected from the coherent dacite facies at Triades, interpreted to be part a submarine lava dome. Sample MIL 243 is porphyritic dacite (coherent dacite facies) from a submarine cryptodome associated with syn-volcanic mineralisation in the Triades area on the western coast of Milos. Sample MIL 343 is a moderately porphyritic dacite collected from the coherent dacite facies of the Kalogeros cryptodome (Chapter 5) on the northern coast of Milos. Sample MIL 365 is a juvenile rhyolitic pumice taken from the Filakopi Pumice Breccia (Chapter 6).

Methods

Sample preparation and analyses were carried out at the Australian National University, Canberra, Australia, by Dr Marc Norman. Heavy-mineral concentrates were obtained from pulverised samples (typically varying in weight from 0.5 to 3 kg) using standard density and electromagnetic separation techniques. Zircons from all samples were mounted in epoxy, together with several chips of the FC1 and SL13 reference zircons, and polished for inspection and SHRIMP analysis. Backscattered electron (BSE) and cathodeluminescence (CL) images of all zircon crystals analysed were acquired with a scanning electron microprobe (SEM) to provide information about the internal structure of the sectioned grains and to target specific areas within the zircons suitable for determining the magmatic crystallisation age of crystals.

U-Pb isotopic analyses of the zircons were made using the SHRIMP RG. Zircon grains were selected at random for analysis, and in most cases all suitable grains were analysed. The data were collected during several 24-hour sessions; with each analysis consisted of six scans through the mass range. The data have been reduced in a manner similar to that described by Williams (1998, and references therein), using the SQUID Excel Macro of Ludwig (2000). The Pb/U ratios have been normalised relative to a value of 0.1859 for the 206Pb/238U ratio of the FC1 (Duluth Gabbro) reference zircons,

equivalent to an age of 1099 Ma (Paces and Miller 1993). Uncertainties given for single analyses (ratio and ages) are at the 1 σ level, however, the uncertainties in calculated weighted mean ages are reported as 95% confidence limits and include uncertainties associated with the reference zircon FC1.

Table 8.1 A summary of SHRIMP U-Pb ages

Sample number	Sample description	Crystallisation age (Ma)
MIL 130	Coherent dacite facies, Triades	1.44 ± 0.08
MIL 243	Coherent dacite facies, Triades	2.18 ± 0.09
MIL 343	Coherent dacite facies (Kalogeros cryptodome)	2.70 ± 0.04
MIL 365	Filakopi Pumice Breccia	2.66 ± 0.07

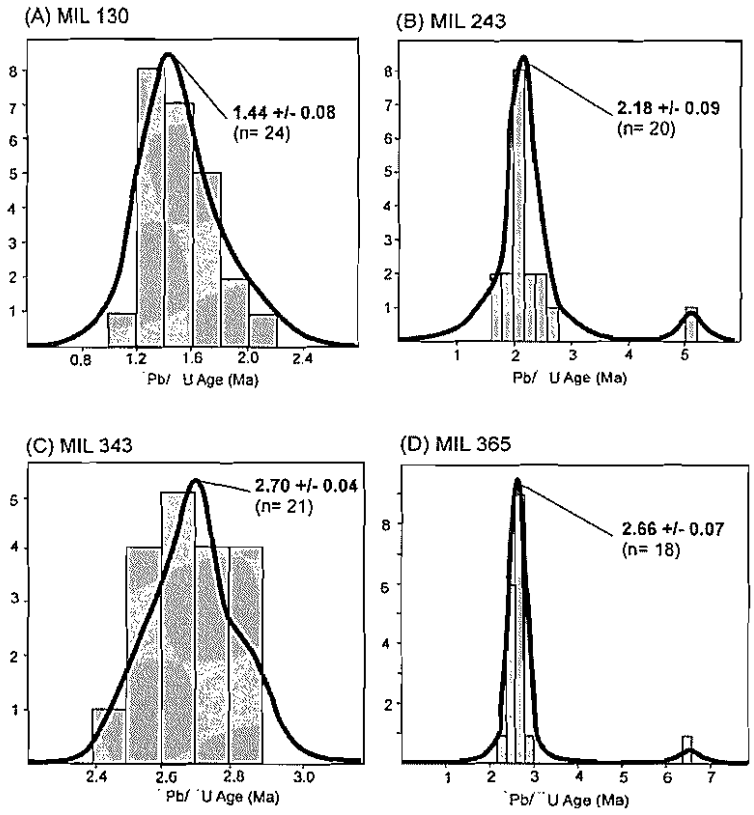

Figure 8.2 U-Pb SHRIMP data for the four samples plotted on probability plots. **A** Sample MIL 130 is porphyritic dacite. Twenty-four analyses form a single age population with a weighted mean age of 1.44 ± 0.08 Ma. **B** Sample MIL 243 is porphyritic dacite. Twenty analyses form a single age population with a weighted mean age of 2.18 ± 0.09 Ma. **C** Sample MIL 343 is a moderately porphyritic dacite. Twenty-one analyses form a single age population with a weighted mean age of 2.70 ± 0.04 Ma. **D** Sample MIL 365 is juvenile rhyolitic pumice taken from the Filakopi Pumice Breccia (Chapter 6). Eighteen analyses form a single age population with a weighted mean age of 2.66 ± 0.07 Ma.

Results

Each of the four dated zircon separates contains abundant equant to elongate grains, with euhedral pyramidal terminations. Some of the grains are fragments of what were originally doubly terminated crystals and appear to have been modified by post-crystallisation processes, giving rise to ragged or serrated grain outlines. Between 18 and 24 analyses were obtained per sample (Appendix B). All samples show a relatively simple age population which is interpreted to reflect the time of magmatic crystallisation. Virtually all of the zircons analysed contained significant amounts of common Pb, a feature not uncommon in mineralised terrains (Norman 2002). SHRIMP data for all four samples are presented in Appendix B and summarised in Table 8.1 and Figure 8.2.

Basal pyroclastic series

At its thickest, near Profitis Illias (Figure 8.3A-section E), the basal pyroclastic series comprises thickly bedded rhyolitic and dacitic, syn-eruptive pumiceous units (pumice breccia facies association) and volcanic breccias (polymictic breccia facies), intercalated with bioturbated and fossiliferous mudstone and graded sanstone. The abundance of bioturbated and fossiliferous sedimentary units and graded volcaniclastic mass-flow units, and the presence locally of turbidites (grade sandstone), indicate a marine environment of deposition. The in situ and intact bivalve shells and burrows in these beds imply deposition in a relatively shallow-water environment, up several hundred metres water depth being most likely (Chapter 6).

In the southwest, between the Kontaro and Kleftiko Faults (Figure 8.1), particularly in the Profitis Illias and Chondro Vouno area, the upper part of this series has been previously mapped as "pyroclastic flow deposits" (e.g. Fytikas 1977; Fytikas et al. 1986). Although rich in pumice (>90 vol. %) that is most likely pyroclastic in origin, there is no textural evidence preserved in the facies for hot emplacement. Altered pumice clasts are compacted, defining a bedding-parallel foliation. However, unaltered or less altered pumice clasts are randomly oriented, and uncompacted. Hence, the foliation is interpreted to be the result of compaction during diagenesis (c.f. Allen 1990; Gifkins and Allen 2001) rather than welding (eutaxitic foliation).

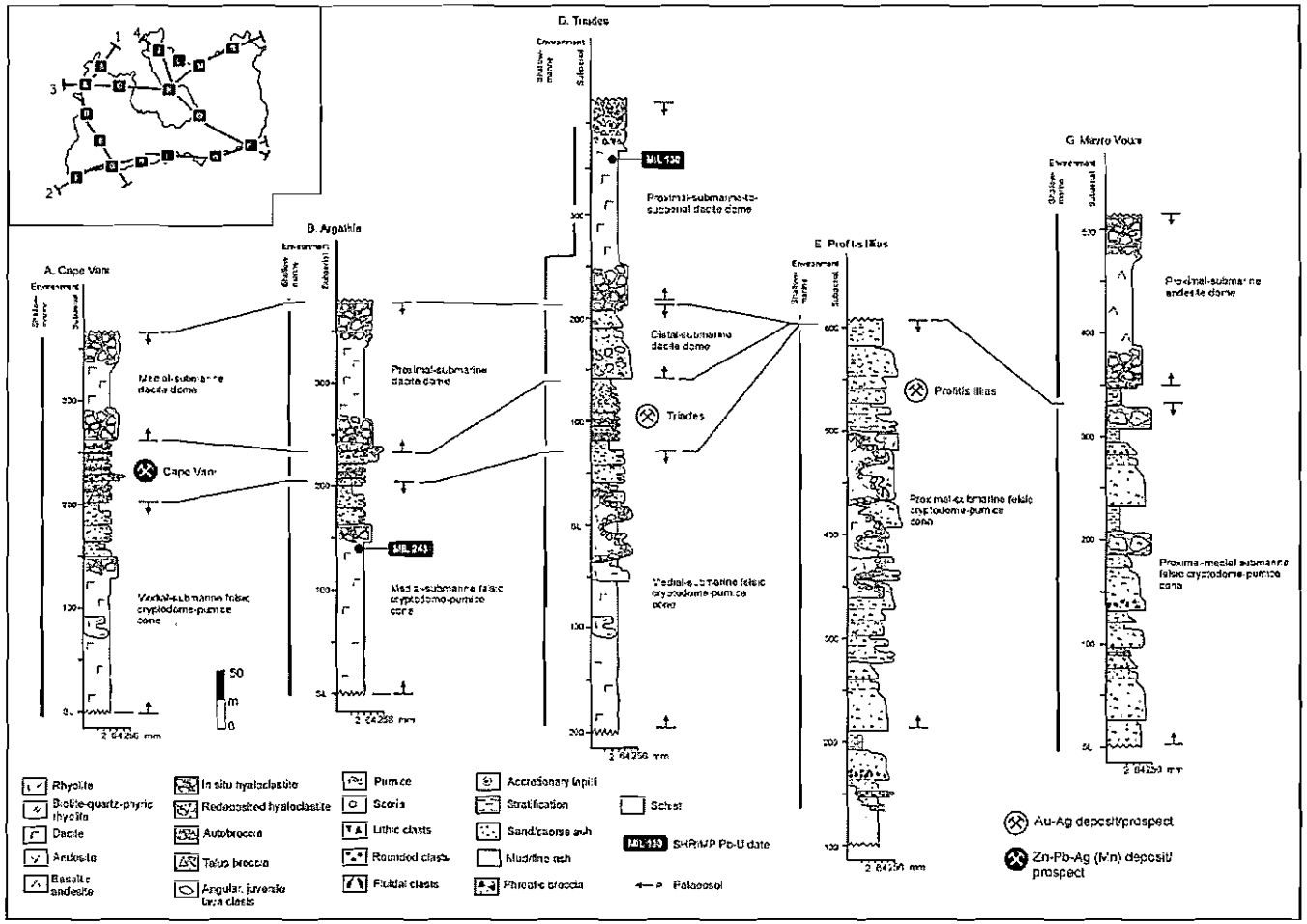

Figure 8.3A Stratigraphic columns for Milos along transect 1 (inset), showing contact relationships, vertical distribution of facies associations and interpreted environments of emplacement. Thicknesses shown are calculated true thickness. Locations of the columns are shown in the map.

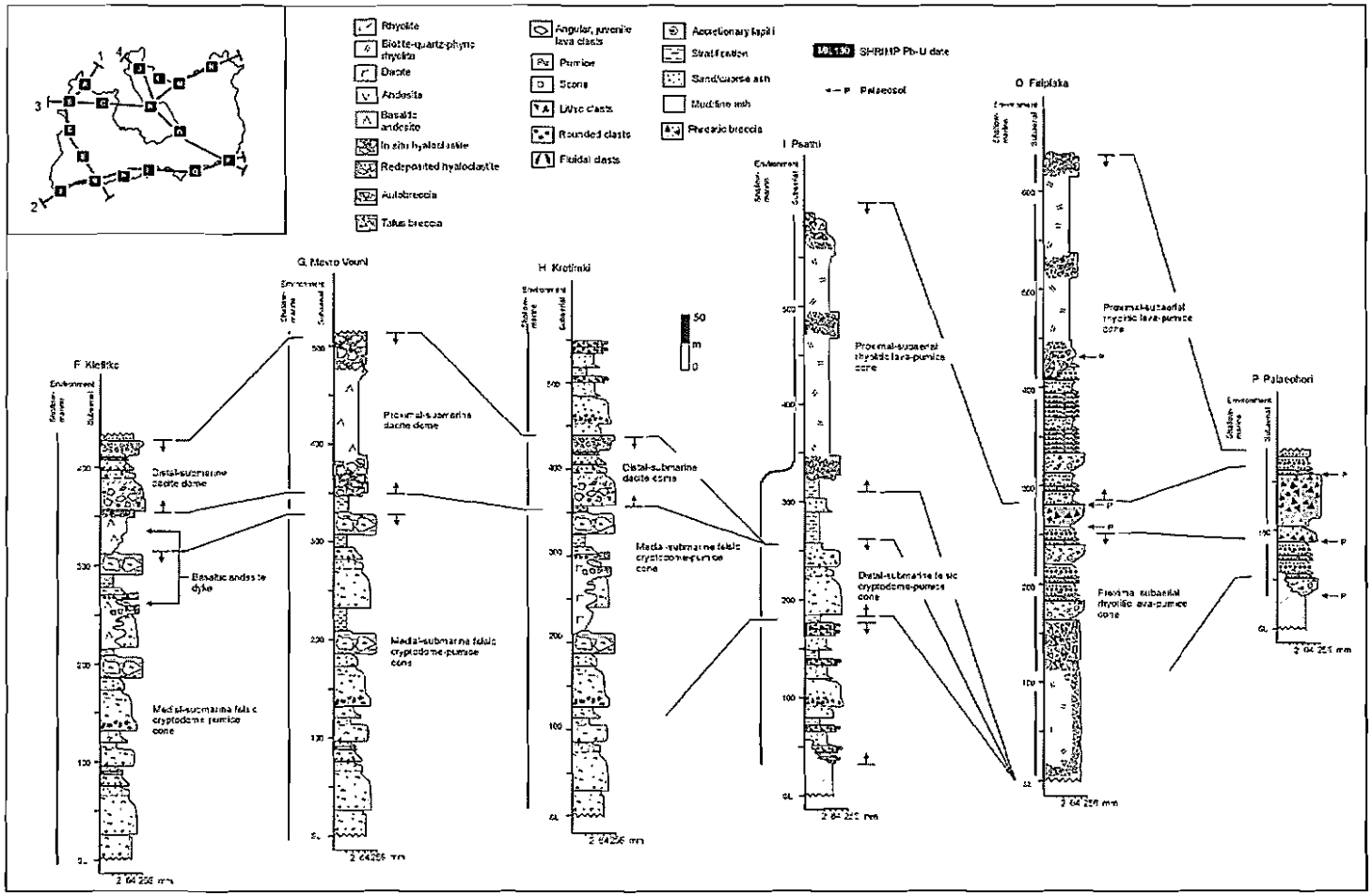

Figure 8.3B Stratigraphic columns for Milos along transect 2 (inset), showing contact relationships, vertical distribution of facies associations and interpreted environments of emplacement. Thicknesses sown are calculated true thickness. Locations of the columns are shown in the map.

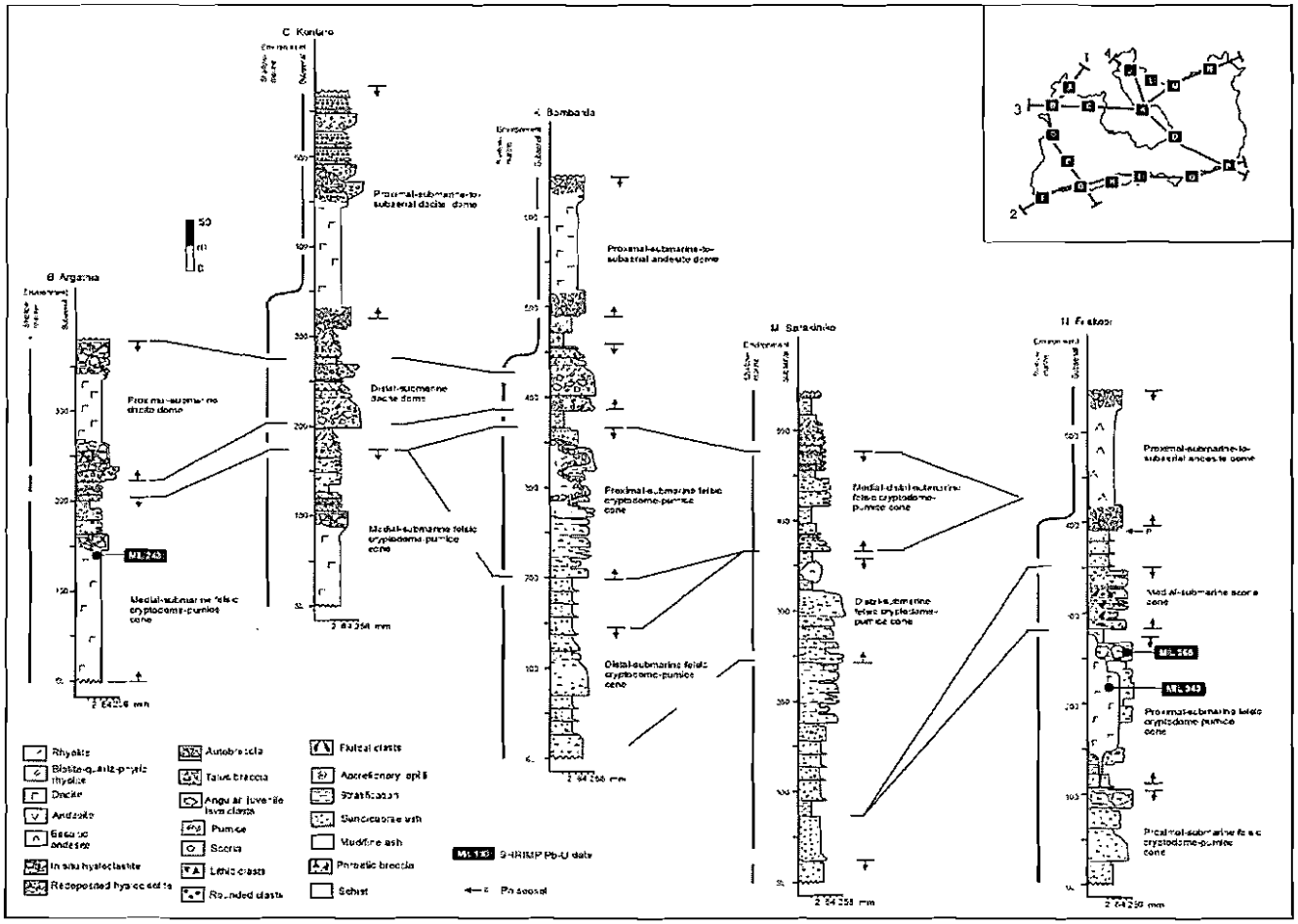

Figure 8.3C Stratigraphic columns for Milos along transect 3 (inset), showing contact relationships, vertical distribution of facies associations and interpreted environments of emplacement. Stratigraphic thicknesses are calculated true thickness. Locations of the columns are shown in the map.

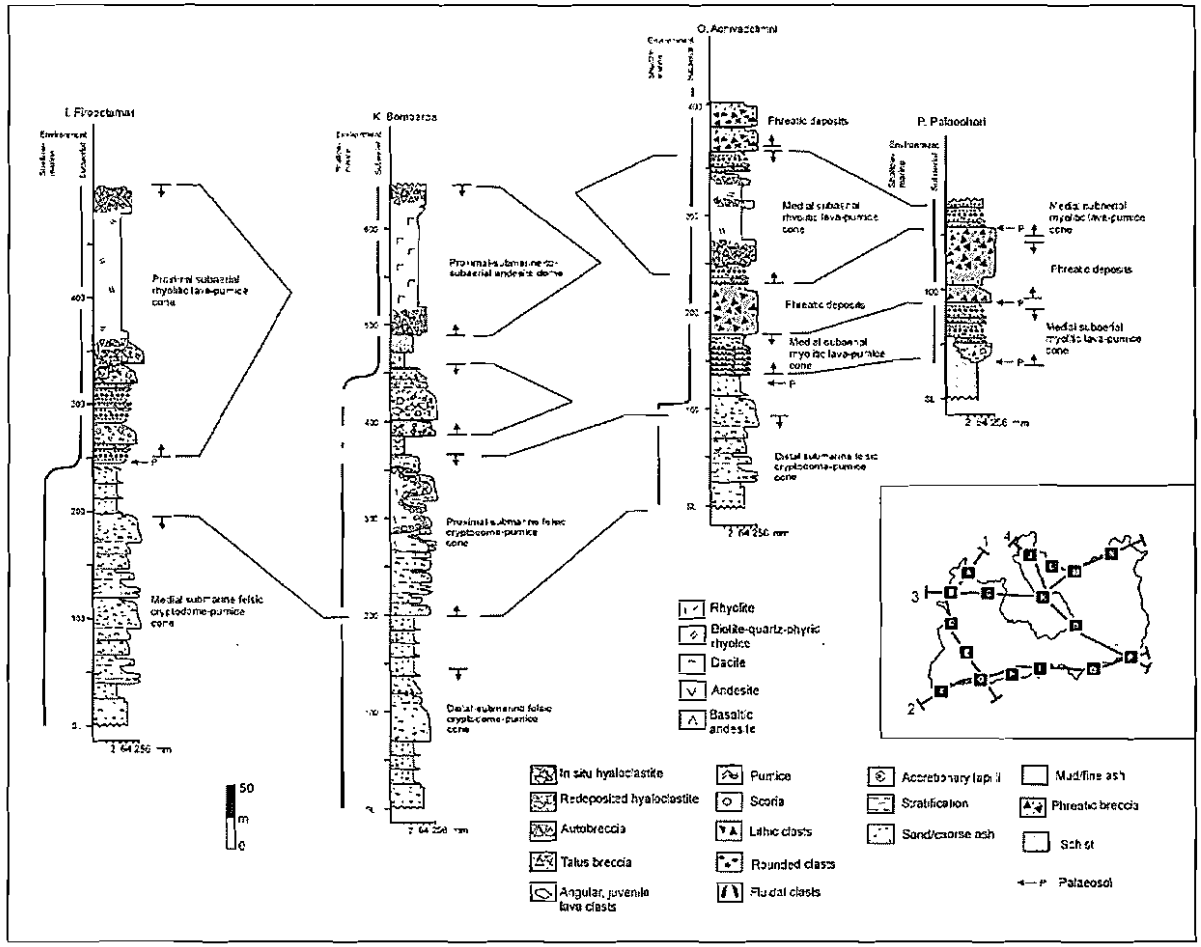

Figure 8.3D Stratigraphic columns for Milos along transect 4 (inset), showing contact relationships, vertical distribution of facies associations and interpreted environments of emplacement. Thicknesses shown are calculated true thickness. Locations of the columns are shown in the map.

A new informal stratigraphic unit in the basal pyroclastic series is the Pahina Formation in the north, containing the Filakopi Pumice Breccia and Agios Konstantinos Pumice Breccia (Chapter 6). Overlying basaltic-andesite units (Fytikas et al. 1986) around Kleftiko are excluded in this study from the basal pyroclastic series and incorporated into the overlying complex of domes and lava flows. In the south and west (east of the Firiplaka Fault), the basal pyroclastic series unconformably overlies the Mesozoic metamorphic basement, both conformably and unconformably overlies the Neogene sedimentary group and is intruded and conformably overlain by the complex of domes and lava flows (Figure 8.1). The basal pyroclastic series hosts most of the precious and base metal ores, including the Profitis Illias, Chondro Vouno, Triades and Cape Vani deposits.

The age of the basal pyroclastic series is relatively poorly constrained. The series contains marine fossils that are consistent with a Late Pliocene age (c.f. Fytikas et al. 1977). A K-Ar date on a non-juvenile rhyolite clast from the base of the series suggests a maximum age of 3.08 ± 0.14 Ma. U-Pb in zircon dating of the Filakopi Pumice Breccia provides an upper age limit for the unit at about 2.66 ± 0.07 Ma (Table 8.1).

Complex of domes and lava flows

Fytikas et al. (1986) defined the complex of domes and lava flows as comprising dominantly subaerial intermediate lavas, domes and associated autoclastic facies. However, this study has shown that the group includes several significant submarine felsic intrusions (mostly in the rhyolite and dacite facies association), such as the Kalogeros cryptodome at Kalogeros (Chapter 5).

The discovery of major felsic syn-volcanic intrusions significantly extends the compositional range of the complex of domes and lava flows (Fytikas et al. 1986), and indicates that a period of intrusion-dominated activity followed the explosive volcanism that produced the basal pyroclastic series. On a regional scale, the rhyolitic and minor dacitic intrusions make up a substantial part of the succession and are spatially and temporally associated with epithermal mineralisation.

The thickness of the complex of domes and lava flows is extremely variable, ranging up to a maximum thickness of 150 m between the Kontaro and Ralaki faults in the Triades area (Figure 8.3A-section B and C). The sedimentary facies within the complex of domes and lava flows contain marine fossils. Intrusive hyaloclastite provides evidence for interaction of magma or lava with wet unconsolidated sediment at the contacts of shallow intrusions and lavas. The widespread occurrence of thick intervals of mudstone suggests that most of the succession accumulated below storm wave base. Depth of storm wave base varies in modern environments range from 10 to 200 m. Locally, and towards the top of the complex of domes and lava flows, traction current structures indicative of wave activity (e.g. cross-bedding) are present, as are block-and-ash flow deposits (pyroclastic facies association) implying that at least in some areas, this group was partly subaerial (Figure 8.3C-section C).

New informal stratigraphic units in the complex of domes and lava flows include the Papafragas Formation and the Kalogeros Dacite (Chapter 5) in the north. SHRIMP U-Pb zircon dating of the Kalogeros dacite cryptodome within the complex of domes and lava flows on the northern coast, has given an age of 2.70 ± 0.04 (Table 8.1; Figure 8.3C-section N). Taking analytical error into consideration, the Kalogeros cryptodome is approximately contemporaneous with the Filakopi Pumice Breccia. SHRIMP U-Pb zircon dating of a dacite intrusion, stratigraphically mid-way through the complex of domes and lava flows at Triades on the western coast, has yielded an age of 2.18 ± 0.09 Ma (Table 8.1). The upper age of the complex of domes and lava flows is constrained at around 1.44 ± 0.08 Ma (Table 8.1) by a subaerial dacite dome. These results suggest that the upper age limit of the complex of domes and lava flows is younger than previously thought (around 2 Ma, Fytikas et al. 1986). Based on newly obtained dates and field mapping, the complex of domes and lava flows has mainly gradational, interfingering, conformable contact relationships with the underlying basal pyroclastic series. The upper contact relationships between the complex of domes and lava flows vary, even over short distances, from conformable to disconformable.

Pyroclastic series and lava domes

The pyroclastic series and lava a domes has an extremely variable internal stratigraphy and is dominated by rhyolitic, dacitic and andesitic lavas and felsic submarine pumiceous

volcaniclastic units. The pyroclastic series and lava domes occurs in the central and northeastern parts of the island (Fytikas et al. 1986), east of the Kontaro Fault and west of the Zefiria Fault (Figure 8.1). Rhyolitic intrusions and syn-eruptive pumiceous units dominate the basal part of the group (Rinaldi and Campos Venuti 2003). The presence of hyaloclastite, laminated mudstone containing marine fossils, turbidites and other mass-flow units overlying the Bombarda and Dhemeneghakia rhyolites are evidence for a submarine setting (Fytikas et al. 1986; Rinaldi and Campos Venuti 2003). Traction-current structures, such as large-scale cross bedding, indicate that deposition was predominantly above wave base (Figure 8.3C-section K). The upper part of the pyroclastic series and lava domes is characterised by dacitic and andesitic lavas and a single, laterally extensive rhyolitic lava at Halepa (Figure 8.3B-section I). These lavas are overlain and locally interbedded with thick, non-welded pyroclastic deposits of the pyroclastic facies association, indicating that upper part of the group was probably wholly subaerial.

New informal lithostratigraphic units in the pyroclastic series and lava domes include the Sarakiniko Formation and the Korakia Andesite. No new dates have been obtained for the pyroclastic series and lava domes during this study. However, K-Ar dates of units within the pyroclastic series and lava domes are consistent with an Early Pleistocene age (<1.5 Ma; Angelier et al. 1977; Fytikas et al. 1986). K-Ar dates of biotite have further constrained the age of the pyroclastic series and lava domes. Within the Halepa area on southern coast of Milos, the Halepa rhyolite lava from the stratigraphic top of the series has been dated at 0.95 ± 0.08 Ma (Fytikas et al. 1986).

Contact relationships between the pyroclastic series and lava domes and other lithostratigraphic units are typically complex. The unit interfingers with the complex of domes and lava flows in the northern and central part of the island, west of the Firiplaka Fault and unconformably overlies the pre-volcanic rocks east of the Firiplaka Fault (Fytikas et al. 1986). To the east, the unit is disconformably overlain by the products of rhyolitic complexes of Firiplaka and Trachilas and locally by products of phreatic activity on the southeastern coast (Figure 8.3D-section J).

Rhyolitic complexes of Firiplaka and Trachilas and phreatic products

These two units require no redefinition. The rhyolitic products of the Firiplaka and Trachilas volcanoes disconformably overlie the complex of domes and lava flows. In the south (Firiplaka centre), the unit unconformably overlies the Mesozoic basement (Figure 8.3B-section Q), interfingers with the pyroclastic series and lava domes and is conformably overlain by the phreatic products. Intercalated palaeosols and abundant pyroclastic facies indicate that both units were emplaced in an entirely subaerial environment.

K-Ar dates for the Firiplaka volcanic centre range from 0.48 ± 0.05 to 0.09 ± 0.02 Ma (Fytikas et al. 1976; Fytikas et al. 1986). The single K-Ar date of 0.37 ± 0.09 (Fytikas et al. 1986) from the Trachilas volcanic centre falls within that range. ^{14}C dating of Roman pot fragments contained within the phreatic deposits in the Agia Kiriaki area, indicate an age 200 BC-200 AD (Traineau and Dalabakis 1989), which is consistent with archaeological findings (Renfew and Wagstaff 1982).

8.4 Volcanic and sedimentary facies architecture of Milos

The volcanic activity on Milos began at 2.66 ± 0.07 Ma and has been more or less continuous since then. Subaerial emergence probably occurred across the island around 1.44 ± 0.08 Ma, in response to a combination of volcanic constructional processes and fault-controlled volcano-tectonic uplift. Three aspects of the volcanic facies architecture will be discussed in the following section: (1) facies associations and depositional environments; (2) thickness variation within the volcanic succession; (3) volcano types and facies architecture.

Facies associations and depositional environments

The pumice breccia facies association is the most common facies association and comprises thickly bedded (tens of metres), diffusely stratified, rhyolitic to dacitic submarine pumice breccia (Figure 8.3B-section E, Figure 8.3B-section F and G) interbedded with locally abundant graded sandstone and mudstone facies. The pumice breccia facies is characterised by unmodified juvenile particles produced by explosive fragmentation,

but transported and deposited by water-supported gravity currents.

Next in abundance are the submarine rhyolite, dacite, andesite and basaltic andesite facies associations. These associations comprise various combinations of coherent facies, in situ hyaloclastite, intrusive hyaloclastite, and redeposited hyaloclastite that collectively represent shallow intrusions, lavas and domes. Contacts of intrusions, lavas and domes show the effects of quenching and interaction with poorly consolidated, water-saturated host sequences, indicating that they were mainly emplaced in a submarine environment. Some of these lava and dome complexes may have been locally emergent above sea level, and are therefore considered to be spatially and temporally related to compositionally similar, subaerial facies associations (biotite-quartz-phyric rhyolite, dacite and andesite facies associations; Chapter 7). The biotite-quartz-phyric rhyolite, dacite and andesite facies associations comprise combinations of thick (up to 300 m), porphyritic coherent lava and enveloping carapaces of autobreccia. The common occurrence of palaeosols, autobreccia and absence of intercalated sedimentary facies in these associations indicate that the lavas were mainly emplaced in a subaerial environment.

Although volumetrically minor, the sandstone-conglomerate facies association includes facies that provide good constraints on the depositional setting. In particular, bioturbation and fossils in the mudstone facies imply deposition in a relatively shallow-water environment, up to a few hundred metres deep. The presence of tabular, massive to graded beds typical of deposits from gravity currents and sedimentary structures indicative of wave action and currents (e.g. cross-stratification) are also consistent with a shallow submarine environment close to wave base. The inclusion of clasts derived from Mesozoic and Neogene successions suggests that this facies was sourced from east of the Firiplaka Fault (Figure 8.1), where Mesozoic basement and Neogene sedimentary formations are exposed.

Despite being volumetrically subordinate, the pyroclastic and mud-matrix breccia facies associations occur in many areas of Milos, especially in the eastern and southern parts of the island. Facies in these associations are interbedded with palaeosols and some contain charcoal. The pyroclastic facies are characterised by a dominance of unmodi-

fied juvenile pyroclasts and bedforms that indicate transport by hot, pyroclastic density currents. In contrast explosive eruptions that generated the mud-matrix breccia facies association were steam-driven and produced deposits dominated by basement-derived lithic pyroclasts.

The distribution of shallow submarine versus subaerial environments in time and space through the Milos succession is shown alongside each stratigraphic column in Figure 8.3. The results indicate that shallow-marine environments were most abundant during accumulation of the lower part of the succession (basal pyroclastic series and the complex of domes and lavas). The transition from a shallow marine environment to a subaerial one probably occurred around 1.44 ± 0.08 Ma, being the age of one of the oldest subaerial dacites, and is attributed to a combination of tectonic uplift, emplacement of shallow intrusions (cryptodomes), construction of domes and lavas, and rapid syn-eruptive accumulation of volcaniclastic strata.

Thickness variation

The volcanic and sedimentary succession at Milos varies in thickness from a minimum of tens of metres in the Paliochori area (Figure 8.3B-section P) in the eastern part of the island, up to ~700 m in the northeastern part of the island (Figure 8.3A-section E). The variations across the island are directly attributed to a combination of constructional volcanism, topography and syn-volcanic faulting. The western and northeastern sectors of Milos are dominated by a laterally extensive succession of syn-eruptive pumice breccia and sedimentary facies more than 300 m thick. This part of the succession displays very little internal heterogeneity (Figure 8.2B-section E) but thins towards and is absent from the southeastern sector of the island, east of Psathi (Figure 8.3B-section I) and south of Dhemeneghakia (Figure 8.3B-section P). This thickness trend suggests that the southeastern part of the island was a topographic high (possibly shoaling or subaerial) throughout most of the Upper Pliocene-Pleistocene, and therefore receiving relatively little sediment.

Syn-volcanic normal faults are well exposed in basal parts of the succession, some of which have displacements up to several hundred metres (Fytikas et al. 1986). The structure of Milos is dominated by subvertical normal faults (Figure 3.9) that interacted dur-

ing periods of extension to produce horsts and grabens (Fytikas and Marinelli 1976). Local extension must have been important in shaping topography and creating depositional basins. However, extension evidently also kept pace with the rapid accumulation of volcanic and sedimentary facies, especially in the western and northeastern sectors of the island.

Volcano types and architecture

The volcanic facies architecture comprises interfingering proximal (near vent), medial (volcano flanks), and distal (volcano margin) facies related to five main volcano types (Table 8.2): (1) submarine felsic cryptodome-pumice cone volcanoes; (2) submarine dacitic and andesitic lava domes; (3) submarine to subaerial scoria cones; (4) submarine-to-subaerial dacitic and andesitic lava domes and (5) subaerial lava-pumice cone volcanoes (Figure 8.4). The facies characteristics of each volcano type are described and illustrated below.

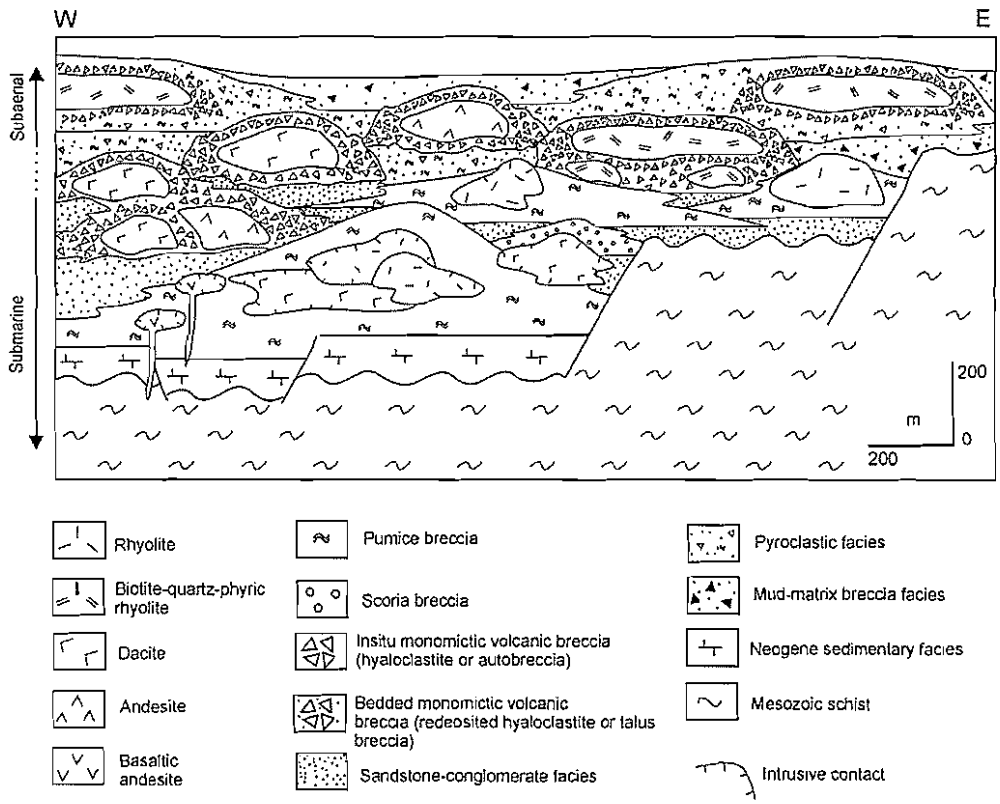

Figure 8.4 Schematic east-west section summarising the volcanic facies architecture of Milos.

Table 8.2 Proximal, medial and distal facies associations of the principal volcano types on Milos.

	Submarine felsic cryptodome-pumice cone volcano	Submarine dacitic and andesitic lava domes	Submarine to subaerial scoria cone	Submarine-to-subaerial dacitic and andesitic lava domes	Subaerial rhyolitic lava-pumice cone volcano
Extent x thickness	10-25 km² x 300-450 m	5-10 km² x 250 to 350 m	At least 18 km² x 2-45 m	2.5-10 km² x 250-350 m	5-10 km² x 120 m
Proximal facies association	Coherent rhyolite and dacite facies (coherent facies of cryptodomes and sills) Sediment-matrix rhyolite and dacite breccia facies (intrusive hyaloclastite) Stratified felsic pumice breccia and polymictic lithic-pumice breccia facies	Coherent dacite and andesite facies (coherent facies of lavas and domes) Non-stratified monomictic dacite and andesite breccia facies (in situ hyaloclastite) Sediment-matrix dacite and andesite breccia facies (intrusive hyaloclastite)	Not exposed	Coherent dacite and andesite facies (coherent facies of lavas and domes) Clast-supported monomictic dacite and andesite breccia facies (in situ autobreccia)	Coherent biotite-quartz-phyric rhyolite facies (coherent facies of lavas) Clast-supported monomictic biotite-quartz-phyric rhyolite breccia facies (in situ autobreccia)
Medial facies association	Coherent rhyolite and dacite facies (coherent facies of cryptodomes and sills) Sediment-matrix rhyolite and dacite breccia facies (intrusive hyaloclastite) Coarse pumice breccia, stratified felsic pumice breccia and polymictic lithic-pumice breccia	Non-stratified monomictic dacite and andesite breccia facies (in situ hyaloclastite) Sediment-matrix dacite and andesite breccia facies (intrusive hyaloclastite) Stratified monomictic dacite and andesite breccia (redeposited hyaloclastite)	Cross-stratified scoria breccia facies, massive andesitic breccia facies, fine scoria sandstone facies	Coherent dacite and andesite facies (coherent facies of lavas and domes) Clast-supported monomictic dacite and andesite breccia facies (in situ autobreccia) Bedded monomictic dacite and andesite breccia facies (redeposited autobreccia)	Clast-supported monomictic biotite-quartz-phyric rhyolite breccia facies (in situ autobreccia) Matrix-supported coarse breccia facies (pyroclastic block-and-ash-flow deposits) Cross-bedded lapilli-ash facies (pyroclastic surge) deposits
Distal facies association	Coarse pumice breccia, stratified felsic pumice breccia polymictic lithic-pumice breccia and graded pumice breccia Graded sandstone or thickly bedded to laminated mudstone	Stratified monomictic dacite and andesite breccia (redeposited hyaloclastite) Graded sandstone or thickly bedded to laminated mudstone facies	Cross-stratified scoria breccia facies, massive andesitic breccia facies, fine scoria sandstone facies Graded sandstone or thickly bedded to laminated mudstone facies	Bedded monomictic dacite and andesite breccia facies (redeposited autobreccia) Matrix-supported coarse breccia facies (pyroclastic block-and-ash-flow deposits) Graded sandstone or thickly bedded to laminated mudstone	Bedded ash facies (pyroclastic fall deposit) deposits

Submarine felsic cryptodome-pumice cone volcanoes

Parts of four large submarine felsic cryptodome-pumice cone volcanoes have been identified on Milos, and collectively cover more than 85 % of the total area of the island (Figure 8.5A). They occur at Profitis Illias, Bombarda, Filakopi and Dhemeneghaki (Figure 8.5A). The essential elements of these volcanic centres comprise thick intervals of felsic pumice breccia intruded by compositionally similar porphyritic rhyolitic and dacitic cryptodomes and sills. They are broadly circular in plan and each one covers an area of tens of square kilometres. Thicknesses of the proximal sections are typically 300-350 m and range up to 450 m. Distal sections are much thinner (<2 m). These volcanoes are similar in style to subaqueous rhyolitic dome-intrusion-tuff cone volcanoes described by Horikoshi (1969), Cas et al. (1990), Allen et al. (1996) and (Ayres and Peloquin 2000). The Profitis Illias cryptodome-pumice cone volcano is larger than many otherwise similar ancient examples. All ancient examples described to date are relatively small-volume (<5 km^3) complexes dominated by small-to-moderate volume, high-aspect ratio felsic domes and an outer apron of pumiceous pyroclastic units. However, the Profitis Illias centre is very similar in dimensions to the modern pre-caldera stage of the Myojiin Knoll in the Izu-Bonin arc, Japan (cf. Fiske et al. 2001), and is of similar size to volcanoes regarded as subaerial analogues, such as felsic dome complexes with pyroclastic aprons (e.g. Mt Tarawera, New Zealand, Cole 1970). To a large extent, the apparent size contrasts result from the relatively small amount of published information on these types of volcanoes, despite their apparent abundance in modern oceans and in ancient volcanic terrains.

The proximal parts of felsic cryptodome-pumice cone volcanoes on Milos are characterised by large-volume, syn-eruptive, felsic pumice breccia intruded by a series of small-volume cryptodomes and sills, comprising aphyric or weakly quartz-feldspar ± biotite-phyric rhyolite or less commonly dacite. Single intrusions have lateral extents less than 1.2 km, although groups of close-spaced intrusions cover areas of several square kilometres, such as in the Chondro Vouno-Profitis Illias area. Contacts typically involve intrusive hyaloclastite, indicating that the intrusions were emplaced into wet and poorly consolidated pumice breccia at relatively shallow levels below the seafloor (e.g. Snyder and Fraser 1963; Hanson and Wilson 1993; Goto and McPhie 1998). Lateral facies changes away from the proximal area mainly involve a decrease in the volume of intrusions and thickness of pumice breccia facies. Single beds of pumice breccia decrease in thickness and grainsize outwards towards the distal zones. The abundance of

interbedded volcanogenic sedimentary facies (graded sandstone and mudstone) and distal facies from other volcanoes also increases (Figure 8.5B).

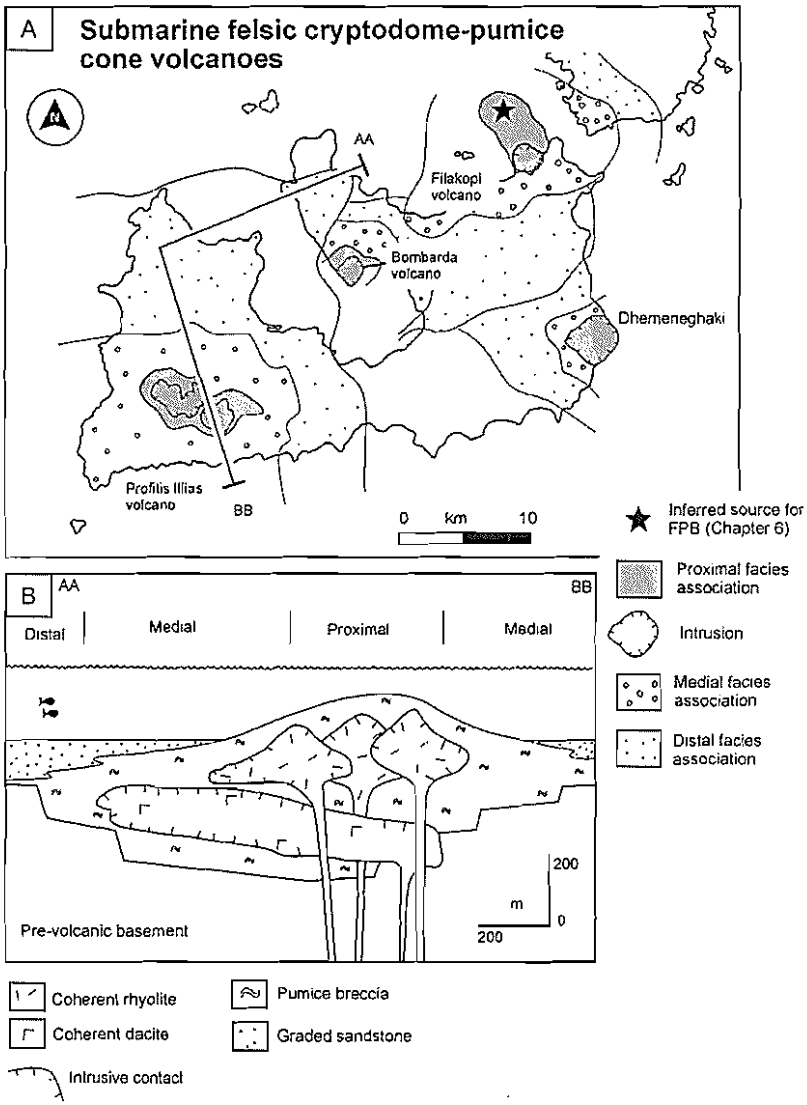

Figure 8.5 Submarine felsic cryptodome-pumice cone volcanoes. **A** Map showing the proximal, medial and distal parts of the three main submarine felsic cryptodome-pumice cone volcanoes on Milos. Location of the Filakopi Pumice Breccia (FPB) source (black star) based on data presented in Chapter 6. **B** A Facies model for submarine felsic cryptodome-pumice cone volcanoes on Milos. The schematic cross-section of the Profitis Illias volcano displays the spatial distribution of facies and internal structure. Location of cross-section on Figure 8.5A.

There are two main types of proximal to medial pumice breccia facies (Chapter 6): (1) very thick (tens of metres), massive or diffusely stratified rhyolitic to dacitic pumice breccia. This facies consists of pyroclasts transported and deposited by water-supported

gravity currents; (2) very thick (up to 20 m), tabular beds of well sorted, reversely graded, coarse (up to 6.5 m) pumice clasts in grain-to-grain contact and set in a fine matrix (coarse monomictic pumice breccia facies (Chapter 6). The coarse pumice clasts settled from suspension and the framework was progressively infilled by fine pumice clasts and water-settled ash. This type of pumice breccia is a variety of water-settled fall deposit.

The felsic cryptodome-pumice cone volcanoes are interpreted to have been entirely submarine. However, given the relatively shallow-water depositional setting, it is plausible that rapid accumulation of pyroclastic units resulted in the net growth toward sea level and that high-level intrusion of cryptodomes caused up-doming of the pumice breccia pile (c.f. Minakami et al. 1951). Therefore, it is possible that some of the volcanoes grew to sea level and breached the air-water interface.

Submarine dacitic and andesitic lava domes

Submarine dacitic and andesitic lava dome volcanoes cover approximately 10 % of the island, and range from 2.5 to 10 km in diameter and 250 to 350 m thick in the proximal parts. Several volcanic centres of this type are inferred, but those in the Triades area of northwestern Milos are the best exposed (Figure 8.6A). These domes are dominated the products of submarine, effusive, dacitic and andesitic eruptions and are composed of variable amounts of coherent facies and in situ and redeposited autoclastic facies (Table 8.2).

The dacitic and andesitic lava domes on Milos form thick (up to 300 m), high-aspect-ratio units similar to lava domes in other modern and ancient submarine settings (c.f. Horikoshi 1969; Kano et al. 1991; Yamagishi and Dimroth 1985; Yamagishi and Dimroth 1987, 1991; Yamagishi and Goto 1992; Figure 8.6). They are strongly constructional and characterised by a broadly concentric internal structure, consisting of a massive coherent core, flow-banded outer zone, in situ brecciated margin and an enveloping carapace of hyaloclastite (Figure 8.6B). The coherent core is volumetrically dominant, uniformly microcrystalline and columnar jointed. Commonly surrounding the core facies is a massive 30-40-m-thick perlitic or flow banded rind. Flow bands are approximately parallel to the adjacent margin. The coherent facies is overlain by or enclosed in non-stratified monomictic dacite or andesite breccia, interpreted to be hyaloclastite produced by quench fragmentation of the margins of the dome. Where ex-

posed, the basal contacts of the domes comprise intrusive hyaloclastite and the underlying sediments are locally deformed. This suggests that the domes flowed over and locally burrowed into wet, unconsolidated sediments.

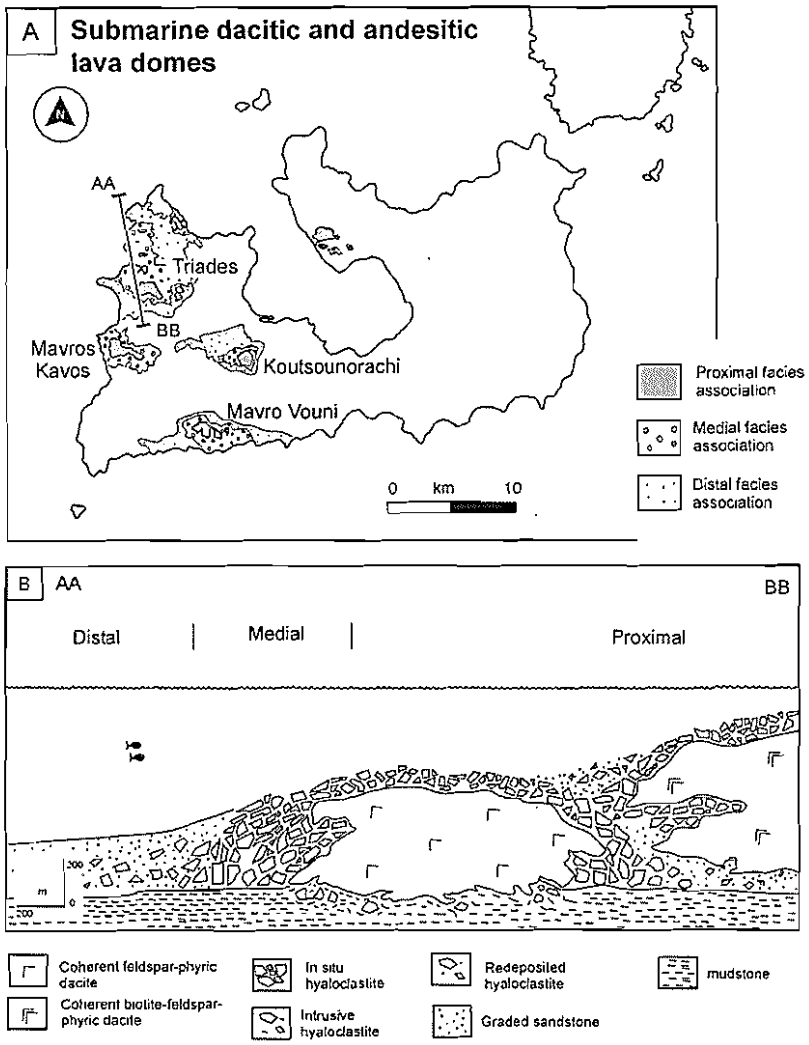

Figure 8.6 Submarine dacitic and andesitic lava domes. **A** Map showing the proximal, medial and distal parts of the main submarine dacitic and andesitic lava domes on Milos. **B** Facies model for submarine dacitic and andesitic lava dome volcanoes on Milos, based on a schematic cross-section of the Triades volcano. Location of cross section on Figure 8.6A.

The medial to distal parts of these volcanoes on Milos are characterised by stratified dacite or andesite breccia (Figure 8.6B), generated by down-slope remobilisation of unconsolidated hyaloclastite and autobreccia. Resedimentation probably accompanied dome growth and involved submarine grain flows or debris flows.

Submarine to subaerial scoria cone

The andesitic scoria-rich breccia facies association is restricted to the northeastern part of Milos and covers an area of 18 km^2 (Figure 8.7). The thickest (up to 45 m) and coarsest sections occur at Pollonia. The association of cross-stratified scoria breccia facies, massive andesitic breccia facies and fine scoria sandstone facies containing large fluidal clasts is interpreted as the product of weakly explosive, magmatic-volatile-driven strombolian volcanic activity. Although the depositional setting of all preserved sections was submarine, the source was probably a scoria cone that may have been partly emergent.

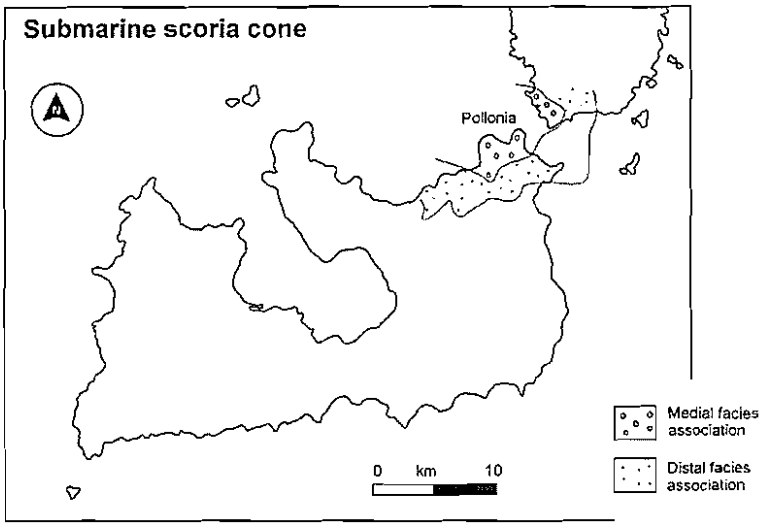

Figure 8.7 Map showing the medial and distal parts of the submarine scoria cone on Milos

Single units near the eastern limits of outcrop are thinner (~2 m) and finer than those near Pollonia. Feeder dykes and coarse agglutinate-like deposits expected to mark near-vent positions (Houghton and Landis 1989; Smith and Batiza 1989) are absent, suggesting that the proximal parts are not exposed onshore. Hence, the preserved sections of the andesitic scoria facies association are probably medial and distal. The overall grading and sedimentary structures are consistent with deposition from, moderate- to high-concentration turbidity currents, with possible modifications by traction currents during accumulation to form cross-stratified intervals. These characteristics are similar of those found in other submarine successions thought to be composed of the primary and redeposited products of strombolian eruptions (c.f. Staudigel and Schmincke 1984; Cas et al. 1989; Houghton and Landis 1989; Dolozi and Ayres 1991; Kano 1998).

Submarine-to-subaerial dacitic and andesitic domes

Submarine-to-subaerial dacitic and andesitic dome volcanoes are restricted to the Kontaro, Korakia and Krotiraki areas, and Arkadies Island (Figure 8.8A). They cover <5% of the island and range from 2.5 to 10 km in diameter and 250 to 350 m in thickness in the proximal parts. These volcanoes are similar in style to intermediate lava domes in modern subaerial volcanic sessions (c.f. Huppert et al. 1982; Swanson and Holcomb 1990; Nakada 1992; Nakada et al. 1995). The proximal parts of submarine-to-subaerial dacitic and andesitic domes on Milos are characterised by thick (up to 250 m), high-aspect-ratio intervals of dacite and andesite lava. Single domes comprise a massive coherent core, flow-banded rind, and an envelope or carapace of in situ autobreccia.

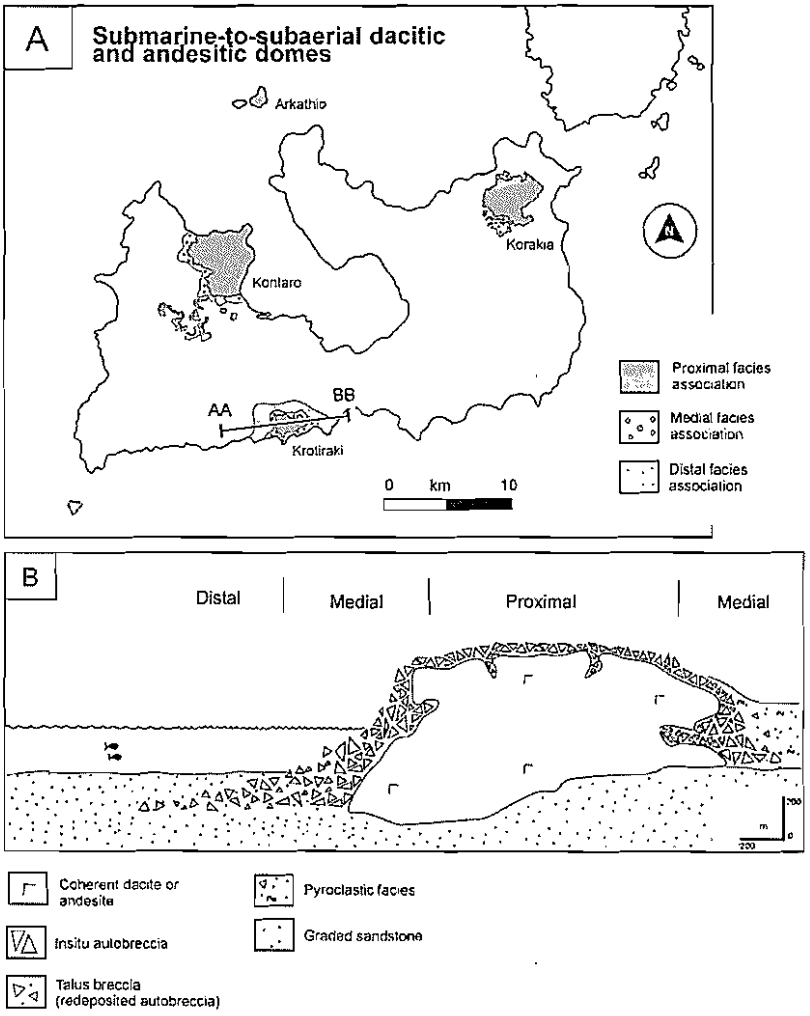

Figure 8.8 Submarine-to-subaerial dacitic and andesitic domes. **A** Map showing the proximal, medial and distal parts of submarine to subaerial dacitic and andesitic lava domes on Milos. **B** Facies model for submarine-to-subaerial dacitic and andesitic domes on Milos, based on a schematic cross section of the Krotiraki volcano. Location of cross-section on Figure 8.8A.

Lateral facies changes away from the proximal area mainly comprise decreases in the volume of coherent lava and the thickness of autoclastic facies. The medial areas characterised by abundant bedded monomictic dacite breccia facies; pyroclastic facies (matrix-supported coarse breccia) and distal facies from other volcanoes also increases in the medial sections. The bedded monomictic dacite breccia is considered to represent redeposited autobreccia, analogous to aprons of talus breccia that accumulate at the margins of subaerial lavas or domes either during or following emplacement (c.f. Fink 1983). The presence of graded sandstone facies intercalated with the bedded monomictic dacite breccia is consistent with the interpretation that at least some of these dome-derived breccias were deposited in a shallow marine environment.

In distal sections, the pyroclastic facies intercalated with palaeosols are interpreted to be block-and-ash flow deposits generated by explosive and/or gravitational collapse of active lava domes.

Subaerial rhyolitic lava-pumice cone volcanoes

Three large subaerial rhyolitic lava-pumice cone volcanoes are present on Milos, at Trachilas in the north, Firiplaka in the south and Halepa on the southern coast (Figure 8.9A). They are broadly circular in plan and each one covers an area of tens of square kilometres. The proximal zones of these volcanic centres are about 120 m thick, and the distal parts are much thinner (several metres; Figure 8.9B). Detailed study of the Firiplaka centre by Campos Venuti and Rossi (1996) indicated that initial explosive eruptions were phreatic and evolved to a cone-building phreatomagmatic episode represented by surge deposits. Later eruptions produced ash fall deposits and lavas.

The proximal parts of subaerial rhyolitic lava-pumice cone volcanoes on Milos are dominated by thick felsic pyroclastic deposits overlain by small-volume lavas, comprising biotite-quartz-phyric rhyolite, up to 100 m in thickness, and cover several square kilometres. The lavas display similar tabular geometries similar to felsic lavas in modern subaerial environments (c.f. Fink 1980; Bonnichsen and Kauffman 1987). They are strongly constructional and characrised by a broadly concentric internal structure, consisting of a massive coherent core, with an outer flow-banded zone and an in situ brecciated margin. Outer parts of single lavas are typically composed of autobreccia and talus breccia (redeposited autobreccia).

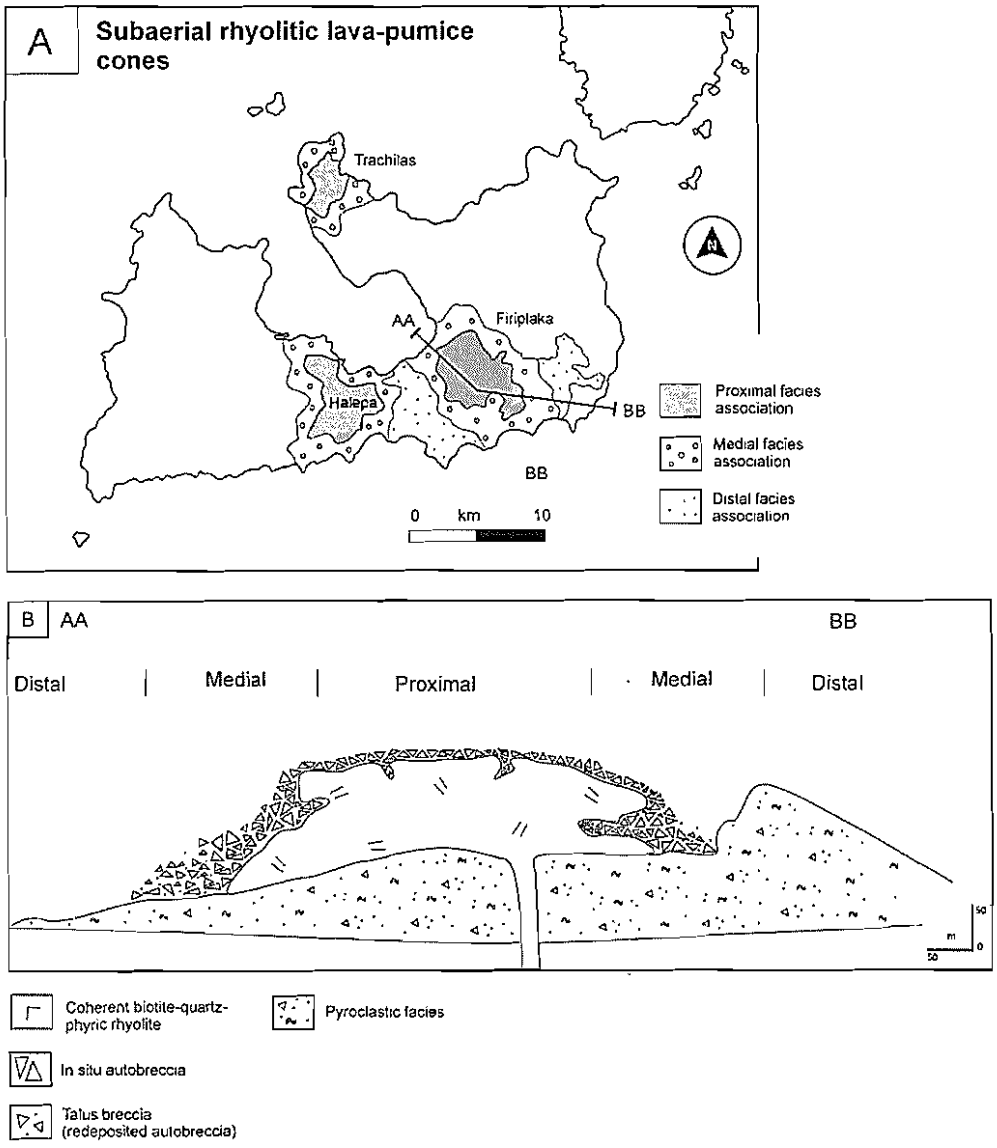

Figure 8.9 Subaerial rhyolitic lava-pumice cone volcanoes. **A** Proximal, medial and distal of subaerial rhyolitic lava-pumice cone volcanoes on Milos. **B** Facies model for subaerial rhyolitic lava-pumice cone volcanoes on Milos, based on a schematic cross-section of the Firiplaka volcano. Location of cross-section on Figure 8.9A.

There are two main pyroclastic facies in the proximal to medial sections: (1) very thick (tens of metres), massive and poorly sorted intervals of cross-bedded lapilli-ash (pyroclastic surge deposits); and (2) thin (<1 m) intervals of bedded ash (fall deposits). Lateral facies changes away from the proximal area mainly involve decreases in the volume of lavas and in thicknesses of pyroclastic facies (Figure 8.9B). Distal pyroclastic facies are dominated by bedded ash intervals.

8.5 Summary

The volcanic architecture of the Upper Pliocene-Pleistocene, dominantly felsic-intermediate volcanic succession on Milos reflects contrasts in eruption style, proximity to source, depositional environment and emplacement processes. The volcanic activity began at about 2.66 ± 0.07 Ma and has been more or less continuous since then. Subaerial emergence probably occurred at about 1.44 ± 0.08 Ma, in response to a combination of volcanic constructional processes and fault-controlled volcano-tectonic uplift. The essential elements of the volcanic facies architecture are interfingering proximal (near vent), medial (volcano flanks), and distal (volcano margin) facies associations related to: (1) submarine felsic cryptodome-pumice cone volcanoes; (2) submarine dacitic and andesitic lava domes; (3) submarine to subaerial scoria cones; (4) submarine-to-subaerial dacitic and andesitic domes; (5) subaerial rhyolitic lava-pumice cone volcanoes. The submarine volcanic associations are intercalated with graded sandstone and/or fossiliferous mudstone mainly derived from erosion of pre-existing volcanic and basement units. The subaerial volcanic associations are intercalated with palaeosols.

Chapter 9

Setting of epithermal mineralisation in the evolution and facies architecture of Milos: implications for exploration

9.1 Introduction

Many modern volcanic islands are characterised by geothermal activity at or near sea level, and both epithermal- and volcanic-hosted massive sulfide (VHMS)-style mineralisation are known to occur in these settings (Hannington and Herzig 1993; Sillitoe et al. 1996; Hannington and Herzig 2000). A genetic link between these two end-member systems has been a long-held premise of magmatic-hydrothermal models of island arcs (e.g. Hedenquist and Lowenstern 1994).

In the past, shallow subaqueous to partly emergent environments have generally been considered non-prospective for ore deposits, owing largely to geological models that require epithermal mineralisation to be restricted to subaerial and VHMS deposits to deep marine environments. Recent integrated studies suggest a number of very sizeable precious metal and base metal deposits (e.g. Eskay Creek, Roth et al. 1999; Boliden, Allen et al. 1996; Lerokis and Kali Kuning, Sewell and Wheatley 1994) may have formed in such settings highlighting their potential economic importance. Moreover, active hydrothermal systems have been discovered in shallow marine settings of some young arcs (e.g. Panarea, Gamberi et al. 1999; Kavachi and Kana Keoki, McConachy and McInnes, 2001). However, little is known about the volcanic host rocks or internal architecture of these deposits, despite their economic significance and probable abundance in todays oceans and ancient volcanic arcs.

Milos provides a rare opportunity to study the relationships between volcanism and mineralisation in a hydrothermal system formed in a shallow submarine to partly emergent felsic volcanic dome complex, where the setting is unambiguous. In this chapter,

these relationships will be investigated in the context of the volcanic facies architecture presented in Chapter 8. Textural and lithological characteristics of the host succession are used to constrain the setting and eruption style of the volcanic host sequence. The research presented in this chapter broadens the current understanding of mineralisation processes found in shallow submarine island arc settings, providing facies models for mineralised felsic volcanic centres and volcanological guides for mineral exploration of ore deposits within these settings.

9.2 What is the definition of shallow-water epithermal mineralisation?

In the last decade, the concept that 'shallow submarine' epithermal deposits exist, and are even common, has gained a credence. Part of the controversy surrounding these types of ore deposits stems from the combination of a shallow submarine setting and epithermal deposit character. Hence, based on geological characteristics that indicate the setting and water depth during time of mineralisation. The most practical geological definition of 'shallow water' is water depths above storm wave base (i.e. 200-300 m; c.f (Johnson and Baldwin 1986) because these can be recognised using depositional structures and fossils. Shallow water settings are marked by sedimentary structures developed under conditions, where tidal currents and waves produce tractional sedimentary structures in coarse sediment (e.g. cross-beds and oscillatory ripples).

The epithermal environment is defined as being shallow in depth (Lindgren 1922). There are characteristic mineral textures and assemblages associated with epithermal deposits and, coupled with fluid inclusion data, that indicate most epithermal deposits form in a temperature range of about 160^0 to 270^{0}c (Hedenquist 1987; White 1995; Cooke and Simmons 2000). In subaerial settings, this temperature interval corresponds to a depth below the surface of about 50 to 700 m (Henley 1985).

9.3 Precious & base metal exploration history

Milos is a relatively small (151 km^2) island, but hosts some of the most significant mineral deposits in the Southern Aegean Volcanic Arc. The presence of mineralisation on

Milos has been known since ancient times. However, economic precious and base metal mineralisation was first discovered in the Triades area by the Sifnos and Euboea Company in 1884. The area then became the focus of small-scale open-pit and underground mining that produced approximately 20,000 tonnes of Ba-Ag-Pb-Zn concentrate.

Figure 9.1 Locations of main ore deposits and prospects in western Milos. Also shown are the major, currently active kaolinite mining operations.

A joint venture between BRGM and Silver and Baryte Ores Mining SA explored for gold at Triades (Figure 9.1) in the late 1980's, identifying a probable resource of 1.2 million tonnes at 1 g/t Au and 124 g/t Ag (Vickery 1995). In 1992, a renewed exploration focus on high-level, epithermal precious metal deposits was established on the island by a joint venture between Renison Goldfields Holdings Ltd., Silver and Baryte Ores Min-

ing SA and Niugini Mining Ltd. After extensive geological mapping, sampling and drilling of 13 diamond holes, a probable resource of 5 million tonnes at 4.4 g/t Au and 43 g/t Ag was identified at Profitis Illias (Figure 9.1). The joint venture was terminated in 1996. In 1998, a joint venture was formed between Royal Gold Inc, Silver and Baryte Ores Mining SA and Goldmax Resources (Midas SA), and resulted in the drilling of 60 holes at Amethyst Ridge, East Amethyst, Amethyst, Chondro Vouno and Profitis Illias. This resulted in the definition of 3.3 million tonnes at 4.4 g/t Au at Chondro Vouno, East Amethyst and Amethyst (Figure 9.1).

9.2 Review of epithermal mineralisation on Milos

The main characteristics of ore deposits on Milos are summarised below and in Table 9.1, with emphasis on the relationships between the ores and their host rocks. Based on their mineralogy, hypogene alteration characteristics, and simple metal ratios (Figure 9.2), all deposits, with exception of the Cape Vani deposit have been assigned to the broad epithermal field. Detailed descriptions of some deposits are given in Liakopoulos (1987), Hauck (1988), Spartali (1994), Sillitoe (1995), Christanis and Seymour (1995), Vickery (1995), Vavelidis and Melfos (1998), Kilias et al. (2001), and Liakopoulos et al. (2001).

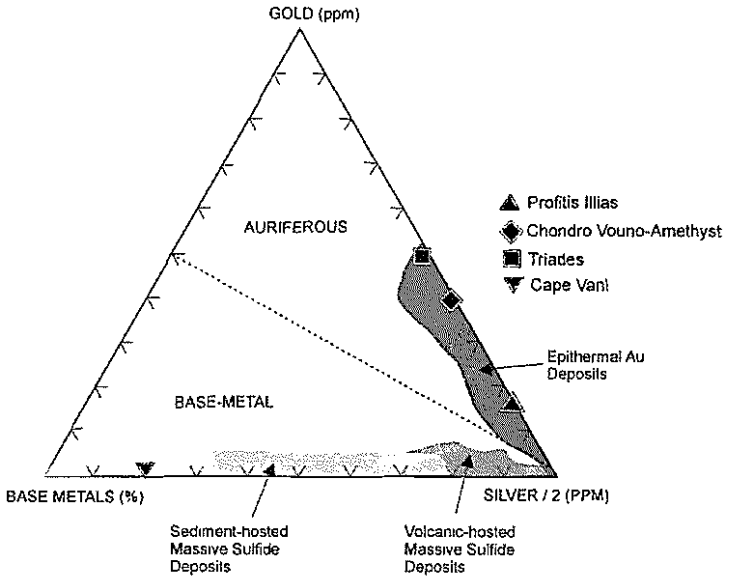

Figure 9.2 Ternary plot of the relative abundance of gold, silver, and base metals (Cu+Pb+Zn) for the three principal epithermal deposits on Milos and Cape Vani. The diagonal line separates distinctly auriferous deposits (high gold-to-base metal ratios) from conventional base metal massive sulfides. Compositional fields for typical epithermal gold deposits, volcanic-hosted massive sulfide deposits and sedimentary-hosted massive sulfide deposits are also shown (after Poulsen and Hannington 1995).

Table 9.1 Characteristics of five selected precious and base metal deposits on Milos

Deposit/ prospect	Ore type	Tonnage[1], grade	Host facies	Footwall facies	Mineralisation style	Ore-related hypogene alteration	Hypogene minerals	Type	Reference(s)
Profitis Illias	Au-Ag	5 Mt @ 4.4 g/t Au, 43 g/t Ag	Felsic pumice breccia	Felsic intrusion	Vein	Quartz, adularia, kaolinite, illite +/- montmorillonite	Pyrite, sphalerite, chalcopyrite, galena, electrum, tetrahedrite	Low sulfidation epithermal	Christanis and Seymour (1995); Constadinidou et al. 1996; Kilias et al. 2001
Chondro Vouno-Amethyst	Au-Ag	3.3 Mt @ 4.4 g/t Au	Felsic pumice breccia	Felsic intrusion	Vein, breccia, disseminated	Quartz, adularia, kaolinite, illite +/- montmorillonite	Pyrite, sphalerite, chalcopyrite, galena, electrum, tetrahedrite	Low sulfidation epithermal	Kilias et al. 2001
Triades	Au-Ag-Pb-Zn	1.2 Mt @ 1 g/t Au, 124 g/t Ag	Graded sandstone, mudstone and felsic pumice breccia	Felsic intrusion	Breccia, stratabound	Quartz, alunite, kaolinite, illite, halloysite, montmorillonite	Galena, sphalerite, chalcopyrite, bornite, pyrite, covellite, pyrargyrite, proustite	High sulfidation epithermal – VHMS, sub-sea floor replacement	Hauck 1988
Cape Vani	Mn-Ba-Ag	2.1 Mt of Mn ore	Graded sandstone, mudstone and felsic pumice breccia	Felsic intrusion	Stratabound replacement	Chlorite, K-feldspar, kaolinite, sericite, montmorillonite	Pyrolusite, ramsdellite, cryptomelane, hollandite, coronadite	Submarine hydrothermal manganese replacement	Liakopoulos et al. 2001

[1]Mt=million metric tonnes

Figure 9.3 View north over the Profitis Illias and Chondro Vouno-Amethyst deposits. The summit of Profitis Illias is 752 m.

Profitis Illias

The Profitis Illias deposit (Figures 9.1 and 9.3) is currently the largest recognised gold-silver resource (5 Mt @ 4.4 g/t Au, 43 g/t Ag) on Milos and was the first significant deposit discovered in the active Southern Aegean Volcanic Arc. Gold-silver epithermal veins are hosted by a thick succession (up to 300 m) of thickly bedded, massive to diffusely stratified pumice breccia (pumice breccia facies association), graded sandstone and mudstone (sandstone-conglomerate facies association). The footwall to mineralisation consists of coherent rhyolite and dacite, and varying amounts of intrusive hyaloclastite (rhyolite and dacite facies association), associated with syn-volcanic cryptodomes and sills. The spatial distribution of the main facies associations are shown in Figure 9.4A.

The deposit consists of three main, partly connected epithermal low-sulfidation veins, P, M and J (Figure 9.4B and C). A multitude of subordinate veins are present between these main veins. Single veins vary in thickness from 1 mm to 10 m. Larger veins occupy steep-dipping, north-striking normal faults. The veins occur over an area of 2.4 km^2 and have been intersected in drill core to a depth of 300 m. The P vein (Figure 9.4B and C) forms the contact between the pumice breccia facies and the coherent rhyolite for much of its length and truncates other veins. It is thought to be the main fluid conduit, and effectively forms the footwall to economic mineralisation (Crossing 1994; Sillitoe 1995). Post-mineralisation faults have dismembered a large percentage of the veins.

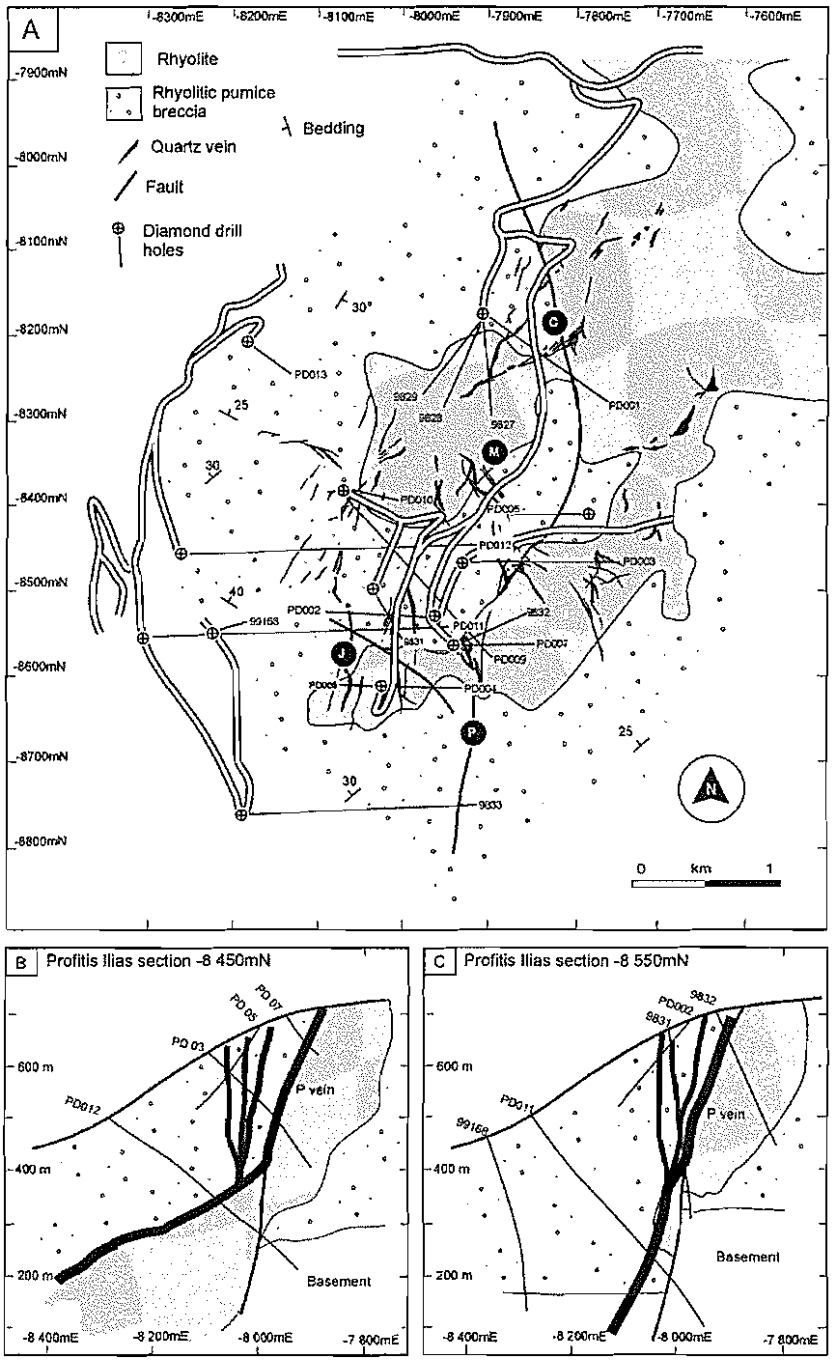

Figure 9.4 **A** Geological map of the Profitis Illias area (modified after Crossing 1994) showing the distribution of the main geological units, structure and mineralisation. **B** and **C** Schematic cross-sections of the Profitis Illias Au-Ag vein deposit on sections -8450mN and -8550mN. Most of the gold is contained in the P-vein, which forms the contact between the pumice breccias and the rhyolite for much of its length. Basement refers to Mesozoic schist. Local grid from 1:5000 scale Greek topographic maps.

All the veins display similar morphological and textural characteristics. The veins are composed largely of fine grained quartz, which, at shallow levels, displays crustiform banding and abundant quartz-lined cavities. The margins of the veins are sharp (Figure 9.5A) and there is a rapid decrease in gold grades from the vein to the country rock.

Barite and adularia occur as thin bands in the quartz (Figure 9.5B). The original sulfide contents of the veins are difficult to estimate, given the deep supergene weathering overprint, although pyrite, sphalerite, chalcopyrite and galena are present as remnants in oxidised veins (Sillitoe 1995; Kilias et al. 2001). Gold is associated with silver-rich electrum in quartz or in limonite after sulfides (Constadinidou et al. 1998). Based on the measurement of fluid inclusions and stable isotopes, the ore forming fluids were relatively saline (0.93-11.4 wt. % NaCl equiv), hot (145-399 °C) chloride waters of predominantly seawater origin (Kilias et al. 2001).

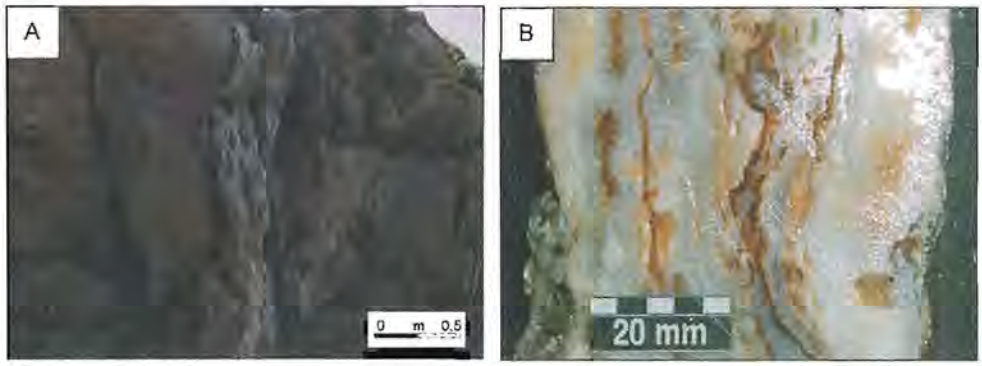

Figure 9.5 Quartz-adularia veins at Profitis Illias. **A.** A large banded quartz-adularia vein (C-vein) hosted by coherent flow-banded rhyolite (GR 7850E-8220N). **B** Cut slab of the same vein, showing crustiform banded texture.

Alteration associated with the Profitis Illias veins are weakly zoned. Alteration covers several square kilometres and can be traced several hundred metres below the present exposure. The hypogene alteration haloes around veins are generally masked to drilling depths by pervasive supergene kaolinite. A sericite-quartz-barite ± kaolinite assemblage is characteristic of wallrock closest to the veins. Rare adularia also occurs disseminated in the host rocks adjacent to veins. This is surrounded by an irregular, pervasive, broad zone comprising a sericite-chlorite-montmorillonite assemblage. Supergene alteration has resulted in secondary alunite and sulfide oxidation. The supergene alteration profile is complex and controlled by the enhanced permeability of veins and post-mineralisation faults.

Chondro Vouno-Amethyst

The Chondro Vouno-Amethyst prospects (Figure 9.1) are located less than 2 km northwest from the Profitis Illias deposit (Figure 9.3), and consist of vein-hosted and minor

breccia-hosted low-sulfidation epithermal mineralisation (Chondro Vouno, East Amethyst, Amethyst and Amethyst Ridge, Figure 9.6A) containing an inferred resource of 3.3 Mt grading 4.4 g/t gold. Gold bearing veins and breccias are hosted within the same thick succession of felsic pumice breccias and rhyolitic to dacitic cryptodomes and sills (Figure 9.6B and C) as the Profitis Illias deposit.

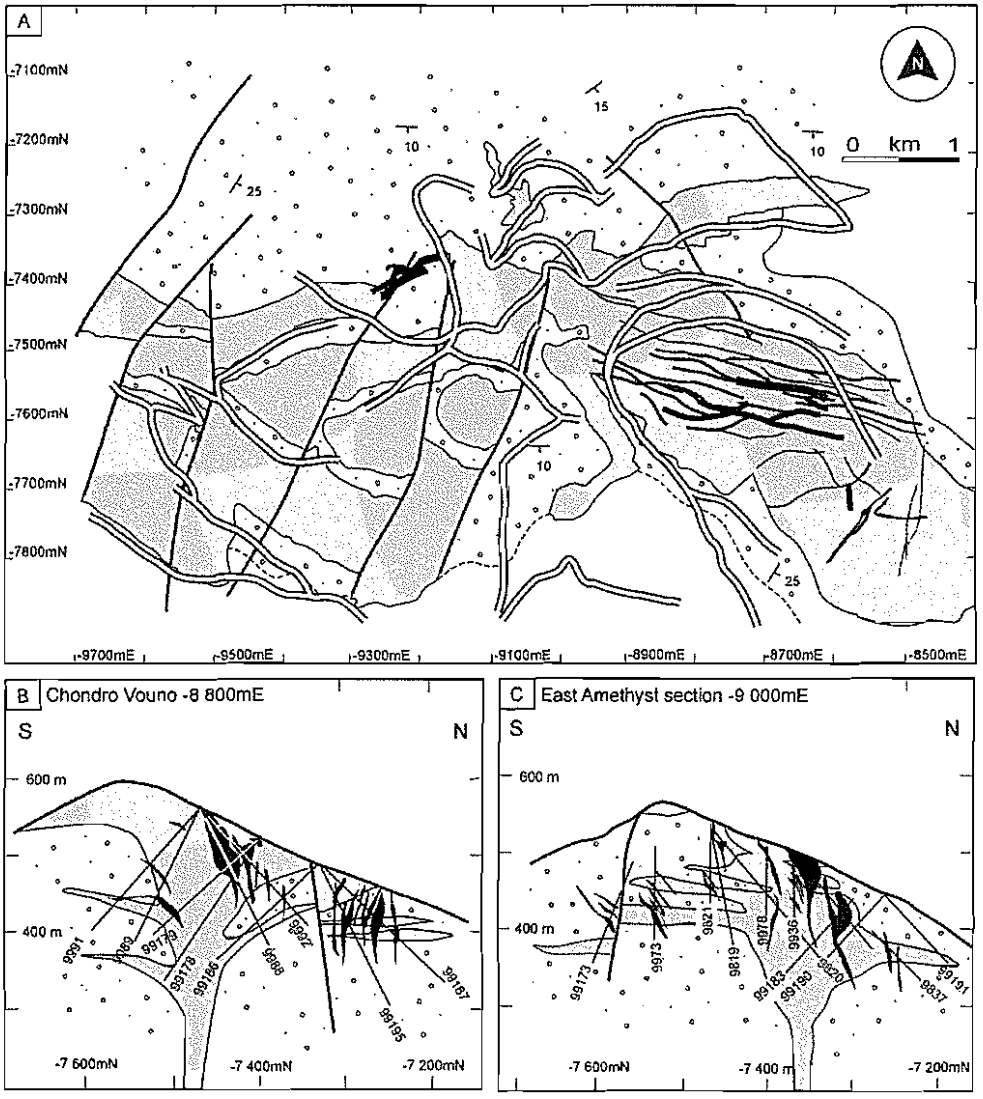

Figure 9.6 **A** Geological map of the Chondro Vouno-Amethyst area (modified after Crossing 1994) showing the distribution of the main geological units, structure and mineralisation. Schematic cross-sections of the Chondro Vouno (**B**) Au-Ag vein deposit on section -8800mE and East Amethyst (**C**) section 9000mE. Local grid from 1:5000 scale Greek topographic maps. Symbols the same as Figure 9.4.

Veins of quartz and sulfides occupy several discrete, discontinuous, stockwork zones (Figure 9.6B and C). Veins vary in width from <1 mm up to 5 m, occur over an area of 2 km^2, and have been intersected in drill core to a depth of 350 m. The highest grade ore zones are localised at the contacts between intrusions (cryptodomes and sills) and

pumice breccia units (Figure 9.7A). Veins in the coherent rhyolite facies are typically thin (<1 m) and low grade.

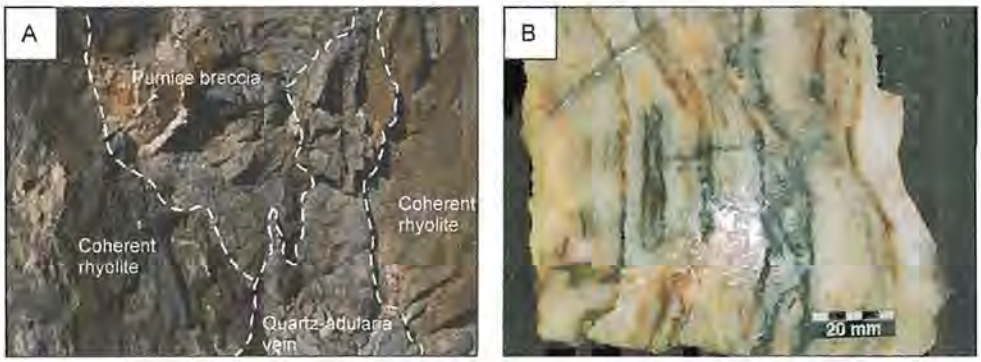

Figure 9.7 Epithermal quartz-adularia veins from Chondro Vouno. **A** High-grade banded quartz-adularia-barite vein hosted by coherent flow banded rhyolite (GR 7500E-8750N). **B** Cut slab of the same vein.

The veins are similar to those of Profitis Illias and composed largely of fine-grained quartz, adularia and barite (Figure 9.7B). Veins are characterised by crustiform texture, comprising quartz and barite (Nethery 1999). Colliform textures are subordinate. The original sulfide contents of the veins are difficult to estimate, given the deep supergene development, although pyrite, sphalerite, chalcopyrite and galena are present as remnants in oxidised veins. The succession in the immediate vicinity of the veins is altered to an assemblage of quartz-sericite-pyrite ± adularia. An outer zone of sericite-chlorite alteration has been interpreted to reflect cooler, near-neutral fluids away from the main upflow zones (Nethery 1999).

Triades

The Triades Au-Ag-barite deposit occurs on the western coast of Milos (Figure 9.8A), approximately 10 km northwest of the Profitis Illias and Chondro Vouno-Amethyst deposits. The deposit is hosted by a diverse succession of submarine graded sandstone, mudstone and polymictic conglomerate facies (sandstone-conglomerate facies association), intercalated with thick (1-8 m) beds of graded pumice breccia (pumice breccia facies association). The footwall to mineralisation consists of coherent rhyolite and dacite, and minor autoclastic facies (intrusive hyaloclastite and peperite). The hanging-wall to mineralisation is made up of varying amounts of coherent dacite associated with thick autoclastic shells (insitu hyaloclastite and autobreccia) and, in some cases, pyroclastic facies (block-and-ash flow deposits and surge deposits).

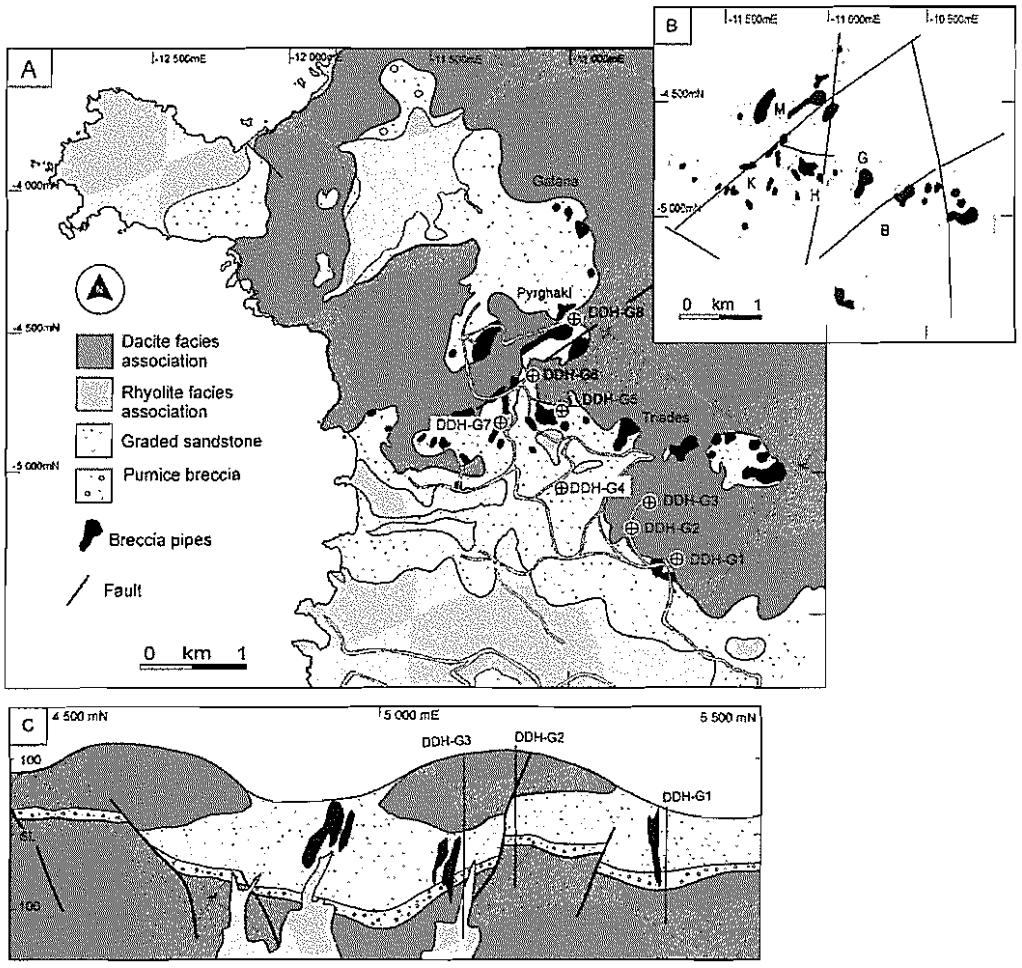

Figure 9.8 **A** Geological map of the Triades area (modified after Vickery 1995) showing the distribution of the main geological units, structure and ore deposits. **B** Simplified map showing the distribution of breccia pipes. Simplified geological cross-section through the Triades area at mine section 11 500mE (**C**) and 10 750mE. Local grid from 1:5000 scale Greek topographic maps.

The Triades deposit consists of five main breccia pipes; B, G, H, K and M (Figure 9.8B), which combined contain a probable resource of 1.2 million tonnes grading 1g/t Au and 124 g/t Ag (Vickery 1995). The breccia pipes are oval in plan and funnel- or mushroom-shaped in section (Figure 9.8C). Although the original extent of breccia in the Triades area has been severely reduced by open pit mining, the overall geometry may be deduced from remaining outcrops (Figure 9.9A). The high-grade mineralisation (3-5 g/t Au) is typically present in the silicified cores of the pipes and less commonly, occurs in argillic alteration zones. Massive silica and breccia form irregular bodies and veins with predominantly vertical extension (Figures 9.9B and 9.9C). The ore bodies range from a few metres to 100 m in width (Figure 9.8B). The depth extent of breccia pipes remains unknown. In an unoxidized state, the breccia matrix contains up to 10 volume % finely disseminated pyrite, galena, sphalerite, chalcopyrite, bornite, covellite,

pyrargyrite and prousite (Hauck 1988). Silver occurs in tetrahedrite and gold occurs in chalcopyrite (Liakopoulos 1987). In oxidised zones, most of the primary sulfides have been destroyed, and the mineral assemblage mainly consists of jarosite, gypsum, covellite and minor Fe-Mn hydroxides.

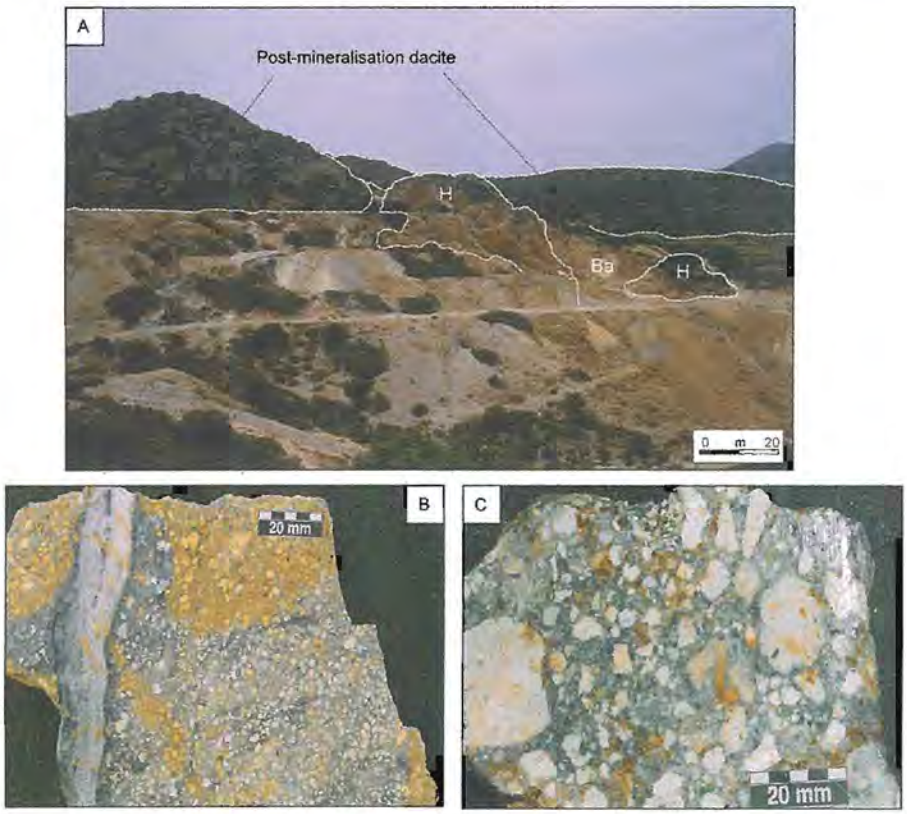

Figure 9.9 A
shaped in section. The associated massive barite (Ba) zone has been reduced by open pit mining. Stratigraphically above the breccia pipes is the post-mineralisation dacite. **B** Polymictic, open framework breccia, containing angular clasts set in a matrix of fine polymictic lithic fragments and sulfides. A late banded quartz-barite-galena vein cross cuts the breccia on the left side of the slab (Breccia pipe G, GR 10600E-4800N). **C** High-grade polymictic breccia containing strongly altered rhyolite and sedimentary clasts, set in a black cement of silica and sulfides (Breccia pipe H, GR 11000E-4900N).

Alteration zones associated with the deposit are strongly zoned and cover approximately 4 km^2. The aerial extent is hard to estimate because of the thick cover of unaltered dacite domes. Alteration can be traced several hundred metres below the surface. The controls on alteration are structural and lithological. Sedimentary and volcaniclastic rocks are more intensely altered than massive coherent facies. Hydrothermal alteration in the Triades deposit consists of an inner silicic core (quartz + kaolinite + alunite + pyrite) surrounded by an irregular zone of argillic alteration (kaolinite + barite+ dickite)

and a broad outer zone (sericite + calcite + montmorillonite). Supergene alteration resulted in secondary alunite, kaolinite and sulfide oxidation (e.g. goethite, limonite).

The crosscutting character of breccia pipes, combined with the absence of exhalative or stratiform ores, prompted Sillitoe (1995) and Vickery (1995) to suggest that this deposit and others at nearby Galana (Figure 9.8A) formed by syn-volcanic replacement in a submarine volcanic pile. The deposit has been interpreted as a unique, shallow submarine example of Kuroko type mineralisation (Hauck 1988). In particular, the presence of pyrite-sphalerite-galena-barite veins at Triades suggested comparison with Kuroko black ore (Figure 9.2). However, the hydrothermal fluid that formed the Triades ores closely resembled epithermal fluids (Liakopoulos 1987). Vaveldis and Melfos (1998) reported homogenisation temperatures of 310^0, and concluded that boiling may have been important in sulfide deposition and considered Triades an example of epithermal style-mineralisation.

Cape Vani

The Cape Vani Mn-Ba-Ag deposit is located on a peninsular of Milos several kilometres north of the Triades deposit (Figure 9.1). The deposit covers approximately 1 km^2 and contains an inferred resource of 2.1 Mt of manganese ore (Liakopoulos et al. 2001). The deposit is interpreted as a syn-genetic, subseafloor replacement ore body (Liakopoulos et al. 2001). Replacement-style mineralisation is hosted by a sequence of graded sandstone, mudstone, polymictic breccia-conglomerate and subordinate graded pumice breccia facies (up to 60 m thick). The immediate footwall to mineralisation consists of coherent rhyolite and dacite and minor autoclastic facies (intrusive hyaloclastite) (Figure 9.10A). The hanging-wall to mineralisation is made up of coherent dacite characterised by thick autoclastic aprons (insitu hyaloclastite and autobreccia).

The Mn-Ba-Ag mineralisation occurs in a series of beds (up to 4 m thick, Figure 9.10A). The ore beds are strongly silicified and impregnated by manganese oxides. K-feldspar, chlorite, barite and sericite are the principal mineral phases (Liakopoulos et al. 2001) in the ore zone. Barite occurs in variable amounts (averaging 12.5%) in the ore zones. A series of northeast-striking veins crosscut the ore zone (Figure 9.10B). The veins are up to 1.5 m thick and best developed in the footwall rhyolite. The banded

quartz-carbonate-barite veins consist of disseminated sphalerite, galena, chalcopyrite and pyrite (Liakpoulos et al. 2001).

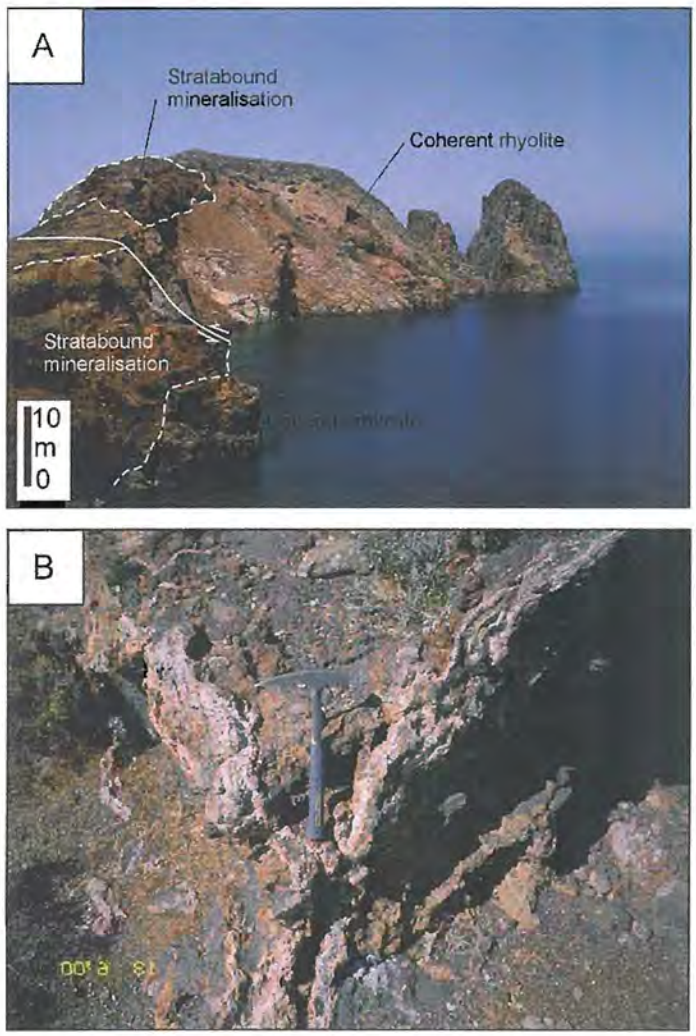

Figure 9.10 A Photograph looking west over the Cape Vani Mn-Ba-Ag deposit. Most of the foreground comprises the stratabound Mn-Ba-Ag mineralisation (red to black colour). **B** Two intersecting banded quartz-carbonate-barite veins consist of sphalerite, galena, chalcopyrite and pyrite, cross cutting stratabound Mn mineralisation (GR 10800E-1900N).

The rhyolite and dacite facies in the footwall and volcanogenic sedimentary rocks hosting mineralisation are intensely altered to an assemblage of K-feldspar, sericite, chlorite and kaolinite, gradually passing into an outer zone of pervasive montmorillonite-chlorite alteration. Although largely stratiform, the presence of veins and some compositional attributes (enriched in K, Ba, Pb, Zn and As) are features commonly considered to be characteristic of epithermal Au-Ag deposits.

Based on sulfur isotope data (Hauck 1984), REE contents and Sr-S isotopic ratios (Hein et al 2000), the mineralising fluids at Cape Vani were derived from seawater. However, the Cape Vani deposit shows marked differences in mineralogy and composition (e.g. trace element suite including Ag, As, Sb, and Hg) from known submarine hydrothermal manganese deposits and is considered by Liakopoulos et al. (2001) to be analogous to base-metal-rich epithermal deposits.

9.5 Timing and environment of epithermal mineralisation

The age constraints on epithermal mineralisation on Milos are poorly known, despite the strong stratigraphic control on mineralisation. New SHRIMP U-Pb dates of ca 2.18 ± 0.09 and 1.44 ± 0.08 Ma reported in Chapter 8 (section 8.2), from two major felsic volcanics units spatially associated with mineralisation on Milos, provide the first firm constraints on the age of epithermal mineralisation. Sample MIL 243 is a porphyritic dacite collected from the footwall of the Triades Au-Ag-barite deposit. The coherent dacite facies is mineralised and represents a pre- to syn-mineralisation intrusion. Sample MIL 130 is a coherent dacite facies also from the Triades area. The sample comes from a lava dome emplaced during the waning stages of mineralisation, and represents a post-mineralisation unit.

These new dates indicate that epithermal mineralisation at Triades occurred between the 2.18 ± 0.09 and 1.44 ± 0.08 Ma. Stratigraphic positions, ore types and alteration assemblages are similar at the other major epithermal deposits on Milos, strongly suggesting that they are all spatially and genetically related. Therefore, the new dates reported here are considered to bracket the age of epithermal mineralisation on the western sector of Milos. Importantly, these new dates, together with previously published K-Ar dates (Chapter 3), imply that a strong genetic link exists between a period of felsic volcanism and extension on Milos and mineralisation.

The palaeogeography of Milos during this time is believed to have comprised scattered islands (volcanic domes) flanked by shallow-water areas (c.f. Chapter 8). The exact water depth of the flanking shallow marine areas cannot be determined from volcanological studies, but given presence of in situ and intact bivalve shells and burrows in these

facies, water depths up to a few hundred metres are most likely (c.f. Johnson and Baldwin 1986).

The depositional setting of the Triades and Cape Vani deposits are well constrained as shallow marine (up to a few hundred metres) by the overlying post-mineralisation submarine volcanic successions and fluid inclusion data (c.f. Liakopoulos 2000). However, the setting of the Profitis Illias and Chondro Vouno deposits during mineralisation is less well constrained. The position of the palaeosurface at the time of was ~200 m above the present exposed level (Kilias et al. 2000). Both deposits occur in the proximal facies associations of a felsic cryptodome-pumice cone volcano which probably occupied a topographic high. In addition, detailed fluid inclusion data indicates that the source of the mineralising fluids at Profitis Illias was seawater (Kilias et al. 20001). Thus, it is inferred that the Profitis Illias and Chondro Vouno deposits formed on a topographic high that was shallow marine or perhaps, partially subaerial.

9.6 Exploration for epithermal ores in subaerial-shallow submarine environments: Volcanic facies models & relevant observations from Milos

The facies interpretations and facies architecture presented in Chapter 8 provide a framework for unravelling the setting of epithermal mineralisation on Milos and developing integrated exploration strategies. This section focuses on the relationships between the ores and their host rocks, with emphasis on the processes and resulting products relevant to exploration. Based on detailed volcanological observations, a general model for the development of epithermal deposits will be presented and implications of this model for global exploration strategies will be discussed.

Stratigraphic distribution and controls on mineralisation on Milos

The major epithermal ore deposits on Milos (e.g. Profitis Illias, Chondro Vouno-Amethyst and Triades) occur within a thick (up to 300 m) submarine pumice breccia and volcanogenic sedimentary succession. The submarine succession probably corresponds to a period of widespread explosive felsic volcanism (Figure 9.11). Although this host succession is very porous in nature, most of the epithermal ores crosscuts

stratigraphy (e.g. vein or breccia pipes). The main exception is the stratiform ore at Cape Vani.

Localisation of mineralisation at specific stratigraphic positions has been documented in many ancient submarine volcanic-hosted massive sulfide districts (e.g. Cambrian Mount Read Volcanics, Tasmania; Large 1992; Cambro-Ordovician Mount Windsor Subprovince, Queensland, Large et al. 2001; Skellefte district, Sweden, Allen et al. 1996). Many active sea-floor sulfide occurrences (e.g. PACMANUS hydrothermal field, eastern Manus Basin, Papua New Guinea, Binns and Scott 1993) are also characterised by mineralisation at specific stratigraphic positions. However, given boiling was an important depositional mechanism for the epithermal ores on Milos (c.f. Spartali 1994; Kilias et al. 2001), ore deposition will have been governed by temperature and ambient pressure conditions, as opposed to mixing with seawater. Therefore, epithermal mineral deposition in a shallow submarine setting is not be expected to be stratigraphically controlled, as in conventional VHMS environments.

Related volcano type

All of the main epithermal ores at Milos are spatially associated with a single submarine felsic cryptodome-pumice cone volcano (Chapter 8), and occur either in the proximal facies or medial to distal facies of this volcano. This volcano is similar in style to subaqueous-emergent rhyolitic dome-intrusion-tuff volcanoes found in other mineralised submarine successions (e.g. Kosaka district, Japan, Horikoshi 1969; Skellefte district, Sweden, Allen et al. 1996; Mount Windsor Subprovince, Australia, Paulick and McPhie 1999). On Milos, the volcanic succession is dominated of the area by proximal, medial and distal lithofacies of these volcanoes (c.f. covering ~85% of the area; Chapter 8). The Profitis Illias submarine felsic cryptodome-pumice cone volcano ranges in thickness from 400 m at the centre to several tens of metres at the margins, and ranges in diameter from 10 to 20 km.

The proximal facies association of the submarine felsic cryptodome-pumice cone volcanoes on Milos are characterised by thick, large-volume, syn-eruptive, felsic pumice breccias intruded by aphyric or weakly quartz-feldspar ± biotite-phyric rhyolite or rarely dacite cryptodomes and sills. Multiple intrusions are present and their contacts with

pumice breccia units typically involve peperite and intrusive hyaloclastite. The medial-distal facies (volcano flanks) are composed of thick intervals of felsic pumice breccia intercalated with units of the sandstone-conglomerate facies association (Chapter 4).

The Profitis Illias cryptodome-pumice cone volcano on Milos is interpreted to have been entirely subaqueous. However, given the relatively shallow-water depositional setting, it is plausible that rapid accumulation of pyroclastic units resulted in the net growth toward sea level in some cases. Furthermore, the subsequent high-level intrusion of cryptodomes probably caused up-doming of the pumice breccia pile (c.f. Minakami et al. 1951). Therefore, it is possible that part of the volcano reached sea-level and may have breached the air-water interface.

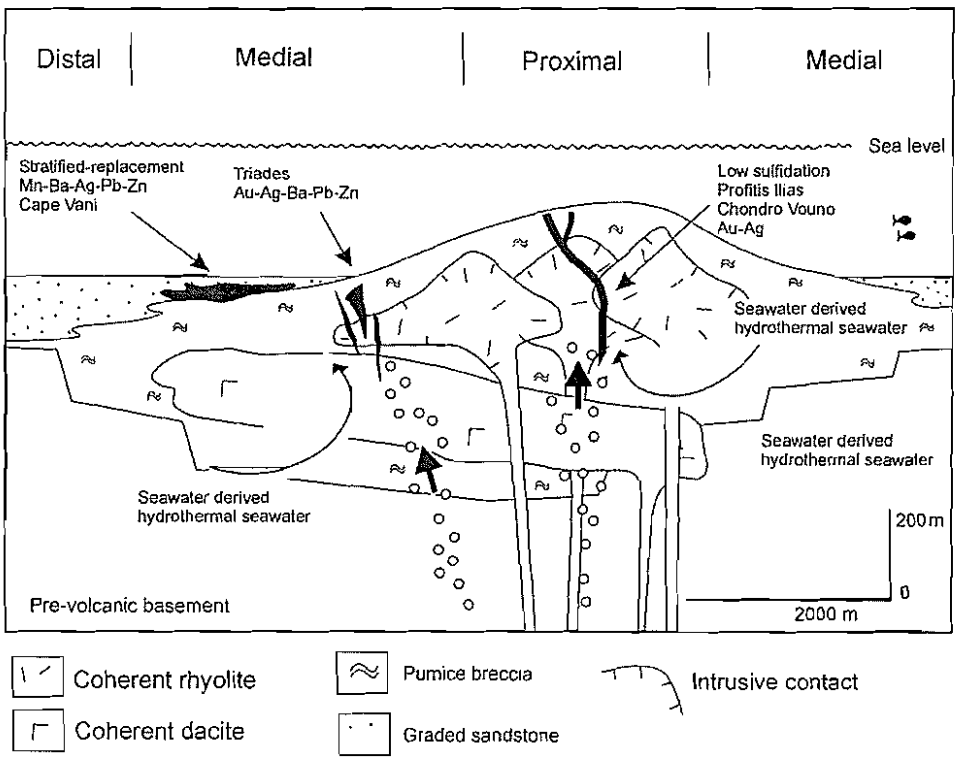

Figure 9.11 Schematic diagram illustrating the position of epithermal ore deposits within the Profitis Illias submarine felsic cryptodome-pumice cone volcano (Chapter 8). Epithermal deposits (e.g. Profitis Illias and Chondro Vouno) occupy a position which is closest to the

Role of depositional environment in mineralisation

Recent reviews of major epithermal deposits revealed that they are restricted to subaerial environments (Sillitoe 1989, 1999, 2002, in press; John 2001). In most modern subaerial volcanic environments, hydrothermal systems are dominated by meteoric water, which is heated by sub-volcanic intrusions and rises to the surface along favourable

structures. Where a volcano is dominantly very shallow submarine or partly emergent, as is interpreted for Milos, seawater replaces meteoric water. In shallow submarine settings the main influence on hydrothermal fluid flow will be buoyancy forces rather than gravity-driven fluid flow typical of subaerial environments. Hence, hydrothermal discharge will be concentrated in the summit region of the volcano, rather than the flanks (Hannington et al. 1999). Consequently, low-sulfidation, neutral-chloride hydrothermal fluids would have prevailed in the proximal facies associations (e.g. Profitis Illias and Chondro Vouno-Amythest). Secondary hydrothermal cells dominated by cooler denser seawater, may develop on the flank, resulting in extensive leaching of base metals and other chloride-complexed elements (e.g. barium) from the volcanic rocks (e.g. Triades and Cape Vani).

Boiling is generally recognised as an important mechanism for ore precipitation because of cooling of the fluids during decompression and the large increase in pH that accompanies loss of dissolved gases (Drummond and Ohmoto 1985). At such depths below ocean surface (<100-300 m), processes such as boiling would have played an important role in ore deposition on Milos.

9.7 Global perspective

Transitional shallow submarine-to-subaerial volcanic environments in present-day volcanic arcs or within ancient successions are characterised by a wide range of mineral deposit types (Sillitoe 1989; Table 9.2). A number of the mineral deposits being discovered in these environments have characteristics in part typical of subaerial epithermal deposits, but they also resemble submarine VHMS deposits (Hannington and Herzig 2001).

Chapter 10
Synthesis: a Pliocene-Pleistocene palaeogeographic reconstruction and volcanic evolution of Milos Island

10.1 Introduction

In this chapter, the Pliocene-Pleistocene palaeogeographic setting and volcanic evolution of Milos Island are summarised. The similarities between the volcanic evolution of Milos and another mineralised submarine-subaerial volcanic succession (Panarea Island, Aeolian arc, Italy) are also considered. Detailed analysis of volcanic facies (Chapter 4 and 7), in particular those associated with felsic cryptodomes (Chapter 5) and generated by submarine explosive eruptions (Chapter 6), has helped to constrain the facies architecture, depositional environment, stratigraphy and setting of mineralisation. Major advances have been made in understanding the location, character and geometry of the dominantly felsic, shallow submarine to subaerial volcanic centres (Chapter 8), and the genetic links between volcanic processes, the growth of the island and epithermal-style mineralisation (Chapter 9).

10.2 Palaeogeographic reconstruction and evolution of Milos Island

Schematic reconstructions of the inferred Pliocene-Pleistocene palaeogeography and range of volcanic and sedimentary environments are presented in Figures 10.1 to 10.4. Constraints on the Eocene to Miocene setting of volcanic activity are reviewed, followed by a discussion of the palaeogeographic model.

Mesozoic basement and Neogene sedimentary formations

The oldest exposed rocks on Milos belong to the Mesozoic Cycladic Crystalline Complex, and form the basement to the volcanic and sedimentary units. On Milos, the complex consists principally of isoclinally folded chlorite, actinolite and glaucophane schists of greenschist and blueschist metamorphic grade.

In the northern, southern and western sectors of Milos, the Mesozoic metamorphic rocks are unconformably overlain by the Neogene sedimentary group. This succession of distinctive brown to red limestone intercalated with conglomerate, breccia and sandstone is best exposed along the southern coast of Milos. The group has a maximum measured stratigraphic thickness of 180 m. Sedimentary rocks in this group have mixed provenance that includes the Mesozoic basement and other sedimentary sources. This implies that the Mesozoic metamorphic rocks were exposed to erosion during the Neogene. At locations that are the present-day margins of the island, basement debris was shed onto a shallow marine shelf (Neogene sedimentary group).

The Neogene sedimentary group is exposed to the west of the Firiplaka Fault (Figure 10.1). Conversely, the absence of the dominantly marine Neogene sedimentary rocks east of the Firiplaka Fault indicates that the Mesozoic metamorphic rocks of the southeastern sector of the island were most likely topographically high (possibly shoaling or subaerial), therefore reducing Neogene sedimentation in this area. The undulating topography exhibited by basement outcrops suggests that the palaeogeography during the Neogene comprised a small island or perhaps a group of small islands in the southeast, flanked by shallow- to deep-marine areas.

Upper Pliocene-Pleistocene volcanic evolution

The Upper Pliocene-Pleistocene volcanic succession of Milos was constructed on Mesozoic metamorphic basement and Neogene sedimentary rocks. A compilation of radiometric dates (Chapter 8) indicates that the volcanic succession formed within about 3 million years and there is neither field nor geochronological evidence for any significant breaks. The facies architecture suggests depositional environments evolved from below to above wave base to subaerial in most areas, except at the southeastern sector of the island where pre-existing subaerial environments persisted.

Prior to volcanism, the Milos area is envisaged to have been a broad, relatively shallow marine shelf (up to a few hundred metres), with a shoreline and probably small islands in the southeast comprising mainly basement blocks. Conditions in the depositional environment during the onset of felsic volcanism are recorded by the sandstone-conglomerate facies association facies. Bioturbated and fossiliferous mudstone intervals

interbedded with pumice breccia near the base of the succession indicate deposition in a relatively shallow submarine environment. The presence of tabular, massive to graded beds typical of deposits from sediment gravity currents, and the absence of sedimentary structures indicative of wave action (e.g. oscillatory ripples or hummocky cross-stratification) are consistent with a setting below wave base.

Submarine felsic cryptodome-pumice cone volcanoes

The onset of explosive felsic volcanism generated thick pumice breccia facies (1 in Figure 10.1). Source vents were probably in water less than a few hundred metres deep. Close to the vent, water-logged pumice clasts, shards and crystals were deposited by water-supported gravity currents and settling. The initial gravity currents were overloaded with dense lithic clasts derived from vent-clearing explosions but later currents were pumiceous, reflecting open-vent explosivity and rapid waterlogging of abundant hot, pumice lapilli. The water column would have quickly become choked with glassy pumice lapilli and ash. Buoyant coarse pumice clasts accumulated at the water surface, forming pumice rafts that drifted away from the source. Waterlogging affected the finer pumice clasts first and eventually also the coarse pumice clasts. Initial fallout of water-logged coarse pumice clasts coincided with the waning stages of gravity-current deposition on the sea floor (Chapter 6).

Rhyolitic and dacitic cryptodomes (c.f. Chapter 5), partially emergent cryptodomes and sills subsequently intruded the thick pumice pile (2 in Figure 10.1). In most cases, the upper contacts of the intrusions are characterised by intrusive hyaloclastite, indicating emplacement into poorly consolidated, probably wet pumiceous volcaniclastic units. The intrusion of cryptodomes and sills disrupted the pumice breccia succession, and in many cases, presumably domed the sea floor. At least two felsic cryptodome-pumice cone volcanoes formed irregular low mounds on the sea floor. Parts of the original volcanic edifices emplaced subaqueously above wave base were probably easily eroded. Some observed historical shallow marine rhyolitic eruptions formed ephemeral islands that underwent several cycles of construction and degradation. For example, the 1953-57 submarine eruption of Tuluman volcano repeatedly formed islands, subject to erosion and submergence (Reynolds et al. 1980).

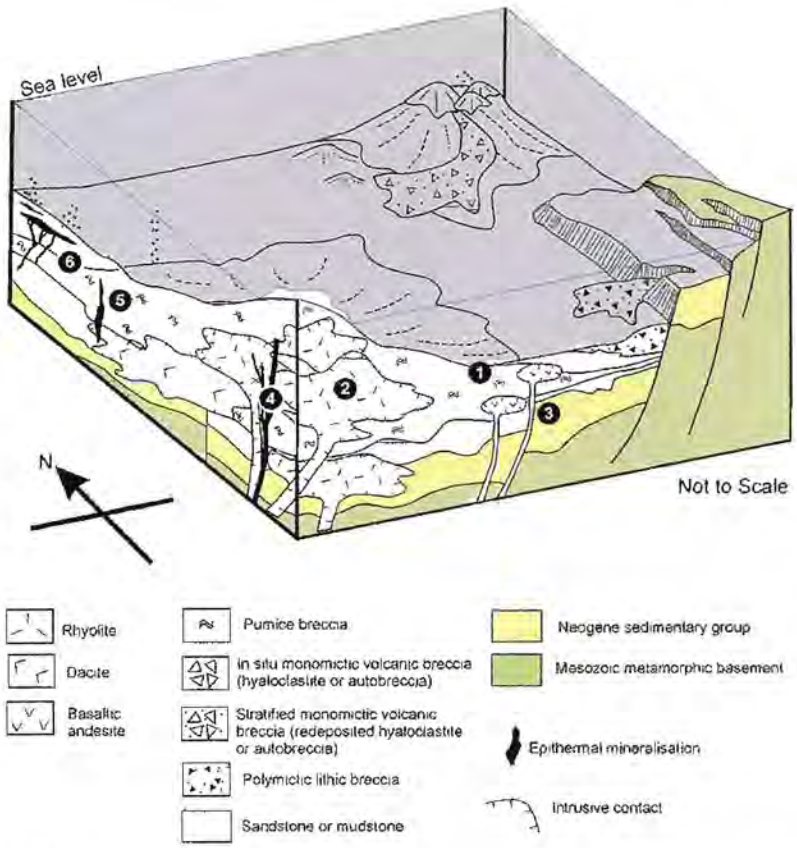

Figure 10.1 Schematic palaeogeographic reconstruction and facies architecture of Milos during the Late Pliocene (3 to 2.5 Ma). 1-Thick pumice breccia facies generated by submarine felsic explosive volcanism; 2-Rhyolitic and dacitic cryptodomes and sills; 3-Basaltic andesite intrusions. Hydrothermal systems, 4-Profitis Illias-Chondro Vouno; 5-Triades; 6-Cape Vani.

Basaltic andesite dykes are volumetrically minor and restricted in occurrence to the margins of the Profitis Illias felsic cryptodome-pumice cone volcano (3 in Figure 10.1). The dykes intruded the pumice breccia and lower part of the overlying sandstone-conglomerate facies.

The palaeogeography generated by the initial volcanism was topographically subdued, comprising low-angle fans of pumice breccia around rhyolitic-dacitic intrusion centres rising gently from the sea floor. Depositional environments of the proximal and medial parts of these cryptodome-pumice cone volcanoes were mainly shallow marine, whereas the medial to distal settings were mainly shallow to deeper marine. The depositional setting remained submarine. It is likely that accumulation of the main pumiceous units resulted in net growth towards sea level, countered by subsidence that kept pace with the rapid accumulation of volcanic and sandstone-conglomerate facies.

This episode of felsic volcanism is marked by the onset of significant hydrothermal activity in the southern and western part of the island. Strong buoyancy forces acting on hydrothermal fluids and the absence of gravity-driven fluid flow typical of subaerial environments may have concentrated hydrothermal discharge in the summit (proximal) area of the Profitis Illias volcanic centre, rather than the flanks (Hannington et al. 1999). Hence, low-sulfidation, neutral-chloride hydrothermal fluids would have prevailed in the proximal facies associations (e.g. Profitis Illias and Chondro Vouno; 4 in Figure 10.1). In the distal submarine parts of the volcanic centre, secondary hydrothermal cell dominated by denser, cooler seawater, resulted in extensive leaching of base metals and other chloride-complexed elements (e.g. barium) from the volcanic rocks (Liakopoulos 2000). Ensuing submarine mineralisation on the flanks of the crypto-dome-pumice cone volcano (e.g. Triades and Cape Vani; 5 and 6 in Figure 10.1) was largely synchronous with sedimentation of graded sandstone and mudstone facies.

Submarine dacitic and andesitic lava domes

The dominantly rhyolitic explosive and intrusive activity was followed by widespread effusive volcanism. Dacitic and andesitic lavas and domes (1 in Figure 10.2) were primarily erupted from a series of vents dispersed along north-northeast-striking faults. Autoclastic facies (non-stratified and stratified monomictic dacite and andesite breccia) and intercalated sandstone and conglomerate facies association provide a record of the character and setting of volcanic activity at the source vents during this phase of volcanism and indicate the initial depositional setting was shallow marine (below wave base).

Eruptions from sea floor vents built overlapping, thick (up to 300 m), dacitic and andesitic lava domes and hyaloclastite breccia, flanked and partially overlain by graded sandstone and minor mudstone facies. Periodic collapse of these domes and lavas resulted in aprons of redeposited hyaloclastite. Between Triades and Agathia, there are at least two thick, high-aspect-ratio dacitic lavas without intervening sedimentary facies, suggesting that these dacitic centres were emplaced rapidly (2 in Figure 10.2). Dacitic lavas and domes were constructional and formed local topographic highs rising several hundred metres above the adjacent sea floor. Local subsidence along north-northeast-striking faults accompanied and followed the emplacement of lavas.

Eruption and emplacement of the dacitic and andesitic lavas occurred syn- to post-mineralisation, as indicated by their stratigraphic position relative to the mineralisation. At Triades and Cape Vani, the basal parts of the lavas and domes are weakly altered, indicating that they were emplaced during the waning stages of hydrothermal activity and mineralisation.

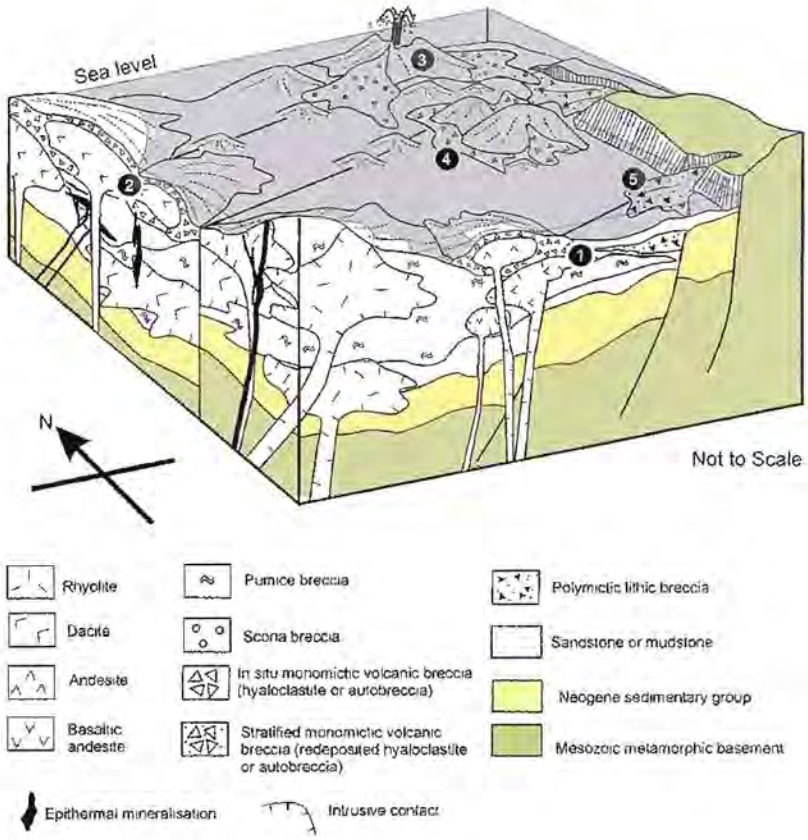

Figure 10.2 Schematic palaeogeographic reconstruction and facies of Milos during the Late Pliocene-Early Pleistocene (2.5 to 1.5 Ma). 1-Dacitic and andesitic lavas and domes; 2-Resedimented autobreccia and hyaloclastite associated with the growth of dacitic and andesitic domes; 3-Construction of a submarine andesitic scoria cone; 4-Syn-eruptive deposition of volcaniclastic breccia derived from dome collapse; 5-Post-eruptive basement-derived polymictic-lithic breccia.

In the northeastern part of the island, sedimentation was dominated by scoriaceous turbidity currents and accompanied by extrusion of minor andesitic lava. The abundance and morphology of juvenile andesitic scoria lapilli and bombs in the scoria-rich facies association are consistent with them being pyroclasts derived from weakly explosive, magmatic-volatile-driven strombolian eruptions. The eruptions built an ephemeral scoria cone subject to collapse and resedimentation, delivering scoria and bombs into deeper-water flanking environments. Given the relatively shallow sea water setting, the

edifice may have shoaled (3 in Figure 10.2). More powerful explosions produced lapilli and bombs that landed on the sea surface and settled rapidly to the sea floor. Disintegration of the quench-fragmented margins of a coeval andesitic lava or dome generated beds of massive andesite breccia intercalated with the scoria lapilli– and bomb-rich facies.

The sea floor was uneven, consisting of elevated volcanic centres (4 in Figure 10.2) separated by low-lying regions where stratigraphically equivalent sand and mud were deposited. The sandstone and mudstone units are dominated by volcanic quartz and feldspar, pumice and glass shards, suggesting a largely felsic volcanic source. The remaining fragment populations are clearly non-volcanic (detrital mica and polycrystalline quartz) and imply input from basement sources. Intervals of polymictic breccia-conglomerate facies contain abundant rounded rhyolitic and dacitic clasts that indicate reworking in high-energy environments (above storm wave base) and source areas that were subaerial to shallow marine. However, the graded thick beds in this facies were deposited below wave base. In other sections, sandstone beds display traction current structures (e.g. cross-beds) indicate that deposition was most likely above wave base in a high-energy, shoreline environment. Hence, depositional environments ranged from below to above wave base, and source areas were in very shallow water or subaerial.

Submarine-to-subaerial dacitic and andesitic domes

The submarine dacitic effusive volcanism was followed by construction of the Bombarda volcanic centre in the central part of the island (1 in Figure 10.3). Explosive rhyolitic eruptions generated thick, submarine, pumiceous volcaniclastic facies. Rinaldi and Campos Venuti (2003) suggested that the pumice breccia units were deposited in sea water about 50 m deep but that parts of the volcanic centre were in shallow water or subaerial. The Bombarda rhyolite dome occurs adjacent to the most proximal facies and probably occupies the vent. East-west extension and local subsidence accompanied and followed the explosive eruption (s).

Voluminous dacitic and andesitic lavas effectively culminated in emergence and established much of the present-day outline of the island. The lavas and domes were strongly constructional and formed local topographic highs rising up to 200 m above the adjacent area (2 in Figure 10.3). The occurrence of in situ pyroclastic facies (block-and-ash

and surge deposits) spatially associated with the domes and presence of palaeosols provide evidence that some areas were subaerial (3 in Figure 10.3). The large, biotite-quartz-phyric Halepa rhyolite lava was emplaced in the central part of the island (4 in Figure 10.3).

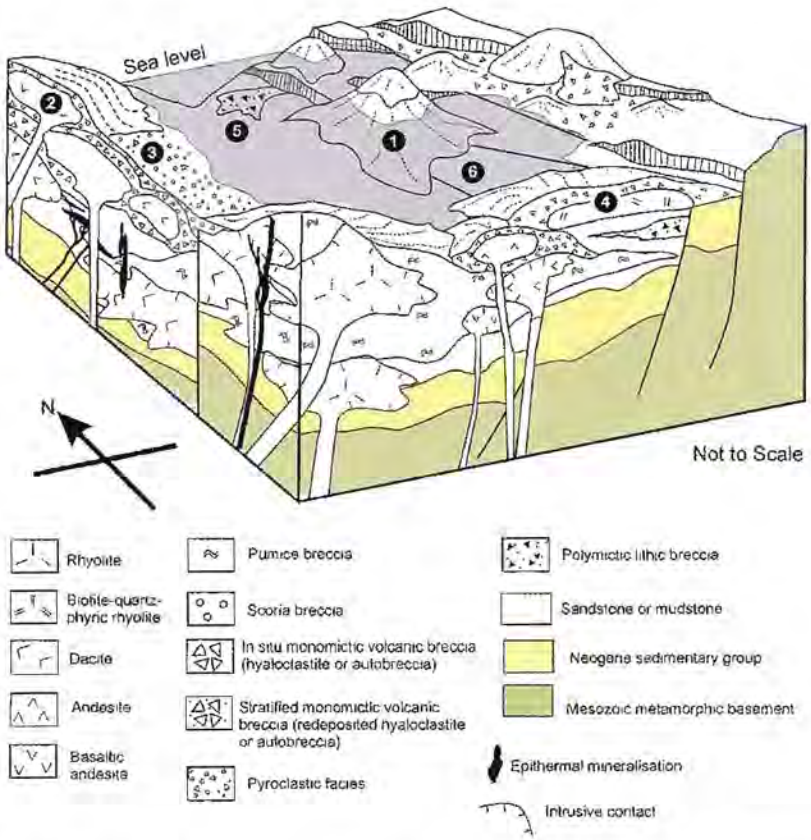

Figure 10.3 Schematic palaeogeographic reconstruction and facies of Milos during the Early Pleistocene (1.5-0.5 Ma). 1-Construction of a submarine felsic dome-cryptodome-pumice cone volcano; 2- Submarine-to-subaerial dacitic and andesitic lavas and domes; 3-Syn-eruptive deposition of volcaniclastic breccia derived from dome collapse; 4-Rhyolitic lava and associated autoclastic breccia; 5-Local influx of turbidites from reworking of detritus from dormant volcanic centres; 6-Syn-volcanic faults.

Thick (5-70 m) and laterally restricted intervals of graded sandstone, pumice breccia, polymictic breccia-conglomerate and fossiliferous mudstone indicate that the central part of Milos was still partly occupied by a relatively low-lying depression (Gulf of Milos), possibly open to the ocean in the west (5 in Figure 10.3). Sedimentation was dominated by the primary and reworked products of felsic explosive eruptions and the depositional setting was shallow marine. Several N-S-striking normal faults were active at this time, predominantly in the central and eastern sectors of the island, forming the Zefiria Graben (6 in Figure 10.3) and probably influenced the location of later volcanic centres.

Subaerial rhyolitic volcanism and phreatic explosions

Extensive subaerial emergence was achieved by the beginning of the Pleistocene (1.44 ± 0.08 Ma; Figure 10.3) in response to a combination of volcanic constructional processes and fault-controlled volcano-tectonic uplift. Subaerial rhyolitic volcanic activity since then has produced the two centres of Trachilas (1 in Figure 10.4) and Firiplaka (2 in Figure 10.4). Initial explosive rhyolitic eruptions from wholly subaerial vents built broad (up to 2.5 km in diameter), relatively high (up to 200 m) and circular pumice cones at each centre. A combination of phreatic and phreatomagmatic eruptions generated small-volume pyroclastic surge deposits (Campos Venuti and Rossi 1996). At both centres, the final phase of activity was characterised by the effusion of extensive, thick biotite-quartz-phyric rhyolitic lavas (3 in Figure 10.4). The lavas disrupted the outer pumice cone and flowed into the Gulf of Milos.

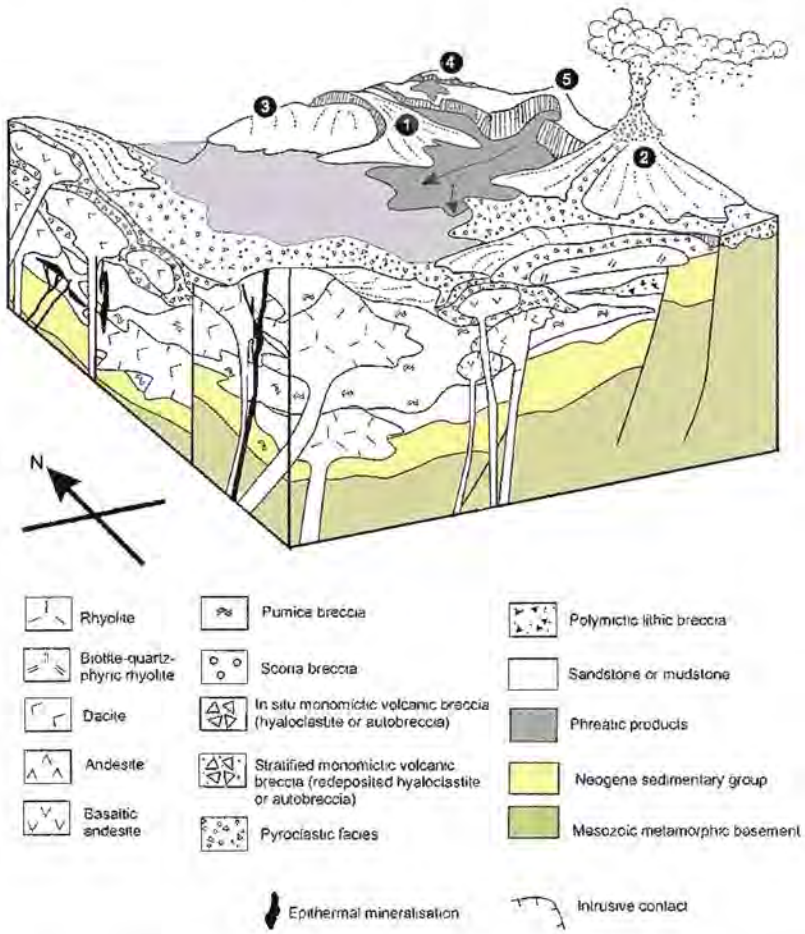

Figure 10.4 Schematic palaeogeographic reconstruction and facies of Milos during the Late Pleistocene (0.5 Ma) to present. 1 and 2-Construction of two subaerial rhyolitic pumice cone volcanoes at Trachilas and Firiplaka respectively; 3-Rhyolitic lava and associated autoclastic breccia; 4-Small phreatic craters; 5-Basement-derived mass-flow deposit.

Over much of the northern and southern parts of Milos, subaerial rhyolitic volcanism was accompanied by phreatic activity. Small steam-driven explosions formed numerous overlapping craters in the northern part of the Zefiria Graben (4 in Figure 10.4). Pyroclastic breccias (polymictic mud-matrix breccia facies) containing abundant altered clasts suggest that some explosions were caused by pressure variations within the upper 300 m of an active hydrothermal system (Fytikas et al. 1989). Principe et al. (2002) speculated that this phreatic activity originated in part from the failure of the metamorphic basement once located offshore from the present-day basement outcrops on the coast of Paliochori. The more proximal outcrops of lithic breccia in the cliffs at Paliochori are composed mainly of variably altered metamorphic basement clasts (massive schist-rich breccia facies). Phreatic activity has continued to very recent times (200 BC-200 AD; Traineau and Dalabakis 1989) and coincided with human habitation of the island.

10.3 A modern analogue for the Late Pliocene palaeogeography of Milos—Panarea Island, Aeolian arc, Italy

A modern analogue for the setting of Milos during the Late Pliocene is the shallow submarine to subaerial volcanic complex around the island of Panarea, in the western Mediterranean. Panarea is located between the Tyrrhenian back-arc and the Sicilian and Calabrian continental margin (Tyrrhenian Sea, Italy; Figure 10.5). The Panarea volcanic complex (PVC) is a region of major Quaternary calc-alkaline volcanism and crustal extension resulting from W-NW-directed subduction of the oceanic Ionian lithosphere beneath the continental lithosphere of the Sicilian and Calabrian plate (Barberi et al. 1994). The 8-km-long by 6-km-wide submerged PVC, from which the island of Panarea emerges, rises abruptly 800 m above the surrounding ocean floor, to water depths between 120 and 130 m and locally 100 m (Gamberi et al. 1997; Figure 10.6). The PVC comprises an area of approximately 70 km^2. The main tectonic feature of the submerged PVC is a NE-SW-trending extension zone (Gamberi et al. 1997) that controls hydrothermal activity (Figure 10.6).

The calc-alkaline lavas of the PVC range in composition from rhyolite to basalt, however, dacite is dominant (Gamberi et al. 1997). The submerged part of the PVC comprises rhyolite and dacite (dated from 0.143 to 1.01 Ma; Gabbianelli et al. 1990). The youngest part of the PVC consists of subaerial rhyolitic lavas contemporaneous with

submarine basaltic lavas (Gabbianelli et al. 1990). Bimodal volcanism affected the central part of the PVC between 133 ± 9 ka and 10-20 ka (Gamberi et al. 1997). This volcanism produced the emergent rhyolitic dome of Bassiluzzo Island in the northeastern part of the volcanic complex and basaltic tuff cones on Panarea Island. Dacitic eruptions have generated submarine pyroclastic deposits and lavas and domes.

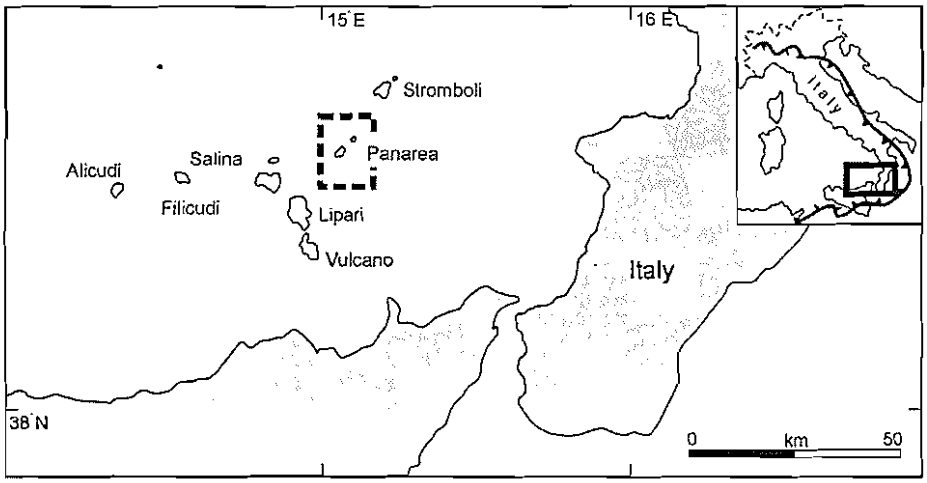

Figure 10.5 Panarea is located at the southern end of the Aeolian arc in southern Italy (inset). The black barbed line represents the W-NW-directed subduction of the Ionian lithosphere (north and east) beneath the continental Sicilian and Calabrian plate (west). Panarea Island (dashed black line) is located north of Sicily, between Lipari and Stromboli.

Sea floor low-temperature hydrothermal Fe-rich deposits have been identified in three zones of the PVC: the SW platform, the Basiluzzo area and the Secca dei Pesci (Figure 10.6). Seafloor hydrothermal discharges and associated mineralisation are widely distributed around the PVC and are related to topographic depressions, active faults and recent lavas (Savelli et al. 1999). Several active high-temperature sediment-hosted sulfide deposits (16.89 wt% Zn, 4.7 wt% Pb, 11.60 wt% Ba) occur in a small submarine depression (about 1 km^2) located south of the emergent rhyolitic dome of Basiluzzo in water ranging from 55 to 80 m deep (Savelli et al. 1999). Hydrothermal mineralisation is accompanied by argillic alteration, composed of kaolinite, montmorillonite, quartz and cristobalite (Gamberi et al. 1999). Significantly, mineralisation occurs in volcaniclastic-dominated stratigraphy and is spatially and possibly temporally associated with rhyolitic to dacitic volcanic centres. Most deposits occur in the central parts of these volcanic centres.

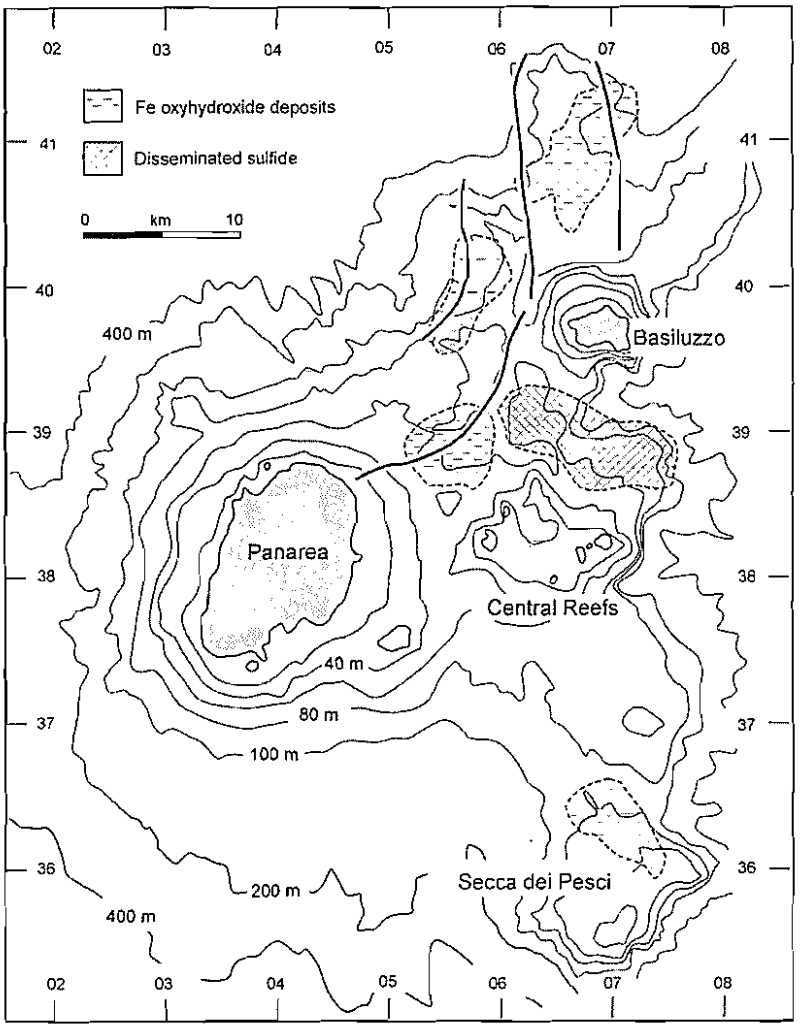

Figure 10.6 Sea floor multibeam bathymetry and metalliferous deposits of the Panarea volcanic complex (after Savelli et al. 1999).

The early palaeogeographic setting of Milos (3 to 2.5 Ma; Figure 10.1) is envisaged to have been similar to that of the modern PVC (Figure 10.7). Both cases involve compositionally and texturally diverse successions of calc-alkaline volcanic rocks in a relatively shallow but dominantly below-wave-base submarine settings. In addition, sedimentation includes episodic influxes of pyroclasts from explosive felsic eruptions of shallow-submarine vents and detritus from other non-volcanic sources. The style and setting of eruptions represented by the dominantly felsic-intermediate volcanic succession on Milos during the Late Pliocene are interpreted to have been similar to the volcanism in the PVC (e.g. Gabbianelli et al. 1990).

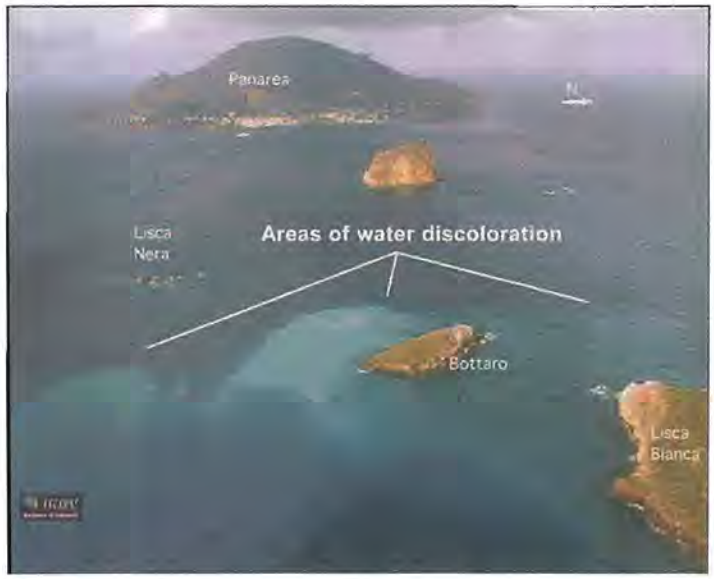

Figure 10.7 Aerial photograph of the Panarea Island (Central Reefs) with water discolouration evident on 4 November 2002. Courtesy of the Istituto Nazionale di Geofisica Vulcanologia (Catania).

10.4 Implications for comparable volcanic successions

The research undertaken here has significant relevance to understanding comparable modern and ancient felsic submarine-subaerial volcanic successions and assessing their prospectivity for either epithermal- or massive sulfide-style mineralisation.

1. The present study has contributed detailed information on the volcanic facies associations generated by felsic to intermediate eruptions in a shallow submarine-subaerial environment. Submarine parts of the volcanic succession are characterised by marine fossils, bioturbation, and bedforms typical of gravity current and water-settling processes. Palaeosols and primary pyroclastic density current deposits occur in the subaerial sections.

2. Relatively shallow-water submarine explosive eruptions of felsic magmas appear to have been relatively common in this island arc volcano. These eruptions generated distinctive facies which reflect the fact that the ambient fluid was seawater rather than air. One of the most conspicuous characteristics is the larger size of juvenile pumice clasts in submarine compared with subaerial products: in the FPB (Chapter 6), juvenile pum-

ice clasts are very coarse (up to 6.5 m), presumably due to enhanced preservation of large pyroclasts erupted and deposited in water and also possibly because magmatic-volatile-driven fragmentation may be less efficient in a subaqueous setting, given the higher confining pressures and reduced rates of decompression. Hence, the products of submarine explosive eruptions can be readily identified, and help constrain the eruption style, proximity to source and environment of deposition.

3. Research on the chemistry of subaerial epithermal and submarine volcanogenic massive sulfide deposits has revealed a great deal with regard to ore genesis. However, few of these studies have evaluated the interrelationships between volcanism and mineralisation. Facies analysis of the host succession on Milos has constrained the style and setting of volcanism during mineralisation. The locations of the mineralising hydrothermal systems in relation to the host volcanic centre have identified. Facies models have been provided for mineralised felsic volcanic centres that can assist mineral exploration in shallow submarine volcanic settings.

4. The literature on epithermal gold deposits reveals the common belief that they are restricted to subaerial settings (e.g. Sillitoe 1989, 1999, 2002, in press; John 2001). The epithermal veins on Milos add to the increasing number of exceptions to the general scheme. This analysis has shown that epithermal-style mineralisation was temporally and spatially related to felsic cryptodome-pumice cone volcanoes. These volcanoes formed scattered small islands flanked by shallow-water areas.

10.5 Avenues for future research

This comprehensive analysis of the volcanic succession exposed on Milos concentrated on the recognition of distinctive facies and facies associations, with the aim of reconstructing the Upper Pliocene to Pleistocene volcanic and sedimentary facies architecture. However, the character of the volcanic and sedimentary successions exposed on the neighbouring islands of Kimolos and Polyegos remain poorly understood. Neither have these islands been extensively explored for epithermal- or VHMS-related mineralisation. The limited reconnaissance mapping carried out during this research indicates that the volcanic successions are similar in character to those on Milos, and would be amenable to this type of study.

This research provides a detailed, internally consistent geological framework for future geochemical and isotope studies of Milos. In addition, this framework is an excellent basis for determining the textural modification of volcanic facies subject to alteration. Textural and compositional criteria that discriminate between diagenetic and hydrothermal alteration associated with both epithermal and VHMS mineralisation could help in the identification of prospective areas on Milos and in other similar successions. An in-depth evaluation of the application of short-wave infrared spectral analysis (PIMA) to alteration studies around mineralisation is highly desirable. No study of this type has been previously completed at Milos.

Further age dating would clarify and refine the field stratigraphy, and give more detailed information on the longevity of the volcanic field as a whole, the longevity of single volcanic centres and frequency of explosive eruptions and tectonic events.

10.6 Summary

A detailed and multidisciplinary analysis of the Upper Pliocene to Pleistocene volcanic succession on Milos has led to a better understanding of the stratigraphy and palaeogeographic setting. Milos comprises a compositionally and texturally diverse succession of calc-alkaline volcanic rocks that record a transition from a relatively shallow, but dominantly below-wave-base setting to a subaerial one. The present island was constructed in the past ~3 Ma from the products of multiple, mainly felsic volcanic centres, involving:

- growth of large submarine felsic cryptodome-pumice cone volcanoes broadly synchronous with the formation of epithermal mineralisation (basal pyroclastic series);
- submarine effusion and intrusion of several dacitic to andesitic lavas and domes (complex of domes and lava flows);
- subaerial emergence via effusion of dacitic and andesitic lavas and domes associated with small-volume pyroclastic deposits (pyroclastic series and lava domes) and;
- subaerial explosive eruptions, forming rhyolitic pumice-cone volcanoes, followed

by rhyolite lavas (rhyolitic complex of Firiplaka and Trachilas), and accompanied by widespread phreatic activity.

The palaeogeography during mineralisation is interpreted to have comprised scattered islands (cryptodome-pumice cone volcanoes) flanked by shallow-marine areas. A modern analogue for this setting is the submerged volcanic complex around Panarea Island, Aeolian volcanic arc (Italy).

References

Akaku K (1988) Geochemistry of mineral deposition from geothermal waters: Deposition processes of common minerals found in various geothermal fields and case study in the Fushime geothermal field. Chinestu 25: 44-61 (in Japanese)

Allen RL (1990) Subaqueous welding, or alteration, diagenetic compaction and tectonic dissolution? IAVCEI Congress, Mainz, Germany, September 3-8, Abstracts Volume, p 2

Allen RL (1992) Reconstruction of the tectonic, volcanic and sedimentary setting of strongly deformed Zn-Cu massive sulfide deposits at Benambra, Victoria. Econ Geol 87: 825-854

Allen RL, Weihed P, Svenson S-A (1996) Setting of Zn-Cu-Au-Ag massive sulfide deposits in the evolution and facies architecture of a 1.9 Ga marine volcanic arc, Skellefte district, Sweden. Econ Geol 91: 1022-1053

Allen SR, Stewart AL (in press) Products of explosive subaqueous felsic eruptions based on examples from the Hellenic Island Arc, Greece. In: White JDL, Smellie JL, Clague D (Eds.) Explosive subaqueous volcanism. AGU monograph.

Allen SR, Cas RAF (1998) Lateral variation within coarse co-ignimbrite lithic breccias of the Kos Plateau Tuff, Greece. Bull Volcanol 59: 356-377

Allen SR, McPhie J (2000) Water-settling and resedimentation of submarine rhyolite pumice at Yali, eastern Aegean, Greece. J Volcanol Geotherm Res 95: 285-307

Altherr R, Henjes-Kunst F, Matthews A, Friedrichsen H, Hansen BT (1988) O-Sr isotope variations in Miocene granitoids from the Aegean: evidence for an origin by combined assimilation and fractional crystallisation. Contrib Mineral Petrology 100: 528-541

Altherr R, Kreuzer H, Wendt I, Lenz H, Wager GA, Keller J, Harre W, Hohndorf A (1992) A late Oligocene/early Miocene high temperature belt in the Attic-Cycladic crystalline Complex (SE Pelagonian, Greece). Geologisches ahrbuch, Reihe E Geophysik 23: 97-164

Andriessen PAM (1978) Isotopic age relations within the polymetamorphic complex of the island of Naxos (Cyclades, Greece). PhD Thesis Verhergen ZWO-aboratotium Voor Isotopen Geologie, Amsterdam

Andriessen PAM, Banga G, Hebeda EH (1987) Isotopic age study of Pre-Alpidic rocks in the basal units on Naxos, Sikinos and Ios, Greek Cyclades. Geolo en Mijnbouw 6: 3-14

Angelier J, Cantagrel JM, Vilminot JC (1977) Neotectonique cassante et volcanisme plio-quaternaire dans l'arc égéen interne: L'Ile de Milos (Grece). Bull Soc Géol France 19: 119-121

Angelier J, Lydéris N, Le Pichon X, Barrier E, Huchon P (1982) The tectonic development of the SAVA and the Sea of Crete: a synthesis. Tectonophysics 86: 159-196

Ayres LD, Peloquin AS (2000) Subaqueous, Paleoproterozoic, metarhyolite dome-flow-cone complex, Flin Flon greenstone belt, Manitoba, Canada. Precambrian Res 101: 211-235

Bagnold RA (1956) The flow of cohesionless grains in fluid. Phil Trans Royal Soc London A242:235-297

Baksa C, Nemeth JC, Csillag J, Foldessy J, Zelenka T (1980) The Recsk porphyry and skarn copper deposit, Hungary. In: Jankovic S, Sillitoe RH (Eds) European copper deposits. Society for Geology Applied to Mineral Deposits, Special Publication 1, pp 73-82

Barberi F, Innocenti F, Manetti P, Peccerillo A, Villari L, Poli G (1981) The evolution of the SAVA and the Aeolian arc volcanism in space and time: a comparison. IAVCEI symposium Aug 18-Sept 9 1981, Tokyo, pp 32-33

Barberi F, Gandino A, Gioncada A, La Torre P, Sbrana A, Zenucchini C (1994). The deep structure of the Eolian arc (Filicudi-Panarea-Vulcano sector) in light of gravity, magnetic and volcanological data. J Volcanol Geotherm Res 61: 189-206

Batiza R, Fornari DJ, Vanko DA, Lonsdale P (1984) Craters, calderas, and hyaloclastites on young Pacific seamounts. J Geophys Res 89: 8371-8390

Barrett TJ, Sherlock RL (1996) Geology, lithogeochemistry, and volcanic setting of Eskay Creek Au-Ag-Cu-Zn deposit, northwestern British Columbia. Explor Mining Geol 5: 339-368

Barton M, Salter VJM, Huijsmans JPP (1983) Sr isotope and trace element evidence for the role of continental crust in calc-alkaline volcanism on Santorini and Milos, Aegean Sea, Greece. Earth Planetary Sci Lett 63: 273-291

Bentz A, Martini H (1968) Lehrbuch der angewandten Geologie 2. Band 1. Teil Ferdinard Enke Verlag, Stuttgart, 280 pp.

Bigazzi G, Radi D (1981) Datazione con trace di fissione per l'identificazione della provenienza dei manufatti di ossidiana. Riv Sci Preist 36: 223-250

Binns RA, Scott SD (1993) Actively forming polymetallic sulfide deposits associated with felsic volcanic rocks in the eastern Manus back-arc basin, Papua New Guinea. Econ Geol 88: 2226-2236

Blake Jr MC, Bonneau M, Geyssant J, Kienast JR, Lepvrier C, Maluski H, Papanikolaou D (1981) A geological reconnaissance of the Cycladic blueschist belt, Greece. Geological Society of America Bulletin 92: 247-254

Blake S (1990) Viscoplastic models of lava domes. In: Fink JH (ed) Lava flows and domes. Emplacement mechanisms and hazard implications. Berlin, Springer-Verlag, pp 88-126

Bonnichsen B, Kauffman DF (1987) Physical features of rhyolite lava flows in the Snake River Plain volcanic province, southwestern Idaho. Geo Soc Am Spec Paper 212: 119-145

Boudon G, Camus GAG, Lajoie J (1993) The 1984 nuée-ardente deposits of Merapi volcano, Central Java, Indonesia: stratigraphy, textural characteristics, and transport mechanism. J Volcanol Geotherm Res 55: 327-342

Bottomer LR (1986) Epithermal silver-gold mineralisation in the Drake area, northeastern New South Wales. Aust J Earth Sci 33: 457-473

Botz R, Stuben D, Winckler G, Bayer R, Schmitt M, Faber E (1996) Hydrothermal gases offshore Milos Island, Greece. Chemical Geology 130: 161-173

Briqueu L, Javoy M, Lancelot JR, Tatsumoto M (1986) Isotope geochemistry of recent magmatism in the Aegean arc: Sr, Nd, Hf, and O isotopic ratios in the lavas of Milos and Santorini-geodynamic implications. Earth Planetary Sci Lett 80: 41-54

Brooks ER (1995) Palaeozoic fluidization, folding, and peperite formation, northern Sierra Nevada, California. Can J Earth Sci 32: 314-324

Brooks ER, Wood MW, Garbutt PL (1982) Origin and metamorphism of peperite and associated rocks in the Devonian Elwell Formation, northern Sierra Nevada, California. Geol Soc Am Bull 93: 1208-1231

Brown SJA, Barley ME, Krapež B, Cas RAF (2002) The Late Archean Melita Complex, Eastern Goldfields, Western Australia: shallow submarine bimodal volcanism in a rifted arc environment. J Volcanol Geotherm Res 115: 3003-327

Busby-Spera CJ (1986) Depositional features of rhyolitic and andesitic volcaniclastic rocks of the Mineral King submarine caldera complex, Sierra Nevada California. J Volcanol Geotherm Res 27: 43-76

Busby-Spera CJ, White JDL (1987) Variation in peperite textures associated with differing host-sediment properties. Bull Volcanol 49: 765-775

Bull S W, Cas R A F (1989) Volcanic influences in a storm and tide dominated shallow marine depositional system: the Late Permian Broughton Formation, southern Sydney Basin, Kiama, NSW, Australia. Aust J Earth Sci 36: 569-584

Campos Venuti M, Rossi RL (1996) Depositional facies in the Firiplaka rhyolitic Tuff Ring, Milos Island (Cyclades, Greece). Acta Vulcanologica 8 (2): 47-63

Carey S (1997) Influence of convective sedimentation on the formation of widespread tephra fall layers in the deep sea. Geology 25 (9): 389-842

Carman GD (1993) Transitional magmatic to epithermal mineralisation at Lihir Island gold deposit, PNG: Implications for the evolution of ore forming fluids from fertile magmas. National meeting SGEG Geol Soc Aus, pp 12

Cas RAF, Wright JV (1987) Volcanic successions, modern and ancient. London, Allen Unwin, pp 1-528

Cas RSF, Landis CA, Fordyce RE (1989) A monogenetic, Surtla-type, Surtseyan volcano from the Eocene-Oligocene Waiareka-Deborah volcanics, Otago, New Zealand: a model. Bull Volcanol 51: 281-298

Cas RAF, Allen RL, Bull SW, Clifford BA, Wright JV (1990) Subaqueous, rhyolitic dome-top tuff cones: a model based on the Devonian Bunga Beds, southeastern Australia and a modern analogue. Bull Volcanol 52: 159-174

Cashman KV, Fiske RS (1991) Fallout of pyroclastic debris from submarine volcanic eruptions. Science 253: 275-280

Christiansen RL, Lipman PW (1966) Emplacement and thermal history of a rhyolite lava flow near Fortymile Canyon, southern Nevada. Geol Soc Am Bull 77: 671-684

Christanis K, Seymour K, St (1995) A study of scale formation: an analogue of meso- to epithermal ore formation in the volcano of Milos, Aegean Arc, Greece. Geothermics 24: 541-552

Christidis GE (1995) Mechanism of illitization of bentonites in the geothermal field of Milos island Greece: Evidence based on mineralogy, chemistry, particle thickness and morphology. Clay and Clay Mineral 43: 569-585

Christidis G, Dunham AC (1993) Compositional variation in smectites: Part I. Alteration of intermediate volcanic rocks. A case study from Milos Island, Greece. Clay Minerals 28: 255-273

Christidis GE, Macropoulos T (1995) Origin and mineralogical characteristics of the bentonite deposits of eastern Milos. Geol Soc Greece Sp Pub 4: 677-683

Christidis GE, Scott PW, Marcopoulos T (1995) Origin of the bentonite deposits of eastern Milos, Aegean, Greece: geological, mineralogical and geochemical evidence. Clay and Clay Mineral 43: 63-77

Christidis G, Dunham AC (1997) Compositional variations in smectites. Part II: alteration of acidic precursors, a case study from Milos Island, Greece. Clay Minerals 32: 253-270

Clift P, Blusztajn J (1999) The trace-trace element characteristics of Aegean and Aeolian volcanic arc marine tephra. J Volcanol Geotherm Res 92: 321-347

Clough BJ, Wright JV, Walker GP (1981) An unusual bed of giant pumice in Mexico. Nature 289: 49-50

Cole JW (1970) Structure and eruptive history of the Tarawera volcanic complex: New Zealand Journal of Geology and Geophysics 13: 879-902

Cole PD, Calder ES, Druitt TH, Hoblitt R, Robertson RS, Sparks RSJ, Young SR (1998) Pyroclastic flows generated by gravitational instability of the 1996-97 lava dome Soufriere Hills Volcano, Montserrat. Geophys Res Lett 25: 3425-3428

Colley H, Rice CM (1975) A kuroko-type ore deposit in Fiji. Econ Geol 70: 1373-1386.

Constatinidou H, Kilias S, Cheliotis I, Naden J, Shephard T, Simos I, Crossing J (1998) Mineralogy and chemistry of gold in the Profitis Illias epithermal deposits, Milos Island, Aegean Sea, Greece. Bull Geol Soc Greece XXXII (3): 157-164

Compston W, Williams IS, Kirschvink JL, Zhang Z, Ma Guogan (1992) Zircon U-Pb ages for Early Cambrian time-scale. J Geo Soc London 149: 171-184

Constatinidou H, Kilias S, Cheliotis I, Naden J, Shephard T, Simos I, Crossing J (1998) Mineralogy and chemistry of gold in the Profitis Illias epithermal deposits, Milos Island, Aegean Sea, Greece. Bull Geol Soc Greece XXXII (3): 157-164

Cooke D R, Simmons S F (2001) Characteristics and genesis of epithermal gold deposits. Reviews in Economic Geology 8: 221-244

Cronan DS, Varnavas SP (1999) Metalliferous sediments off Milos, Hellenic Volcanic Arc. Explor Mining Geol 8: 289-297

Crossing DJF (1994) The Midas project Milos, Greece. Internal report prepared for RGC Exploration Pty Ltd: 10 pp

D'Erasmo G (1924) Su alcuni fossili dell'isola di Milos raccolti dal dott. Zeitsch Volc 8: 230-237

De Ronde C, Hannington M, Stoffers P, Wright I, Gennerich H-H, Browne P, Herzig P (2000) Massive sulfide mineralisation associated with frontal arc volcano: Brothers hydrothermal systems, South Kermadec Arc, New Zealand. In: Gemmell JB, Pongratz J (Eds) Volcanic environments and massive sulfide deposits, programs and abstracts. CODES Special Publication 3: pp 75-77

de Rosen-Spence AF, Provost G, Dimroth E, Gochnauer K, Owen V (1980) Archean subaqueous felsic flows, Rouyn-Noranda, Quebec, Canada, and their Quaternary equivalents. Precambrian Res 12: 43-77

Dando PR, Hughes JA, Leahy Y, Niven SJ, Taylor LJ, Smith C (1995) Gas venting rates from submarine hydrothermal areas around the island of Milos, Hellenic Volcanic Arc. Cont Shelf Res 15: 913-929

Decher A, Bechtel A, Echle W, Friedrich G, Hoernes S (1996) Stable isotope geochemistry of bentonites from the island of Milos (Greece). Chem Geo 129: 101-113

Delliou EE (1989) Milos demonstration project. In: K Lowen, Straaste E, Garnish JD (eds) European Geothermal Uptake. Kluwer Academic Publication Dordrecht, pp 652

Dewey JF, Pittman III WC, Ryan WBF, Bonnin J (1973) Plate tectonics and evolution of the Alpine system. In RS Harmon, CW Rapela (eds) Andean Magmatism and its tectonic setting. Geological Society of America Bulletin 84: 3137-3180

Dewey JF, Sengőr AMC (1979) Aegean and surrounding regions: complex multiplate and continuum tectonics in a convergent zone. Geol Soc Am Bull 90: 84-92

Dimroth E, Cousineau P, Leduc M, Sanschagrin Y (1978) Structure and organization of Achaean basalt flows, Rouyn-Noranda area, Quebec, Canada. Can J Earth Sci 15: 902-918

Dimroth E, Yamagishi H (1987) Criteria for the recognition of ancient subaqueous pyroclastic rocks. Geol Surv Hokkaido Rep 58: 55-88

Dolozi MB, Ayres LD (1991) Early Proterozoic, basaltic andesite tuff-breccia: downslope, subaqueous mass transport of phreatomagmatically generated tephra. Bull Volcanol 53: 477-495

Doyle M.G, McPhie J (2000) Facies architecture of a silicic intrusion-dominated volcanic centre at Highway-Reward, Queensland, Australia. J Volcanol Geotherm Res 99: 79-96

Doyle MG, McPhie J (2001) Shallow-water microbialite-volcaniclastic facies association in the Cambro-Ordovician Mt Windsor subprovince, Australia. Aust J Earth Sci 48: 815-831

Druitt TH, Sparks RSJ (1982) A proximal ignimbrite breccia facies on Santorini, Greece. J Volcanol Geotherm Res 13: 147-171

Drummond SE and Ohmoto H (1985) Chemical evolution and mineral deposition in boiling hydrothermal systems. Econ Geol 80: 126-147

Duermeijer CE, Nyst M, Meijer PTh, Langereis CG, Spakman W (2000) Neogene evolution of the Aegean arc: paleomagnetic and geodetic evidence for a rapid and young rotation phase. Earth Planetary Sci Lett 176: 509-525

Eaton S, Robertson AHF (1993) The Miocene Pakhna Formation, Cyprus and its relationship to the Neogene tectonic evolution of the Eastern Mediterranean. Sediment Geol 86: 273-296

Ericsson T, Papatheodourou K, Sklavounos S, Filippidis A (1992) Oxidation state of biotite from heated perlite samples from Chivadolomni deposits in Milos island, Greece. Neues Jahrbuch fur Miner 1: 1-12

Fink JH (1980) Gravity instability in the Holocene Big and Little Glass Mountain rhyolitic obsidian flows, northern California. Tectonophysics 66: 147-166

Fink JH (1983) Structure and emplacement of a rhyolitic obsidian flow: Little Glass Mountain, Medicine Lake Highland, northern California. Geol Soc Am Bull 94: 362-380

Fink JH (1993) The emplacement of silicic lava flows and associated hazards. In: Kilburn CJ, Luongo G (eds.) Active Lavas. University College London Press, pp 5-24

Fink JH, Manley CR (1987) Origin of pumiceous and glassy textures in rhyolitic flows and domes. Geol Soc Am Spec Pap 212: 77-88

Fink JH, Griffiths RW (1990) Radial spreading of viscous-gravity currents with solidifying crust. J Fluid Mechanics 221: 485-510

Fink JH, Malin MC, Anderson SW (1990) Intrusive and extrusive growth of the Mount St. Helens lava dome. Nature 348: 435-437

Fisher RV (1960) Classification of volcanic breccias. Geol Soc Am Bull 71: 973-982

Fisher RV (1966) Rocks composed of volcanic fragments. Earth Sci Rev 1: 287-298

Fisher RV and Waters AC (1970) Base surge bedforms in maar volcanoes. Am J Sci 268: 157-180

Fiske RS (1963) Subaqueous pyroclastic flows in the Ohanapecosh Formation, Washington. Geol Soc Am Bull 74: 391-406

Fiske RS, Matsuda T (1964) Submarine equivalents of ash flows in the Tokiwa Formation, Japan. Am J Sci 262: 76-161

Fiske RS, Cashman KV, Shibata A, Watanabe K (1998) Tephra dispersal from Myojinsho, Japan, during its shallow submarine eruption of 1952-1953. Bull Volcanol 59: 262-275

Fiske RS, Naka J, Iizasa K, Yuasa M, Klaus A (2001) Submarine silicic caldera a the front of the Izu-Bonin arc, Japan: Voluminous seafloor eruptions of rhyolite pumice. GSA Bull 113: 813-824

Fitzsimons MF, Dando PR, Hughes JA, Thiermann F, Akoumianaki IO, Pratt SM (1997) Submarine hydrothermal brine seeps off Milos, Greece: observations and geochemistry. Marine Chemistry 57: 325-340

Fouquet Y, Stackelberg U, Charlou JL, Erzinger J, Herzig PM, Muhe R, Wiedicke M (1993) Metallogenesis in back-arc environments: the Lau basin example. Econ Geol 88: 2154-2181

Fytikas M (1977) 1:25 000 Geological Map of Milos. Institute of Geology and Mineral Exploration (Greece)

Fytikas M (1989) Updating of the geological and geothermal research on Milos Island. Geothermics18 (4): 485-496

Fytikas M, Marinelli G (1976) Geology and geothermics of the island of Milos (Greece). Inst of Geological and Mining Research (IGME). (unpubl), 58pp

Fytikas M, Innocenti P, Manetti R, Mazzuoli R, Peccerillo A, Villari L (1984) Tertiary to Quaternary volcanism in the Aegean region. In: Dixon JE, Robertson AHF (eds) The geological evolution of the Eastern Mediterranean. Geol Soc London Spec Publ 17, pp 687-699

Fytikas M, Innocenti F, Kolios N, Manetti P, Mazzuoli R, Poli G, Rita F, Villari L (1986) Volcanology and Petrology of volcanic products from the island of Milos and neighboring islets. J Volcanol Geotherm Res 28:297-317

Fytikas M, Vougioykalakis G (1993) Volcanic structure and evolution of Kimolos and Polyegos (Milos island group). Bull Geol Soc Greece XXVII/2:221-237

Gabbianelli G, Gillot PY, Lanzafame G, Romagnoli C, Rossi PL (1990) Tectonic and volcanic evolution of Panarea (Aeolian Islands, Italy). Marine Geology 92: 313-326

Gamberi F, Marani M, Savelli C (1997) Tectonic, volcanic and hydrothermal features of a submarine portion of the Aeolian arc (Tyrrhenian Sea). Marine Geo 140: 167-181

Gautier P, Brun J-P (1994) Crustal-scale geometry and kinematics of late-orogenic extension in the central Aegean (Cyclades and Evvia Island). Tectonophysics 238: 399-424

Gemmell JB, Binns RA, Parr JM (1999) Submarine, high sulfidation alteration within DESMOS caldera, Manus Basin, PNG. In: Stanley CJ et al. (Eds) Mineral deposits: Processes to processing. Fifth Biennial SGA Meeting and the Tenth Quadrennial IAGOD Symposium, London, Proceedings, pp 503-506

Gifkins CC, Allen RL (2001) Textural and chemical characteristics of diagenetic and hydrothermal alteration in glassy volcanic rocks: examples from the Mount Read Volcanics, Tasmania. Econ Geol 96 (5): 973-1002

Goto Y, McPhie J, (1998) Endogenous growth of a Miocene submarine dacite cryptodome, Rebun Island, Hokkaido, Japan. J Volcanol Geotherm Res 84: 273-286

Graff JM, Long PE, Aydin A (1989) Use of joint-growth directions and rock textures to infer thermal regimes during solidification of basaltic lava flows. J Volcanol Geotherm Res 38: 309-324

Griffiths RW, Fink JH (1993) Effects of surface cooling on the spreading of lava flows and domes. J Fluid Mechanics 252: 667-702

Grossenbacher KA, McDuffie SM (1995) Conductive cooling of lava: columnar joint diameter and stria width as functions of cooling rate and the thermal gradient. J Volcanol Geotherm Res 69: 95-103

Hamasaki S (1994) The internal structure of a rhyolite intrusion and the process of emplacement; an example from the Izu-miyama porcelain stone deposit, Saga prefecture, southwestern Japan. Bull Volcanol Soc Jpn 39: 91-98

Hannington MD, Herzig PM (1993) Shallow submarine hydrothermal systems in modern island arc settings. Geological Association of Canada Program with Abstracts 18: p A40

Hannington MD, Herzig PM (2000) Submarine epithermal deposits and the VMS-epithermal transition: a new exploration target. CODES Special Publication 3: pp 75-77

Hanson RE, Wilson TJ (1993) Large-scale rhyolite peperites (Jurassic southern Chile). J Volcanol Geotherm Res: 54: 247-264

Hauck M (1988) Kuroko-type ore deposits on the Aegean Islands, Greece. In Friedrich G M, Herzig P M (Eds.) Base Metal Sulfide Deposits. Springer Verlag, Berlin, pp 216-228

Hedenquist JW (1987) Mineralisation associated with volcanic-related hydrothermal systems in the circum-Pacific basin. In: Horn MK (ed) Transactions of the 4th Circum-Pacific Energy and Mineral Resources Conference, Singapore, 1986. Tulsa, Oklahoma, American Association of Petroleum Geologists, pp 513-524

Hedenquist JW, Henley RW (1985) Hydrothermal eruption in the Waiotapu Geothermal System, New Zealand: their origin, associated breccias, and relation to precious metal mineralisation. Econ Geol 80: 1640-1668

Hendenquist JW, Lowenstern JB (1994) The role of magmas in the formation of hydrothermal ore deposits. Nature 370: 519-526

Heiken GH (1971) Tuff rings: Examples from the Fort-Rock-Christmas Lake valley Basin, south-central Oregon. J Geophys Res 76: 5615-5626

Hein JR, Stamatakis MG, Dowling J (2000) Trace metal-rich Quaternary hydrothermal manganese-oxide and barite deposit, Milos Island, Greece. Trans Inst Min Metall Sect B 109: B67-B76

Henley RW (1985) The geothermal framework of epithermal deposits. Soc Econ Geol, Review in Econ Geol 2: 1-24

Hezig PM, Petersen S, Hannington MD (1999) Epithermal-type gold mineralisation at Conical seamount: A shallow submarine volcano south of Lihir island, Papua New Guinea. In: Stanley CJ et al. (Eds) Mineral deposits: Processes to processing. Fifth Biennial SGA Meeting and the Tenth Quadrennial IAGOD Symposium, London, Proceedings, pp 527-530

Hoffmann C, Keller J (1979) Xenoliths of lawsonite-ferroglaucophane rocks from a Quaternary volcano of Milos (Aegean Sea, Greece). Lithos 12: 209-219

Horikoshi E (1969) Volcanic activity related to the formation of the Kuroko-type deposits in the Kosaka district, Japan. Mineral Deposita 4: 321-345

Houghton BF, Wilson CJN (1989) A vesicularity index for pyroclastic deposits. Bull Volcanol 51: 451-462

Houghton BF, Landis CA (1989) Sedimentation and volcanism in a Permian arc-related basin, southern New Zealand. Bull Volcanol 51: 433-450

Huppert HE, Shepard JB, Sigurdson H, Sparks RSJ (1982) On lava dome growth, with application to the 1979 lava extrusion of the Soufriere of St. Vincent. J Volcanol Geotherm Res 14: 199-222

Ingram RL (1954) Terminology of the thickness of stratification and parting units in sedimentary rocks. Bull Geol Soc Am 65: 130-165

Innocenti F, Manetti P, Peccerilo A, Poli G (1979) Inner arc volcanism in NW Aegean arc: geochemical and geochronological data. Neues Jahrbuch Fur Mineralogie Monashefte H4: 145-158

Innocenti F, Manetti P, Peccerilo A, Poli G (1981) South Aegean volcanic arc: geochemical variations and geotectonic implications. Bull Volcanol 44: 377-391

Iverson RM (1990) Lava domes modelled as brittle shells that enclose pressurized magma, with application to Mount St. Helens. In: Fink JH (ed) Lava flows and domes. Emplacement mechanisms and hazard implications. Berlin, Springer-Verlag, pp 47-69

Jackson JA (1994) Active tectonics of the Aegean region. Annual Reviews of Earth and Planetary Sciences 22: 239-271

Jankovic S (1990) Types of copper deposits related to volcanic environments in the Bor district, Yugoslavia. Geologische Rundschau 79: 467-478

John DA (2001) Miocene and early Pliocene epithermal gold-silver deposits in the northern Great Basin, western USA: characteristics, distribution, and relationship to magmatism. Econ Geol 96: 1827-1853

Johnson H D, Baldwin C T (1986) Shallow siliclastic seas. In: Reading HG (ed) Sedimentary environments and facies. Oxford, Blackwell, pp 229-282

Jolivet L (2001) A comparison of geodetic and finite strain pattern in the Aegean, geodynamic implications. Earth Planetary Sci Lett 187: 95-104

Jolivet L, Brun J-P, Gautier P, Lallemant S, Patriat M (1994) 3D-kinematics of extension in the Aegean region from the Early Miocene to Present: insights from the ductile crust. Bull Geol Soc Fr 165: 195-209

Kalogeropoulos S, Paritsis S (1990) Geological and geochemical evolution of the Santorini volcano: a review. In DA Hardy (ed) Thera and the Aegean World III 2. The Thea Foundation, London, pp164-171

Kaneko T, Wooster MJ, Nakada S (2002) Exogenous and endogenous growth of the Unzen lava dome examined by satellite infrared image analysis. J Volcanol Geotherm Res 116: 151-160

Kano K, Takeuchi K (1989) Origin of mudstone clasts in turbidities of the Miocene Ushikiri Formation, Shimane Peninsula, Southwest Japan. Sediment Geol 62: 79-87

Kano K (1996) A Miocene coarse volcaniclastic mass-flow deposit in the Shimane Peninsula, SW Japan: product of a deep submarine eruption ? Bull Volcanol 58: 131-143

Kano K (1998) A shallow-marine alkali-basalt tuff cone in the Middle Miocene Jinzai Formation, Izumo, SW Japan. J Volcanol Geo Res 87: 173-191

Kano K, Yamanamoto T, Ono K (1996) Subaqueous eruption and emplacement of the Shinjima Pumice, Shinjima (Moeshima) Island, Kagoshima Bay, SW Japan. J Volcanol Geotherm Res 71: 187-206

Kato Y (1987) Woody pumice generated with submarine eruption. J Geol Soc Japan 93: 11-20

Katsui Y, Komuro H, Uda T (1985) Development of faults and growth of Usu-Shinzan cryptodome in 1977-1982 at Usu Volcano, North Japan. J Fac Sci Hokkaido Univ Ser IV 21: 339-362

Kelepertsis AE (1989) Formation of sulfates at the Thiaphes area of Milos island: possible precursors of kaolinite mineralisation. Canadian mineral 27: 241-245

Kelepertsis A, Economou K, Skounakis S, Porfyris S (1990) Mineral and chemical composition of kaolins from Milos Island, Greece-procedure of kaolinite enrichment. Appl Clay Sci 5: 277-293

Keller J (1982) Mediterranean island arcs. In: Thorpe RS (ed) Andesites. J Wiley & Sons, pp 307-325

Keller J, Rehren TH Stadlbauer E (1990) Explosive volcanism in the Hellenic Arc: a summary and review. In DA Hardy, Keller J, Galanopoulos VP, Flemming NC, Druitt TH (eds.) Thera and the Aegean World III. Proceedings of the Third International Congress on the Volcano of Thera, Santorini: 13-26

Kerr DJ, Gibson HL (1993) A comparison of the Horne volcanogenic massive sulfide deposit and intracauldron deposits of the mine sequence, Noranda, Quebec. Econ Geol 88: 1419-1442

Kesler SE, Russell N, Seaward M, Rivera J, McCurdy K, Cumming GL, Sutter JF (1981) Geology and geochemistry of sulfide mineralisation underlying the Pueblo Viejo gold-silver oxide deposit, Dominican Republic. Econ Geol 76: 1096-1117

Kilias SP, Naden J, Cheliotis I, Shepherd TJ, Constandinidou H, Crossing J, Simos I (2001) Epithermal gold mineralisation in the active Aegean Volcanic Arc: the Profitis Illias deposit, Milos Island, Greece. Mineral Deposita 36: 32-44

Kissel C, Laj C (1988) The Tertiary geodynamic evolution of the Aegean Arc, paleomagnetic reconstruction. Journal 146: 183-201

Kissel C, Kondopoulou D, Laj C, Papadoupoulos P (1986) New paleomagmatic data from Oligocene formations of northern Aegean. Journal 13: 1039-1042

Kokelaar BP (1982) Fluidization of wet sediments during the emplacement and cooling of various igneous bodies. J Geol Soc London 139: 21-33

Kokelaar BP (1983) The mechanism of Surtseyan volcanism. J Geol Soc London 140: 939-944

Kokelaar BP (1986) Magma-water interaction in subaqueous and emergent basaltic volcanism. Bull Volcanol 48: 275-289

Kokelaar BP, Durant GP (1983) The submarine eruption and eruption of Surtla (Surtsey), Iceland. J Volcanol Geotherm Res 19: 239-246

Kokelaar BP, Busby CJ (1992) Subaqueous explosive eruption and welding of pyroclastic deposits. Science 257:196-201

Kondopoulou DP, Pavlides SB (1990) Paleomagnetic and Neotectonic evidence for different deformation patterns in the south Aegean Volcanic Arc: the case of Milos island. Proceedings of International Earth Science Congress on Aegean Regions 1-6 October Izmir Turkey, pp210-233

Kornprobst J, Kienast J-R, Vilminot J-C (1979) The high-pressure assemblages at Milos, Greece: a contribution to the petrological study of the basement of the Cyclades Archipelago. Contrib Mineral Petrol 69: 49-63

Kilias S P, Naden J, Cheliotis I, Shepherd T J, Constandinidou H, Crossing J, Simos I (2001) Epithermal gold mineralisation in the active Aegean Volcanic Arc: the Profitis Ilias deposit, Milos Island, Greece. Min Dep 36: 32-44

Lacroix A (1904) La Montagne Pelée et ses Eruptions. Masons, Paris, pp 1-622

Laj C, Jamet M, Sorel D, Valente JP (1982) First paleomagnetic results from Mio-Pliocene series of the Hellenic sedimentary arc. Tectonophysics 86: 45-67

Large RR (1992) Australian volcanic-hosted massive sulfide deposits: Features, styles, and genetic models. Econ Geol 87: 471-512

Large RR, McPhie J, Gemmell JB, Herrmann W, Davidson GJ (2001) The spectrum of ore deposits types, volcanic environments, alteration halos, and related exploration vectors in submarine volcanic successions: some examples from Australia. Econ Geol 96: 913-938

Lee J, Lister GS (1992) Late Miocene ductile extension and detachment faulting, Mykonos, Greece. Geology 20: 121-124

Le Maitre RW (1989) A classification of igneous rocks and glossary of terms. Blackwell, Oxford

LePichon X, Angelier J (1979) The Hellenic arc and trench system: a key to the neotectonic evolution of the eastern Mediterranean area. Tectonophysics 60: 1-42

Liatsikas N (1955) Geology of some useful minerals of Milos Island. Geol Exped 20: 1-30

Liakopoulos A (1987) Hydrothermalisme et Minralisations Mettallifres de I'le de Miols (Cyclades, Greece). Thse de Doctorate, Universit Pierre et Marie Curie, Paris. 87-36pp

Liakopoulos A, Glasby G P, Papavassiliou C T, Boulegue J (2001) Nature and origin of the Vani manganese deposit, Milos, Greece: and overview. Ore Geology Reviews 18: 181-209

Ligdas CN, Main IG, Adams RD (1992) Three-dimensional structure and constraints on the nature of the coupled subduction-spreading process in the Aegean area. Tectonophysics 201 (3-4): 199-207

Lindgren W (1922) A suggestion for the terminology of certain mineral deposits. Econ Geol 17: 292-294

Lister GS, Banga G, Feenstra A (1984) Metamorphic core complexes of cordilleran type in the Cyclades, Aegean Sea, Greece. Geology 12: 221-225

Long PE, Wood BJ (1986) Structures, textures and cooling history of Columbia River basalt flows. Geol Soc Am Bull 97: 1144-1155

Lorenz V (1970) Some aspects of the eruption mechanism of the Big Hole Maar, central Oregon. Bull Geol Soc Am 81: 1823-1830.

Lorenz V (1973) On the formation of maars. Bull Volcanol 37: 183-204

Lowe DR (1976) Grain flow and grain flow deposits. J Sediment Petrol 46: 188-199

Ludwig K R (2000) SQUID 1.00, A user's Manual; Berkeley Geochronology Center Special Publication No. 2, 2455 Ridge Road, Berkley CA 94709, USA

Macdonald GA (1967) Forms and structures of extrusive basaltic rocks. In: Hess HH, Poldervaart A (eds) Basalts. The Poldervaart treatise on rocks of basaltic composition. Wiley Interscience. New York, pp 1-61

MacDonald AJ, Lewis PD, Thompson JFH, Nadaraju G, Bartsch RD, Bridge DJ, Rhys DA, Roth T, Kaip A, Godwin CI, Sinclair AJ (1996) Metallogeny of and Early to Middle Jurassic arc, Iskut River area, northwestern British Columbia. Econ Geol 91: 1098-1114

Marani MP, Gamberi F, Savelli C (1997) Shallow-water polymetallic sulfide deposits in the Aeolian island arc. Geology 25 (9): 815-818

McConachy T. F., McInnes B. I. A. 2001. Submarine vs. subaerial epithermal systems in arc environments: are there implications for mineral exploration? A Solomon Island Example. A Hydrothermal Odyssey, Townsville May 17-19, 2001. James Cook University EGRU, pp 71

Mahood G (1980) Geological evolution of a Pleistocene rhyolitic center–Sierra La Primavera, Jalisco, Mexico. J Volcanol Geotherm Res 8: 199-230

McKenzie DP (1970) Plate tectonics of the Mediterranean region. Nature 226: 239-243

McKenzie DP (1978) Active tectonics of the Alpine-Himalayan belt: the Aegean Sea and surrounding regions. Geophys J R Astron Soc 55: 217-254

McPhie J, Doyle M, Allen R (1993) Volcanic textures: a guide to the interpretation of textures in volcanic rocks. Centre for Ore Deposit and Exploration Studies, University of Tasmania, Hobart, pp 198

Makris J (1978) The crust and upper mantle of the Aegean region from deep seismic soundings. Tectonophysics 46: 251-268

Mastin LG (1991) The roles of magma and groundwater in the phreatic eruptions at Inyo Craters, Long Valley Caldera, California. Bull Volcanol 53: 579-596

Mendrinos D (1988) Modelling of Milos Geothermal field in Greece. M. Eng. Thesis, University of Auckland.

Mercier JL, Sorel D, Vergely P, Simeakis K (1989) Extensional tectonic regimes in the Aegean basins during the Cenozoic. Basin Res 2: 49-71

Messenger PR (1996) Relationship between Devonian magmatism and Au-Cu mineralisation at Mt Morgan central Queensland. PhD thesis, University of Queensland, Brisbane (unpubl.)

Meulenkamp JE, van der Zwann GJ, Van Wamel WA (1994) On late Miocene to Recent vertical motions in the Cretan segment of the Hellenic Arc. Tectonophysics 146: 203-215

Meulenkamp JE, Wortel MJR, Van Wamel WA, Spakman W, Hoogerduyn Strating E (1988) On the Hellenic subduction zone and the geodynamic evolution of Crete since the late middle Miocene. Tectonophysics 146: 203-215

Middleton G V (1970) Experimental studies related to problems of flysch sedimentation. In: Lajoie J (ed) Flysch sedimentology in North America. Soc Econ Paleontol Mineral Pacific Sect, pp 1-38

Minakami T, Ishikawa T, Yagi K (1951) The 1944 eruption of Volcano Usu in Hokkaido, Japan. Bull Volcanol 11: 45-160

Minissale A, Duchi V, Kolios N, Verruchi C (1997) Chemical patterns of thermal aquifers in the volcanic islands of the Aegean Arc, Greece. Geothermics 26: 501-518

Miyabuchi Y (1999) Deposits associated with the 1990-1995 eruption of Unzen Volcano. J Volcanol Geotherm Res 89: 139-158

Moore JG, Nakamura K, Alcaraz A (1966) The 1965 eruption of Taal volcano. Science 151: 955-960

Moore JG, Fiske RS (1969) Volcanic sudstructure inferred from dredge samples and ocean-bottom photographs, Hawaii. Bull Geol Soc Am 80: 1191-1202

Moore JG, Clague DA (1992) Volcano growth and evolution of the island of Hawaii. Bull Geol Soc Am 104: 1471-1484

Morris A, Anderson M (1996) First paleomagnetic results from the Cycladic Massif, Greece, and their implications for Miocene extension directions and tectonic models in the Aegean. Earth Planet Sci Lett 142: 397-408

Moyle AJ, Doyle BJ, Hoogvliet H, Ware AR (1990) Ladolam gold deposit, Lihir Island. In: Hughes FE (Ed) Geology of the mineral deposits of Australia and Papua New Guinea. Australasian Institute of Mining and Metallurgy, Melbourne, pp 1793-1805

Mitropoulos P, Saunders AD, Marsh NG (1987) Petrogenesis of Cenozoic volcanic rocks from the Aegean island arc. J Volcanol Geotherm Res 32: 177-193

Muffler LJP, White DE, Truesdell AH (1971) Hydrothermal explosion craters in Yellowstone National Park. Geo Soc Am Bull 82: 723-740

Nairn IA, Wiradiradja S (1980) Late Quaternary hydrothermal explosion breccias at Kawerau Geothermal Field, New Zealand. Bull Volcanol 43-1:1-13

Nelson CE (2000) Volcanic domes and gold mineralisation in the Pueblo Viejo district, Dominican Republic. Mineral Deposita 35: 511-525

Nethery JE (1999) Milos project: Chondro Vouno-East Amethyst mapping program report. Internal report prepared for Midas Exploration Pty Ltd, pp 1-12

Nilsson CA (1968) Wall rock alteration at Boliden deposit, Sweden. Economic Geology 63: 472-494

Norman MD (2002) Report A02-010: SHRIMP U-Pb zircon age determination of Upper Pliocene mineralising domes, west Milos, Greece. (unpubl. report), pp 1-20

Ochmann N, Hollnack D, Wohlenberg J (1989) Seismological exploration of Milos geothermal reservoir, Greece. Geothermics 18(4): 563-578

Papanikolaou D, Lekkas E, Syskakis D, Adamopoulou E (1993) Correlation on the Neotectonic structures with the Geodynamic activity in Milos during the earthquakes of March 1992. Bull Geol Soc Greece XXVII/3: 413-428

Papazachos BC (1990) Seismicity of the Aegean and the surrounding area. Tectonophysics 178: 287-308

Paulick H, McPhie J (1999) Volcanic facies architecture of the felsic host rock sequence at the Thalanga massive sulphide deposit, Early Ordovician, northern Queensland. Aust J Earth Sci 46: 391-405

Papzachos BC, Pangiotopoulos DG (1993) Normal faults associated with volcanic activity and deep rupture zones in the southern Aegean volcanic arc. Tectonophysics 220: 301-308

Pe-Piper G, Piper DJW, Matarangas D (2002) Regional implications of geochemistry and style of emplacement of Miocene I-type diorite and granite, Delos, Cyclades, Greece. Lithos 60: 47-66

Pe Piper G, Piper DJW, Reynolds PH (1983) Paleomagnetic stratigraphy and radiometric dating of the Pliocene volcanic rocks of Aegina, Greece. Bull Volcanol 46: 1-7

Perkins C (1986) The Red Rock Deposit, Drake Volcanics, New South Wales, Australia-an example of a submarine epithermal system. In: Proceedings of Symposium 5: Volcanism, hydrothermal systems and related mineralisation. International Volcanological Congress, New Zealand, February 1986, pp 79-80

Perkins C (1988) Origin and provenance of submarine volcaniclastic rocks in the Late Permian Drake Volcanics, New South Wales. Aust J Earth Sci 35: 325-337

Pichler H (1965) Acid hyaloclastite. Bull Volcanol 28: 293-310

Popov P, Kovachev V (1996) Geology, composition and genesis of mineralisation in the central and southern part of Elatsite-Chelopech ore field. In: Popov P (ed) Plate tectonic aspects of the Alpine metallogeny in the Carpatho-Balkan region, vol 1. UNESCO-Proceedings of the IGSP Project 356 Annual meeting, Sofia, p 159-170

Popov P, Petrunov R, Kovachev V, Strashimirov S, Kanazirski M (2000) Elatsite-Chelopech ore field. Geology and metallogeny of the Panagyurishte ore region (Srednogorie zone, Bulgaria). ABCD-GEODE 2000 Workshop, Borovets. Guides A and C, pp 8-18

Postma G (1986) Classification for sediment gravity-flow deposits based on flow conditions during sedimentation. Geology 14: 291-294

Poulsen K H, Hannington M D (1995) Volcanic-associated massive sulfide gold. In R O Eckstrand, W D Sinclair, R I Thorpe (eds) Geology of Canadian mineral deposit types, Geological Society of America, DNAG P-1, Geology of Canada 8: 183-196

Principe C, Arias A, Zoppi U (2002) Origin, transport and deposition of a debris avalanche deposit of phreatic origin on Milos Island (Greece). Montagne Pelee 1902-2002, Explosive Volcanism in Subduction Zones, Martinique 12-16 May, 2002. Abstracts p. 71

Renfrew C, Wagstaff M (1982) An island polity: the archaeology of exploitation in Melos. Cambridge Uni Press, pp. 330

Reynolds MA, Best JG, Johnson RW (1980) 1953-57 eruption of Tuluman volcano: rhyolitic volcanic activity in the northern Bismarck Sea. Geol Surv Papua New Guinea Mem 7: 1-44

Rinaldi M, Campos Venuti M (2003) The submarine eruption of the Bombarda volcano, Milos Island, Cyclades, Greece. Bull Volcanol 65: 282-293

Robertson AHF, Dixon JE (1984) Introduction: aspects of the geological evolution of the Eastern Mediterranean. In JE Dixon, AHF Robertson (eds) The geological evolution of the eastern Mediterranean. Geol Soc London Spec Publ 17

Roth T, Thompson J F H, Barrett T J (1999) The precious metal-rich Eskay Creek deposit, northwestern British Columbia. Reviews in Economic Geology 8: 357-373

Savelli C, Marani M, Gambero F (1999) Geochemistry of metalliferous, hydrothermal deposits in the Aeolian arc (Tyrrhenian Sea). J Volcanol Geotherm Res 88: 305-323

Schliestedt M, Altherr R, Matthews A (1987) Evolution of the Cycladic Crystalline Complex: petrology, isotope geochemistry and geochronology. In: HC Helgeson (ed) Chemical transport in metasomatic processes. Reidel Pub Co: 389-428

Scutter CR, Cas RAF, Moore L, De Rita D (1998) Voluminous submarine rhyolite volcanism, island of Ponza, Italy. J Geophys Res 103 (B11): 27551-27566

Self S (1983) Large-scale phreatomagmatic volcanism: a case study from New Zealand. J Volcanol Geotherm Res 17: 433-469

Self S. Sparks RSJ, Booth B, Walker GPL (1974) The Heimaey Strombolian scoria deposit, Iceland. Geological Magazine 111: 539-548

Self S, Sparks RSJ (1978) Characteristics of widespread pyroclastic deposits formed by the interaction of silicic magma and water. Bull Volcanol 41: 196-212

Self S, Goff F, Gardner GN, Wright JV, Kite WM (1986) Explosive rhyolitic volcanism in the Jemez Mountains: vent locations, caldera development, and relation to regional structure. J Geophys Res 91(B2):1779-1798

Selley RC (1978) Ancient sedimentary environments. 2nd edn. London: Chapman & Hall.

Sewell D M, Wheatley C J V (1994) The Lerokis and Kali Kunning submarine exhalative gold-silver-barite deposits, Wetar Island, Mauku, Indonesia. J Geochem Exploration 50: 351-370

Sillitoe RH (1983) Enargite-bearing massive sulfide deposits high in porphyry copper systems. Econ Geology 78: 348-352

Sillitoe RH (1989) Gold deposits in western Pacific island arcs: the magmatic connection. Econ Geol Mono 6: 274-291

Sillitoe R H (1995) An appraisal of the Midas gold project, Milos Island, Greece. Internal report prepared for RGC Exploration Pty Ltd: 12 pp

Sillitoe RH (1999) Styles of high-sulfidation gold, silver and copper mineralisation in porphyry and epithermal environments. In: Weber G (Ed) Pacrim '99 Congress, Bali, Indonesia, 1999, Proceedings. Parkville, Australia, Australasian Institute of Mining and Metallurgy, p. 29-44.

Sillitoe RH (2002) Rifting, bimodal volcanism, and bonanza gold veins. Society of Economic Geologists Newsletter 48: p 24-26

Sillitoe RH, Hedenquist JW (in press) Linkage between volcanotectonic settings, ore-fluid compositions, and epithermal precious-metal deposits. Econ Geol

Simpson K, McPhie J (2001) Fluidal-clast breccia generated by submarine fire fountaining, Trooper Creek Formation, Queensland, Australia. J Volcanol Geotherm Res 109: 339-355

Skilling IP, White JDL, McPhie J (2002) Peperite: a review of magma-sediment mingling. J Volcanol Geotherm Res 114: 1-17

Smith TL, Batiza R (1989) New field and laboratory evidence for the origin of hyaloclastite flows on seamount summits. Bull Volcanol 51: 96-114

Snyder GL, Fraser GD (1963) Pillowed lavas: I. Intrusive layered lava pods and pillowed lavas, Unalaska Island, Alaska. Geol Surv Prof Paper 454 B, B1-B-B23

Sohn YK (1995) Geology of Tok Island, Korea: eruptive and depositional processes of a shoaling to emergent island volcano. Bull Volcanol 56: 660-674

Sonder RA (1924) Zur geologie und petrography der inselgruppe von Milos. Zeitschr Volc 8: 181-231

Sparks RSJ (1976) Grain size variation in ignimbrites and implications for the transport of pyroclastic flows. Sedimentology 23: 147-188

Sparks R S J (1978) The dynamics of bubble formation and growth of magmas. J Volcanol Geotherm Res 3: 1-37

Sparks RSJ, Self S, Walker GPL (1973) Products of ignimbrite eruptions. Geology 1:115-118

Spartali E (1994) Current exploration for epithermal gold mineralisation in Post-Tertiary volcanic rock, Milos Island, Greece. Unpubl. MSc thesis (Imperial College, London): 141pp

Staudigel H, Schmincke H-U (1984) The Pliocene seamount series of La Palma/Canary Islands. J Geophys Res 89: 11195-111215

Stewart AL, McPhie J (2003) Internal structure and emplacement of an Upper Pliocene dacite cryptodome, Milos Island, Greece. J Volcanol Geotherm Res 124: 129-148

Stewart AL, McPhie J (in Press) An Upper Pliocene coarse pumice breccia generated by a shallow submarine explosive eruption at Milos, Greece. Bull Volcanol

Stuben D, Glasby GP (1999) Geochemistry of shallow submarine hydrothermal fluids from Paleohori Bay, Milos, Aegean Sea. Explor Mining Geol 8: 273-287

Swanson DA, Holcomb RT (1990) Regularities in growth of the Mount St. Helens dacite dome, 1980-1986. In: Fink JH (ed) Lava Flows and Domes. IAVCEI Proceedings in Volcanology 2. Springer-Verlag, Berlin Heidelberg, pp 3-24

Taube A (1986) The Mt Morgan gold-copper mine and environment, Queensland: a volcanogenic massive sulphide deposit associated with penecontemporaneous faulting. Econ Geol 81: 1322-1340

Taymaz T, Jackson J, McKenzie D (1991) Active tectonics of north and central Aegean Sea. Geophys J Int 106: 433-490

Tera F, Wasserburg G (1972) U-Th-Pb systematics in three Apollo 14 basalts and the problem of initial Pb in lunar rocks. Earth Planetary Sci Lett 14: 281-304

Thanassoulas K (1983) Gravity surveys on Milos island. IGME (Institute for Geology and Mineral Exploration), Greece (unpubl) report pp 3866

Thanassoulas K (1989) Application of the self potential technique over the Milos geothermal test site. Geothermics 18(4): 497-506

Traineau H, Dalabakis P (1989) Mise en evidence d'une eruption phreatique historique sur l'ile de Milos (Grece). C-R Acad Sci Paris: pp1-308

Tsokas GN (1985) A geophysical study of Milos and Kimolos island. PhD (thesis) University of Thessaloniki, Greece, pp 240

Tsokas GN (1996) Interpretation of Bouguer anomaly of Milos island (Greece). J Volcanol Geotherm Res 72: 163-181

Tsuya H, Morimoto R, Ossaka G (1953) A brief note on the petrography of the pumice ejected from Myojin-sho (reef), near the Beyonnaise rocks, September 23, 1952. J Tokyo Univ Fisheries 40: 16-18

Vavelidis M Melfos V (1998) Fluid inclusion evidence for origin of the barite silver-gold-bearing Pb-Zn mineralisation of the Triades area, Milos Island, Greece. Bull Geol Soc Greece 32 (3): 137-144

Vennemann TW, Muntean JL, Kesler SE, O'Neil JR, Valley JW, Russell N (1993) Stable isotope evidence for magmatic fluids in the Pueblo Viejo epithermal acid sulfate Au-Ag deposit, Dominican Republic. Econ Geol 88: 55-71

Vickery M (1995) Report on work done at Triades May-July 1995. Unpub report to RGC, pp 1-30

Walcott CR, White SH (1998) Constraints on the Kinematics of post-orogenic extension imposed by stretching lineations in the Aegean region. Tectonophysics 298: 155-175

Walker GPL (1971) grain size characteristics of pyroclastic deposits. J Geol 79: 696-714

Walker GPL (1973) Explosive volcanic eruptions-a new classification scheme. Geologische Rundschau 62: 431-436

Walker GPL (1985) Origin of coarse lithic breccias near ignimbrite source vents. J Volcanol Geotherm Res 25:157-171

Walker GPL (1973) Explosive volcanic eruptions-a new classification scheme. Geologische Rundschau 62: 431-436

Walker GPL, Croasdale R (1972) Characteristics of basaltic pyroclasts. Bull Volcanol 35: 308-317

Watanabe KK, Katsui Y (1976) Pseudo-pillow lavas in the Aso Caldera, Kyushu, Japan. J Jap Assoc Min Pet Econ Geol 71: 44-49

Walker GPL (1984) Characteristics of dune-bedded pyroclastic surge bedsets. J Volcanol Geotherm Res 20: 281-296

Waters AC and Fisher RV (1971) Base surges and their deposits: Capelinhos and Taal volcanoes. J Geophys Res 76: 5596-5614

Wetzenstein W (1972) Die Bentonitlagerstatten im Osteil der Insel Milos/Griechland und ihre mineralogische Zussamensetzung. Geol Soc Greece 9: 144-171

White JDL (2000) Subaqueous eruption-fed density currents and their deposits. Precambrian Res 101: 87-109

White JDL, McPhie J, Skilling IP (2000) Peperite: a useful genetic term. Bull Volcanol 62: 65-66

White NC (1995) Epithermal gold deposits: styles, characteristics, and exploration. Soc Econ Geol Newsletter 23: 1, 9-13.

White NC, Leake MJ, McCaughey SN, Parris BW (1995) Epithermal deposits of the southwest Pacific. J Geochem Explor 54: 87-136

Whitham A, Sparks, RSJ (1986) Pumice. Bull Volcanol 48:.209-223

Wijbrans JR, McDougall I (1988) Metamorphic evolution of the Attic-Cycladic metamorphic belt on Naxos (Cyclades, Greece) utilizing $^{40}Ar/^{39}Ar$ age spectrum measurements. J Meta Geo 6: 571-594

Williams I S (1998) U-Th-Pb Geochronology by Ion Microprobe. In McKibben M A, Shanks III W C, Ridley W I (eds) Applications of microanalytical techniques to understanding mineralizing processes, Reviews in Economic Geology 7: 1-35

Wilson CJN (1985) The Taupo eruption, New Zealand II. The Taupo Ignimbrite. Philo Trans Royal Soc London A314:229-310

Wilson CJN, Walker GPL (1985) The Taupo eruption, New Zealand. I: General aspects. Philos Trans R Soc London Ser A 314:199-228

Winchester JA, Floyd PA (1977) Geochemical discrimination of different magma series and their differentiated products using immobile elements. Chemical Geology 20: 325-343

Wright IC, Gamble JA (1999) Southern Kermadec submarine caldera arc volcanoes (SW Pacific): caldera formation by effusive and pyroclastic eruption. Mar Geol 161: 207-227

Wright IC, Gamble JA, Shane PAR (2003) Submarine silicic volcanism of the Healy caldera, southern Kermadec arc (SW Pacific): I-volcanology and eruption mechanisms. Bull Volcanol 65: 15-29

Yamagishi H (1979) Classification and features of subaqueous volcaniclastic rocks of Neogene age in southwest Hokkaido. Geol Surv Hokkaido Rep 51: 1-20

Yamagishi H (1987) Studies on the Neogene subaqueous lavas and hyaloclastites in Southwest Hokkaido. Geol Surv Hokkaido Report 59: 55-101

Yamagishi H, Dimroth E. (1985) A comparison of Miocene and Archean rhyolite hyaloclastites: evidence for a hot and fluid rhyolite lava. J Volcanol Geotherm Res 23:337-355

Yamagishi H, Dimroth E (1987) Studies on the Neogene subaqueous lavas and hyaloclastites in southwest Hokkaido. Rep Geol Surv Hokkaido 59: 55-117

Yamagishi H (1991) Morphological features of Miocene submarine coherent lavas from the "Green Tuff" basins: examples from basaltic and andesitic rocks from the Shimokita Peninsula, northern Japan. Bull Volcanol 53: 173-181

Yamagishi H, Goto Y (1992) Cooling joints of subaqueous rhyolite lavas at Kuroiwa, Yaumo, southern Hokkaido, Japan. Bull Volcanol Soc Japan 37: 205-207

Yamamoto T, Tatsunori S, Shigeru S, Kozo U, Akira T, Keiichi S, Koji O (1991) The

1989 submarine eruption of eastern Izu Peninsula, Japan: ejecta and eruption mechanisms. Bull Volcanol 53: 301-308

Yamaoto T, Takarada S, Sato S (1993) Pyroclastic flows from the 1991 eruption of Unzen volcano, Japan. Bull Volcanol 55: 166-175

Voreadis G, Mourabas T (1935) The silver-bearing ores of Milos. Geo Surv Greece 22: 45-56

Yuasa M (1995) Myojin Knoll, Izu-Ogasawara arc: Submersible study of submarine pumice volcano. Kazan 40: 277-284 [in Japanese with English abstract]

Yuasa M, Murakami F, Saito E, Watanabe K (1991) Submarine topography of seamounts on volcanic front of the Izu-Ogasawara (Bonin) arc. Geological Survey of Japan Bull 42: 703-743

Sample no.	MIL140	MIL141	MIL151	MIL155	MIL142	MIL150	MIL152	MIL164	MIL166	MIL232	MIL 344	MIL362L	MIL362P	MIL384	MIL127	MIL122
Rock type	Pumice breccia	Pumice breccia	Pumice breccia	Pumice breccia	Pumice breccia	Pumice breccia	Pumice breccia	Pumice breccia	Pumice breccia	Pumice breccia	Pumice breccia	Pumice breccia	Pumice breccia	Pumice breccia	Lava	Lava
Easting	364505	364505	364405	364505	364505	364405	364405	242700	243205	242802	364405	364505	364505	364505	364500	364406
Northing	2428000	2428000	2426050	2428000	2428000	2426050	2426050	3645000	3645060	3644080	2426050	2428000	2428000	2428000	2422000	2422010
Major elements (wt%)																
SiO_2	68.57	67.13	68.13	68.32	71.01	70.31	71.32	72.25	70.25	71.36	71.71	70.75	69.27	68.79	65.38	63.29
TiO_2	0.15	0.15	0.11	0.12	0.16	0.15	0.17	0.16	0.16	0.15	0.15	0.19	0.13	0.22	0.39	0.48
Al_2O_3	11.87	11.75	12	11.55	12.51	11.92	12.44	12.73	12.61	12.69	12.09	12.17	9.61	13.45	16.68	15.19
Fe_2O_3	1.48	1.13	1.13	0.98	1.3	1.01	1.21	1.1	1.44	1.1	1.14	1.62	1.06	1.31	1.64	4.53
MnO	0.05	0.04	0.04	0.03	0.05	0.03	0.04	0.04	0.04	0.05	0.03	0.02	0.04	0.03	0.02	0.12
MgO	0.85	0.47	0.46	0.46	0.29	0.37	0.31	0.24	0.49	0.57	0.23	0.60	1.61	0.44	0.27	1.96
CaO	1.41	1.2	1.35	1.14	1.22	1.24	1.2	1.57	1.14	1.27	1.15	1.66	1.25	1.59	0.13	4.64
Na_2O	4.49	4.22	3.61	4.35	2.88	3.44	3.05	3.05	2.83	2.84	2.81	3.83	2.90	4.01	0.76	2.86
K_2O	3.93	3.76	4.45	3.56	4.35	3.81	4.04	4.25	3.9	3.91	4.40	3.17	3.16	3.95	10.66	2.37
P_2O_5	0.04	0.04	0.02	0.03	0.04	0.02	0.03	0.03	0.02	0.03	0.02	0.04	0.03	0.05	0.05	0.09
L.O.I.	6.87	9.52	8.64	8.94	6.03	8.24	6.49	4.51	6.91	5.66	5.47	5.93	10.35	5.73	3.85	4.57
Total	99.71	99.41	99.93	99.48	99.85	100.53	100.3	99.93	99.79	99.63	99.20	99.98	99.41	99.57	99.83	100.10
Trace elements (ppm)																
Nb	5.6	6.7	6.1	7.2	8	7.6	8.9	8.3	7.7	7.9	4.9	6.7	5.7	11.6	5.0	5.0
Zr	99	114	75	103	134	112	139	136	128	112	139	123	92	169	101	110
Sr	77	79	77	118	85	98	101	99	82	94	201	109	125	141	137	211
Cr	<1	<1	<1	<1	1	<1	2	<1	4	3	22	4	1	2	4	3
Ba	271	448	506	835	592	858	797	1004	507	488	285	597	894	705	1175	397
Sc	<2	3	3	2	4	2	3	3	3	3	18	3	2	3	11	15
V	3	5	4	4	5	6	7	5	15	6	127	12	5	14	99	105
La	11	22	19	39	27	32	26	28	26	24	19	23	17	35	17	16
Ce	24	40	36	61	50	59	50	51	48	47	33	38	31	60	33	32
Nd	9	16	12	17	18	20	18	21	17	17	16	15	10	19	10	15
Y	17	20	15	17	22	16	19	20	19	15	25	42	15	18	16	19
Rb	112	160	137	454	131	229	138	119	120	108	45	136	95	145	312	94
U	2.6	2.3	3.1	2.9	3.8	3.7	4.2	3.5	4.9	3.1	2	3	2	5	2.2	<1.5
Th	13	13	17	13	13	16	14	14	14	14	7	12	11	20	7	5
Pb	15	19	16	17	18	13	20	17	25	12	9	11	12	18	50	8
Zn	25	37	23	26	36	21	33	31	109	32	52	23	25	29	185	64
Cu	2	13	3	3	5	4	4	3	12	2	32	4	3	4	7	11
Ni	1	7	3	4	4	3	4	2	8	5	11	3	1	1	4	2

Sample no.	MIL223	MIL147	MIL391	MIL328	MIL248	MIL249	MIL189	MIL132	MIL212	MIL209	MIL185	MIL358	MIL359	MIL112	MIL104	MIL234
Rock type	Lava	Lava	Lava	Lava	Lava	Lava	Lava	Lava	Lava	Lava	Lava	Lava	Lava	Lava	Lava	Lava
Easting	364209	364500	364500	363903	364300	364300	364302	364009	364100	364300	364409	364908	364500	3643090	364000	364509
Northing	2422000	2430050	2430050	2424000	2422050	2422050	2433000	2430000	2425050	2422090	2431000	2424000	2424050	2425090	242800	24266000
Major elements (wt%)																
SiO_2	66.68	65.33	63.68	59.11	64.99	63.76	75.15	74.27	72.05	62.79	59.27	58.76	60.63	67.20	74.87	74.46
TiO_2	0.41	0.41	0.55	0.6	0.50	0.54	0.19	0.10	0.23	0.58	0.81	0.58	0.56	0.36	0.13	0.07
Al_2O_3	16.21	15.81	16.33	16.91	15.45	16.92	13.48	12.77	13.76	16.34	17.65	16.78	16.26	15.51	12.87	12.42
Fe_2O_3	2.75	3.33	4.05	6.18	4.97	5.65	1.46	0.89	2.01	5.62	6.16	6.25	5.71	3.87	1.11	0.84
MnO	0.04	0.04	0.08	0.11	0.08	0.10	0.06	0.10	0.07	0.11	0.05	0.12	0.1	0.09	0.05	0.07
MgO	1.21	0.66	1.62	3.32	1.63	0.62	0.32	0.23	0.65	2.72	0.91	3.66	3.43	1.68	0.23	0.16
CaO	4.26	2.95	4.32	7.44	4.33	4.58	1.68	0.87	2.25	5.87	5.53	7.05	6.27	4.30	1.23	0.72
Na_2O	3.83	4.14	3.96	3.07	3.67	3.73	4.09	3.49	3.72	3.67	3.54	3.47	3.07	3.83	4.05	3.54
K_2O	2.07	3.14	3.09	1.38	1.86	1.82	3.33	4.51	3.15	1.53	2.53	1.56	1.53	2.37	3.23	4.75
P_2O_5	0.09	0.10	0.15	0.09	0.08	0.06	0.05	0.02	0.06	0.10	0.20	0.11	0.1	0.08	0.03	0.02
L.O.I.	2.56	3.80	1.73	1.61	2.31	2.05	0.29	2.63	1.95	0.90	3.16	1.06	2.33	1.11	2.65	3.28
Total	100.11	99.70	99.56	99.82	99.87	99.83	100.09	99.88	99.90	100.23	99.80	99.40	99.99	100.40	100.45	100.33
Trace elements (ppm)																
Nb	5.5	11.6	8.7	10.3	4.7	4.2	7.5	14.1	9.0	4.8	8.3	4.8	5	10.1	7.6	13.1
Zr	141	266	215	226	103	100	123	67	113	110	154	100	103	110	82	73
Sr	701	364	471	464	175	229	110	45	132	290	661	384	314	294	72	28
Cr	8	2	3	3	3	3	<1	<1	1	12	4	31	32	5	<1	<1
Ba	540	895	854	912	331	331	500	385	499	342	1224	256	267	482	501	464
Sc	9	6	10	9	15	20	2	5	5	17	20	18	19	12	4	5
V	66	54	90	83	101	89	13	6	27	126	148	138	129	84	7	3
La	19	36	33	38	16	15	24	16	29	14	39	14	16	24	25	27
Ce	40	63	61	63	29	27	44	37	53	34	82	34	32	53	46	53
Nd	17	23	23	27	13	12	16	14	21	15	39	14	16	23	17	20
Y	18	15	18	19	19	17	16	33	22	21	24	19	22	22	18	33
Rb	47	126	101	103	50	50	108	149	96	47	77	37	48	60	91	141
U	1.8	3.2	4	4	2	2	3.6	4.9	3.1	1.7	1.8	<1.5	2	2	2.6	4.7
Th	9	16	15	15	6	5	13	12	15	5	10	5	6	8	12	20
Pb	49	14	13	12	9	8	12	11	10	7	14	6	6	13	9	12
Zn	388	43	50	49	47	42	29	19	26	54	37	56	50	53	24	19
Cu	17	8	13	9	15	21	3	1	3	22	21	23	17	9	4	2
Ni	7	2	3	3	2	3	1	2	3	5	7	10	10	3	1	2

Sample no.	MIL124	MIL262	MIL180	MIL367	MIL371	MIL305	MIL308	MIL311	MIL 316	MIL235	MIL102	MIL118	MIL128	MIL175	MIL229	MIL145
Rock type	Lava	Lava	Lava	Lava	Lava	Lava	Lava	Lava	Lava	Lava	Lava	Lava	Lava	Lava	Lava	Lava
Easting	364400	364300	364300	364305	364305	364200	364200	364200	364200	364507	364000	364000	364308	364400	364400	364500
Northing	2420000	2422000	2422090	2422090	2422090	2422050	2421090	2422050	2421080	2430050	2420000	2422050	2421070	2421090	2423000	2430000
Major elements (wt%)																
SiO_2	62.08	69.09	67.25	69.9	67.93	74.53	71.25	72.78	70.82	76.70	54.15	60.99	66.41	61.69	62.45	58.17
TiO_2	0.35	0.44	0.40	0.44	0.49	0.34	0.36	0.33	0.38	0.15	0.64	0.60	0.49	0.54	0.61	0.68
Al_2O_3	16.63	16.06	14.82	15.96	16.84	12.77	13.83	13.31	13.20	12.18	17.73	16.05	15.95	16.88	16.52	16.33
Fe_2O_3	3.68	1.87	2.92	1.6	1.89	1.48	1.85	0.88	3.61	0.93	7.12	5.34	4.73	5.59	5.85	5.66
MnO	0.08	0.01	0.01	0.01	0.01	0.01	0.02	0.03	0.06	0.02	0.14	0.10	0.04	0.09	0.12	0.07
MgO	1.21	0.33	0.25	0.35	0.38	0.16	0.29	0.86	0.97	0.21	4.28	3.55	0.30	2.13	2.74	1.72
CaO	1.26	3.21	1.24	3.12	3.32	0.07	0.03	0.08	0.12	1.12	9.68	7.29	3.06	6.16	5.86	5.28
Na_2O	1.80	3.83	1.84	3.62	3.71	1.72	0.35	1.05	3.38	3.52	2.89	2.99	3.44	3.47	3.69	3.36
K_2O	9.61	2.69	8.34	3.18	3.41	7.03	10.57	8.11	4.27	3.93	1.57	1.83	2.86	1.37	1.53	1.87
P_2O_5	0.04	0.11	0.11	0.11	0.12	0.07	0.08	0.05	0.07	0.03	0.12	0.10	0.05	0.09	0.12	0.16
L.O.I.	2.67	2.14	2.38	1.73	1.96	1.67	1.56	2.07	2.65	1.35	1.80	1.55	2.61	2.01	0.32	6.38
Total	99.42	99.78	99.56	100.02	100.06	99.85	100.19	99.55	99.54	100.14	100.12	100.38	99.94	100.03	99.81	99.68
Trace elements (ppm)																
Nb	6.4	5.4	4.3	5.3	6.4	5.8	6.8	5.1	6.1	8.2	4.8	5.9	5.6	4.2	3.8	7.0
Zr	109	140	128	145	141	147	155	125	145	129	94	160	111	101	109	156
Sr	109	630	273	517	491	118	70	41	48	84	236	189	161	257	206	586
Cr	8	6	6	6	6	2	2	1	2	<1	40	48	3	7	8	16
Ba	1870	553	936	478	473	1188	1757	1828	946	545	289	313	1381	312	436	661
Sc	12	9	7	7	12	5	7	7	7	3	21	18	16	21	17	14
V	76	72	84	72	89	32	38	24	46	3	179	145	124	139	128	122
La	28	19	20	19	22	17	19	19	27	25	13	21	18	12	14	24
Ce	56	42	46	36	36	33	44	41	52	47	32	40	41	29	30	44
Nd	23	17	18	16	16	12	15	14	19	17	16	19	20	12	14	22
Y	19	13	15	12	15	17	19	14	20	18	22	26	27	18	22	16
Rb	350	67	236	89	96	166	217	176	104	104	44	60	109	33	41	76
U	1.9	2	2.5	3	3	2	2	2	3	3.6	<1.5	1.8	2	1.5	1.6	2.6
Th	9	8	9	8	8	10	10	10	11	14	5	7	6	4	6	9
Pb	57	11	1280	15	22	751	1258	1121	1189	6	18	10	48	10	7	9
Zn	1003	114	3190	55	138	524	234	717	825	11	83	57	111	93	54	56
Cu	19	13	23	9	16	22	58	88	474	4	47	23	28	25	21	17
Ni	6	4	6	2	5	1	2	3	3	1	25	19	2	6	6	8

Table A-1 Summary of SHRIMP U-Pb zircon results for sample MIL365

							Total				Radiogenic		Age (Ma)	
Grain spot	U ppm	Th ppm	Th/U	$^{206}Pb^{*}$ppm	$^{204}Pb/^{206}Pb$	f_{206}%	$^{238}U/^{206}Pb$	±	$^{207}Pb/^{206}Pb$	±	$^{206}Pb/^{238}U$	±	$^{206}Pb/^{238}U$	±
1.1	259	119	0.46	0.07	0.021765	24.40	33345.00	234.00	0.2389	0.0281	0.00023	0.00002	1.46	0.14
2.1	167	114	0.68	0.05	0.048841	42.80	2730.00	150.00	0.3837	0.0393	0.00021	0.00003	1.35	0.19
3.1	145	75	0.52	0.04	0.045760	39.20	2910.00	310.00	0.3555	0.0412	0.00021	0.00003	1.35	0.21
4.1	143	69	0.48	0.04	0.033750	28.60	2938.00	182.00	0.2715	0.0366	0.00024	0.00003	1.57	0.16
5.1	397	227	0.57	0.09	0.012390	17.00	3933.00	170.00	0.1805	0.0284	0.00021	0.00001	1.36	0.09
6.1	189	100	0.53	0.06	0.012763	47.60	2695.00	226.00	0.4219	0.0662	0.00019	0.00004	1.25	0.27
7.1	315	171	0.54	0.08	0.039249	34.00	3199.00	234.00	0.3144	0.0484	0.00021	0.00003	1.33	0.18
8.1	302	196	0.65	0.09	0.029917	31.80	3022.00	205.00	0.2969	0.0382	0.00023	0.00003	1.46	0.17
9.1	174	97	0.56	0.07	-	45.50	2166.00	222.00	0.4055	0.0527	0.00025	0.00005	1.62	0.31
10.1	243	153	0.63	0.07	0.009294	37.80	3197.00	175.00	0.3443	0.0364	0.00019	0.00002	1.25	0.15
11.1	132	54	0.41	0.05	0.062779	32.70	2342.00	213.00	0.3041	0.0373	0.00029	0.00004	1.85	0.24
12.1	110	50	0.46	0.05	0.069279	45.30	1835.00	213.00	0.4041	0.0592	0.0003	0.00006	1.92	0.4
13.1	189	111	0.58	0.07	0.028442	40.10	2468.00	168.00	0.3627	0.0738	0.00024	0.00005	1.56	0.3
14.1	217	129	0.6	0.06	0.061290	47.70	2947.00	314.00	0.4230	0.0408	0.00018	0.00003	1.14	0.21
15.1	334	248	0.74	0.1	0.023452	27.70	2892.00	150.00	0.2650	0.0447	0.00025	0.00003	1.61	0.17
16.1	119	69	0.58	0.05	0.013578	45.30	2119.00	134.00	0.4036	0.0599	0.00026	0.00005	1.66	0.31
17.1	210	103	0.49	0.05	0.041788	31.20	3382.00	238.00	0.2923	0.0785	0.0002	0.00003	1.31	0.22
18.1	220	113	0.52	0.08	0.027277	32.60	2492.00	122.00	0.3037	0.0595	0.00027	0.00004	1.74	0.24
19.1	177	120	0.68	0.06	0.048443	35.50	2590.00	238.00	0.3261	0.0549	0.00025	0.00004	1.61	0.25
20.1	236	97	0.41	0.08	0.057098	43.70	2685.00	285.00	0.3908	0.0430	0.00021	0.00004	1.35	0.24
21.1	217	141	0.65	0.06	0.034610	28.90	3142.00	160.00	0.2742	0.0291	0.00023	0.00002	1.46	0.13
22.1	194	93	0.48	0.07	0.029968	25.90	2313.00	126.00	0.2510	0.0361	0.00032	0.00003	2.06	0.19
23.1	96	47	0.49	0.04	-	44.90	2230.00	251.00	0.4003	0.0541	0.00025	0.00005	1.59	0.31
24.1	192	126	0.65	0.05	0.012637	27.80	3244.00	179.00	0.2655	0.0420	0.00022	0.00002	1.43	0.15
CRYSTALLISATION AGE:													**1.44**	**0.08**

Notes:

1. Uncertainties given at the 1s level. Uncertainty on Crysatllisation Age includes error on calibration standard FC1.
2. Error in FC1 Reference zircon calibration was 0.83 & 0.76% for the two analytical sessions (not included in above errors but required when comparing data from different mounts).
3. f_{206} % denotes the percentage of ^{206}Pb that is common Pb.
4. Correction for common Pb made using the measured $^{238}U/^{206}Pb$ and $^{207}Pb/^{206}Pb$ ratios following Tera and Wasserberg (1972) as outlined in Compston et al. (1992).

Table A-2 Summary of SHRIMP U-Pb zircon results for sample MIL243

							Total				Radiogenic		Age (Ma)	
Grain spot	U ppm	Th ppm	Th/U	$^{206}Pb^{*}$ppm	$^{204}Pb/^{206}Pb$	f_{206}%	$^{238}U/^{206}Pb$	±	$^{207}Pb/^{206}Pb$	±	$^{206}Pb/^{238}U$	±	$^{206}Pb/^{238}U$	±
1.1	333	106	0.32	0.1	0.0369870	30.47	1995	98	0.2867	0.05710	0.00035	0.00004	2.25	0.29
2.1	5183	10863	2.1	4.3	0.0370020	64.55	1041	12	0.5558	0.01760	0.00034	0.00008	2.19	0.53
3.1	318	150	0.47	0.1	0.0275830	28.73	2143	149	0.2729	0.04130	0.00033	0.00004	2.14	0.24
4.1	1069	947	0.89	0.4	0.0101610	11.48	2502	77	0.1367	0.00880	0.00035	0.00001	2.28	0.08
5.1	443	227	0.51	0.2	0.0254200	53.08	1763	56	0.4652	0.02560	0.00027	0.00004	1.71	0.28
6.1	517	301	0.58	0.4	0.0318680	68.71	1008	43	0.5887	0.03530	0.00031	0.00010	2	0.63
7.1	405	238	0.59	0.2	0.0243480	15.91	2221	74	0.1718	0.01500	0.00038	0.00002	2.44	0.11
8.1	358	214	0.6	0.1	0.0136800	19.96	2497	96	0.2037	0.02500	0.00032	0.00002	2.07	0.13
9.1 core	250	172	0.69	10.8	0.0000203	0.58	19.89	0.2	0.0573	0.00090	0.04998	0.00052	314.4	3.2
9.2 rim	799	397	0.5	0.2	0.0103060	5.78	2777	74	0.0917	0.00920	0.00034	0.00001	2.19	0.07
10.1	179	144	0.81	0.1	0.0237990	45.73	1251	47	0.4072	0.04600	0.00043	0.00007	2.8	0.44
11.1	719	465	0.65	0.2	-0.0005840	12.42	2768	80	0.1442	0.01410	0.00032	0.00001	2.04	0.08
12.1	369	202	0.55	0.3	0.0382830	76.46	916	27	0.6498	0.02090	0.00026	0.00011	1.66	0.71
12b.1	788	486	0.62	0.6	0.0361020	64.63	1178	27	0.5564	0.03190	0.0003	0.00008	1.93	0.5
13.1	163	74	0.45	0.3	0.0397600	85.26	505	27	0.7194	0.03600	0.00029	0.00023	1.88	1.5
14.1	1005	766	0.76	0.4	0.0214010	27.76	2303	59	0.2653	0.02050	0.00031	0.00002	2.02	0.13
16.1	828	711	0.86	0.3	0.0190020	30.21	2153	103	0.2846	0.03450	0.00032	0.00003	2.09	0.2
23.1 core	92	62	0.97	16.6	0.0005150	<0.01	4.772	0.059	0.0807	0.00100	0.2097	0.00275	1227	15
23.2 rim	662	53	0.08	0.5	0.0111190	11.49	1122	25	0.1369	0.01810	0.00079	0.00003	5.08	0.19
24.1	923	974	1.06	0.4	0.0124330	32.18	1792	53	0.3002	0.01260	0.00038	0.00003	2.44	0.17
CRYSTALLISATION AGE:													**2.18**	**0.09**

Notes:
1. Uncertainties given at the 1s level. Uncertainty on Crysatllisation Age includes error on calibration standard FC1.
2. Error in FC1 Reference zircon calibration was 0.83 & 0.76% for the two analytical sessions (not included in above errors but required when comparing data from different mounts).
3. f_{206} % denotes the percentage of ^{206}Pb that is common Pb.
4. Correction for common Pb made using the measured $^{238}U/^{206}Pb$ and $^{207}Pb/^{206}Pb$ ratios following Tera and Wasserberg (1972) as outlined in Compston et al. (1992).

Table A-3 Summary of SHRIMP U-Pb zircon results for sample MIL243

							Total				Radiogenic		Age (Ma)	
Grain spot	U ppm	Th ppm	Th/U	$^{206}Pb^{*}$ppm	$^{204}Pb/^{206}Pb$	f_{206}%	$^{238}U/^{206}Pb$	±	$^{207}Pb/^{206}Pb$	±	$^{206}Pb/^{238}U$	±	$^{206}Pb/^{238}U$	±
1.1	3144	5308	1.69	1.2	0.000427	1.59	2232	49	0.0587	0.005	0.00044	0.00001	2.84	0.06
2.1	1265	972	0.77	0.5	0.002513	2.95	2178	47	0.0694	0.0052	0.00045	0.00001	2.87	0.07
3.1	1028	683	0.66	0.4	0.001626	3.19	2154	51	0.0713	0.0089	0.00045	0.00001	2.90	0.08
4.1	4462	6647	1.49	1.6	0.000000	1.26	2354	31	0.0561	0.0024	0.00042	0.00001	2.70	0.04
5.1	1916	2364	1.23	0.7	0.001069	1.02	2273	39	0.0542	0.0036	0.00044	0.00001	2.81	0.05
6.1	4456	7172	1.61	1.6	0.000100	1.04	2330	30	0.0543	0.0023	0.00042	0.00001	2.74	0.04
7.1	1611	1133	0.70	0.6	0.004013	2.25	2324	43	0.0639	0.0042	0.00042	0.00001	2.71	0.05
8.1	595	593	1.00	0.2	0.007601	7.30	2246	63	0.1037	0.0162	0.00041	0.00002	2.66	0.1
9.1	1586	1085	0.68	0.7	0.009604	13.89	2078	39	0.1558	0.0108	0.00041	0.00001	2.67	0.09
10.1	2082	1955	0.94	0.7	0.001445	0.55	2494	84	0.0504	0.0037	0.00040	0.00001	2.57	0.09
11.1	2058	3275	1.59	0.7	0.003872	2.75	2379	41	0.0678	0.0059	0.00041	0.00001	2.63	0.05
15.1	1883	1713	0.91	0.7	0.003944	3.37	2289	71	0.0727	0.0071	0.00042	0.00001	2.72	0.09
16.1	1280	1207	0.94	0.5	0.001171	5.61	2387	50	0.0904	0.0067	0.00040	0.00001	2.55	0.06
17.1	1870	1735	0.93	0.7	0.001044	4.53	2372	65	0.0819	0.0072	0.00040	0.00001	2.59	0.08
18.1	3121	3814	1.22	1.1	0.001654	2.77	2360	35	0.0679	0.0032	0.00041	0.00001	2.66	0.04
19.1	3639	4221	1.16	1.3	0.001337	2.39	2331	34	0.065	0.0047	0.00042	0.00001	2.70	0.04
20.1	1222	725	0.59	0.4	0.009348	6.40	2414	54	0.0697	0.0109	0.00039	0.00001	2.50	0.07
22.1	1183	1363	1.15	0.4	0.004021	5.37	2402	76	0.0885	0.0131	0.00039	0.00001	2.54	0.09
CRYSTALLISATION AGE:													2.7	0.04

Notes:
1. Uncertainties given at the 1s level. Uncertainty on Crysatllisation Age includes error on calibration standard FC1.
2. Error in FC1 Reference zircon calibration was 0.83 & 0.76% for the two analytical sessions (not included in above errors but required when comparing data from different mounts).
3. f_{206} % denotes the percentage of ^{206}Pb that is common Pb.
4. Correction for common Pb made using the measured $^{238}U/^{206}Pb$ and $^{207}Pb/^{206}Pb$ ratios following Tera and Wasserberg (1972) as outlined in Compston et al. (1992).

Table A-4 Summary of SHRIMP U-Pb zircon results for sample MIL343

							Total				Radiogenic		Age (Ma)	
Grain spot	U ppm	Th ppm	Th/U	$^{206}Pb^{*}$ppm	$^{204}Pb/^{206}Pb$	f_{206}%	$^{238}U/^{206}Pb$	±	$^{207}Pb/^{206}Pb$	±	$^{206}Pb/^{238}U$	±	$^{206}Pb/^{238}U$	±
1.1	376	365	0.97	0.15	0.016376	10.46	2229	76	0.12870	0.0263	0.00040	0.00002	2.59	0.14
2.1	253	172	0.68	0.1	0.024734	12.83	2145	87	0.14740	0.0305	0.00041	0.00003	2.62	0.16
3.1	255	134	0.52	0.12	0.026587	22.01	1901	71	0.21990	0.0517	0.00041	0.00004	2.64	0.26
4.1	469	306	0.62	0.2	0.222480	13.25	2173	71	0.15070	0.0119	0.00040	0.00002	2.57	0.11
5.1	873	387	0.44	0.31	0.001217	4.92	2389	71	0.08490	0.0130	0.00040	0.00001	2.56	0.09
6.1	210	112	0.53	0.08	0.027604	16.4	2136	102	0.17560	0.0224	0.00039	0.00002	2.52	0.16
8.1	1510	1317	0.87	0.6	0.002470	5.31	2164	44	0.08800	0.0081	0.00044	0.00001	2.82	0.07
9.1	618	463	0.75	0.24	0.009919	7.65	2195	74	0.10650	0.0102	0.00042	0.00002	2.71	0.10
10.1	294	193	0.66	0.11	0.013334	9.66	2380	117	0.12240	0.0173	0.00038	0.00002	2.45	0.14
11.1	225	117	0.52	0.11	0.022628	31.35	1804	70	0.29370	0.0487	0.00038	0.00004	2.45	0.28
13.1	156	90	0.58	0.12	0.054216	61.82	1075	44	0.53430	0.0737	0.00036	0.00011	2.29	0.74
14.1	276	176	0.64	0.13	0.011155	25.57	1793	82	0.24800	0.0360	0.00042	0.00004	2.68	0.23
15.1	184	81	0.44	0.1	0.024675	31.64	1616	71	0.29600	0.0366	0.00042	0.00004	2.73	0.27
16.1	362	260	0.72	0.17	0.000000	23.07	1857	61	0.22830	0.0316	0.00041	0.00003	2.67	0.19
18.1	238	122	0.51	0.11	0.025613	20.6	1889	81	0.20880	0.0205	0.00042	0.00003	2.71	0.17
19.1	1157	910	0.79	0.49	0.011754	16.83	2010	44	0.17900	0.0287	0.00041	0.00002	2.67	0.15
21.1	424	352	0.83	0.39	0.009144	6.44	939	29	0.09710	0.0136	0.00100	0.00004	6.42	0.24
23.1	135	65	0.48	0.08	0.043896	37.57	1489	126	0.34280	0.0657	0.00042	0.00007	2.70	0.47
CRYSTALLISATION AGE:													**2.66**	**0.07**

Notes:
1. Uncertainties given at the 1s level. Uncertainty on Crysatllisation Age includes error on calibration standard FC1.
2. Error in FC1 Reference zircon calibration was 0.83 & 0.76% for the two analytical sessions (not included in above errors but required when comparing data from different mounts).
3. f_{206} % denotes the percentage of ^{206}Pb that is common Pb.
4. Correction for common Pb made using the measured $^{238}U/^{206}Pb$ and $^{207}Pb/^{206}Pb$ ratios following Tera and Wasserberg (1972) as outlined in Compston et al. (1992).

Table A Rock catalogue.

Field Number	Utas Number
MIL140	154062
MIL141	154063
MIL151	154064
MIL155	154065
MIL142	154066
MIL150	154067
MIL152	154068
MIL164	154069
MIL166	154070
MIL232	154071
MIL344	154072
MIL362L	154073
MIL362P	154074
MIL384	154075
MIL127	154076
MIL122	154077
MIL124	154078
MIL262	154079
MIL180	154080
MIL367	154081
MIL371	154082
MIL305	154083
MIL308	154084
MIL311	154085
MIL316	154086
MIL235	154087
MIL102	154088
MIL118	154089
MIL128	154090
MIL175	154091
MIL229	154092
MIL223	154093
MIL145	154094
MIL147	154095
MIL391	154096
MIL328	154097
MIL248	154098
MILL249	154099
MIL189	154100
MIL132	154101
MIL212	154102

Field Number	Utas Number
MIL209	154103
MIL185	154104
MIL358	154105
MIL359	154106
MIL112	154107
MIL104	154108
MIL234	154109